Electronic Thesis and Dissertation Repository

5-16-2024 2:00 PM

Microstructural MRI Evolution During Adult Mouse Brain Maturation and Concussion Recovery

Naila Rahman, *The University of Western Ontario*

Supervisor: Baron, Corey A., *The University of Western Ontario*
A thesis submitted in partial fulfillment of the requirements for the Doctor of Philosophy degree in Medical Biophysics
© Naila Rahman 2024

Follow this and additional works at: https://ir.lib.uwo.ca/etd

Part of the Biophysics Commons, Computational Neuroscience Commons, and the Developmental Neuroscience Commons

Recommended Citation

Abstract

Mild traumatic brain injury (mTBI), also called concussion, has become a significant public health concern. Current clinical neuroimaging techniques lack the sensitivity and specificity required to reliably detect signs of concussion, as large-scale changes are absent. Diffusion magnetic resonance imaging (dMRI) has arguably had the greatest influence to-date of neuroimaging modalities in mTBI, but previous studies have reported inconsistent findings, as standard dMRI lacks specificity and provides a limited model of neuroanatomy. This thesis explores the application of microstructural MR methods, that go beyond standard dMRI to improve sensitivity and specificity, to a preclinical model of mTBI and adult brain maturation. These methods include: frequency-dependent dMRI, which can probe smaller spatial scales than standard dMRI; tensor-valued dMRI, which removes the confound of fiber orientation dispersion on the diffusion measurement; and magnetization transfer saturation (MTsat) MRI, which provides specificity to myelin content.

We first characterize the reproducibility of the microstructural MR metrics applied and provide preclinical sample sizes required to detect relevant effect sizes. Given feasible sample sizes (10-15), tensor-valued and frequency-dependent dMRI metrics may provide sensitivity to subtle microstructural changes (4-8%) and moderate changes (>6%), respectively, while MTsat could detect small changes (<10%) with sample sizes of 15-20. Our investigation of brain maturation reinforces that there are continuing microstructural changes in the brain after 3 months of age, when mice are considered adults. We observe for the first time that total diffusional kurtosis increases over time are driven by increases in isotropic kurtosis during brain maturation, which may be related to glial cell diversification.

For studies that only calculate total kurtosis, we suggest caution in attributing neurobiological changes to changes in total kurtosis as we show constant anisotropic kurtosis in the presence of increasing myelin content. Finally, we provide for the first time, *in vivo* evidence of changes post-mTBI detectable with microstructural MR methods in subacute and chronic stages, while the standard dMRI metrics did not show changes. The sexually dimorphic patterns observed here, both during brain maturation and concussion recovery, may motivate more sex-dependent mTBI research, as females remain underrepresented in mTBI research.

Keywords

Summary for Lay Audience

Concussion, also known as mild traumatic brain injury (mTBI), has become a significant public health concern, with 200,000 new concussion cases in Canada every year. Many concussion patients develop long-term impairments, and the underlying brain changes remain largely unknown. Unfortunately, current clinical computed tomography (CT) and magnetic resonance imaging (MRI) techniques are unable to detect mTBI, as large-scale changes, such as hemorrhages, are absent. The changes that occur after an mTBI are on the cellular scale and include changes to cell shape and size, loss of myelin (electrical insulator that helps with brain signal transmission), and damage to cells, to name a few. As the presence and resolution of these subtle "microstructural" changes to cells cannot be detected, this results in an inability to predict who will recover completely, who will have long-term impairments, or when it is safe to return to play in contact sports. The microstructure refers to brain tissue components on the micrometer scale, such as cells and axon fibers, through which information is transmitted.

MRI is a good candidate to identify brain microstructural changes due to its strong soft tissue contrast. Conventional MRI techniques lack the specificity and sensitivity required to inform about the distinct pathological changes post-concussion. This thesis explores the capabilities of microstructural MRI methods, which focus on identifying cellular changes, in a mouse model of mTBI and healthy brain maturation. The microstructural MRI methods applied here (1) probe smaller length scales (<5 µm) than conventionally possible, providing sensitivity to cellular length scales; (2) remove the confounds that can happen when cells are not neatly aligned with each other; (3) provide specificity to myelin content.

During healthy brain maturation, continuing microstructural changes are observed, even after 3 months of age, when mice are considered adults. Overall, the trends observed in conventional metrics are comparable to previous brain maturation studies, while the trajectories of the more advanced metrics provide novel insight. We provide for the first time, *in vivo* evidence of changes post-mTBI detectable with microstructural MR methods 1-5 months post-mTBI, while the standard metrics did not show changes. This thesis indicates that these microstructural MR techniques have potential to be further optimized to better understand concussion neuropathology and its time-course, and to be applied in clinical settings to study human mTBI.

Co-Authorship Statement

I, Naila Rahman, attest that I am the principal contributor to this Thesis and the work presented herein. Below are the full author lists for Chapters 2-5 and descriptions of their contributions.

Chapter 2

Full Author List: **Naila Rahman**, Kathy Xu, Mohammad Omer, Matthew D. Budde, Arthur Brown, Corey A. Baron

Contributions:

- Conceptualization: Naila Rahman, Arthur Brown, Corey A. Baron.
- Data curation: Naila Rahman, Kathy Xu, Corey A. Baron.
- Formal analysis: Naila Rahman, Mohammad Omer.
- Funding acquisition: Corey A. Baron.
- Investigation: Naila Rahman.
- Methodology: Naila Rahman, Kathy Xu, Arthur Brown, Corey A. Baron.
- Project administration: Naila Rahman.
- Resources: Kathy Xu, Matthew D. Budde, Arthur Brown, Corey A. Baron.
- Software: Naila Rahman, Matthew D. Budde, Corey A. Baron.
- Supervision: Arthur Brown, Corey A. Baron.
- Validation: Naila Rahman, Corey A. Baron.
- Visualization: Naila Rahman.
- Writing – original draft: Naila Rahman.
- Writing – review & editing: Naila Rahman, Kathy Xu, Mohammad Omer, Matthew D. Budde, Arthur Brown, Corey A. Baron.

Chapter 3

Full Author List: **Naila Rahman**,* Jordan Ramnarine,* Kathy Xu, Arthur Brown, Corey A. Baron

Contributions:

- Conceptualization: Naila Rahman, Arthur Brown, Corey A. Baron.
- Data curation: Naila Rahman, Kathy Xu, Corey A. Baron.
- Formal analysis: Naila Rahman, Jordan Ramnarine.
- Funding acquisition: Corey A. Baron.
- Investigation: Naila Rahman, Jordan Ramnarine.
- Methodology: Naila Rahman, Kathy Xu, Arthur Brown, Corey A. Baron.

- Project administration: Naila Rahman.
- Resources: Kathy Xu, Arthur Brown, Corey A. Baron.
- Software: Naila Rahman, Corey A. Baron.
- Supervision: Arthur Brown, Corey A. Baron.
- Validation: Naila Rahman, Jordan Ramnarine, Corey A. Baron.
- Visualization: Naila Rahman, Jordan Ramnarine.
- Writing – original draft: Naila Rahman, Jordan Ramnarine.
- Writing – review & editing: Naila Rahman, Jordan Ramnarine, Kathy Xu, Arthur Brown, Corey A. Baron.

Notes: * Naila Rahman and Jordan Ramnarine contributed equally as co-first authors.

Chapter 4

Full Author List: **Naila Rahman**,* Jake Hamilton,* Kathy Xu, Arthur Brown, Corey A. Baron

Contributions:

- Conceptualization: Naila Rahman, Jake Hamilton, Arthur Brown, Corey A. Baron.
- Data curation: Naila Rahman, Kathy Xu, Corey A. Baron.
- Formal analysis: Naila Rahman, Jake Hamilton.
- Funding acquisition: Corey A. Baron.
- Investigation: Naila Rahman, Jake Hamilton.
- Methodology: Naila Rahman, Jake Hamilton, Kathy Xu, Arthur Brown, Corey A. Baron.
- Project administration: Naila Rahman.
- Resources: Kathy Xu, Arthur Brown, Corey A. Baron.
- Software: Naila Rahman, Corey A. Baron.
- Supervision: Arthur Brown, Corey A. Baron.
- Validation: Naila Rahman, Jake Hamilton, Corey A. Baron.
- Visualization: Naila Rahman, Jake Hamilton.
- Writing – original draft: Naila Rahman, Jake Hamilton.
- Writing – review & editing: Naila Rahman, Jake Hamilton, Kathy Xu, Arthur Brown, Corey A. Baron.

Notes: * Naila Rahman and Jake Hamilton contributed equally as co-first authors.

Chapter 5

Full Author List: **Naila Rahman**, Kathy Xu, Arthur Brown, Corey A. Baron

Contributions:

- Conceptualization: Naila Rahman, Arthur Brown, Corey A. Baron.
- Data curation: Naila Rahman, Kathy Xu, Corey A. Baron.
- Formal analysis: Naila Rahman.

- Funding acquisition: Corey A. Baron.
- Investigation: Naila Rahman.
- Methodology: Naila Rahman, Kathy Xu, Arthur Brown, Corey A. Baron.
- Project administration: Naila Rahman.
- Resources: Kathy Xu, Arthur Brown, Corey A. Baron.
- Software: Naila Rahman, Corey A. Baron.
- Supervision: Arthur Brown, Corey A. Baron.
- Validation: Naila Rahman, Corey A. Baron.
- Visualization: Naila Rahman.
- Writing – original draft: Naila Rahman.
- Writing – review & editing: Naila Rahman, Kathy Xu, Arthur Brown, Corey A. Baron.

Appendix A

Full Author List: **Naila Rahman**, Kathy Xu, Matthew D. Budde, Arthur Brown, Corey A. Baron

Contributions:

- Conceptualization: Naila Rahman, Corey A. Baron.
- Data curation: Naila Rahman, Kathy Xu, Corey A. Baron.
- Formal analysis: Naila Rahman.
- Funding acquisition: Corey A. Baron.
- Investigation: Naila Rahman.
- Methodology: Naila Rahman, Kathy Xu, Arthur Brown, Corey A. Baron.
- Project administration: Naila Rahman.
- Resources: Kathy Xu, Matthew D. Budde, Arthur Brown, Corey A. Baron.
- Software: Naila Rahman, Matthew D. Budde, Corey A. Baron.
- Supervision: Arthur Brown, Corey A. Baron.
- Validation: Naila Rahman, Corey A. Baron.
- Visualization: Naila Rahman.
- Writing – original draft: Naila Rahman.
- Writing – review & editing: Naila Rahman, Kathy Xu, Matthew D. Budde, Arthur Brown, Corey A. Baron.

Dedication

This work is dedicated to Sulaiman al Mahdi.

Thanks for everything, Nana.

Acknowledgments

I would like to start by thanking my supervisor, Dr. Corey Baron, who has truly been an ideal supervisor. Thank you, Corey, for concocting the perfect balance of guidance, supervision, mentorship, freedom, flexibility, science conversations, and life conversations, which allowed me to grow as a researcher as well as pursue various avenues outside the lab. Your genuine care for the wellbeing of your trainees was highly appreciated and kept me afloat through stressful times. Without exaggerating, I feel that I have won the lottery in terms of my graduate supervisor and lab.

I am grateful to my advisory committee: Dr. Arthur Brown, Dr. Robert Bartha, and Dr. Jean Théberge. Each of you has challenged me to think critically and I thank you for your guidance and insight. Thank you, Kathy Xu, for your support, commitment, and patience with me, and training me on histology. Thank you, Alex Li, Miranda Bellyou, and Scott Charlton, for your support and banter through countless hours of scanning. Thank you to all the faculty and staff at the Robarts Research Institute and the Medical Biophysics Department who have supported me over the past 5 years. I would also like to thank all my co-authors throughout this thesis – it was a team effort to design, execute, and analyze. Special thanks to Jake Hamilton for always being down to bounce off ideas and work together to interpret puzzling results.

Working at Robarts has been a very enjoyable experience and I have made some life-long comrades here, with my Baron Lab mates (Farah, Paul, Jake, Nico, Tales, Kevin, Mayuri, Filipe, Ricardo) and other Robarts mates (Maryam, Esmin, Athena, Alicia, Sam, Amr, Renil). The shared moments, from coffee breaks to celebrations and beach outings, have left me with cherished memories and invaluable lessons in both science and life. I am grateful to have met you and hope we continue to support each other.

I am exceptionally grateful to my family for their love and support. Mama and Papa, thank you for positioning us to achieve our dreams. To Omari, my mischievous but fun little brother, thanks for always telling me the harsh truth and going on random side quests together. I am also profoundly grateful for the love and support of my new-found family and second set of parents, Jaqueline and Enrique.

Finally, to Gab - my better half - I am immensely grateful for your unwavering love, support, and confidence in me. Thank you for being my best friend, for listening to my ever-present stress-rants, and all the little things every day. Your presence in my life makes every moment more beautiful, and I am forever thankful for you.

Table of Contents

List of Tables

List of Figures

List of Acronyms and Abbreviations

ΔMD   Difference in mean diffusivity between high and low oscillating gradient frequency acquisitions

Λ   Diffusion dispersion rate

μA   Microscopic anisotropy

μFA   Microscopic fractional anisotropy

ADC   Apparent diffusion coefficient

AD   Axial diffusivity

ANOVA   Analysis of Variance

APP   Amyloid precursor protein

ATP   Adenosine triphosphate

BA   Bland-Altman

BBB   Blood-brain barrier

CBF   Cerebral blood flow

CC   Corpus callosum

CHI-RF   Cortical head injury with rotational force

CNS   Central nervous system

CP   Cerebral peduncle

CSF   Cerebrospinal fluid

CT   Computed tomography

CV	Coefficient of variation
CX	Cortex
DAI	Diffuse axonal injury
DDE	Double diffusion encoding
DGM	Deep gray matter
DKI	Diffusion kurtosis imaging
dMRI	Diffusion magnetic resonance imaging
DTI	Diffusion tensor imaging
EAA	Excitatory amino acid
EPI	Echo planar imaging
f	frequency
FA	Fractional anisotropy
GM	Gray matter
HC	Hippocampus
IC	Internal capsule
K_{aniso}	Anisotropic kurtosis
K_{iso}	Isotropic kurtosis
K_{LTE}	Kurtosis arising from linear tensor encoding acquisitions
K_{STE}	Kurtosis arising from spherical tensor encoding acquisitions
K_{total}	Total kurtosis

LTE	Linear tensor encoding
MANOVA	Multivariate analysis of variance
MD	Mean diffusivity
MK	Mean kurtosis
MRI	Magnetic resonance imaging
MRS	Magnetic resonance spectroscopy
MT	Magnetization transfer
mTBI	Mild traumatic brain injury
MTR	Magnetization transfer ratio
MTsat	Magnetization transfer saturation
NMR	Nuclear magnetic resonance
OGSE	Oscillating gradient spin scho
OL	Oligodendrocyte
OLF	Olfactory region
OPC	Oligodendrocyte precursor cell
PET	Positron emission tomography
PFC	Prefrontal cortex
PGSE	Pulsed gradient spin echo
qMRI	Quantitative magnetic resonance imaging
RD	Radial diffusivity

RF	Radiofrequency
ROI	Region of interest
ROS	Reactive oxygen species
SNR	Signal-to-noise ratio
SPECT	Single photon emission computed tomography
STE	Spherical tensor encoding
T	Tesla
TE	Echo time
TH	Thalamus
TR	Repetition time
WM	White matter

Chapter 1

1 Introduction

1.1 Overview

The development of *in vivo* brain imaging methods has provided a basis for studying the anatomy and physiology of the normal and the diseased central nervous system (CNS), helping to elucidate the underlying mechanisms of neurological diseases. High sensitivity, specificity, and spatial resolution are hallmarks of ideal brain imaging techniques, to allow the study of cellular structures underlying mechanisms of brain processes. These *in vivo* techniques include computed tomography (CT) and magnetic resonance imaging (MRI) (for structural imaging); positron emission tomography (PET), single-photon emission CT (SPECT), and functional MRI (for functional imaging); and optical imaging (for both structural and functional imaging) (1,2). Among these techniques, MRI is highly versatile and unique as it provides high soft-tissue contrast; is capable of imaging at any depth in the body without the use of potentially harmful ionizing radiation; and has customizable contrast mechanisms to reflect structural, functional, water diffusion, and perfusion contrasts (to name a few).

Quantitative magnetic resonance imaging (qMRI) goes beyond conventional MRI, as it provides specific physical parameters which carry information about the local microstructural environment of protons (3), in addition to qualitative images. Examples include (but are not limited to) magnetization transfer, diffusion MRI, quantitative susceptibility mapping, and perfusion MRI. Compared to conventional MRI, qMRI can provide more sensitive measures of pathology and more specific information regarding

which tissue component (such as myelin, axons, and glia) has been damaged (4). Thus, qMRI has the potential to make great clinical impact on diagnostics by enabling earlier detection of disease, complementing or replacing biopsy, providing clear numeric differentiation of disease states, and increasing the quality of information available to artificial intelligence algorithms. However, the incredible amount of variability in clinically used image acquisition and post-processing techniques hinders current efforts to extract reliable, consistent, and accurate quantitative information from routine MRI exams (5). Current qMRI research aims to develop methods that are reliable, repeatable, further our understanding of the normal brain development and diseased brain pathology, and may have an impact on the decision-making process for patient care. For many neurological conditions, the gold standard method of diagnosis is through histological assessment of microstructure, which is only possible through biopsies or post-mortem (6). However, biopsies are invasive, not typically done for the brain, and do not provide a complete picture of the lesion/injury site. Thus, imaging brain tissue microstructure *in vivo* to uncover micrometer-scale tissue features, using qMRI, is of great interest to the clinical and MRI community. As there are a myriad of diseases which are challenging to detect via clinical imaging in their early stages, there is a need to develop techniques that are more sensitive to microstructural changes in the brain.

Diffusion MRI (dMRI), a key modality for microstructure imaging, probes tissue microstructure by quantifying the diffusion of water molecules (7). However, standard dMRI lacks the specificity to identify unique microstructural environments (e.g., cannot distinguish between loss of structural integrity and fiber orientation), and leads to an inherently vague and limited model of neuroanatomy (8). Thus, more sophisticated dMRI

acquisition and reconstruction techniques have been developed to overcome the limitations of standard dMRI.

1.2   Scope of Thesis

To enable the specificity required to characterize microstructure, we are implementing multimodal microstructural MRI, wherein each technique will be sensitive to microstructure in complementary ways. The techniques include: frequency-dependent dMRI; tensor-valued dMRI; and magnetization transfer saturation (MTsat) MRI. Frequency-dependent dMRI (9,10) can modify the sensitivity to cellular length scales to probe smaller length scales than possible by conventional dMRI; tensor-valued dMRI (11–13) varies the sensitivity to diffusion anisotropy, reducing fiber orientation dispersion effects on diffusion measurements; magnetization transfer saturation (MTsat) MRI provides increased specificity to changes in myelin content compared to the conventional magnetization transfer ratio (MTR) method (14,15).

These advanced microstructural MRI metrics have been applied to a select number of diseases so far, including multiple sclerosis (16–18), ischemic stroke (19,20), and brain tumour differentiation (16,21). This thesis aims to characterize the reproducibility of these advanced metrics at ultra-high field strength and explore their applications to healthy rodent brain maturation and concussion recovery. Although concussion has become a significant public health concern, current clinical neuroimaging techniques lack the sensitivity and specificity required to reliably detect signs of concussion, as large-scale changes such as hemorrhages are absent (22). This results in an inability to predict who will recover completely, who will have long-term impairments, or when it is safe to return to play in contact sports.

The goals of this thesis were threefold: (a) to implement microstructural MRI protocols at 9.4 Tesla and characterize the test-retest reproducibility of the MR metrics to provide estimates of sample sizes required for future investigations; (b) to further our understanding of the contrast mechanisms of these advanced MR metrics; (c) to explore the evolution of these metrics during adult mouse brain maturation and concussion recovery and disentangle what changes in these metrics may indicate on a neurobiological level. We hypothesized that through this work, we will uncover novel contrast mechanisms of these microstructural MR metrics and gain a better understanding of the time course of both adult mouse brain maturation and concussion recovery, as this is the first time that these advanced metrics are being applied to mouse brain maturation and concussion recovery.

Chapters 2 and 3 present test-retest reproducibility studies of advanced diffusion MRI and magnetization transfer MRI metrics, respectively. Both chapters describe the implementation of the MRI protocols used in this thesis, characterize both region-of-interest based and voxelwise test-retest reproducibility of the *in vivo* MRI metrics, and report sample sizes required to detect a variety of effect sizes. As no test-retest assessment of these advanced MR protocols have been done at ultra-high field strength, there is a need to establish the reproducibility of these metrics, which is essential in planning future preclinical neuroimaging studies involving models of disease/injury.

Although rodent models are a predominant study model in basic neuroscience research, research investigating healthy rodent brain maturation remains limited. This motivates further study of normal brain maturation in rodents to exclude confounds of developmental changes from interpretations of disease mechanisms. Chapter 4

investigates healthy rodent brain maturation in mice scanned longitudinally at 3, 4, 5, and 8 months of age, and provides a discussion of what the evolution of MR metrics suggests on a neurobiological level. We hypothesized that we would see microstructural changes in the brain, even after 3 months of age, at which stage a steady state condition of adulthood is assumed in many neuroimaging studies (23). Furthermore, we hypothesized that the evolution of conventional MR metrics in mice would be comparable to healthy brain maturation studies in the literature (23,24), while the advanced MR metrics would reveal novel insight. Notably, this is the first time that the evolution of these advanced MR metrics is explored during healthy brain maturation.

Chapter 5 explores the evolution of the MR metrics in a mouse model of concussion. Previous dMRI studies in rodent models of mTBI reported no significant changes in metrics (25) or inconsistent findings across studies (22). Thus, we hypothesized that the more advanced dMRI metrics would be more sensitive to microstructural changes post concussion, compared to the conventional dMRI metrics. Importantly, this is the first time that these advanced metrics are applied to a model of concussion.

The rest of this chapter provides background information regarding the brain, adult brain maturation, concussion pathophysiology, MRI, and diffusion and magnetization transfer MRI.

1.3   The Brain

A brief overview of brain microstructure and macrostructure is given below. For a more detailed description, the reader is referred to *Clinical Neuroanatomy* by Waxman (26) and *Neuroanatomy: An Illustrated Colour Text* by Crossman & Neary (27).

1.3.1   Brain Microstructure

The functional unit of the nervous system is the nerve cell or neuron. These cells are highly specialized for the encoding, conduction, and transmission of information. Glial cells, or glia, are support cells of the nervous system and crucial for normal neural function. Approximately 50% of the volume of the brain is occupied by neurons, while the other half of the volume consists of glial cells (28,29).

Neurons:

The function of the neuron is to receive and integrate information from sensory receptors and other neurons and to transmit information to other neurons and other parts of the body, like muscles and glands. Neuronal architecture is highly specialized with each neuron being a separate entity with information passed at specialized regions called synapses. The neuron has a single cell body, also called soma, from which a variable number of branching process emerge, which are called the axon and dendrites (as shown in Figure 1.1). Most neurons have a single axon, to transmit signals, and many dendrites, to receive signals.
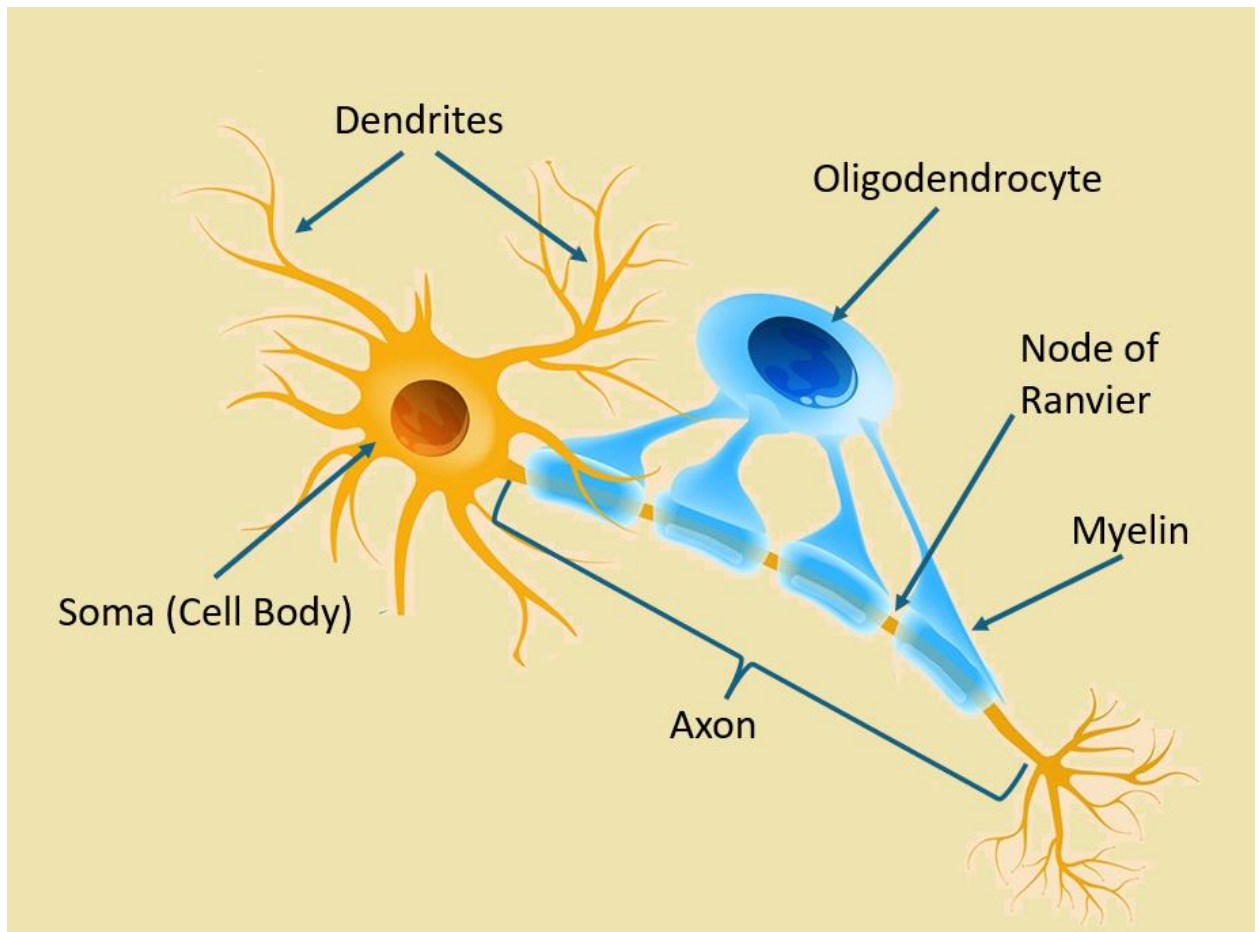
Figure 1.1 – *The structure of a typical neuron, with dendrites, which receive information from other neurons or from sensory receptors, and the axon, which transmits signals to the synapses, extending from the soma (cell body). An oligodendrocyte wraps its processes around the axon, forming myelin. The myelin sheath is separated by small gaps, called the nodes of Ranvier, where myelin is absent. Image adapted from Salas et al.* (30) *(no permission required).*

Axons:

The axon is a cylindrical tube of cytoplasm covered by a membrane, the axolemma. A cytoskeleton consisting of neurofilaments and microtubules runs through

the axon. In addition to conducting action potentials, axons transport material to and from the synaptic terminals and soma, with the microtubules providing a framework for fast axonal transport.

Communication between neurons usually occurs from the axon terminal of the transmitting neuron (presynaptic terminal) to the receiving region of another neuron (postsynaptic terminal), which together form a complex called a synapse, or synaptic junction. Impulse transmission at synapses is either chemical (involving the release of neurotransmitters) or electrical, where current passes through synapses called gap junctions. Chemical transmission involves the release of neurotransmitters from the presynaptic terminal, which can depolarize (more likely to fire an action potential) or hyperpolarize the postsynaptic neuron, depending on the ions involved.

Myelin:

Myelin is a lipid-rich material produced by oligodendrocytes (in the central nervous system) and by Schwann cells (in the peripheral nervous system). Myelin functions as an electrical insulator by covering axons in concentric layers. The myelin sheath is separated by small gaps, called the nodes of Ranvier, where myelin is absent (as shown in Figure 1.1). This serves to increase the speed of action potentials through axons, as electrical impulses "jump" between the nodes of Ranvier.

Astrocytes:

Astrocytes are star-shaped cells and have small cell bodies with long processes radiating in all directions. They provide structural support to nervous tissue, maintain an

appropriate concentration of ions such as potassium (K^+) within the extracellular space, and have many other supportive roles.

Microglia:

Microglia are scavengers of the central nervous system, constantly surveying the brain to detect and destroy invaders. When an area of the brain is damaged or infected, microglia activate and migrate to the site of injury to remove cellular debris. Some microglia are always present in the brain, but when injury or infection occurs, others can enter the brain from blood vessels.

Oligodendrocytes:

Oligodendrocytes wrap their processes around axons, forming myelin. A single oligodendrocyte can wrap myelin around many (up to 30 – 40) axons. Oligodendrocyte precursor cells (OPCs) proliferate and differentiate to produce myelinating oligodendrocytes (OLs) throughout postnatal and adult life (31).

1.3.2   Brain Macrostructure

The major components of the brain are gray matter (GM), white matter (WM), and cerebrospinal fluid (CSF). Gray matter contains neuronal and glial cell bodies, axons, dendrites and synapses; white matter contains myelinated axons and glial cells; CSF is a clear fluid that contains glucose, proteins, electrolytes, and other materials providing essential central nervous system (CNS) nutrition and immune function. Gray matter is comprised of cortical gray matter, which lines the outer surface of the brain, and deep gray matter, which contains GM brain regions such as the hippocampus, thalamus, and

amygdala, segmented based on their function. White matter consists of axonal fiber bundles that facilitate communication between and within different gray matter regions. CSF is made in ventricles, which are fluid-filled cavities in the brain, and surrounds the brain and spinal cord, acting as a shock absorber and maintaining homeostasis by regulating the chemical environment.

1.4   Adult Brain Maturation

Changes in the ageing brain and in the developing brain are well documented in clinically healthy individuals, that is, in humans aged 35–65 years, and from birth to adolescent years (32,33). In rodents, this coincides with ages from 12–24 months, and from birth to 2 months of age. Despite numerous studies on the microstructural changes of the human brain throughout life, we have little knowledge about the changes from early to mid-adulthood. There is increasing evidence that there are ongoing microstructural changes during the brain maturation phase, primarily due to brain plasticity, from early to mid-adulthood.

The term "plasticity" refers to the possible significant neuronal changes that occur in the acquisition of new skills (32,34–36). Neuronal proliferation, rewiring, dendritic pruning, and environmental exposure are important components of brain plasticity during adolescence. Following neuronal proliferation, the brain rewires itself from the onset of puberty up until 24 years old, especially in the prefrontal cortex. The rewiring is accomplished by dendritic pruning and myelination. Dendritic pruning eradicates unused synapses and is generally considered a beneficial process, and myelination increases the speed of impulse conduction across the brain's region-specific neurocircuitry, thus

optimizing communication throughout the CNS and improving information processing speed.

Diffusion MRI study in adults (from young to middle-aged) have provided convincing evidence that considerable microstructural changes of the human brain occur from early to mid-adulthood (33), with regional age-related cortical thinning, white matter volume increases, and changes in diffusion parameters during healthy brain maturation (37). In a lifespan study of healthy subjects aged 5-83 years, Lebel et al. (38) found age-related changes with diffusion MR changes following a U-shaped or inverted U-shaped trajectory, demonstrating rates and timing of development and degradation that vary regionally in the brain. Postmortem studies have also provided valuable insight into white matter development, demonstrating continued myelination of white matter tracts into the second and third decades of human life (39,40).

Glial cells (microglia, astrocytes, and oligodendrocytes) play significant roles in circuit formation, maturation, and maintenance and are key regulators of neuronal plasticity (41,42). There is a strong homeostatic mechanism that matches myelinating OLs to the requirements of neural circuitry and axonal activity (31). This activity-dependent OL plasticity is called "adaptive myelination", implying that it can modify the neuronal circuitry to provide a survival advantage (43–45). In rodents, OPCs are capable of undergoing bursts of rapid proliferation after 6 months of age, resulting in clonal expansion (46).

1.5   Concussion

Concussions are a significant public health concern, with approximately 200,000 cases reported annually in Canada (47). Despite being among the most challenging injuries to diagnose and manage in sports medicine, sports-related concussions remain underreported due to a lack of public awareness about their consequences (48). Traumatic brain injury (TBI) is typically categorized by severity into mild, moderate, and severe forms, with mild TBI (mTBI or concussion) being the most common (49). While structural MRI and CT show sensitivity to TBIs, they often show normal findings in mTBI cases (50,51). Additionally, CT and MR findings are poor indicators of persistent symptoms in patients with mTBI (52). Biomarkers for diagnosing and assessing the severity of mTBI are not yet established, although techniques like diffusion tensor imaging (DTI), described in Section 1.6.5, and magnetic resonance spectroscopy (MRS) are promising (53,54).

Mild TBI is defined as acute neurophysiologic brain dysfunction resulting from impact contact forces or sudden acceleration/deceleration causing a transient alteration of consciousness and/or a period of anterograde (and possibly retrograde) amnesia (55). Symptoms of mTBI include headaches, fatigue, depression, anxiety, confusion, dizziness, visual disturbances, and cognitive impairments, with some individuals experiencing long-term cognitive deficits. Diagnosis of mTBI relies on the symptomatology mentioned above, but this subjective assessment can be imprecise and unreliable.While symptom resolution in most concussion patients occur within 3 months post-injury, 15 % of individuals with a single mTBI demonstrate long-term cognitive impairment (56–58). A more recent review by McInnes et al. (49) found that the 15 % estimate is an

underestimation, and approximately half of individuals with a single mTBI demonstrate long-term cognitive impairment. The pathological mechanisms underlying this incongruence remain largely unknown, presenting a need to continue efforts to better understand the transition from early phase to late phase disorder after mTBI.

1.5.1 Concussion Diagnosis, Imaging, and Treatment in the Clinic

There are a variety of clinical approaches that medical sports physicians use to diagnose and monitor concussed individuals. These protocols involve a battery of neurocognitive tests that measure functional capacity across a wide range of tasks that assess memory, balance, decision-making, and cognition (59). They also provide a way for physicians to monitor a wide range of possible symptoms and the patient's self-reported severity of those symptoms. Sports medicine physicians will first enquire about the injury itself (information like mechanism of injury, direction, acute symptoms such as loss of consciousness or memory) and then, with the help of standard clinical protocols like the Sports Concussion Assessment Tool (SCAT) and Immediate Post-Concussion Assessment and Cognitive Testing (ImPACT), they will assess the patient for symptoms, monitor their recovery, and make decisions about return to play.

The SCAT involves a series of subtests (60), including the Glasgow coma scale (GCS) that assesses eye, verbal, and motor response on a total scale of 15 to objectively record a patient's state of consciousness, where generally an mTBI would be rated greater than or equal to 13 and severe injuries are less than 8 or 9. The Maddocks score is obtained though it is designated for sideline diagnosis of concussion and involves more specific questions targeting orientation and memory such as "did your team win the game

last week?". The physician will enquire about the number and severity (on a scale of 0 [none] to 6 [severe] for a total possible score of 132) of symptoms from a list of 22 possible symptoms including headache, neck pain, nausea, confusion, difficulty remembering, concentrating or sleeping, light and sound sensitivity, and emotional instability or changes. The ImPACT is an online tool that also involves assessing 22 symptoms and their severity as well as neurocognitive tests that evaluate attention, verbal recognition and visual working memory, visual processing speed, reaction time, and impulse control (61).

Impaired reaction time has been shown to be one of the most sensitive indicators of persistent deficit after injury (59). Reaction time has traditionally been measured by computerized testing, usually assessed by pushing a key in response to a prompt. Considerable research has shown that reaction time is prolonged immediately after injury and improves gradually until returning to baseline. Reaction time may even persist beyond resolution of symptoms, thus making it a useful tool in objectively assessing recovery to be used in conjunction with a patient's self-reported symptoms.

However, results from neuropsychological tests may be difficult to interpret when an intrapatient baseline comparison is not available (59). With concussed athletes and military personnel, return to baseline neuropsychological state is important. In the general population, baseline data may not be available. Additional issues with neuropsychological testing include premorbid learning disabilities that are not discernable with testing, underreporting of prior concussions, language issues, administration of testing in a suboptimal environment (including an unsupervised condition, such as computerized testing), and appropriateness of the test for the age of the

injured individual (62). Another challenge is that some individuals may perform perfectly, suggesting a ceiling effect, which limits the ability of the test to detect minor changes, especially in those who perform at the top (63). Similarly, a floor effect may also limit the usefulness of a test for determining changes in an individual who already performs poorly at baseline (64). All current evidence- and consensus-based sports concussion recommendations advise against having a single test to diagnose or manage concussion, and that these tests should be used in conjunction with other evaluation modalities to make diagnostic and management decisions (59). Although symptom recovery can be monitored, it is unknown exactly how and when the brain physically recovers. Non-invasive imaging could aid in understanding the neurophysiology underlying concussion acutely and during the recovery period.

While medical imaging is not the standard of care for assessment of a concussed patient, in some cases the physician may recommend a CT or a structural MRI image to ensure that there is no pathology consistent with a more serious injury or trauma (59). CT has been historically used as the standard of care for assessment of TBI in emergency department settings, but radiation exposure may present its own risks, particularly in children. Previous studies using CT showed a correlation between intracranial hemorrhage and long-term deficits (65). MRI is more sensitive for elucidating small, focal intracranial lesions, and thus may be more sensitive in determining those individuals at risk for prolonged recovery. The TRACK-TBI group studied mTBI patients presenting to the emergency department with CT and MRI, and found the presence of intracranial findings (cortical contusion or four or more microhemorrhages on MRI) predicted 3-month outcome, specifically for determining which patients may be those to

develop persistent dysfunction (66). Clinical MR sequences are sensitive to fluid where excessive liquid (e.g. microbleeds) will produce a hyperintense signal, as well as subcortical white matter lesions that may appear hyper-intense and could indicate a more severe diffuse axonal injury (67). Importantly, these white matter hyper-intensities are not sufficient clinical diagnostic tools because they are only present in a fraction of TBI patients and may appear in healthy individuals at 3T or could be related to other independent pathology, especially in older patients. This demonstrates the clinical difficulty with diagnosis and monitoring mTBI patients and the need for more advanced sequences that can probe subtle brain changes that are not visible on clinical anatomical CT and MR scans.

Concussion management begins with removal from risk if a concussion is suspected, and once diagnosis is made, education and reassurance is provided (59). Management of acute symptoms are addressed individually, such as traditional over-the-counter medication for headaches, antianxiety or antidepressants for mood disorders, melatonin for sleep, and psychotherapy or cognitive-behavioral therapy for various cognitive or behavioral issues. Once symptoms have resolved after a period of rest, a graded return-to-play protocol can be implemented with close supervision and observation for return of symptoms. However, there is no consensus period for which rest should be prescribed, and the exact recommendations of "rest" are not clear (68). Management should be tailored to the individual, and if symptoms are prolonged, further diagnostic evaluation may be necessary. A special consideration in the pediatric and collegiate populations is return-to-learn prior to return-to-play. With these student-

athletes, Choe *et al* recommend that they should be back to full schoolwork without accommodations before returning to full physical activity (59).

1.5.2   Acute Neurometabolic Cascade

As post-concussive deficits are characterized by minimal observable anatomical damage that typically resolves over time, they are believed to stem from transient neuronal dysfunction rather than cell death (69,70). This dysfunction can result from various factors such as ionic shifts, altered metabolism, impaired connectivity, or changes in neurotransmission. The understanding of concussion necessitates a comprehensive grasp of its underlying pathophysiology.

Immediately after biomechanical injury to the brain, there is disruption of neuronal membranes, axonal stretching, and opening of potassium (K^+) channels, which leads to an increase in extracellular K^+ (69,70). As extracellular K^+ increases, neuronal depolarization is triggered, leading to release of excitatory amino acids (EAAs), such as glutamate, and opening of EAA receptor channels, and still greater K^+ flux. Efforts to restore ionic balance prompt activation of sodium-potassium pumps which require adenosine triphosphate (ATP) (71), and thus lead to an increase in glucose utilization, initiating a period of hyperglycolysis. Calcium (Ca^{2+}) influx follows, contributing to mitochondrial dysfunction and decreased oxidative metabolism, ultimately leading to energy failure. This increase in glucose use occurs almost immediately after fluid percussion injury in rats and persists for up to 30 minutes in the hippocampus (72). Calcium accumulation is seen within hours of experimental concussion and may persist for 2 to 4 days (73). Increased axonal Ca^{2+} levels have been shown to lead to microtubule

breakdown from 6 to 24 hours after the initial injury, which can lead to secondary axonal injury, discussed in the next section.

After the initial period of hyperglycolysis, cerebral glucose use is diminished by 24 hours post-injury and remains low for 5 to 10 days in preclinical studies (72). Positron emission tomography (PET) in humans shows similar decreases in global cerebral glucose metabolism that may last 2 to 4 weeks post-TBI (74). In experimental TBI, cerebral blood flow (CBF) may be reduced to 50% of normal (75). The increased glucose use (hyperglycolysis) coupled with lower CBF represents a mismatch in supply and demand, which results in a potentially damaging energy crisis. Injured cells may be capable of recovering after an initial injury, but a second concussion during this energy crisis can lead to cell death (69). Thus, repeated injury within a particular time frame can lead to a much larger anatomical and behavioral impairment.

1.5.3   Subacute Pathophysiology

Subacute pathophysiology caused by the initial neurometabolic cascade include axonal injury, impaired synaptic plasticity, neuroinflammation, blood-brain barrier dysfunction, possible cell death, and demyelination (69,70,76). Each of these aspects are described in detail below.

Axonal Injury:

Diffuse axonal injury (DAI) is a common feature of mTBI, involving axonal stretching, mitochondrial swelling, and disrupted axonal transport mechanisms, often leading to hyperphosphorylation of tau protein and subsequent neurodegenerative processes. This is partly because the anisotropically arranged axonal fibers in white

matter tracts are highly susceptible to compression, tension, and torsion forces during rapid acceleration or deceleration (77,78). Hyperphosphorylation of tau, a protein crucial for stabilizing neuronal microtubules, occurs in TBI, causing reduced microtubule binding and disassembly, ultimately impairing axonal transport and compromising neuronal and synaptic function (79). Moreover, this leads to tau aggregation, which has been linked to subsequent neurodegenerative disease (80). There is an accumulation of other proteins as well, particularly amyloid precursor protein (APP), which leads to the formation of multiple axonal swellings (also referred to as 'axonal beads' and the process of 'axonal beading') hindering axonal transport (81). Figure 1.2 depicts the axonal beading process. This protein buildup can trigger secondary processes that result in the disconnection of axons. While the detached distal segment of the axon undergoes Wallerian degeneration, the proximal segment and its neuronal soma often swell but may not necessarily die (82).
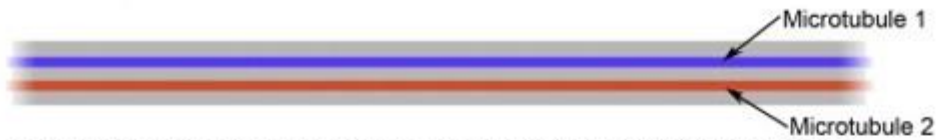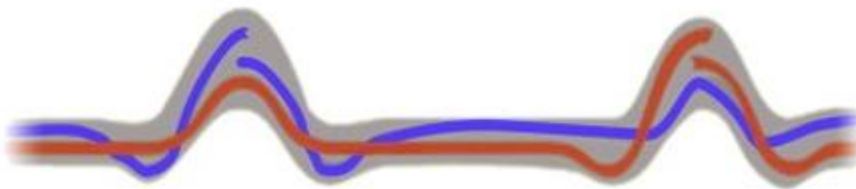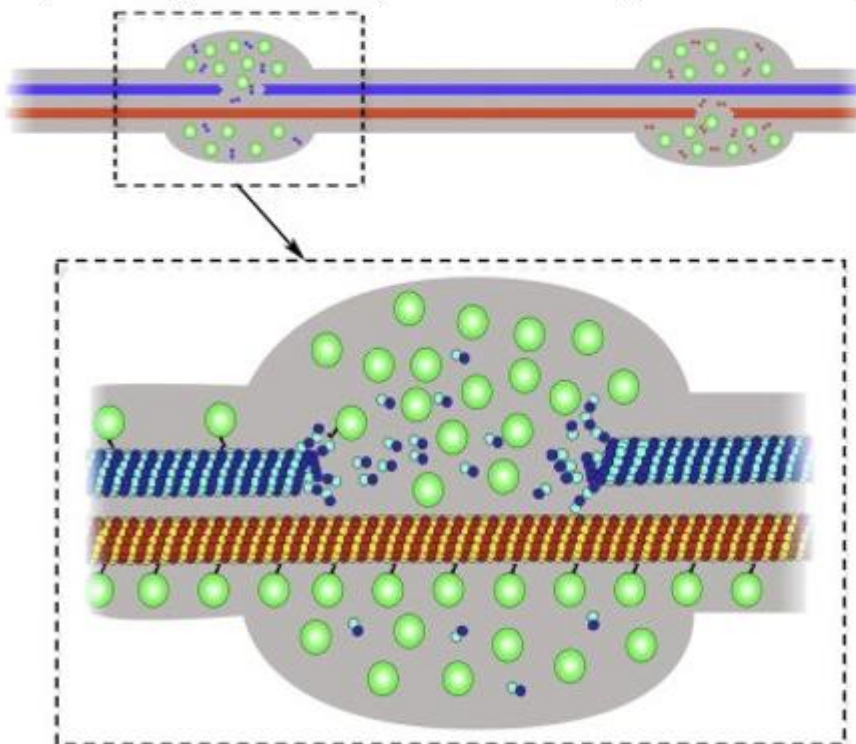
Figure 1.2 – *Mechanism of axonal beading following mTBI. (a) Two microtubules within an intact axon (pre-injury). (b) Following injury, mechanical breaking occurs at different*

sites in both microtubule 1 and microtubule 2. Misalignment of broken microtubules causes deformation of the axon observed as two discrete undulations. (c) Shortly afterward, depolymerization from the broken ends of the microtubules allows the undulations to collapse and the axon recovers its linear morphology. (d) Microtubule breakage leads to impairment of axonal transport and subsequent accumulation of transported cargos near the microtubule breaking point. By contrast, axon transport on the intact microtubules remains normal. This 'partial transport impairment' may account for the formation of serial swellings or axonal beading following mTBI. Image adapted from Tang-Schomer et al. (83) *with copyright permission from Elsevier.*

Impaired Synaptic Plasticity:

During normal development, the reorganization of dendritic spines results in synaptic remodeling (84). An *in vivo* rat model demonstrated that mTBI induces alterations in glutamate receptors and release of the inhibitory neurotransmitter GABA. These changes subsequently disrupt normal developmental plasticity and memory in rats (85).

Neuroinflammation:

Neuroinflammation, characterized by activation of astrocytes, microglia, macrophages, and inflammatory cytokines (a type of cell-signaling molecule), exhibits both neuroprotective and neurotoxic effects, impacting the progression of injury and recovery (70,76). Figure 1.3 shows activated forms of astrocytes and microglia.

Astrocytes act as key responders to changes in the extracellular environment following mTBI (86), becoming reactive through hypertrophy and proliferation. Astrocytes play a pivotal role in regulating the inflammatory process and limit the extent of damage through reactive astrogliosis (87). Reactive astrogliosis can be defined as a finely graded continuum of multiple potential changes that range from reversible alterations in gene expression and cell hypertrophy, to scar formation that involves substantial cell proliferation and permanent rearrangement of tissue structure. Astrocytes can produce immunomodulatory molecules, such as cytokines, and inflammatory mediators to promote clearance of cytotoxic cellular debris and decrease inflammation. In response to focal tissue damage or inflammation, reactive astrocytes form scar borders that segregate damaged tissue from adjacent healthy tissue. However, reactive astrocytes can also release free radicals and proinflammatory cytokines, which can trigger the activation of microglia. The outcome of these dual responses — neuroprotective and neurotoxic — is observed in preclinical models of TBI, with the balance influenced by the nature and severity of the injury (88,89).

Microglia and macrophages are primary contributors to tissue inflammation beyond the core injury site (90). Microglia are highly specialized macrophages that are distributed throughout the brain parenchyma and serve as the primary immune effector cells in the CNS (91). Microglial proliferation is detectable within 24 hours post-injury (92). Peripheral macrophage infiltration is detectable within a few days post-injury, as monocytes infiltrate the blood-brain barrier and are converted into macrophages. Following injury, microglia and macrophages migrate towards the site of damage, engulfing necrotic tissue, cellular debris, and harmful substances (93). As prolonged

microglial activation contributes to the spread of secondary degeneration (94), sustained inflammation plays a critical role in long-term axonal injury, neurodegeneration, and subsequent neurological deficits (93,95,96).
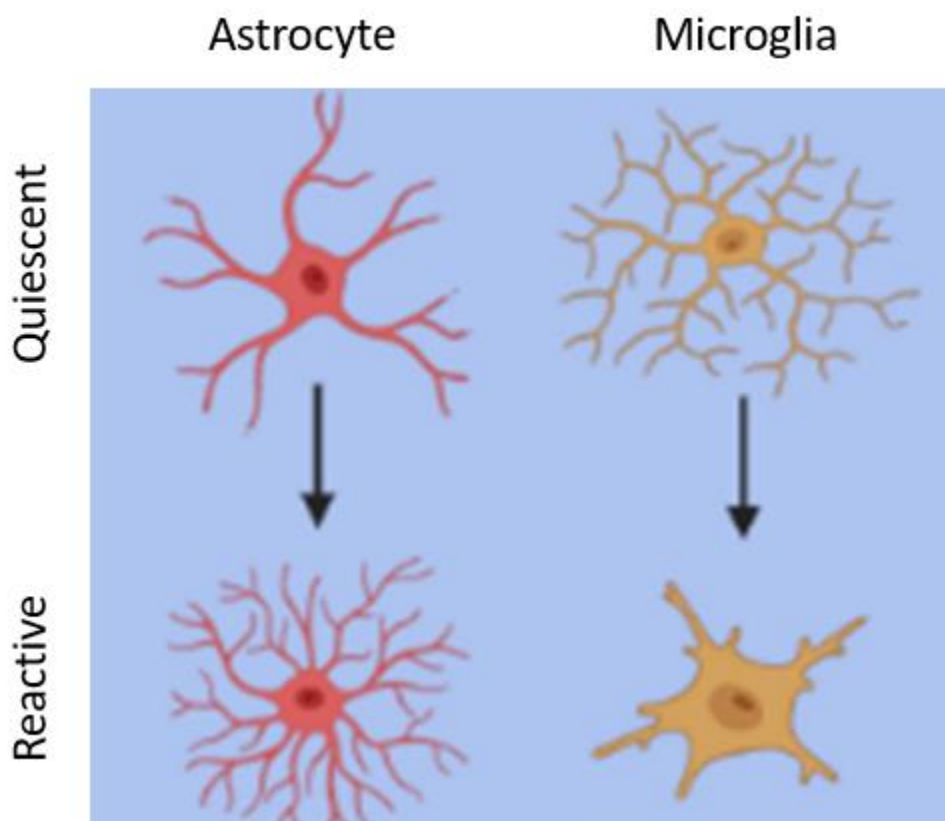
Figure 1.3 – *Astrocyte reactivity and microglial activation post-concussion. In their reactive state, astrocytes have a ramified appearance, and microglia have an ameboid appearance. Image adapted from Freire et al.* (97) *(open access).*

Blood-Brain Barrier Dysfunction:

The blood-brain barrier (BBB) is a complex network of capillaries responsible for maintaining a stable extracellular environment by regulating the passage of blood substances into the brain (70). BBB dysfunction following mTBI exacerbates

neuroinflammation, with disruptions in BBB integrity allowing infiltration of other inflammatory cells, such as neutrophils, monocytes, and lymphocytes. Neuroimaging reveals evidence of BBB disruption following both mild and moderate TBIs, with the BBB typically recovering its integrity within days to weeks (98). BBB disruption has also been observed in American football players due to exposure to subconcussive head impacts (99).

Cell Death:

While cell death is prominent in moderate and severe TBI, preclinical mTBI models have indicated limited cell death (70). One study revealed that patients with recent mTBI exhibit significantly smaller volumes in key brain regions two months after injury, but brain tissue volume is recovered one year post injury (100).

Demyelination:

Demyelination (a loss of myelin with relative preservation of axons) can arise from various mechanisms, including primary axonal injury leading to Wallerian degeneration or the death of myelin-producing cells (oligodendrocytes) (76). Rodent models have demonstrated subacute loss of myelinated axons and changes in myelin structure following moderate TBI (101,102). Oligodendrocytes, which produce significant amounts of reactive oxygen species (ROS), are particularly vulnerable to oxidative stress that occurs after mTBI. Additionally, myelin debris can trigger inflammation, leading to the activation of microglia and astrocytes, which further promote myelin breakdown (103) and the recruitment of oligodendrocyte progenitor cells (OPCs) to damaged brain regions (104). Despite an acute regenerative response observed

with OPC localization to injured areas, dysmyelination (which is atypical myelinogenesis that results in abnormal or delayed myelination) and demyelination can persist and progress for up to one year post-injury (105). This coincides with prolonged microglial and astrocytic activation suggesting sustained myelin debris-induced stimulation (106,107).

1.6   Magnetic Resonance Imaging

Magnetic resonance imaging (MRI) is arguably one of the most versatile *in vivo* imaging techniques because the measured signal can be sensitized to a variety of features of the tissue and thus yield a very broad range of contrasts and information. This section provides a brief overview of classical MR physics, contrast mechanisms, as well as diffusion and magnetization transfer MRI. For more detail, the reader is referred to the following references, which provide in-depth discussions of MR physics and pulse sequences:

- Nishimura, Dwight G. *Principles of Magnetic Resonance Imaging.* Lulu, 2010.

- Bernstein, Matt A., Kevin F. King, and Xiaohong Joe Zhou. *Handbook of MRI pulse sequences.* Elsevier, 2004.

1.6.1   Nuclear Magnetic Resonance

Any nucleus with an odd number of protons and/or an odd number of neutrons possesses a nuclear spin angular momentum (108). These MR-relevant nuclei give rise to a small magnetic moment and are referred to as "spins". In biological tissue, hydrogen (^{1}H), with a single proton, is the most abundant nucleus, and thus most MR research is

based on proton (^{1}H) imaging. In ^{1}H MRI, the signal originates primarily from water molecules in tissue.

In the absence of an external magnetic field, the spins are oriented randomly, and the net macroscopic magnetic moment is zero. However, in the presence of an external magnetic field, B_0, (a) individual magnetic moments have a slight tendency to align in the direction of B_0 (referred to as the z-axis or longitudinal direction, by convention) to create a net magnetization and (b) exhibit precession about the z-axis at a well-defined frequency called the Larmor frequency (ω_0). The Larmor frequency relates to B_0 by:

$$\omega_0 = \gamma B_0 \tag{1.1}$$

Where γ is the gyromagnetic ratio, a known constant unique for each type of atom. For ^{1}H, γ = 42.58 MHz/T. To generate a signal for MRI, the net magnetization within a sample is first tipped into the transverse plane to generate a nonzero transverse magnetization, as described in Section 1.6.2. This is achieved by applying a radiofrequency (RF) magnetic field oscillating at the Larmor frequency and is often referred to as "excitation." The transverse magnetization will oscillate, producing a signal based on the Larmor frequency, in a process known as nuclear magnetic resonance (NMR).

1.6.2   T1, T2, and T2* Contrast

Macroscopically, the B_0 field polarizes the sample, inducing a net magnetization vector along the z-direction of strength M_0. To obtain an MR signal, an RF magnetic pulse (B_1) tuned to the resonant frequency of the spins is applied in the xy (transverse)

plane to excite the spins out of equilibrium. B_1 applies a torque which rotates the magnetization vector away from the z-axis, by a prescribed angle (the flip angle, α) dependent on the strength and duration of B_1, as the magnetization vector continues to precess about the z-axis at the resonant frequency.

Following an excitation, relaxation back to equilibrium occurs as the transverse component of magnetization decays while the longitudinal component returns to its equilibrium state. The time constant characterizing the return of the magnetization vector along the z-axis (longitudinal axis) is called T1 or the spin-lattice time constant, while the time constant characterizing the decay of the vector in the xy (transverse) plane is called T2 or the spin-spin time constant. T1 relaxation arises from the loss of thermal exchange of the nuclei to surrounding lattice, while T2 relaxation arises from the dephasing of individual spins due to interactions with the magnetic moments of surrounding atoms. Due to inhomogeneities in the main magnetic field (B_0), a spatially varying phase accumulates which causes the net transverse magnetization to decrease due to destructive interference between spins. Thus, the observed T2 decays much faster than the "true" T2 and is denoted T2*. T1, T2, and T2* depend on the chemical environment and the MR signal can be sensitized to either contrast. T1 and T2 relaxation are characterized by exponential functions:

$$M_z(t) = M_0 + (M_z(0) - M_0)e^{-t/T1} \qquad (1.2)$$

$$M_{xy}(t) = M_{xy}(0)e^{-t/T2} \qquad (1.3)$$

Where M_z is the net longitudinal magnetization along the z-axis, and M_{xy} is the net

transverse magnetization along the xy-plane. The observed T2 decreases to T2* via:

$$T_2^* = \left(\frac{1}{T_2} + \frac{1}{T_2'}\right)^{-1} \tag{1.4}$$

Where T_2' is the contribution to dephasing due to susceptibility.

1.6.3   Diffusion-weighted MRI

The MRI contrast can also be manipulated to reflect the displacement of water

molecules as a result of the diffusion process (109,110), in a technique referred to as

diffusion-weighted or diffusion MRI. The diffusion process is also known as random

walk, thermal agitation, or Brownian motion, as it was first described by Robert Brown in

1827 (111). Later, in 1855, Adolf Fick first described how solute particles are distributed

over time due to nonuniform concentration, via Fick's second law of diffusion:

$$\frac{\partial \varphi(x,t)}{\partial t} = D \frac{\partial^2 \varphi(x,t)}{\partial^2 t} \tag{1.5}$$

Where φ is the concentration of a particular particle at time t and position x, and D is the

diffusivity in units of $length^2\ time^{-1}$. Half a century later, Albert Einstein demonstrated

that in the absence of a concentration gradient, the above equation can be used to describe

the stochastic nature of Brownian motion and $\varphi(x,t)$ can be interpreted as the probability

density function of a particular particle's location, x, after a time, t (112). In a free

medium, such as a glass of water, where displacement is not limited by any external

barriers, a particle's displacement is governed by a Gaussian probability distribution:

$$\varphi(x,t) = \frac{1}{\sqrt{4\pi Dt}} e^{-\frac{x^2}{4Dt}} \tag{1.6}$$

The variance of this distribution represents the mean squared displacement of the particle:

$$\langle x^2 \rangle = 2Dt \tag{1.7}$$

In biological tissue, Gaussian diffusion alone cannot fully characterize diffusion, due to the presence of barriers such as membranes, molecules, boundaries, and various structures. Molecules in biological tissue can be described as undergoing a) restricted diffusion, b) hindered diffusion, or c) free or Gaussian diffusion, as shown in Figure 1.4. Molecules constrained by the presence of an impermeable barrier, such as within axons and cells, are experiencing restricted diffusion, while molecules impeded by semi-permeable barriers and other obstacles which do not completely restrict their movement, such as in the extracellular space, are experiencing hindered diffusion. Molecules in the cerebrospinal fluid (CSF) pool, which are not encountering barriers, are undergoing free or Gaussian diffusion.
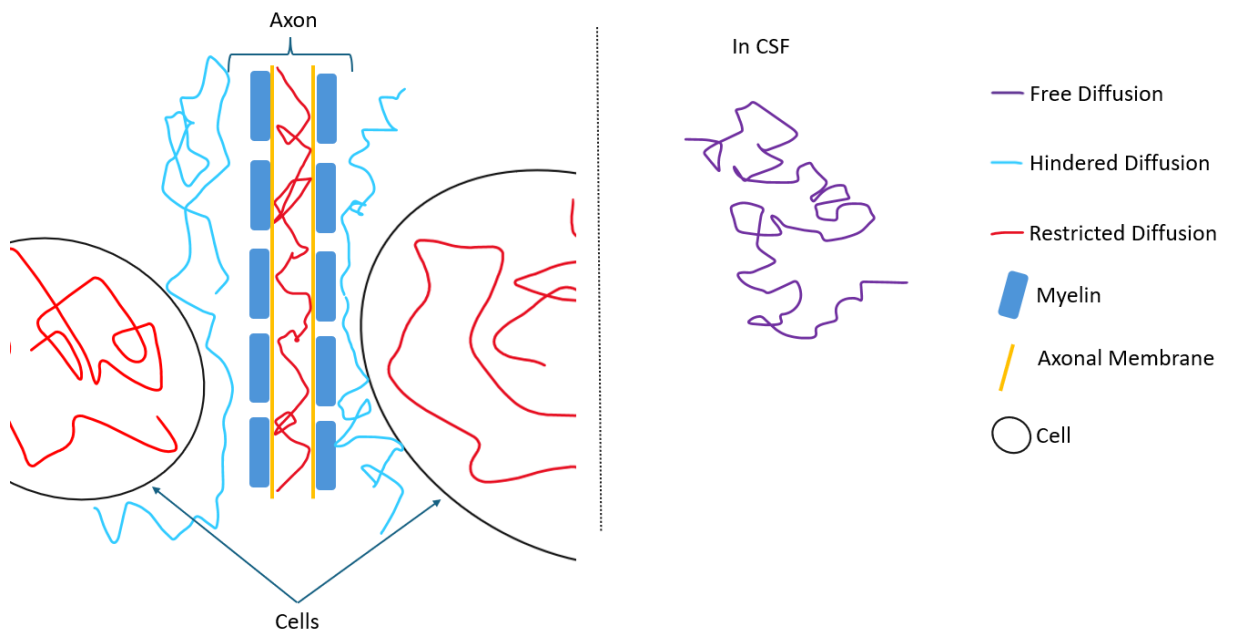
Figure 1.4 - *Visual representation of the diffusion trajectory of a water molecule for the*

following diffusion regimes: restricted diffusion (within impermeable boundaries such as axons and cells), hindered diffusion (impeded by semi-permeable boundaries and other obstacles such as in the extracellular space), free diffusion (not encountering any barriers such as in CSF).

1.6.4   Conventional Diffusion Encoding

The first MRI pulse sequence for diffusion-weighted image contrast, the pulsed gradient spin echo (PGSE) technique, was developed by Stejskal and Tanner in 1965 (113). PGSE resembles a spin echo sequence with the addition of two (usually) identical gradient waveforms inserted before and after the 180° refocusing RF pulse, as depicted in Figure 1.5. In a spin echo (SE) sequence, the 180° refocusing RF pulse rotates the dispersing spins 180° about the transverse plane so that the spins will refocus at a later time; this refocused magnetization is known as the spin echo (114). Thus, the SE sequence compensates for magnetic field inhomogeneities and results in signal that is T2-weighted (not T2*-weighted). In the PGSE sequence, the pulsed gradients (also called the diffusion gradients) first dephase and then, after some time, rephase spins. The phases of stationary spins are unaffected by the diffusion gradients since any phase accumulation from the first gradient lobe is reversed by the second. However, spins diffusing along the direction of the gradients move into different locations between the first and second lobes, acquiring a net phase that accelerates the decay of the transverse magnetization due to phase dispersion. Thus, the diffusion-weighted signal acquired from moving spins is lower than that of stationary spins, due to phase incoherence that arises from motion.
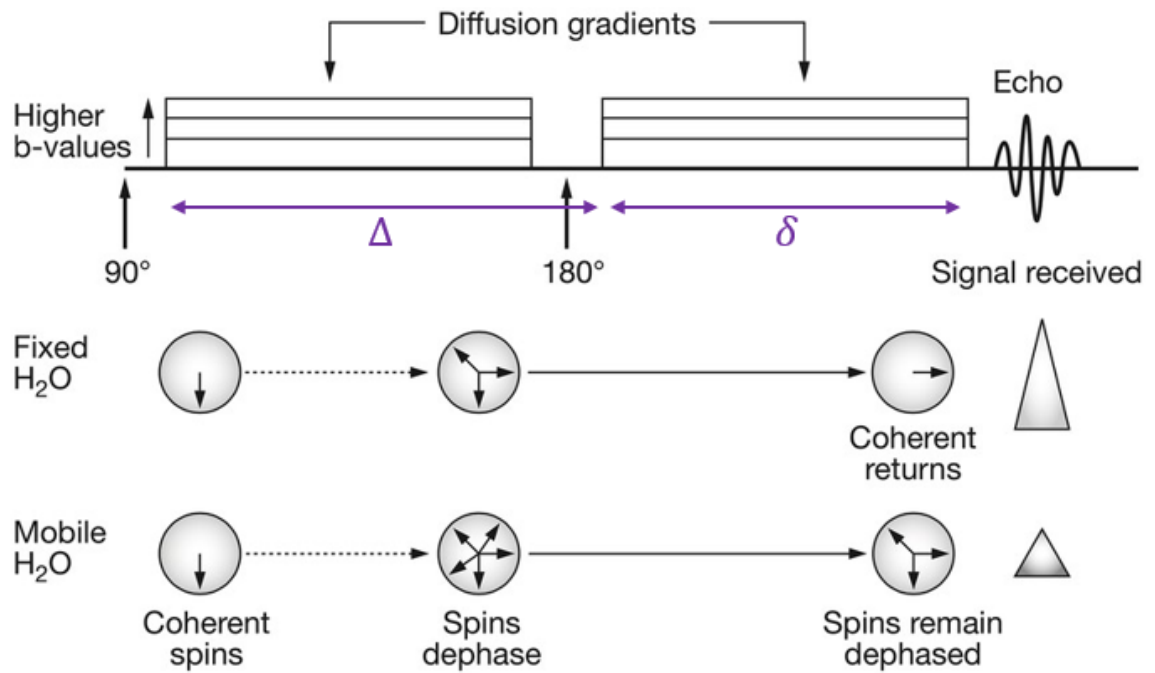
Figure 1.5 - *Pulsed gradient spin echo (PGSE) diffusion encoding sequence. Static spins experience dephasing due to gradients alone which is reverted by the second gradient. Diffusing spins experience additional dephasing due to displacements which is not reverted by the second diffusion gradient resulting in signal loss. Image reprinted from Patterson et al. (115) with permission from Springer Nature.*

According to the work of Le Bihan et al., the diffusion-attenuated signal can be expressed as:

$$S(b) = S_0 e^{-bD} \tag{1.8}$$

Where $S(b)$ is the diffusion weighted signal; S_0 is the signal with no diffusion gradients applied; D is the diffusivity in units of $length^2\ time^{-1}$; b is the b-value, which quantifies the degree of diffusion weighting, in units of $time\ length^{-2}$ to preserve

dimensionality. The b-value gives an indication of the amount of signal attenuation that will occur in an image due to diffusion and includes all variables related to the diffusion gradients:

$$b = \gamma^2 G^2 \delta^2 (\Delta - \frac{\delta}{3})$$
(1.9)

Where γ is the gyromagnetic ratio; G is the gradient amplitude of the diffusion gradients, each of which has a duration δ, and a delay of Δ between them, as depicted in Figure 1.5. As Equation (1.8) assumes Gaussian diffusion, which is usually not true for biological tissue (as discussed in Section 1.6.3), the terms 'apparent diffusion coefficient' (ADC) or 'mean diffusivity' (MD) are used interchangeably in the field to indicate an approximation of diffusivity, rather than true diffusivity (D). For simplicity, this thesis will use the terminology 'mean diffusivity' (MD).

The most successful application of dMRI has been in acute brain ischemia, applying conventional diffusion weighted imaging. dMRI is now the imaging modality of choice for the management of stroke patients, as there is a decrease in water diffusion immediately after ischemic injury (7).

1.6.5   Echo Planar Imaging

A consequence of sensitizing the MR signal to the motion of water molecules is that dMRI is inherently susceptible to patient movement. To reduce the confounding effects of gross head motion and physiological motion on signal measurements, dMRI often uses an acquisition technique called echo planar imaging (EPI), which is one the fastest MRI pulse sequences capable of producing a 2D image within tens of milliseconds

(116,117). MRI collects data in "k-space," which is the frequency content of the object, and the image can be recovered after an inverse Fourier transform to k-space data (Figure 1.6). A typical single shot EPI sequence acquires an entire 2D k-space grid after a single RF excitation, as depicted in Figure 1.7.
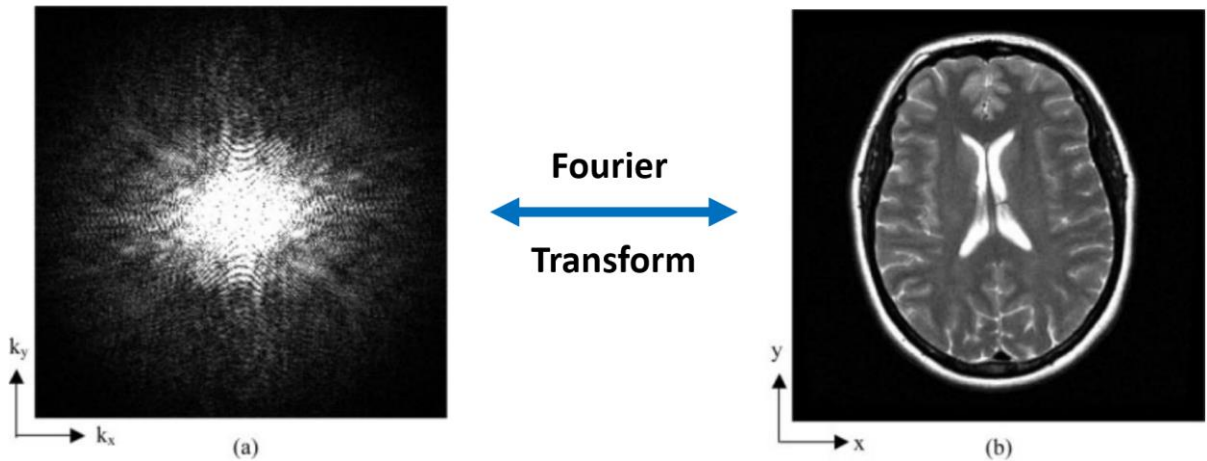
Figure 1.6 – *Raw data in k-space (a) and corresponding image data in image space (b). To acquire image data, an inverse Fourier transform is applied to k-space data. Image adapted from Paschal & Morris* (118) *(open access).*
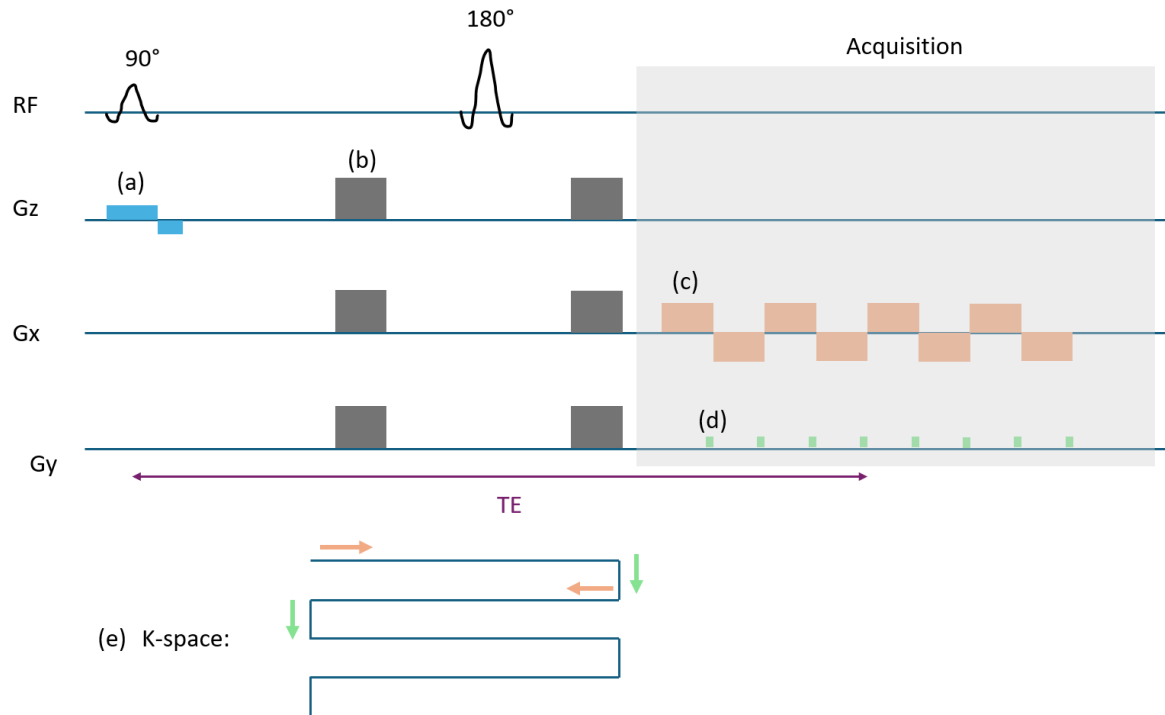
Figure 1.7 - *Simplified pulse sequence diagram for a diffusion-weighted echo planar imaging (EPI) acquisition. The slice selection gradient (blue, (a)) limits excitation from the initial 90° radiofrequency (RF) pulse to a single slice in the z-direction. On either side of the refocusing 180° RF pulse are dephasing and rephasing diffusion-sensitizing gradients (gray, (b)). The gradients applied during acquisition traverse k-space: each rectangular gradient in the x-direction (orange, (c)) moves the k-space sampling trajectory through a line in the x-direction in k-space (frequency-encoding direction), while each "blip" gradient in the y-direction (green, (d)) shifts the sampling trajectory to a new line in the y-direction of k-space (phase-encoding direction). This results in a "zig-zag" traversal of k-space, with alternating lines of k-space sampled in reverse directions (e). Gradient echoes are collected with each lobe of the frequency-encoding gradient. The spin-echo at TE (echo time) occurs at the center of k-space.*

Compared to conventional spin-echo and gradient-echo imaging, EPI is prone to a variety of artifacts (109). A common EPI artifact is Nyquist ghosting along the phase-encoded direction, which appears as "ghost" images displaced from the original image by half the field of view in the phase-encoding direction. Nyquist ghosts can result from many possible sources including gradient coil heating, patient motion, and susceptibility. The most common cause, however, is the induction of eddy currents in the coils and magnet housing in response to the rapidly changing gradients in EPI. These eddy currents, in turn, produce local fields that distort B_0 and add phase shifts to the data. On modern systems, Nyquist ghosting is rare as they can be reduced/removed using calibration or reconstruction techniques. Off-resonance effects arising from magnetic susceptibility variations (e.g., from tissue-air interfaces), B_0-field inhomogeneities, and eddy currents can severely distort echo planar images and lead to signal loss. These effects can be largely mitigated using post-processing techniques that will be noted in the methods section of later chapters. T_2^*-induced image blurring along the phase-encoded direction is also possible, as the k-space lines in EPI are acquired at different times leading to different T_2^* weightings.

1.6.6   Diffusion Tensor Imaging

Signal representation refers to a class of data analysis methods where the MRI signal is fit by a mathematical model that captures its features without making any assumption about the underlying tissue or microstructure (110). The most popular signal representation is diffusion tensor imaging (DTI), which describes diffusion using a Gaussian model (119) based on Equation (1.8). At low diffusion weighting, b up to

$1000s/mm^2$, the natural log of the diffusion signal is well represented by a linear function of the b-value, where the slope yields the mean diffusivity (MD):

$$\ln\left(\frac{S(b)}{S_0}\right) = -bD \tag{1.10}$$

Because biological tissues such as white matter are anisotropic, MD needs to be measured along at least six noncollinear directions of space, from which the diffusion tensor can be calculated as a 3x3 symmetric matrix: $D = [D_{xx}\ D_{xy}\ D_{xz};\ D_{yx}\ D_{yy}\ D_{yz};\ D_{zx}\ D_{zy}\ D_{zz}]$. The diffusion tensor is usually visualized by an ellipsoid, with three principal axes defined by the eigenvectors of the diffusion tensor (v_1, v_2, v_3) and their corresponding eigenvalues (λ_1, λ_2, λ_3), as shown in Figure 1.8. From the tensor, one can derive measures of diffusion magnitude and diffusion anisotropy, including:

- Mean diffusivity (MD), averaged across all directions of space (average of all eigenvalues).

- Axial diffusivity (AD), in the direction diffusion is least impeded (i.e., eigenvalue corresponding to the largest eigenvector, λ_1), such as parallel to the fibers in a white matter bundle.

- Radial diffusivity (RD), averaged over all directions in the plane perpendicular to the axial diffusivity, such as perpendicular to the fibers in a white matter bundle (average of λ_2 and λ_3).

- Fractional anisotropy (FA), describing the anisotropy of the diffusion tensor. FA is a normalized value between 0 and 1, with 1 being highly anisotropic and 0 being completely isotropic.

DTI is mostly used to visualize white matter anisotropy and has been applied extensively in animal models, such as models of Alzheimer's Disease (120) and traumatic brain injury (121).. Although DTI is not used widely in the clinic, its application provides new insights. For example, in stroke, MD and FA in white matter have different time courses, enhancing the potential for the use of dMRI in accurate diagnosis and prognosis of stroke (122).
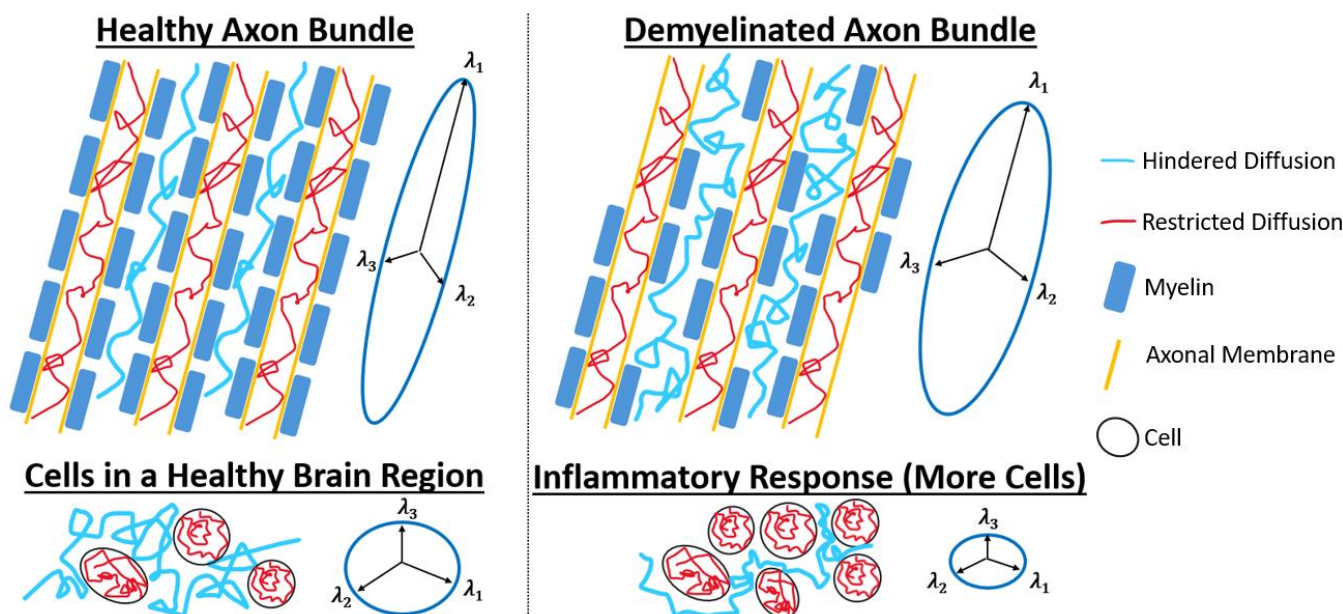
Figure 1.8 – *Diffusion tensor ellipsoids with corresponding eigenvalues (λ_1, λ_2, λ_3) illustrated for various environments within a voxel. For a healthy axon bundle (top left panel), water diffusion is highly anisotropic and directional, resulting in an elongated ellipsoid, with λ_1 in the direction diffusion is least impeded, parallel to the axons. For a demyelinated axon bundle (top right panel), water diffusion within a voxel is less anisotropic in comparison with a healthy axon bundle, resulting in a wider ellipsoid. The diffusion tensor ellipsoid is more spherical for a group of cells in a healthy brain region (bottom left panel). Infiltration of inflammatory cells after injury (bottom right panel) results in a smaller ellipsoid, as diffusion is more hindered in the extracellular space.*

1.6.7   Diffusion Kurtosis Imaging

The deviation from Gaussian diffusion in biological tissues can be quantified using a dimensionless metric called the excess kurtosis. Since the deviation from Gaussian behavior depends on the complexity of the tissue in which water is diffusing, a high diffusion kurtosis suggests a high degree of diffusional heterogeneity and/or microstructural complexity. Complex biological tissues have a positive kurtosis, with the probability distribution having fatter tails, as shown in Figure 1.9, and is associated with restricted diffusion through the reduction of the mean squared displacement.
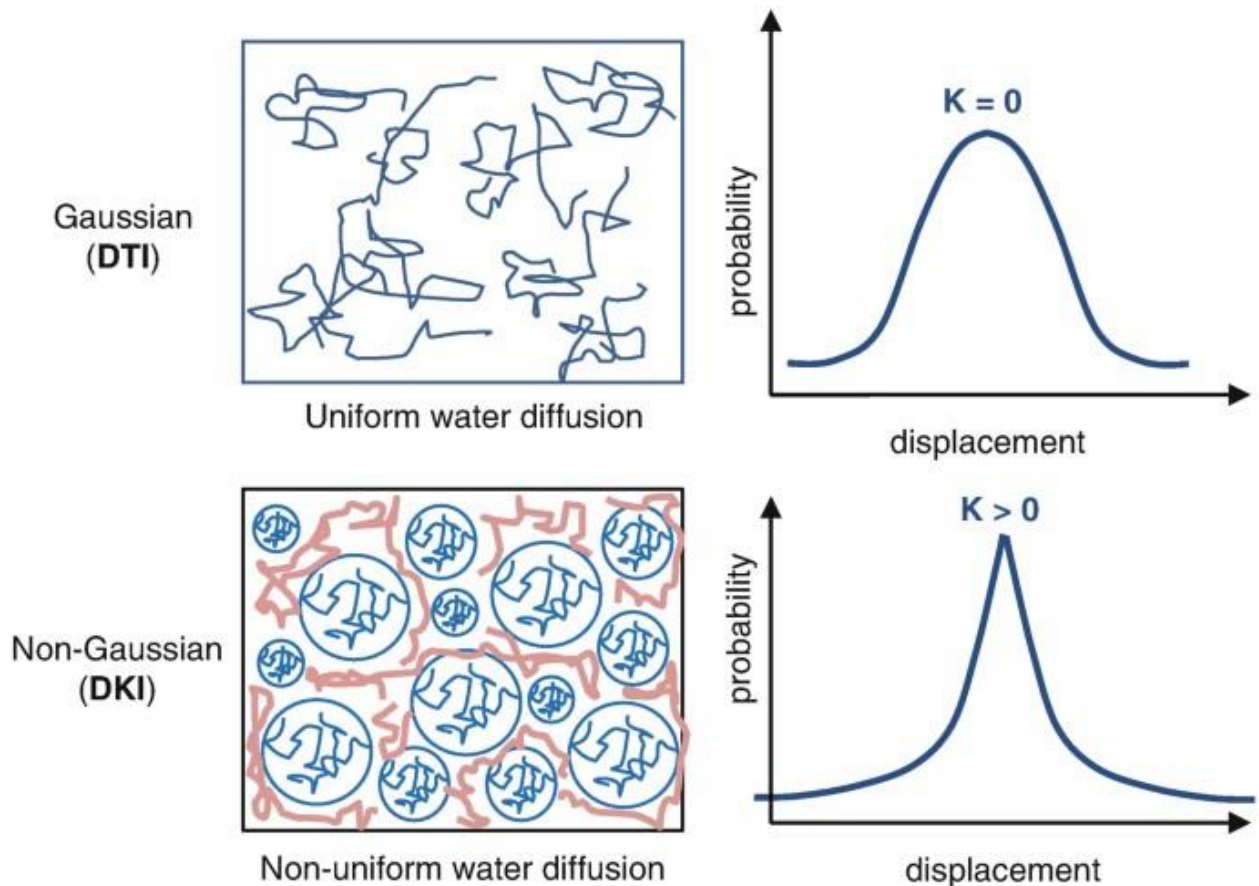
Figure 1.9 – *Gaussian versus non-Gaussian diffusion. Free or uniform water diffusion (top panel) can be modelled by Gaussian diffusion (DTI) and there is no kurtosis (K = 0).*

Complex biological tissue (bottom panel) results in a non-Gaussian probability distribution for any given particle, with positive kurtosis (K > 0). Diffusion in this environment is better modelled by Diffusion Kurtosis Imaging (DKI). Image reprinted from Zhuo & Gullapalli (123) with permission from Springer Nature.

Jensen et al. (124) developed a method to estimate diffusion kurtosis, called Diffusion Kurtosis Imaging (DKI), which is based on the PGSE sequence, but requires higher b-values, as kurtosis is only apparent for high diffusion weighting ($b > 1000$ s/mm^2). DKI extends the DTI formalism through a series expansion of the signal *S(b)* and results in an additional second order term added to equation 1.7:

$$\ln\left(\frac{S(b)}{S_0}\right) = -bD + \frac{b^2 D^2 K}{6}$$

(1.11)

where K denotes the dimensionless kurtosis and all other parameters remain the same as in equation 1.10. The kurtosis tensor has 15 unique elements and thus requires at least 15 different directions to estimate and requires at least 3 b-values (since the method involves a two-parameter quadratic fit) to determine both diffusion and kurtosis from the acquired data. Figure 1.10 depicts DTI and DKI fits to dMRI data, illustrating the inaccuracy associated with the Gaussian diffusion assumption in DTI at b-values greater than 1000 s/mm^2.

DKI is translatable to clinical protocols and has been shown to provide complementary information to DTI, as well as more subtle changes in tissue microstructure resulting from pathological processes (123,125–127).
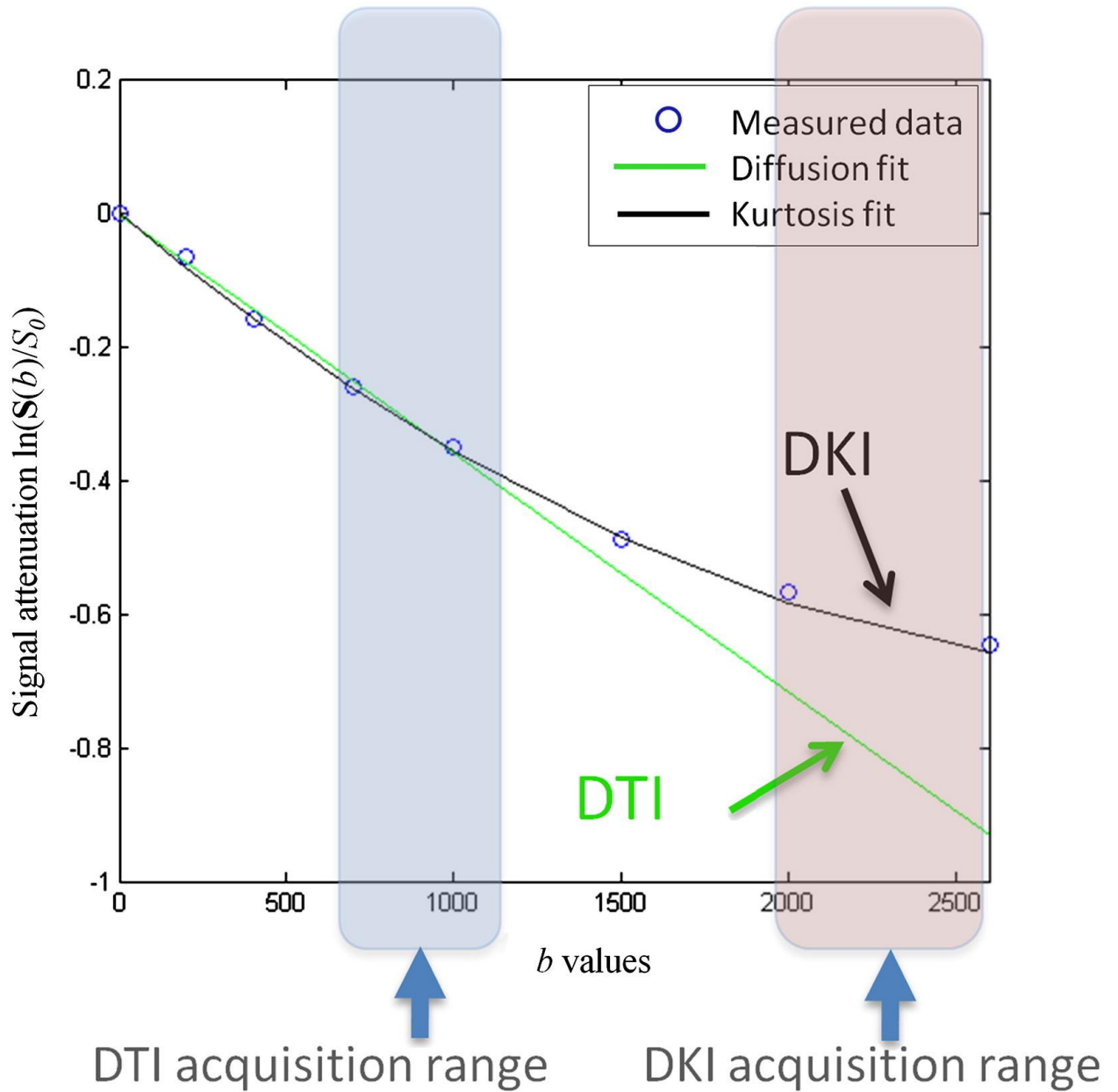
Figure 1.10 - *DTI versus DKI fit to diffusion data. Note that when the b-values exceed 1000 s/mm², the data fits the DKI model significantly better than the DTI model. Image reprinted from Zhuo et al.* (123) *with permission from Elsevier.*

1.6.8   DTI and DKI in Neurological Pathology

This section discusses the temporal evolution of DTI and DKI metrics in models of systemic inflammation, demyelination, traumatic brain injury, and stroke. Table 1-1 summarizes the interpretations from literature in terms of how DTI and DKI metrics may be changing due to different cellular processes, as informed by human and animal studies.

Low-dose lipopolysaccharide (LPS) has been used to evaluate the sensitivity of dMRI to systemic inflammation (128). After LPS injection into rat brains, several studies have shown an initially more restricted environment, characterized by decreased MD (129) and increased mean kurtosis (MK) (130), which is explained by increasing size and number of microglia, astrocytes, and macrophage aggregates as observed with histology. The initial higher degree of diffusion restriction observed can be followed by a reduced restriction, characterized by increased MD 4 days after LPS injection (129), which coincides with an increase in T2 relaxation time indicative of vasogenic edema. Such biphasic changes observed in diffusion metrics and reflecting acute, subacute, and chronic inflammatory processes are hallmarks of dMRI studies.

The cuprizone mouse model of CNS demyelination has also been used to assess the temporal evolution of DTI and DKI metrics following acute inflammatory demyelination and spontaneous remyelination (131–134). Within the first 3 weeks of cuprizone intoxication, MD decreases and MK increases, which is explained histologically by increased cellularity and membrane barriers due to infiltration and proliferation of macrophages and microglia. In addition to microgliosis, quantitative histology also demonstrated extensive demyelination after 3 weeks, which is typically expected to lower diffusion restriction, resulting in higher MD and reduced MK (132).

During the acute phase of cuprizone intoxication, demyelination and microgliosis have competing effects on diffusion, although the observed dMRI changes at 3 weeks correspond to acute inflammation rather than demyelination. Decreasing MD and increasing MK between 6 and 12 weeks are consistent with spontaneous remyelination, confirmed by histology. In addition to microgliosis and demyelination followed by remyelination, quantitative histology detected astrogliosis at 6 weeks, as well as edema reported on T2-weighted MRI. However, the sensitivity of diffusion to astrogliosis and edema was not evident in the cuprizone animal model due to the presence of other cellular processes simultaneously affecting the microstructure.

Another well-studied model that exhibits various microstructural changes is traumatic brain injury (TBI). For TBI as well, biphasic changes are observed over time, with an initial higher diffusion restriction in the acute phase, followed by a lower diffusion restriction in the chronic phase (123,135–138). However, trends in DTI and DKI metrics may not exactly mirror each other when tracking these longitudinal changes. For example, an increase in MK was associated with increased reactive astrogliosis, confirmed by immunohistochemistry, in a mild controlled cortical impact injury rat model by Zhuo et al (123). Increased MK continued during the subacute phase when the DTI metrics already returned to baseline, supporting that DKI provides additional information that is not available through standard DTI.

Biphasic changes in DTI and DKI metrics are also observed in stroke models during the acute, subacute, and chronic stages (139). The acute stage typically presents with more restricted diffusion due to axonal beading and cytotoxic edema (140), followed by pseudonormalization of dMRI metrics due to vasogenic edema (as observed on T2)

during the subacute phase, and subsequent less restricted diffusion due to neuronal and axonal loss in the chronic phase.

These studies illustrate how competing cellular processes reduce the overall net effect of pathology on diffusion and highlight the need to develop and apply dMRI methods with improved sensitivity and specificity.

Table 1-1: Overview of how different cellular processes may affect DTI and DKI parameters

Pathology	FA	MD	AD	RD	MK
Axonal swelling or beading	↓	↓	↓	≈	↑
Vasogenic edema	↓	↑	↑	↑	≈
Cytotoxic edema (cell swelling)	↑	↓	↓	↓	↑
Demyelination	↓	↑	≈	↑	↓
Remyelination	↑	↓	≈	↓	↑
Microgliosis and macrophages	↑	↓	↓	↓	↑
Astrogliosis	↑	↓	↓	↓	↑

FA – fractional anisotropy; **MD** – mean diffusivity; **AD** – axial diffusivity; **RD** – radial diffusivity; **MK** – mean kurtosis

1.6.9   Limitations of DTI and DKI

Despite their widespread use in both animal and human studies, DTI and DKI have some limitations, which reduce their sensitivity and specificity and lead to inaccurate representations of neuroanatomy. Here, four major limitations are discussed: 1) DTI assumes Gaussian diffusion; 2) Both DTI and DKI are dependent on fiber orientation dispersion; 3) Both DTI and DKI cannot differentiate between isotropic and anisotropic sources of diffusion or kurtosis; 4) Both DTI and DKI do not consider time-dependent diffusion.

   1)   DTI assumes Gaussian diffusion:

This limitation was briefly mentioned in Section 1.6.3 but is described in greater detail here for completeness. DTI assumes Gaussian (free) diffusion, which cannot fully characterize complex biological tissue, which includes cells, axons, and other compartments of various sizes. Free diffusion is an oversimplification, because the diffusivity within a voxel represents the sum of diffusivities of all water molecules from multiple water-containing compartments (i.e. axons, soma, extracellular water, etc.) and over multiple directions. Water molecules in different compartments within the voxel may be diffusing at different rates, and the signal would be better characterized by a multiexponential decay function. The logarithm of the dMRI signal should decrease linearly with increasing b-value, based on Equation 1.10, assuming Gaussian diffusion. However, at higher b-values, the signal vs. b-value deviates from this straight line due to the variance in diffusivity (Figure 1.10), and more advanced signal representations that can accurately quantify this deviation may provide more insight about the underlying tissue (124,141).

2) Both DTI and DKI are dependent on fiber orientation dispersion:

Both DTI and DKI are unable to distinguish between microstructural changes and neuron fiber orientation dispersion (8,21), reducing their specificity to microstructural changes in brain regions with crossing fibers. While the mean parameters (mean diffusivity and mean kurtosis) are not sensitive to orientation dispersion, the direction dependent measures (axial and radial diffusivity and kurtosis) are sensitive to this confounding factor, which consequently impacts fractional anisotropy (FA). FA is a parameter related to microstructural features such as axon density, diameter, and myelination, and can act as a metric for neurodegeneration for a bundle of fibers aligned coherently within a voxel, as shown in Figure 1.11. However, the interpretation of FA in terms of microstructure becomes ambiguous when there is a distribution of axon orientations within the image voxel (141). A voxel with crossing fibers will be modelled as having lower macroscopic diffusion anisotropy (a rounder diffusion ellipsoid), resulting in lower FA, while a voxel with parallel fibers will have higher FA, assuming that both voxels have healthy fibers with the same degree of structural integrity and microscopic diffusion anisotropy. This confounding effect of axon orientation limits the specificity of FA to white matter neurodegeneration.
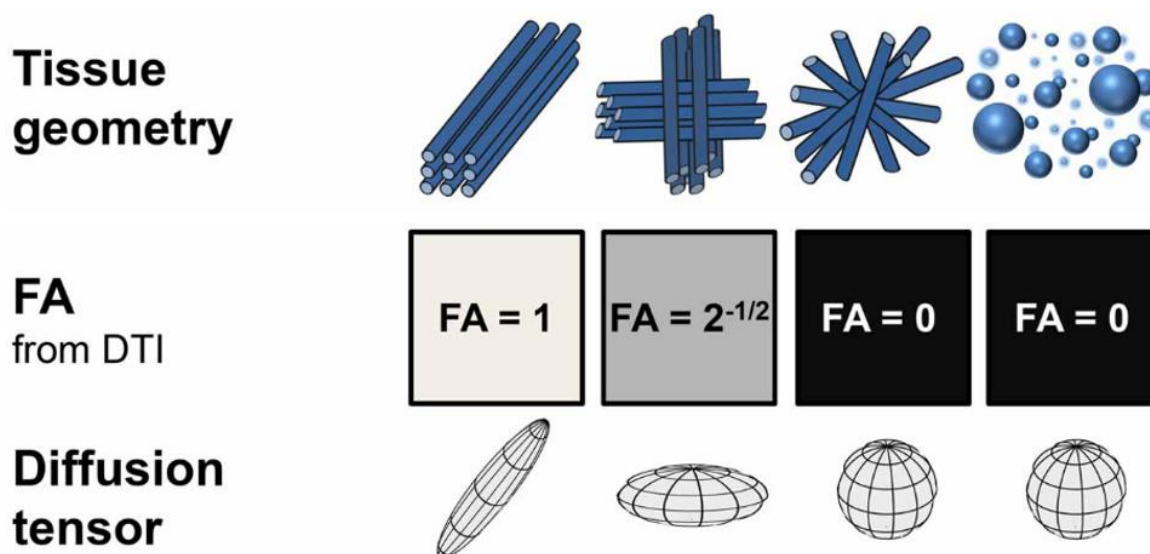
Figure 1.11 - *The effects of various tissue geometries on fractional anisotropy (FA), acquired from DTI. The cylinders (top panel) approximate neuronal axons, while the spheres represent non-neuronal, spherical cells. Though columns 1-3 all depict intact axons, the decreasing orientational coherence from left to right leads to decreasing values of FA. Moreover, the DTI signal representation cannot distinguish between incoherently arranged axons (column 3) and spherical cells (column 4), as diffusion appears isotropic in both cases. Image adapted from Lasic et al.* (141) *(open access).*

This could lead to circumstances in which voxelwise anisotropy increases while microscopic anisotropy decreases (142). For example, FA was found to increase in a region containing crossing axons when axons along one direction were preferentially damaged compared to those in a perpendicular tract (143). Calculating diffusion MRI metrics without the confounding influence of orientation dispersion will provide a more accurate representation of neuroanatomy.

3) *Both DTI and DKI cannot differentiate between isotropic and anisotropic sources*
   of diffusion or kurtosis:

The reason for the previous limitation, in which diffusion anisotropy is confounded by fiber orientation dispersion, is that the DTI and DKI signal representations model both isotropic and anisotropic sources of diffusion together and are unable to disentangle the two, which results in vague interpretations of neuroanatomy. Isotropic diffusion arises from compartments with equal diffusion in all directions, such as round cells, while anisotropic diffusion arises from compartments with highly directional diffusion, such as axons and elongated cells. These concepts are further explored in Section 1.7.1. Disentangling isotropic and anisotropic diffusion sources will result in more specific interpretations of microstructural changes.

4) *Both DTI and DKI do not consider time-dependent diffusion:*

In the Gaussian diffusion scheme, the diffusivity remains constant regardless of the diffusion time (defined primarily by the delay (Δ) between the diffusion gradients). However, in biological tissue the diffusivity exhibits diffusion time-dependence due to the presence of boundaries. If the diffusion time is short enough that most water molecules do not reach any restricting or hindering boundaries within the tissue, the measured MD will be equal to the diffusivity of free water (144). However, if the diffusion time is long enough that most molecules will encounter barriers, the measured MD will decrease to an asymptotic value called the steady state diffusivity (145). Standard DTI experiments, using the PGSE sequence, probe long enough diffusion times to acquire steady-state MD measurements. Given hardware constraints, diffusion times achievable in PGSE can probe displacements on the order of 10 – 30 μm, which is much

larger than typical axonal and cellular diameters (9). In mice, axonal diameters range from 0.1 - 2.9 µm with high frequencies around 0.4 - 0.8 µm (146), and cellular diameters range from 4 - 10 µm (147–151). Probing shorter length scales and the time-dependence of diffusion would provide insight into smaller, previously inaccessible, microstructural features.

1.6.10   Magnetization Transfer MRI

The transverse relaxation time (T2) of protons in macromolecules, such as myelin lipids, is very short due to their restricted mobility and essentially invisible to traditional spin echo or gradient echo MR sequences (109). The signal seen in traditional MR images is generated entirely from the protons in the liquid pool, such as protons in free water molecules, which have longer T2 due to their mobility. The protons in the macromolecular pool have a much broader spectral width, because the full width at half maximum (FWHM) of a spectrum is inversely related to T2. An appropriately chosen off-resonance RF pulse, called the magnetization transfer (MT) pulse, will selectively saturate the macromolecular pool, which will then transfer its magnetization via spin exchange (dipole-dipole interactions across space) to the liquid pool (see Figure 1.12). MT MRI relies on this spin exchange to indirectly image semi-solid tissue such as myelin.
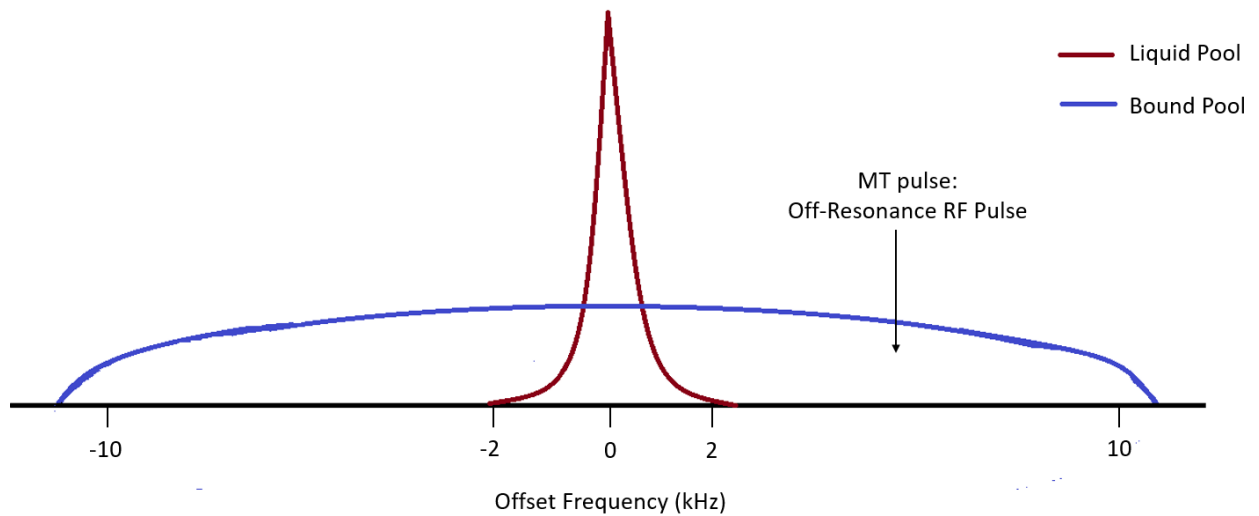
Figure 1.12 – *Schematic of magnetization transfer (MT) pulse application. The MT pulse is typically applied several hundred to several thousand Hz away from the liquid pool Larmor frequency (an offset frequency of 0) to saturate the macromolecular (bound) pool, as the protons in the macromolecular pool have a much broader spectral width.*

After an MT pulse selectively saturates the macromolecular pool, the saturation transfers to the free water proton pool via MT, resulting in a decrease in the observed free water signal. The magnitude of the MT effect can be characterized by the magnetization transfer ratio (MTR):

$$MTR = \frac{PDw - MTw}{PDw} \tag{1.12}$$

where PDw is the reference signal without an MT pulse applied, which is proton density weighted, and MTw is the signal with the MT pulse applied, which is MT weighted. Minimizing the TR and reducing the flip angle, to reduce T1-weighting, in a spoiled gradient echo imaging sequence, allows us to acquire a fast PDw image, commonly known as the Fast Low Angle Shot (FLASH) method (152). To acquire an MTw image,

the same scan parameters are used as the reference *PDw* image, with an MT pulse applied.

Although *MTR* has been shown to correlate well with histological myelin content (153,154), it is also sensitive to the choice of sequence parameters, flip angle inhomogeneities, and longitudinal relaxation time (T1) (14). T1 also correlates strongly with myelin content but is also sensitive to axon size (155) and iron content (156), mitigating the power of *MTR* as a measure of myelin. Thus, decoupling *MTR* from T1 effects could increase the specificity of *MTR* to myelin.

1.7   Advanced Multi-modal Microstructural MRI

To address the limitations of standard DTI, DKI, and MTR protocols and improve sensitivity and specificity to microstructure, advanced multi-modal microstructural MRI is implemented and applied in this thesis, consisting of tensor-valued dMRI, frequency-dependent dMRI, and MTsat MRI. Applications of these microstructural MR methods are discussed in later chapters, and therefore not included in this section.

1.7.1   Tensor-Valued Diffusion MRI

Tensor-valued diffusion encoding is a dMRI concept that can be used to disentangle the effects of microscopic diffusion anisotropy from orientation dispersion, as illustrated in Figure 1.13. While conventional dMRI encodes for diffusion by a single pair of pulsed gradients applied in one direction (113), as shown in Figure 1.5, tensor-valued encoding uses multiple pairs of diffusion gradients that encode for diffusion in more than one direction (11,157,158). In this framework, the conventional description of b-value and encoding direction (159) is replaced by the 'b-tensor', which adds the shape

of the diffusion encoding to the description (11,157,158). As the b-value describes the degree of diffusion sensitivity of the measurement, the b-tensor expands this description to describe the degree of diffusion sensitivity in each direction: $[b_{xx}\ b_{xy}\ b_{xz};\ b_{yx}\ b_{yy}\ b_{yz};\ b_{zx}\ b_{zy}\ b_{zz}]$. Varying the shape of the b-tensor allows us to control the measurement's sensitivity to diffusion anisotropy.
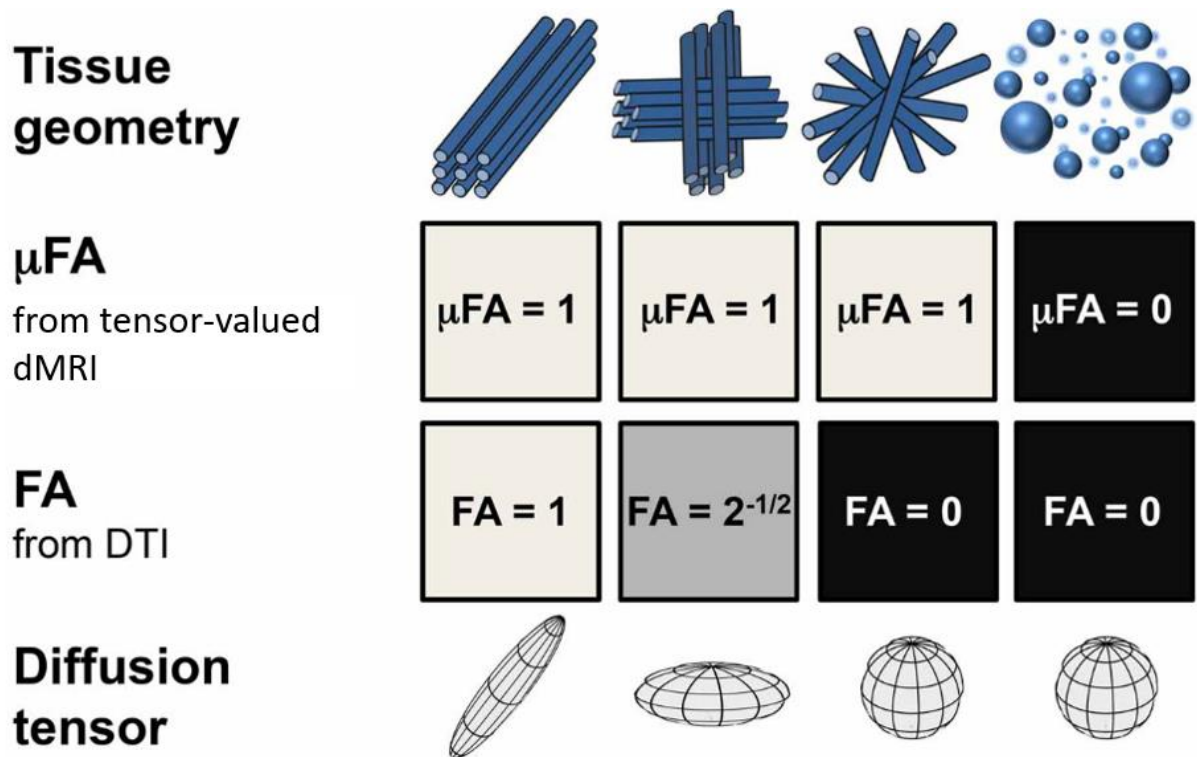
Figure 1.13 – *The effects of various tissue geometries on microscopic fractional anisotropy (μFA), acquired from tensor-valued dMRI, and fractional anisotropy (FA), acquired from DTI. The cylinders (top panel) approximate neuronal axons, while the spheres represent non-neuronal, spherical cells. FA and μFA are equivalent in voxels containing coherently aligned axons (column 1) and voxels containing only spherical cells (column 4), but when voxels contain crossing axons, as in columns 2 and 3, μFA correctly detects anisotropic diffusion whereas FA reports reduced anisotropy due to the*

confounding effects of fiber orientation. Moreover, the DTI signal representation cannot distinguish between incoherently arranged axons (column 3) and spherical cells (column 4), as diffusion appears isotropic in both cases. Image adapted from Lasic et al. (141) *(open access).*

The shape of the b-tensor is quantified by its eigenvalues, and two b-tensors are of identical shapes if they share eigenvalues (11). In conventional dMRI, the b-tensors are of rank 1 (the rank of the b-tensor is given by the number of non-zero eigenvalues) and are shaped like a stick, giving "linear" b-tensors. Rank 2 b-tensors are shaped like a disc or a plane, producing a "planar" b-tensor. Gradient waveforms designed to yield isotropic diffusion encoding have b-tensors of rank 3, shaped like spheres ("spherical" b-tensors). Encoding with linear b-tensors (conventional) is maximally sensitive to diffusion anisotropy on both macro- and microscopic scales, as linear b-tensors only probe diffusion along the main orientation of the diffusion tensor. Planar b-tensors probe diffusion perpendicularly to their main orientation and spherical b-tensors probe isotropic diffusion (11,160). Diffusion encoding with the b-tensor framework is referred to as 'tensor-valued,' since a single b-value and encoding direction cannot describe diffusion encoding in more than one direction per signal acquisition. Thus, in this framework, the conventional diffusion encoding scheme is referred to as linear tensor encoding (LTE). Encoding with planar and spherical b-tensors is referred to as planar tensor encoding (PTE) and spherical tensor encoding (STE), respectively.

By applying both LTE and STE schemes, the effects of microscopic diffusion anisotropy can be disentangled from orientation dispersion. LTE encoding schemes encode for diffusion along a single direction at a time, and thus have diffusion gradients

on along a single direction per signal acquisition. STE encoding schemes encode for diffusion along all directions at the same time, and thus have diffusion gradients on along all three axes per signal acquisition (as portrayed in Figure 1.14).
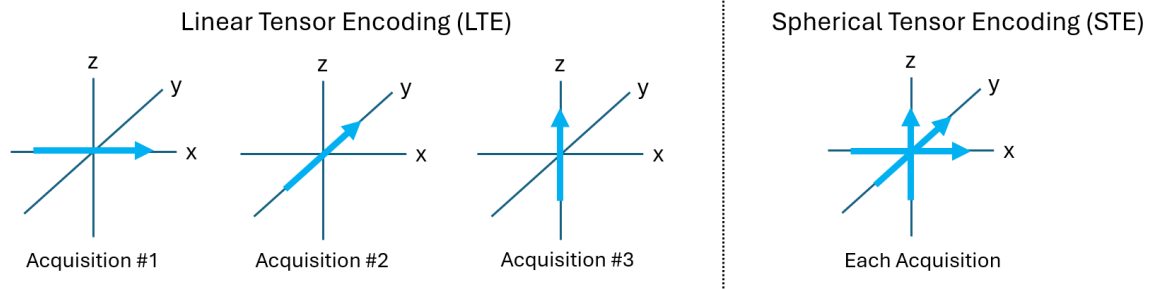
Figure 1.14 – *Schematic of linear tensor encoding (LTE) versus spherical tensor encoding (STE). In LTE, used in conventional DTI and DKI protocols, each diffusion-weighted image is acquired by applying the diffusion gradients in a single direction. In STE, each diffusion-weighted image is acquired by applying the diffusion gradients in all directions at the same time.*

In this framework, the signal representation decomposes the diffusion signal kurtosis into terms originating from either ensemble variance of isotropic diffusivity or microscopic diffusion anisotropy (161). This ability rests on the assumption that diffusion can be described as a sum of multiple non-exchanging Gaussian compartments, although this assumption is not always valid. In such systems, net diffusional kurtosis arises exclusively due to isotropic variance arising from polydispersity in mean diffusivity, and anisotropic variance arising from microscopic anisotropy (21); a general assumption underlying these systems is that LTE signals depend on both isotropic and anisotropic variance while STE signals depend only on isotropic variance. Other sources of non-

Gaussian diffusion that this representation does not account for include time-dependent

diffusion (161,162) and microscopic kurtosis from restricted diffusion and microscopic

structural disorder (21,161,163,164).

Before describing the signal representation of b-tensor encoding, it is necessary to

describe the Taylor series expansion of the natural logarithm of the dMRI signal. Such an

expansion is sometimes referred to as the cumulant expansion since the coefficients of

different terms correspond to the cumulants of the compartment diffusivities (165–167).

Conceptually, cumulants are the most compressed means to characterize a distribution.

The mean diffusivity gives the initial slope of the echo attenuation and corresponds to the

1st central moment and cumulant. The second central moment, μ_2, represents the initial

deviation from mono-exponential attenuation, corresponding to the second term in the

cumulant expansion. Retaining more terms in the Taylor series extends the validity of the

representation toward larger b-values (168).

Calculating the mean of dMRI signal over all acquired directions is referred to as

'powder-averaging'. The normalized signal intensity of powder-averaged dMRI

acquisitions of a multi-component system, assuming negligible time-dependent diffusion,

can be represented by the cumulant expansion (141):

$$\ln\left(\frac{S}{S_0}\right) = -bD + \frac{\mu_2 b^2}{2}$$ (1.13)

where S is the powder-averaged signal, S_0 is the mean signal with no diffusion encoding,

b is the b-value, and μ_2 is the second central moment or variance of diffusivity. The

second central moment is often expressed in terms of kurtosis as $\mu_2 = D^2 K/3$ (141),

which leads to the DKI signal representation, shown in Equation 1.11. For Gaussian diffusion in each component (i.e., within each different cell), the value of μ_2 corresponds to the variance of mean diffusivities.

Microscopic fractional anisotropy is a normalized counterpart of microscopic anisotropy, which is directly comparable to the standard FA metric. Lasic et al. (141) define the microscopic fractional anisotropy in terms of the scaled difference in diffusivity variance between powder-averaged LTE and STE acquisitions:

$$\mu FA = \sqrt{\frac{3}{2}} (1 + \frac{2}{5} \frac{1}{\Delta\tilde{\mu}_2})^{-\frac{1}{2}} \tag{1.14}$$

$$\Delta\tilde{\mu}_2 = \frac{\mu_2^{LTE} - \mu_2^{STE}}{D^2} \tag{1.15}$$

Where μ_2^{LTE} and μ_2^{STE} are the second central moments in the cumulant expansions of powder-averaged LTE and STE acquisitions, respectively. Equation 1.15 can be related to diffusional kurtosis as $\mu_2^{LTE} = D^2 K_{total}/3$ and $\mu_2^{STE} = D^2 K_{iso}/3$. K_{total} is the total kurtosis from LTE acquisitions, which is the conventionally reported mean kurtosis measure in DKI, and K_{iso} is the isotropic kurtosis from STE acquisitions, which is a measure of the variance in the magnitude of diffusion tensors (i.e., D) and can be related to cell size heterogeneity (21). If it is assumed that the only sources of kurtosis are dispersion in size and orientation of diffusion tensors, then the diffusion coefficient D will be equal between LTE and STE powder-averaged acquisitions at the same b-value (21). The powder-averaged LTE and STE signals can be expressed as:

$$S_{LTE} = S_0 e^{-Db + \frac{b^2 D^2 K_{total}}{6}} \tag{1.16}$$

$$S_{STE} = S_0 e^{-Db + \frac{b^2 D^2 K_{iso}}{6}} \tag{1.17}$$

From this framework, the total diffusional kurtosis can be disentangled into isotropic and anisotropic kurtosis components:

$$K_{total} = K_{iso} + K_{aniso} \tag{1.18}$$

Where K_{aniso} is the anisotropic kurtosis. This is depicted conceptually in Figure 1.15. Expressing Equation 1.15 in terms of kurtosis, we have

$$\Delta\tilde{\mu}_2 = \frac{K_{total} - K_{iso}}{3} = \frac{K_{aniso}}{3} \tag{1.19}$$

Substituting Equation 1.19 into Equation 1.14 gives an estimate for μFA:

$$\mu FA = \sqrt{\frac{3}{2}\left(1 + \frac{6}{5}\frac{1}{K_{aniso}}\right)^{-\frac{1}{2}}} \tag{1.20}$$

Accordingly, it is evident that μFA is closely related to K_{aniso} and they have a monotonic relationship with each other. Microscopic anisotropy is another measurement sometimes used that is defined based on the difference in signal between LTE and STE dMRI acquisitions (141) and can also be expressed in terms of K_{aniso}:

$$\mu A = \sqrt{\frac{\ln\left(\frac{S_{LTE}}{S_{STE}}\right)}{b^2}} = \sqrt{\frac{D^2 K_{aniso}}{6}} \tag{1.21}$$

μFA can also be expressed in terms of μA:

$$\mu FA = \sqrt{\frac{3}{2}\frac{\mu A^2}{\mu A^2 + 0.2 D^2}} \tag{1.22}$$

$$\overset{\text{LTE} \qquad \text{STE}}{K_{total} = K_{iso} + K_{aniso}}$$
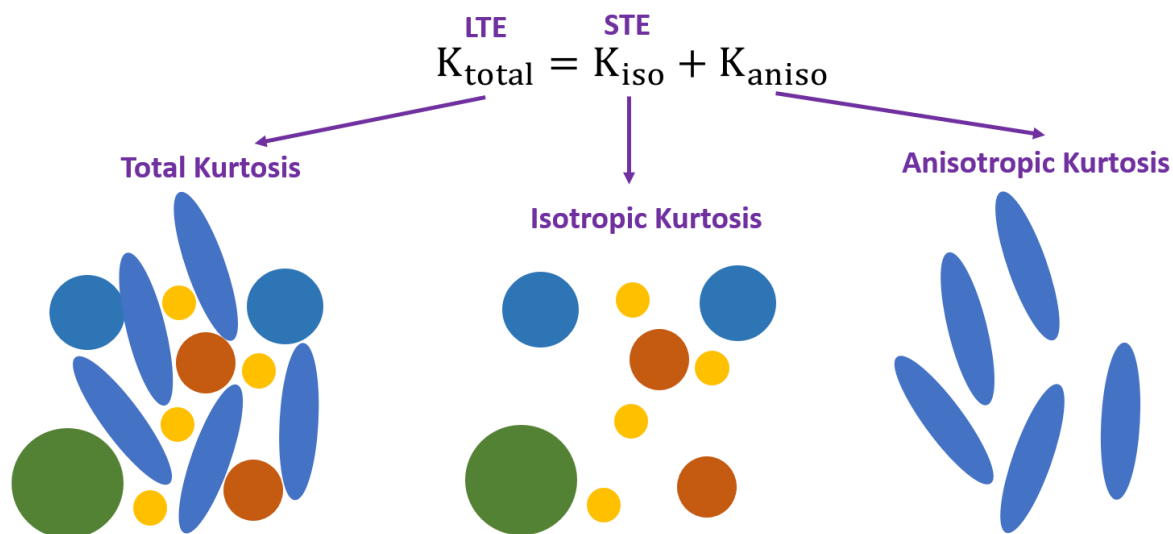
Figure 1.15 – *Total diffusional kurtosis (K_{total}), acquired from LTE acquisitions, can be disentangled into isotropic and anisotropic kurtosis components. Isotropic kurtosis (K_{iso}), acquired from STE acquisitions, arises from the variance in compartment-specific diffusivities and is related to cell size heterogeneity* (21). *Anisotropic kurtosis (K_{aniso}) arises from microscopic diffusion anisotropy, which is related to anisotropic cellular morphology.*

1.7.2   Frequency-Dependent Diffusion MRI

Frequency-dependent dMRI addresses the 4th limitation outlined in Section 1.6.8 and probes diffusion at various length scales, including length scales that are too small to be probed by the PGSE sequence, as described in Section 1.6.8. By varying the effective diffusion time (t_d), which is the time allowed for molecules to probe the environment as defined by the diffusion gradients, molecules will probe varying length scales, allowing us to differentiate boundaries of varying sizes and probe previously inaccessible length scales. This is represented graphically in Figure 1.16. The terms 'frequency-dependent'

and 'time-dependent' are used interchangeably in the field to describe this technique, as various effective diffusion times are probed, since any time dependent phenomena can be recast into frequency dependence through a Fourier transform. In this thesis, 'frequency-dependent' will be used, as explained below.
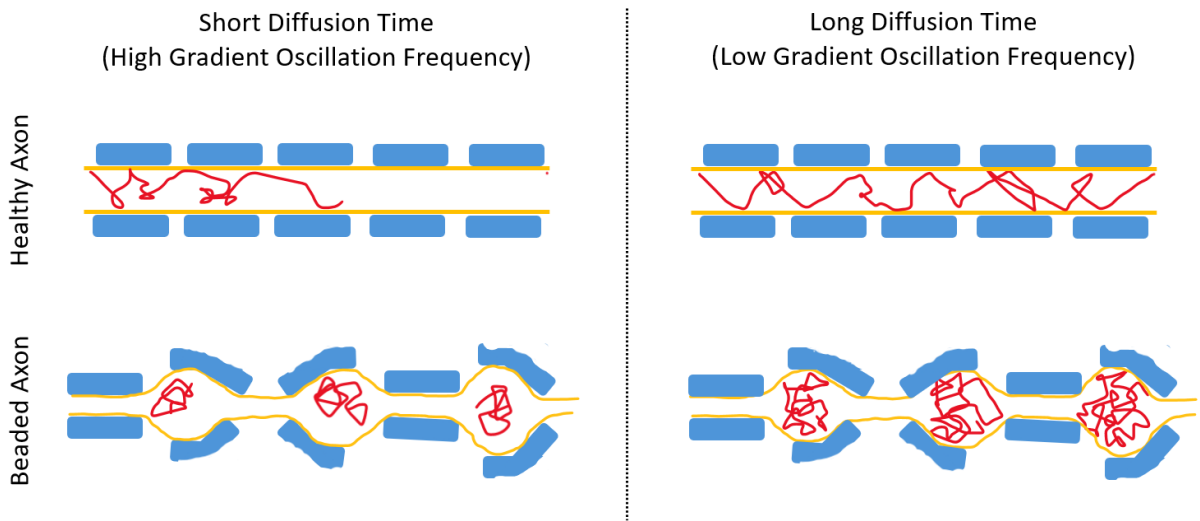
Figure 1.16 – *Schematic of water diffusion behavior in a healthy versus beaded axon for short and long diffusion times (corresponding to high and low gradient oscillation frequencies, respectively). For a lower frequency, MD is measured after a longer diffusion time, where the molecules have enough time to interact with all the barriers in the vicinity. In a beaded axon, the constrictions between the swellings would inhibit the ability of water to diffuse along the axon, leading to water diffusion in a smaller space (within the swellings) and lower MD due to more interaction with boundaries at a low frequency. The shorter diffusion time (higher frequency) lessens interactions with narrowings of the axons, thereby reducing the effect of beading on the diffusion*

measurement, and the MD measured approaches free diffusivity. Thus, the change in MD between different frequencies (diffusion times) will be higher for beaded axons than for healthy axons, providing us with a measure to improve specificity to axonal beading (19,20), as the change in MD (due to changing microstructure) during long diffusion times can be influenced by many factors.

Frequency-dependent dMRI is implemented with oscillating diffusion gradients, using a sequence called 'oscillating gradient spin echo' (OGSE), which replaces pulsed gradients (in the standard PGSE sequence) with oscillating gradients. An example OGSE sequence is shown later in Chapter 2. A key difference between PGSE and OGSE is the estimation of the effective diffusion time. While the t_d for PGSE (if the gradients are assumed to be much narrower than their separation) can be calculated as $t_d = \Delta - \delta/3$, the effective diffusion times of OGSE sequences are not as well defined; the literature demonstrates disagreement on the exact relation of the diffusion time to oscillation frequency (9). The initial solution was to use $t_d = 1/4f$, where $f = \omega/(2\pi)$, ω being the oscillating gradient modulation frequency (169,170). However, later it was suggested a more accurate representation is $t_d = 9/64f$ (171). Nevertheless, it is agreed upon that the use of increasingly higher frequencies translates to shorter effective diffusion times, scaling inversely with frequency. Thus, it can be convenient to work instead in the spectral domain with reference to oscillation frequency as opposed to diffusion time, and this method is referred to as 'frequency-dependent dMRI' in this thesis. Essentially, in frequency-dependent dMRI, higher oscillating gradient frequencies correspond to shorter effective diffusion times, and thus smaller microstructure scales. The highest frequency

(corresponding to the shortest length scale) possible is limited by the system gradient and slew rate characteristics, since $b \sim G^2/f^3$, where G is the gradient strength (9).

Diffusion gradient modulation can take the form of sine or cosine apodization to probe specific frequencies of the gradient modulation spectrum (which is the Fourier transform of the time integral of the gradient amplitude applied). However, measuring diffusion with sine modulation at a particular non-zero frequency can be problematic, as sine modulation produces a peak frequency at zero. Cosine modulation provides increased spectral selectivity by ensuring the peak frequency is non-zero and allowing specific frequencies to be probed (169,172). Additionally, the increase in maximum possible b-value between cosine and trapezoidal-cosine modulated waveforms is significant (170,173), which is why most modern implementations, including this thesis, rely on the trapezoidal-cosine method.

The diffusion spectrum $D(f)$ over a broad range of frequencies and t_d is desirable to characterize comprehensive information on tissue microstructure (174). However, the exact dependence of $D(f)$ on f is determined by the specific f range (175). In the high frequency (short t_d) regime, $D(f) \sim f^{-1/2}$ (176,177). In the low frequency (long t_d) regime, there is a power-law relationship between MD and f as $MD = MD_0 + \Lambda f^\theta$ (162,178), where the constant Λ is defined as diffusion dispersion rate and MD_0 is MD at zero frequency (a PGSE sequence).

For more details on frequency-dependent dMRI, the author recommends the following review papers:

- For basics of the OGSE sequence including the frequency domain analysis: *Gore, John et al. Characterization of Tissue Structure at Varying Length Scales Using Temporal Diffusion Spectroscopy. NMR in Biomedicine (2010).*

- For theories of diffusion time dependency: *Novikov, Dmitry et al. Quantifying brain microstructure with diffusion MRI: Theory and parameter estimation. NMR in Biomedicine (2019).*

- For practical applications of OGSE: *Xu, Junzhong. Probing neural tissues at small scales: Recent progress of oscillating gradient spin echo (OGSE) neuroimaging in humans. Journal of Neuroscience Methods (2020).*

1.7.3   Magnetization Transfer Saturation MRI

Magnetization transfer saturation ($MTsat$) imaging was developed to improve MTR, by correcting for RF inhomogeneity and T1 relaxation, while maintaining a feasible scan time (14). $MTsat$ is defined as the percentage saturation imposed by one MT pulse during a repetition time TR. This is done by acquiring a T1-weighted image ($T1w$), in addition to the proton density-weighted (PDw) image (without an MT pulse applied) and MT-weighted image (MTw), as described in Section 1.6.9. PDw and $T1w$ account for the influence of PD signal and T1 relaxation, respectively, on the MT signal.

The effects of excitation and longitudinal relaxation in the FLASH sequence are given by the Ernst equation. Helms et al. (14) use the relaxation rate, $R_1 = 1/T1$, to simplify the notation. If small flip angles ($\alpha \ll 1$, in radians) and repetition times (TR) much shorter than longitudinal relaxation ($R_1 TR \ll 1$) are employed the signal is in excellent agreement with a rational approximation of the Ernst equation (179):

$$S(\alpha, TR) = A sin\alpha \frac{1-\exp(-R_1 TR)}{1-cos\alpha\exp(-R_1 TR)} \cong A\alpha \frac{R_1 TR}{\alpha^2/2 + R_1 TR} \tag{1.23}$$

$A = A(TE)$ denotes the amplitude of the spoiled gradient echo at the echo time, TE, under fully relaxed conditions ($R_1 TR \gg 1, \alpha = \pi/2$). In the MT FLASH experiment, the additional saturation due to MT is observed as a reduction in steady state signal, and is slightly modified from Equation 1.23:

$$S_{MT} \cong A\alpha \frac{R_1 TR}{\alpha^2/2 + R_1 TR + \delta} \tag{1.24}$$

Where the reduction of the signal imposed by the application of the MT pulse is described by an arbitrary saturation term, δ, the 'MT saturation' or $MTsat$. If A and R_1 are given, δ can be calculated from the MTw signal.

Helms et al. estimate the parameters A and R_1 from two FLASH signals, S_{PD} and S_{T1}, acquired with predominant PD and T1 weighting at different excitation flip angles, α_{PD} and α_{T1}, and repetition times, TR_{PD} and TR_{T1}. These reference images are acquired without the MT pulse and the signals can be described by Equation 1.23. Without correction for local flip angle errors, the following parameter estimates are labeled by the subscript "app." First, the apparent longitudinal relaxation rate, R_{1app}, is calculated as follows:

$$R_{1app} = \frac{1}{2} \frac{S_{T1}\alpha_{T1}/TR_{T1} - S_{PD}\alpha_{PD}/TR_{PD}}{S_{PD}/\alpha_{PD} - S_{T1}/\alpha_{T1}} \tag{1.25}$$

Second, the apparent signal amplitude, A_{app}, is calculated as follows:

$$A_{app} = S_{PD}S_{T1} \frac{TR_{PD}\alpha_{T1}/\alpha_{PD} - TR_{T1}\alpha_{PD}/\alpha_{T1}}{S_{T1}TR_{PD}\alpha_{T1} - S_{PD}TR_{T1}\alpha_{PD}} \tag{1.26}$$

From this, the apparent MT saturation δ_{app} is calculated as follows:

$$\delta_{app} = (A_{app}\alpha_{MT}/S_{MT} - 1)R_{1app}TR_{MT} - \alpha_{MT}^2/2 \tag{1.27}$$

Where S_{MT}, TR_{MT}, and α_{MT} denote signal intensity, TR, and excitation flip angle of MT-weighted image, respectively. The apparent MT saturation is inherently robust against differences in relaxation rates and inhomogeneities of RF transmit and receive field compared with conventional MTR imaging (14,15). Furthermore, small residual higher-order dependencies of the MT saturation on the local RF transmit field can be corrected to further improve spatial uniformity, as suggested by Weiskopf et al. (180):

$$MTsat = \frac{\delta_{app}(1-0.4)}{1-0.4RF_{local}} \tag{1.28}$$

Where RF_{local} is the relative local flip angle compared to the nominal flip angle.

Chapter 2

2   Test-retest reproducibility of *in vivo* oscillating gradient and microscopic anisotropy diffusion MRI in mice at 9.4 Tesla

This chapter was published in *PLoS ONE,* volume 16, Rahman *et al.*, **Test-retest reproducibility of in vivo oscillating gradient and microscopic anisotropy diffusion MRI in mice at 9.4 Tesla** (181), Copyright CC-BY, 2021.

2.1   INTRODUCTION

Diffusion MRI (dMRI) provides a non-invasive means to capture microstructure changes in the brain during development, aging, disease, and injury by probing the diffusion of water molecules (182). The most widely used dMRI techniques are diffusion tensor imaging (DTI) and diffusion kurtosis imaging (DKI). DTI assumes the dMRI signal is entirely characterized by Gaussian diffusion (8) and utilizes a diffusion tensor model to estimate metrics such as mean diffusivity (MD) and fractional anisotropy (FA). DKI provides more information about the underlying tissue via the diffusion kurtosis, which quantifies the deviation from Gaussian diffusion (124). However, both DTI and DKI are unable to distinguish between microstructural changes and neuron fiber orientation dispersion (8,21), reducing their specificity to microstructural changes in brain regions with crossing fibers. Furthermore, DKI cannot differentiate between different sources of kurtosis (non-Gaussian diffusion) (124).

Probing microstructure with diffusion-weighted sequences beyond the conventional Stejskal-Tanner pulsed gradient spin echo (PGSE) sequence (113), used in

DTI and DKI, is currently of broad interest. The aims of these emerging dMRI sequences are to overcome the limitations of DTI and DKI and improve sensitivity and specificity to microstructural changes. In the present work, the reproducibility of *in vivo* oscillating gradient and microscopic anisotropy dMRI, both of which have unique features that go beyond the PGSE sequence, is investigated in mice at 9.4 Tesla. It is important to note that these are two distinct dMRI methods which are evaluated separately in this work.

The conventional PGSE sequence consists of a pair of pulsed gradients applied along a single direction. Here, the diffusion measurement reflects information about diffusion along a single direction and at a single relatively long diffusion time, which is the time allowed for water molecules to probe the local environment. Given hardware constraints, diffusion times achievable in PGSE can probe displacements on the order of $10 – 30 \, \mu m$, which is much larger than typical axon sizes ($\sim 2 \, \mu m$) (9).

To overcome the diffusion time limitations of PGSE, the oscillating gradient spin echo (OGSE) method was developed to modify sensitivity to cellular length scales (10). OGSE allows different microstructure length scales to be probed by varying the frequency of the oscillating diffusion gradients, which is inversely related to diffusion time. For increasing diffusion times (lower oscillating gradient frequencies), the molecules travel greater distances and interact with more barriers such as cell membranes, resulting in lower observed MD values (145). As MD is different at the various frequencies, this provides the ΔMD - the metric of interest in OGSE dMRI, the difference in MD between the highest and lowest frequencies applied. By acquiring diffusion data at multiple frequencies, the power law relationship between MD and frequency (f) can be explored via the "diffusion dispersion rate", Λ (162,178). Evidence

of a linear dependence of MD on the square root of frequency has been demonstrated in healthy and globally ischemic rodent brain tissue (169) and healthy human white matter (183). Thus, Λ can be calculated as

$$MD_f = MD_0 + \Lambda \cdot f^{0.5} \qquad (2.1)$$

where MD_f is the OGSE MD at a frequency f and MD_0 is the MD at f = 0 (162,178,183). Since OGSE is sensitive to structural disorder along one dimension (162), changes in the number and morphology of neurite varicosities will result in changes to Λ (178), which potentially makes OGSE an invaluable tool to probe microstructural changes, such as axonal beading, *in vivo* (19,20).

In contrast to the widely used fractional anisotropy metric (FA), which confounds true microstructural changes with fiber orientation dispersion (8), the microscopic anisotropy (µA) metric quantifies water diffusion anisotropy independent of orientation dispersion (141,184,185). To disentangle orientation dispersion from true microstructure changes, the shape of the b-tensor, which describes the strength of diffusion weighting along each direction, is varied via tensor-valued diffusion encoding (141,185–187). Most tensor-valued encoding protocols are based on double diffusion encoding (DDE) techniques (185,188–191) or a combination of linear tensor encoding (LTE) and spherical tensor encoding (STE) (12,21,141,184). As DDE sequences are implemented via two consecutive diffusion encoding pulses separated by a mixing time, in some cases they may require longer TEs than standard LTE/STE sequences to achieve equal b-values (192). Conventional DTI and DKI utilize only LTE, in which all gradients are along the same axis, so that diffusion is encoded along a single direction at a time. STE, in which

the gradients are distributed throughout all directions, sensitizes the signal to diffusion along all directions at the same time. Here, a combination of LTE and STE is utilized to implement microscopic anisotropy (µA) dMRI (21,184), using an optimized linear regression technique based on the diffusion kurtosis model (12).

This technique makes the assumption that the dMRI signal arises only from multiple Gaussian components, which may not be appropriate in certain cases, such as when time-dependent diffusion is not negligible (161). Nevertheless, the normalized signal intensity of powder-averaged dMRI acquisitions of a multi-component system can be represented by the cumulant expansion (141):

$$\ln\left(\frac{S}{S_o}\right) = -bD + \frac{1}{6}bD^2K\,... \tag{2.2}$$

where S is the powder-averaged signal, S_o is the mean signal with no diffusion encoding, b is the b-value, D is the diffusivity, and K is the kurtosis of the power-averaged signal. Microscopic anisotropy (µA) is defined here based on the difference in signal between LTE and STE dMRI acquisitions, similar to the equation used in DDE protocols (184,193):

$$\mu A = \sqrt{\frac{\ln\left(\frac{S_{LTE}}{S_{STE}}\right)}{b^2}} \tag{2.3}$$

where S_{LTE} and S_{STE} are the powder-averaged LTE and STE signals, respectively. Microscopic fractional anisotropy (µFA), the normalized counterpart of µA, can be expressed in terms of µA:

$$\mu FA = \sqrt{\frac{3}{2}\frac{\mu A^2}{\mu A^2 + 0.2D^2}} \tag{2.4}$$

The complete derivation of equations (2.3) and (2.4) is available in Arezza et al. (12). As the LTE signal depends on variance of both isotropic and anisotropic diffusivity, while the STE signal depends only on variance of isotropic diffusivity, diffusional kurtosis estimated from the µA protocol includes linear kurtosis (K_{LTE} – arising from the LTE acquisitions) and isotropic kurtosis (K_{STE} – arising from the STE acquisitions). K_{STE} is a measure of the variance in the magnitude of diffusion tensors or the mean diffusivity, which can be related to cell size heterogeneity (21).

OGSE and µA dMRI have recently been gaining attention in various disease and injury models and their feasibility has been shown in both preclinical and clinical settings. Importantly, OGSE dMRI can provide measures of mean cell size (194,195) and axonal diameter (196–199), while µA dMRI can provide estimates of cell shape (21,141,185–188,190,191). Low-frequency OGSE has also been shown to provide better contrast, compared to PGSE, to cylinder diameter in the presence of orientation dispersion (197,198,200). The OGSE ΔMD metric has shown increased sensitivity, compared to MD alone, in the assessment of hypoxia-ischemia (201) and radiation therapy treatment response (202) in rodents, and in various pathologies in humans, including muscle contraction abnormalities (203), high- and low-grade brain tumor differentiation (16), and neonatal hypoxic-ischemic encephalopathy (204). Notably, OGSE has helped to identify neurite beading as a mechanism for dMRI contrast after ischemic stroke (19,20). Preliminary studies in humans have found that µA provides better sensitivity than the conventional FA in distinguishing between different types of

brain tumours (21), assessment of multiple sclerosis lesions (16,17), and detecting white matter microstructure changes associated with HIV infection (193). Furthermore, Westin et al. reported that K_{STE} showed significant differences between controls and schizophrenia patients, while conventional mean kurtosis showed no difference (11). The feasibility of μA dMRI has been demonstrated in rodents both *in vivo* (205,206) and *ex vivo* (161,193,207). *In vivo* preclinical rodent μA studies, which have included predominantly DDE techniques and more recently combined LTE/STE techniques, have shown that measurements of eccentricity provide additional sources of contrast for the rat brain, especially in the gray matter (205), and recently, He et al. have shown that K_{STE} may be particularly sensitive to deep gray matter lesions (208).

As dMRI has reached the forefront of tissue microstructure imaging (209), there is a need to establish the reproducibility of these emerging methods. While the reproducibility of DTI and DKI has been investigated extensively (210–213), to the best of our knowledge, no test-retest assessment of OGSE and μA dMRI has been done at ultra-high field strength. The aim of this work was to assess test-retest reproducibility of *in vivo* OGSE and μA dMRI in mice at 9.4 Tesla and provide estimates of required sample sizes, which is essential in planning future preclinical neuroimaging studies involving models of disease/injury.

2.2   METHODS

2.2.1   Subjects

All animal procedures were approved by the University of Western Ontario Animal Use Subcommittee and were consistent with guidelines established by the

Canadian Council on Animal Care. Twelve adult C57Bl/6 mice (six male and six female), between 12 - 14 weeks old, were scanned twice 5 days apart. The sample size was chosen to reflect similar sample sizes used in other pre-clinical imaging studies (214–217). Before scanning, anesthesia was induced by placing the animals in an induction chamber with 4 % isoflurane and an oxygen flow rate of 1.5 L/min. Following induction, isoflurane was maintained during the imaging session at 1.8 % with an oxygen flow rate of 1.5 L/min through a custom-built nose cone. The mouse head was fixed in place using ear bars and a bite bar to prevent head motion. These mice were part of a longitudinal study, at the end of which they were euthanized for histology. The mice were anesthetized with ketamine/xylazine (2:1) and then underwent trans-cardiac perfusion with ice-cold saline, followed by 4% paraformaldehyde in phosphate-buffer saline (PBS).

2.2.2   In vivo MRI

In vivo MRI experiments were performed on a 9.4 Tesla (T) Bruker small animal scanner equipped with a gradient coil set of 1 T/m strength (slew rate = 4100 T/m/s). A single channel transceive surface coil (20 mm x 25 mm), built in-house, was fixed in place directly above the mouse head to maximize signal-to-noise ratio (SNR). The mouse holder (which included the ear bars and bite bar), nose cone, and surface coil were fixed onto a support, which was placed into the scanner. This ensured consistent positioning of the mouse head in the scanner at each session. Each dMRI protocol was acquired with single-shot spin echo echo-planar-imaging (EPI) readout with scan parameters: TR = 10 s; in-plane resolution = 175 x 200 µm; slice thickness = 500 µm; 30 slices to acquire the full brain; field-of-view = 19.2 x 14.4 mm^2; partial Fourier imaging in the phase encode direction with 80% of k-space being sampled; 45 minutes scan time. For each dMRI

protocol, a single reverse phase encoded b = 0 s/mm^2 volume was acquired at the end of

the diffusion sequence for subsequent use in TOPUP (218) and EDDY (219) to correct

for susceptibility and eddy current induced distortions. Averages were acquired

separately on the scanner and combined using in-house MATLAB code which included

reconstruction of partial Fourier data using POCS (Projection onto Convex Sets) (220)

and correction for frequency and signal drift associated with gradient coil heating (221).

Anatomical images were also acquired for each subject within each session using a 2D

T2-weighted TurboRARE pulse sequence (150 μm in-plane resolution; 500 μm slice

thickness; TE/TR = 40/5000 ms; 16 averages; total acquisition time = 22 min).

2.2.2.1   *Oscillating Gradient Spin Echo (OGSE) dMRI*

The OGSE dMRI protocol included a PGSE sequence (with gradient duration =

11 ms and diffusion time = 13.8 ms) and four OGSE sequences with oscillating gradient

frequencies of 50 Hz, 100 Hz, 145 Hz, and 190 Hz. The waveforms and gradient

modulation power spectra are shown in Figure 2.1 (A – E). The 50 Hz sequence is based

on the recently proposed frequency tuned bipolar (FTB) oscillating gradient waveform,

which allows for shorter TEs at lower frequencies (222). The frequencies were chosen

based on a hypoxic-ischemic injury study in mice (201), where the frequencies ranged

from 0 - 200 Hz, which enables probing length scales between 1.2 – 4.2 µm. Other scan

parameters included: gradient separation = 5.5 ms; TE = 39.2 ms; 5 averages; b = 800

s/mm^2; 10 diffusion encoding directions. As the gradient duration was slightly different

for each OGSE sequence, zeroes were added to the start of the first diffusion-encoding

waveform and to the end of the second diffusion-encoding waveform, to ensure that TE

remained the same across all OGSE sequences. 10 b = 0 s/mm^2 volumes were interspersed evenly throughout the acquisition.
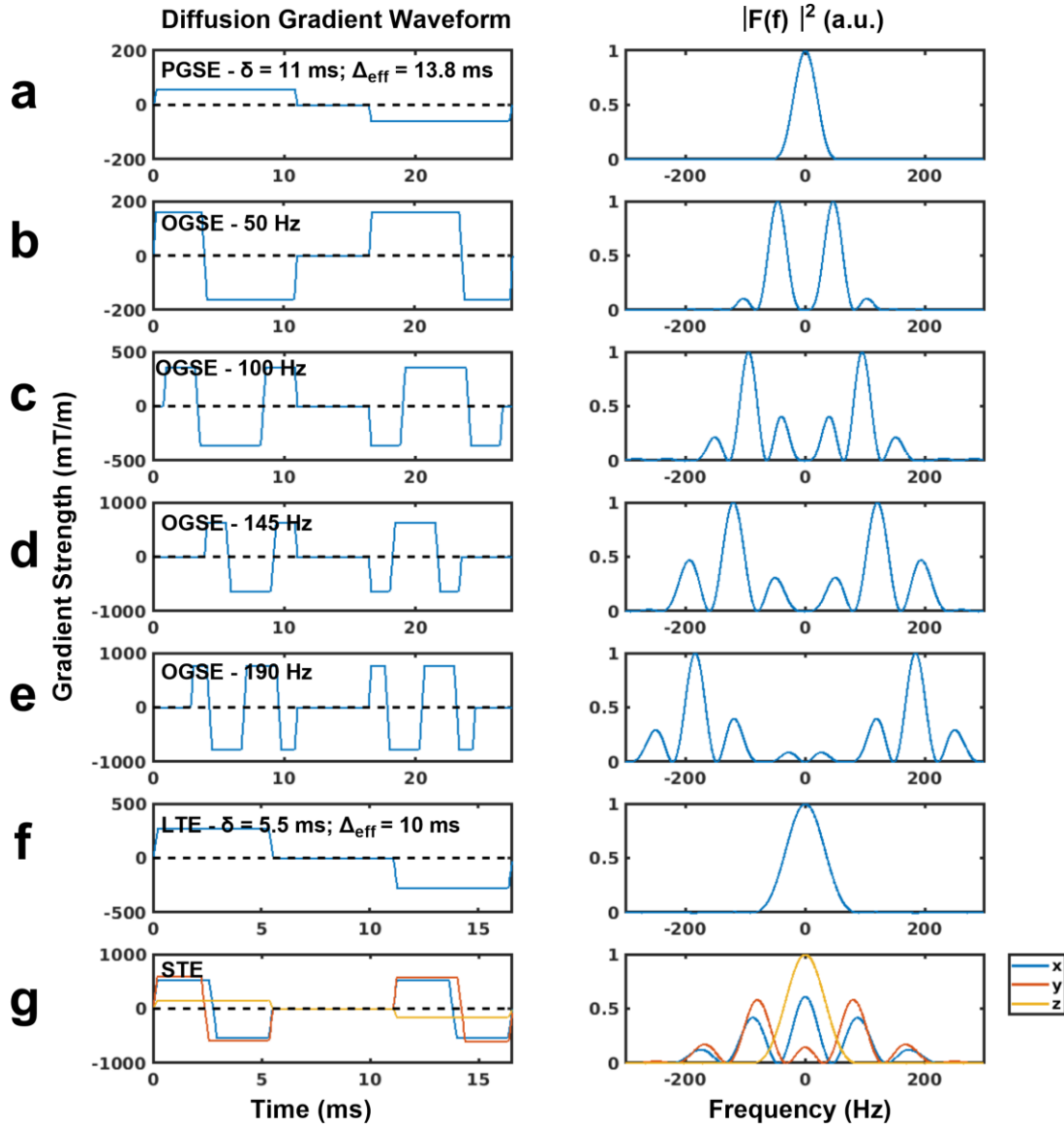
Figure 2.1 - *Schematic representations of the gradient waveforms and gradient modulation power spectra, $|F(f)|^2$, used for the PGSE (a), OGSE (b-e) and μA (f-g) protocols. Diffusion encoding blocks have been inserted on both sides of a 180° pulse and implicit gradient reversal due to the 180° pulse has been applied. The PGSE*

waveform (a) is shown with a gradient duration of 11 ms and diffusion time of 13.8 ms.

OGSE waveforms (b-e) with gradient oscillation frequencies of 50 Hz, 100 Hz, 145 Hz,

and 190 Hz have zeros added to the start of the first gradient and end of the second

gradient to ensure all scans in the OGSE protocol have the same TE. LTE and STE

waveforms, used in the μA protocol, are shown in (f) and (g) respectively.

2.2.2.2   *Microscopic Anisotropy (μA) dMRI*

The STE dMRI gradient waveforms implemented here were similar to the protocol in Arezza et al. (12). The μA sequence was implemented with linear (LTE) and spherical tensor (STE) encodings, as shown in Figure 2.1 (F – G), at b = 2000 s/mm^2 (30 directions for each of LTE and STE) and b = 1000 s/mm^2 (12 directions). Other scan parameters included: gradient duration = 5 ms; gradient separation = 5.54 ms; TE = 26.8 ms; 3 averages. 8 b = 0 s/mm^2 volumes were interspersed evenly throughout the acquisition.

2.2.3   Image Processing

Images were pre-processed using PCA denoising (223) and Gibbs ringing correction from the MRtrix3 package (224), followed by TOPUP (218) and EDDY (219) from FMRIB Software Library (FSL, Oxford, UK) (225). Brain masks were produced using the skull stripping tool from BrainSuite (v. 19b) (226). Image registration was performed using affine and symmetric diffeomorphic transforms with ANTs software (https://github.com/ANTsX/ANTs) (227). Region-of-interest (ROI) masks were acquired from the labeled Allen Mouse Brain Atlas (228). Since registration to an atlas is time-consuming, only one anatomical T2-weighted scan was chosen (the "chosen T2") to be

registered to the atlas. All other anatomical T2-weighted images were registered to the chosen T2. Non-diffusion weighted (b0) volumes were registered to the corresponding anatomical images (from the same subject at the same timepoint). All dMRI volumes were registered to the corresponding anatomical space using the transforms resulting from the previous step (b0 → corresponding T2). For ROI-based analysis, the inverse transforms resulting from these two registration steps (corresponding T2 → chosen T2 → atlas) were then used to bring the labeled atlas to the corresponding T2 space for each subject at each timepoint. Binary masks for each ROI were generated by thresholding the labeled atlas. Each mask was eroded by one voxel, except for the corpus callosum masks, to minimize partial volume errors within a given ROI. The binary masks were visually inspected to ensure good registration quality. Furthermore, to perform whole brain voxel-wise analysis of all subjects across both timepoints, all dMRI volumes were registered to the chosen T2 space using transforms from two registration steps (b0 → corresponding T2 → chosen T2). For voxel-wise analysis targeted to specific ROIs, the labeled atlas was registered to the chosen T2 space.

From the OGSE data, maps of MD at each frequency were generated using MRtrix3 (224,229). ΔMD was calculated as the difference between MD acquired at the highest frequency (190 Hz) and MD acquired at the lowest frequency (0 Hz). To characterize the power law relationship between MD and OGSE frequency (f) (178), the slope of linear regression of MD with $f^{0.5}$, the diffusion dispersion rate (Λ), was calculated. From the µA data, maps of µA, µFA, K_{LTE}, and K_{STE} were generated by fitting the powder-averaged STE and LTE signals versus b-value to the diffusion kurtosis model, using a joint non-negative least squares method assuming consistent diffusivity

between STE and LTE (12). As a reference for the OGSE and µA metrics, DTI metrics (MD and FA) have been included in both ROI-based and voxel-wise variability analyses. MD and FA maps were generated using the PGSE sequence (with b=800 s/mm^2 from the OGSE protocol) and the LTE sequence (with b=1000 s/mm^2 from the µA protocol), separately.

2.2.4 Data Analysis

The test-retest dataset is available online (230). Measurement reproducibility was explored for both ROI-based analysis and whole brain voxel-wise analysis, since both are common analyses techniques in neuroimaging. To mitigate partial volume errors from cerebrospinal fluid (CSF), voxels with MD (0 Hz) > 0.9 µm^2/ms were omitted from the analyses of all scalar maps. Outlier detection was included in both ROI-based and voxel-wise analyses, to remove data both animal-wise and voxel-wise. Outliers were defined as values which were more than three scaled median absolute deviations (MAD) away from the median. The ROI analysis focused on five different tissue regions: corpus callosum, internal capsule, hippocampus, cortex, and thalamus. Bland-Altman analysis was performed for both ROI-based and voxel-wise analyses to identify any biases between test and retest measurements. For both analysis techniques, the scan-rescan reproducibility was characterized using the coefficient of variation (CV). The CV reflects both the reproducibility and variability of these metrics and allows calculation of the sample sizes necessary to detect various effect sizes. CVs were calculated between subjects and within subjects to quantify the between subject and within subject reproducibility respectively. The between subject CV was calculated separately for the test and retest timepoints as the standard deviation divided by the mean value across

subjects 1–12. These two CV values were then averaged for the mean between subject CV. The within subject CV was calculated separately for each subject as the standard deviation divided by the mean of the test and retest scans. The 12 within subject CVs were then averaged to determine the mean within subject CV. Following the procedure presented in van Belle (231), the between subject CVs, from the ROI analysis, were used to determine the sample size required per group to detect a defined biological effect between subjects in each ROI. Assuming paired t-tests, the standard deviations of the differences between test-retest mean values across subjects, were used to determine the sample size required to detect a defined biological effect within subjects in each ROI (232). The minimum sample sizes, using the between and within subject approaches, were both determined at a 95 % significance level ($\alpha = 0.05$) and power of 80 % ($1-\beta = 0.80$).

2.2.4.1   SNR Analysis

As the transceive surface coil used in this study was built in-house, SNR maps were generated for the lowest and highest b-value acquisitions in the OGSE and µA protocols to compare SNR acquired using a commercially available 40-mm millipede (MP40) volume coil (Agilent, Palo Alto, CA, USA) and SNR acquired with fewer averages. SNR maps were calculated by dividing the powder-averaged magnitude signal (of the combined averages) by the noise. Noise was calculated from each of the real and imaginary components of the complex-valued data as the standard deviation of the background signal from a single average of a single direction divided by $\sqrt{(\text{number of averages}) \cdot (\text{number of directions})}$, and averaged over the real and imaginary components. Furthermore, to test the effects of using a different number of

averages on the results, ROI-based between and within-subject CV analysis was performed on subsets of the OGSE and µA data containing only 3 and 2 averages, respectively. Note that preprocessing was performed on the subset of fewer averages separately from the full data set (e.g., denoising only used the subset of averages).

2.2.4.2   ROI Analysis

The mean MD was calculated for each ROI at each frequency. For each ROI, ΔMD was calculated as the difference between the mean MD at 190 Hz and the mean MD at 0 Hz. The apparent diffusion dispersion rate, Λ, was determined for each ROI by performing a least square fit of the mean MD (in each ROI) to $f^{0.5}$. Scalar maps from the µA protocol (µA, µFA, K_{LTE}, K_{STE}) were computed directly from the signal, and mean values for each metric were computed for each ROI. It should be noted that for both OGSE and µA metrics, averaging for each ROI was performed over the first non-signal parameter computed. Bland-Altman and CV analyses were performed using the mean values.

2.2.4.3   Voxel-wise Analysis

ΔMD maps were generated by subtracting the MD maps at 0 Hz from the MD maps at 190 Hz. Λ maps were generated by performing a least square fit of MD to $f^{0.5}$ for each voxel. Voxel-wise Bland-Altman and CV analyses were performed for each metric using the scalar maps (ΔMD, Λ, and scalar maps from the µA protocol).

2.3 RESULTS

2.3.1 SNR Analysis

SNR maps, shown in Figure 2.2, revealed a higher SNR in the cortex when using the surface coil (with 5 and 3 averages for the OGSE and µA protocols respectively) compared to the MP40 volume coil. As expected, a gradient of SNR change can be seen in the superior-inferior direction of the brain with the surface coil.
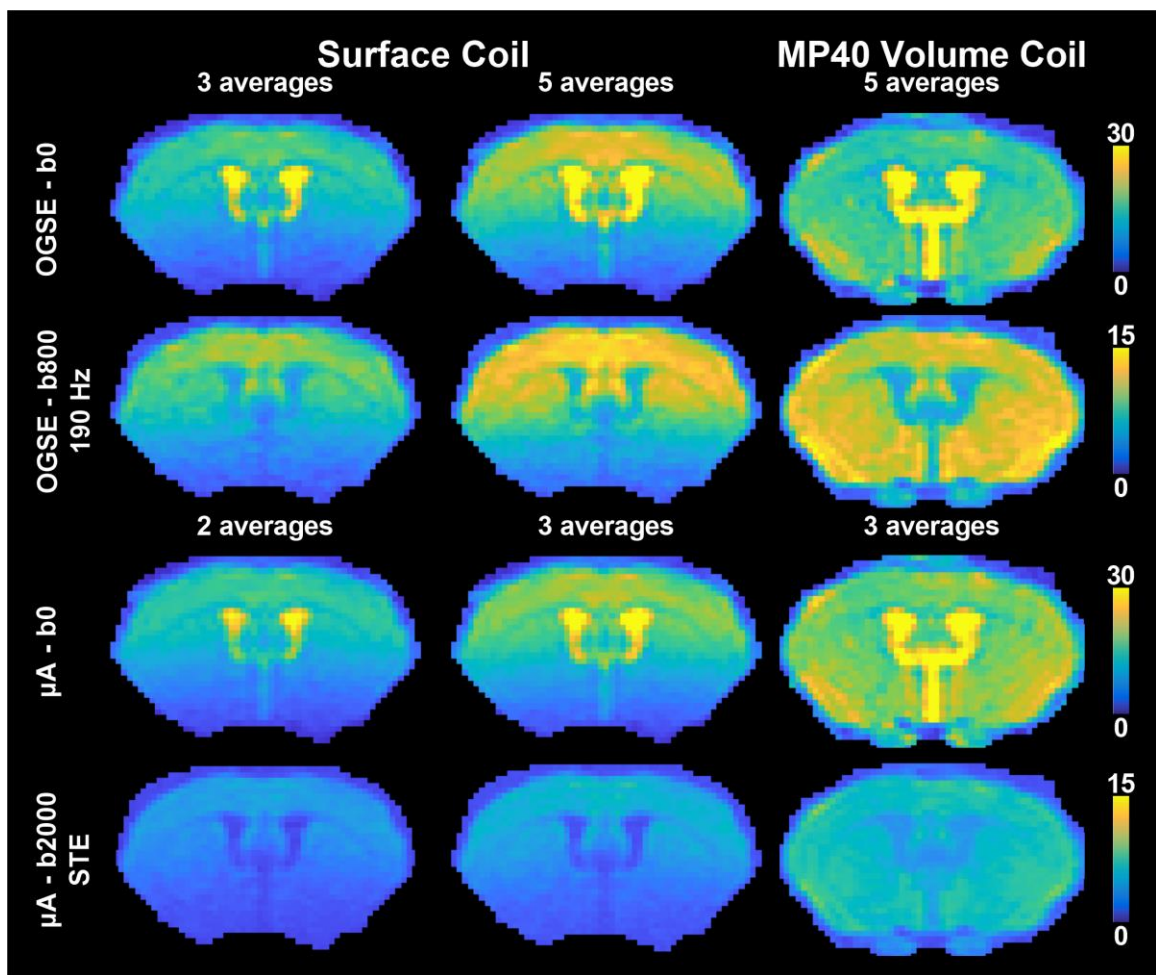
Figure 2.2 - *SNR maps of images acquired with the surface coil and the millipede-40mm (MP40) volume coil. SNR maps for a single b = 0 s/mm² image are shown for both protocols, and SNR maps for the powder average of the highest b-values are shown for*

both protocols (b = 800 s/mm^2 for OGSE-190 Hz and b = 2000 s/mm^2 for µA-STE). The middle column shows SNR maps acquired from the surface coil with the number of averages used in this study (5 averages for the OGSE protocol and 3 averages for the µA protocol). The left column shows the effect of using fewer averages (3 averages for OGSE and 2 averages for µA). The right column shows the effect of using a commercially available MP40 volume coil with same number of averages used in this study.

2.3.2   Raw Data to Parameter Maps

Raw data (after combining all averages) and preprocessed data are shown in Figure 2.3. Representative parameter maps are shown in Figure 2.4. MD (190 Hz) has an overall higher intensity than MD (0 Hz). ΔMD shows selective enhancement of distinct regions in the brain - the dentate gyrus (part of the hippocampal formation) is shown with white arrows. As expected, ΔMD and Λ show similar contrast. ROI-based fitting of Λ showed the expected trends with $f^{0.5}$ in all ROIs and at both test and retest time-points (Figure 2.5). The µA and µFA maps also show similar contrast. K_{LTE} highlights white matter structures as expected and K_{STE} is homogenous throughout the brain, although very high in CSF regions and regions impacted by CSF partial volume effects.
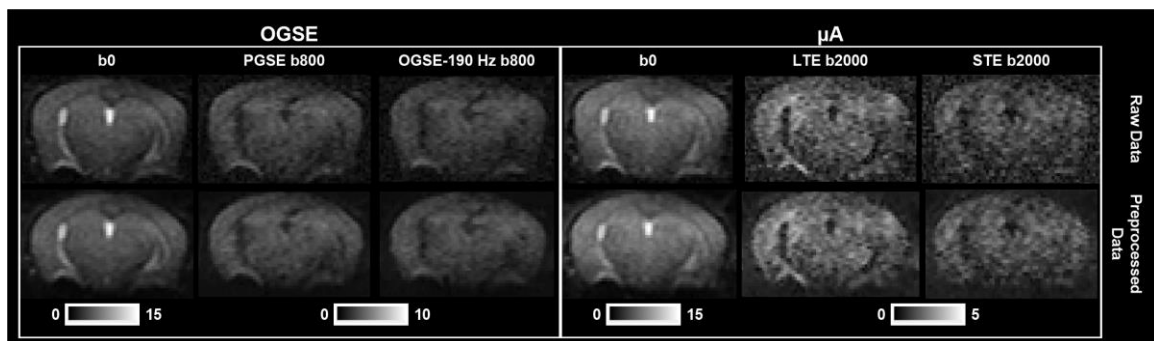
Figure 2.3 - *Raw and preprocessed dMRI data. Raw data (after combining averages) is shown in the top row and preprocessed data is shown in the bottom row. Representative b = 0 s/mm² images are shown for both the OGSE and μA protocols. From the OGSE protocol, representative diffusion weighted images from a single diffusion gradient direction are shown from PGSE and OGSE with the highest frequency used in this study (190 Hz), at b = 800 s/mm². From the μA protocol, diffusion weighted images from a single diffusion gradient direction are shown from the LTE and STE sequences, at b = 2000 s/mm².*
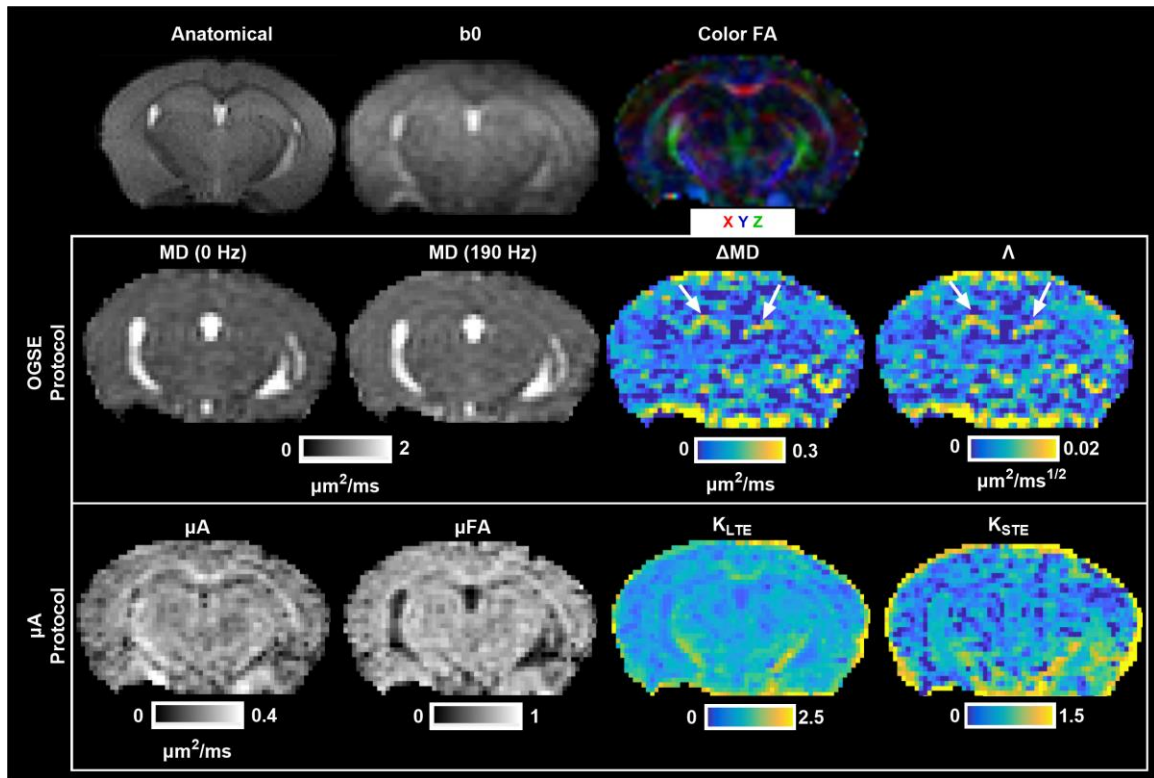
Figure 2.4 - *Example axial cross sections from a single subject showing an anatomical T2-weighted image, a non-diffusion weighted image (b0), and a color fractional anisotropy map (Color FA), where the colors represent the primary direction of diffusion. Parameter maps from the OGSE protocol (MD (0 Hz): Mean Diffusivity from PGSE (0*

Hz); MD (190 Hz): Mean Diffusivity from OGSE (190 Hz); ΔMD: the difference between MD (190 Hz) and MD (0 Hz); Λ: the apparent diffusion dispersion rate) and the μA protocol (μA: Microscopic Anisotropy; μFA: Microscopic Fractional Anisotropy; K_{LTE}: Linear Kurtosis (from linear tensor encodings); K_{STE}: Isotropic Kurtosis (from spherical tensor encodings)) are shown. The white arrows in the ΔMD and Λ maps indicate high OGSE contrast in the dentate gyrus.
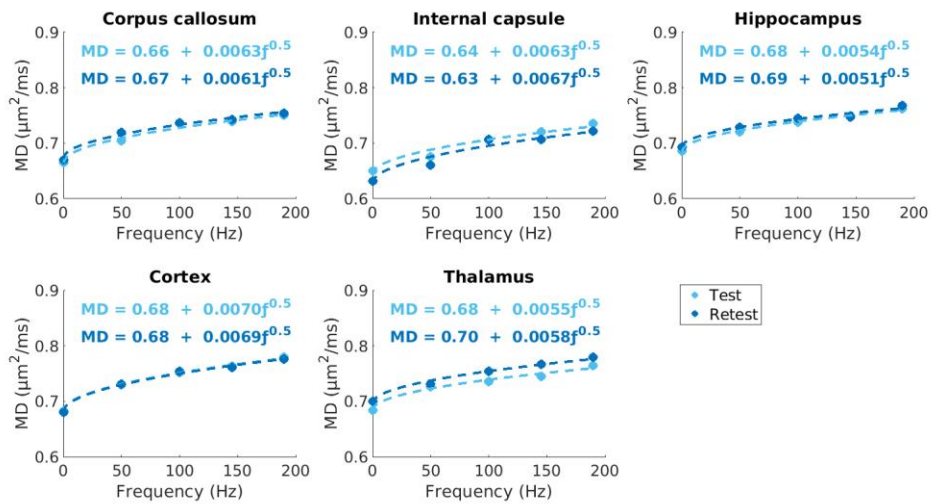
Figure 2.5 - *Least square fitting of mean MD values to $f^{0.5}$, depicted by the dotted lines, in each ROI for test and retest timepoints in one mouse. The diffusion dispersion rate, Λ, ranged from 0.0051 – 0.0070 $μm^2/ms^{1/2}$, depending on the ROI.*

2.3.3   ROI Analysis

Violin plots depict the distribution of the mean values for each metric within each ROI for the twelve subjects (Figure 2.6). Across all metrics, the median and interquartile range are similar for test and retest conditions. In general, the smaller ROIs (the internal capsule and the thalamus) show greater distributions, while the larger ROIs (i.e., the

cortex) showed much tighter distributions. Bland-Altman plots (Figure 2.7) revealed negligible biases between repeat measurements across all metrics. In the variability analysis, outlier removal revealed at most one outlier for most metrics (in some of the ROIs), with K_{STE} and FA containing two outliers in the thalamus and internal capsule. Λ and ΔMD showed similar CVs, with the between subject CVs ranging from 5 – 15 %, and the within subject CVs ranging from 4 – 10 %. (Figure 2.8). µA and µFA show low between and within subject CVs for all ROIs (ranging from 3 – 8 %), with µFA showing slightly lower CVs. K_{LTE} exhibited consistently lower between and within subject CVs (3 – 8 %) compared to K_{STE} (10 – 17 %). In terms of the DTI metrics, the lowest CVs were observed in MD (CVs < 5 %) and FA showed a higher variation of CVs than most of the OGSE and µA metrics. ROI-based between and within-subject CV analysis performed on OGSE and µA data with fewer averages revealed comparable CVs (as shown in Supplemental Figure 2.S1).
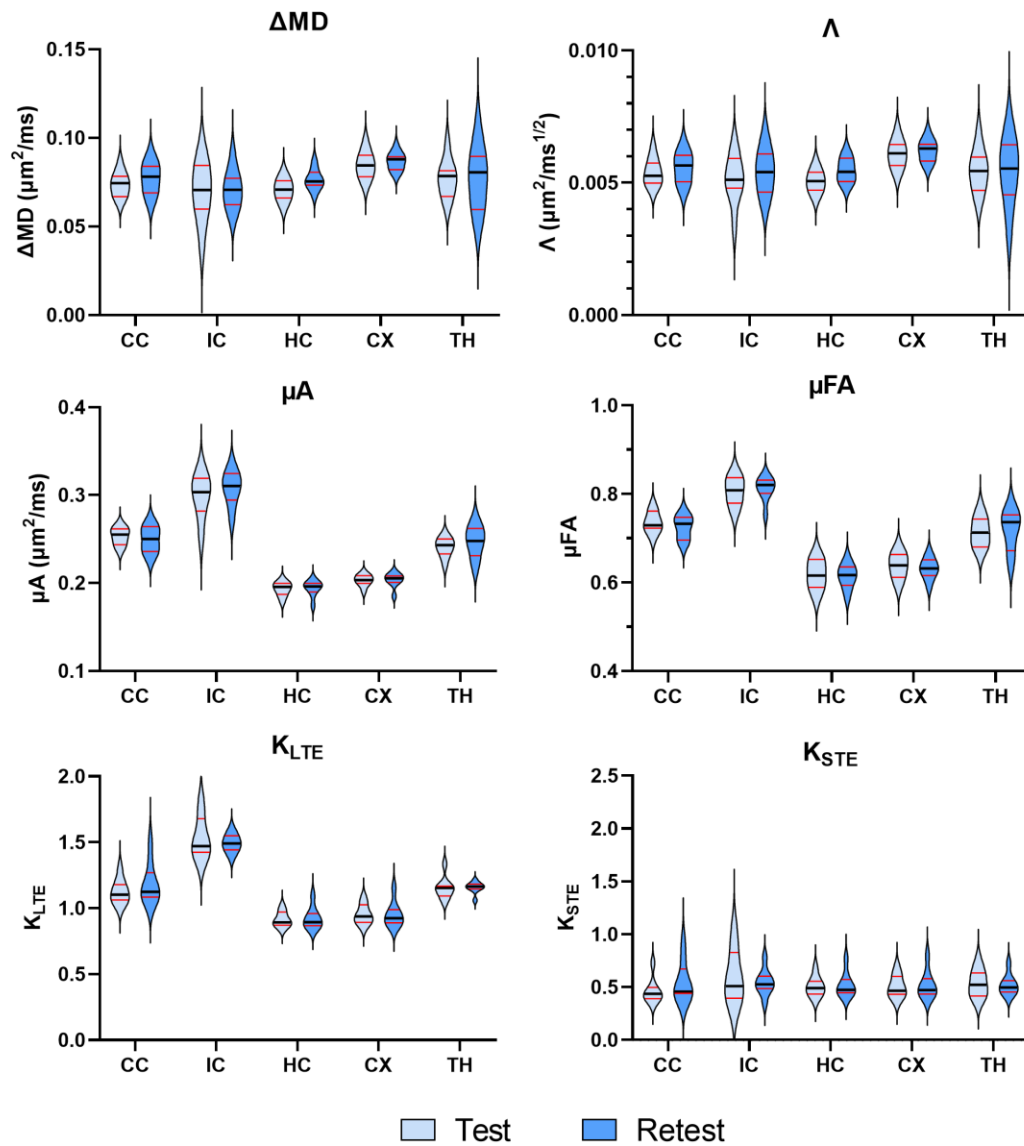
Figure 2.6 - *Violin plots showing the distribution of the OGSE metrics (ΔMD and Λ) and the μA metrics (μA, μFA, K_{LTE}, and K_{STE}) at the test and retest timepoints (five days apart) for twelve subjects in several brain regions. The dark black line represents the median and the red lines depict the interquartile range (25th to 75th percentile). The violin plots extend to the minimum and maximum values of each metric. ROIs are*

abbreviated as follows: CC – corpus callosum; IC – internal capsule; HC – hippocampus; CX – cortex; TH – thalamus.

ΔMD

Λ

μA

μFA

K$_{LTE}$

K$_{STE}$

CC   IC   HC   CX   TH
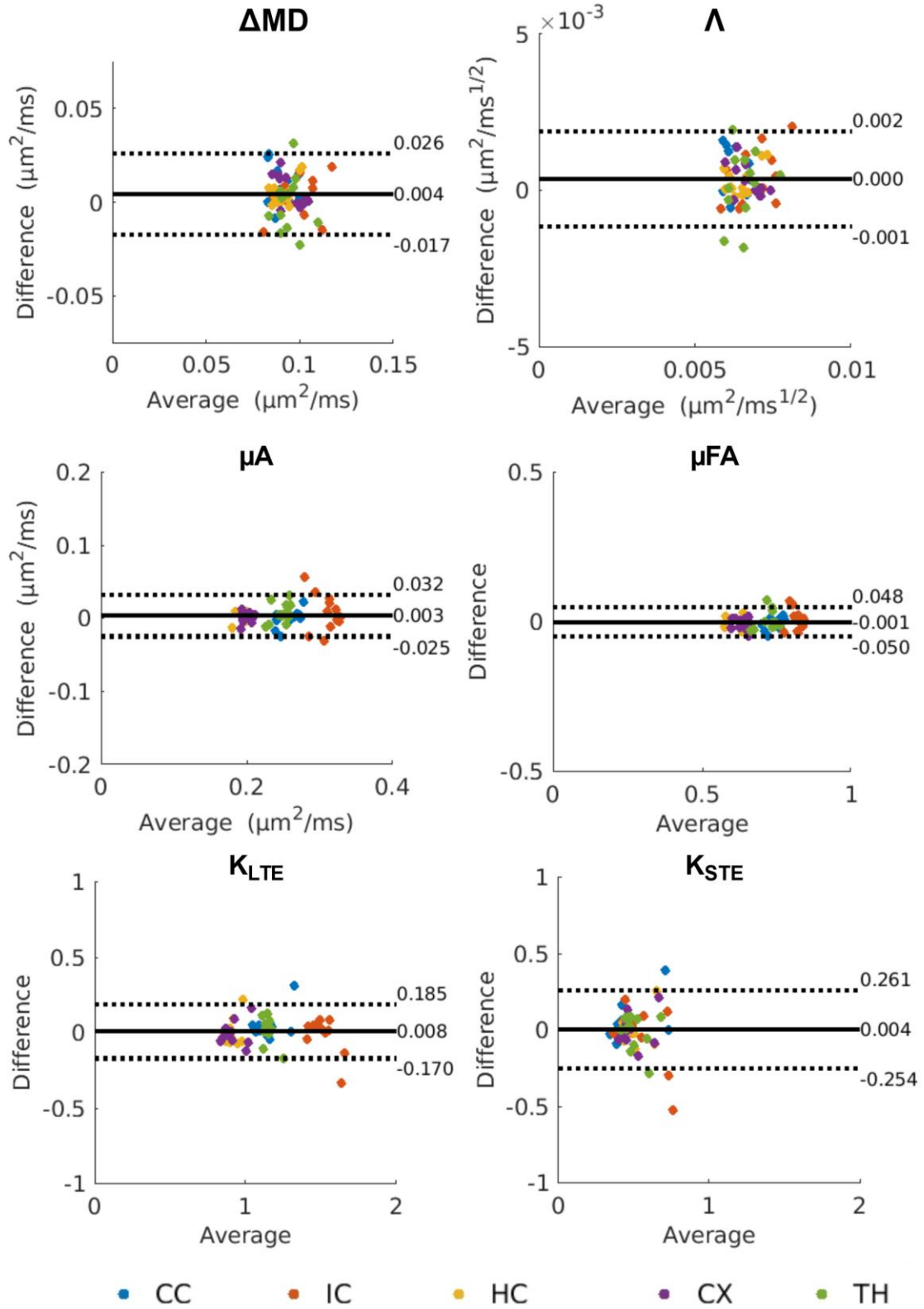
Figure 2.7 - *Bland-Altman plots depicting biases between test and retest scans for mean values of OGSE and µA metrics (from the ROI-based analysis). The solid black lines represent the mean bias, and the dotted black lines represent the ±1.96 standard deviation lines. The average of the test and retest mean values is plotted along the x-axis and the difference between the test and retest mean values is plotted along the y-axis. ROIs in the legend are abbreviated as follows: CC – corpus callosum; IC – internal capsule; HC – hippocampus; CX – cortex; TH – thalamus.*
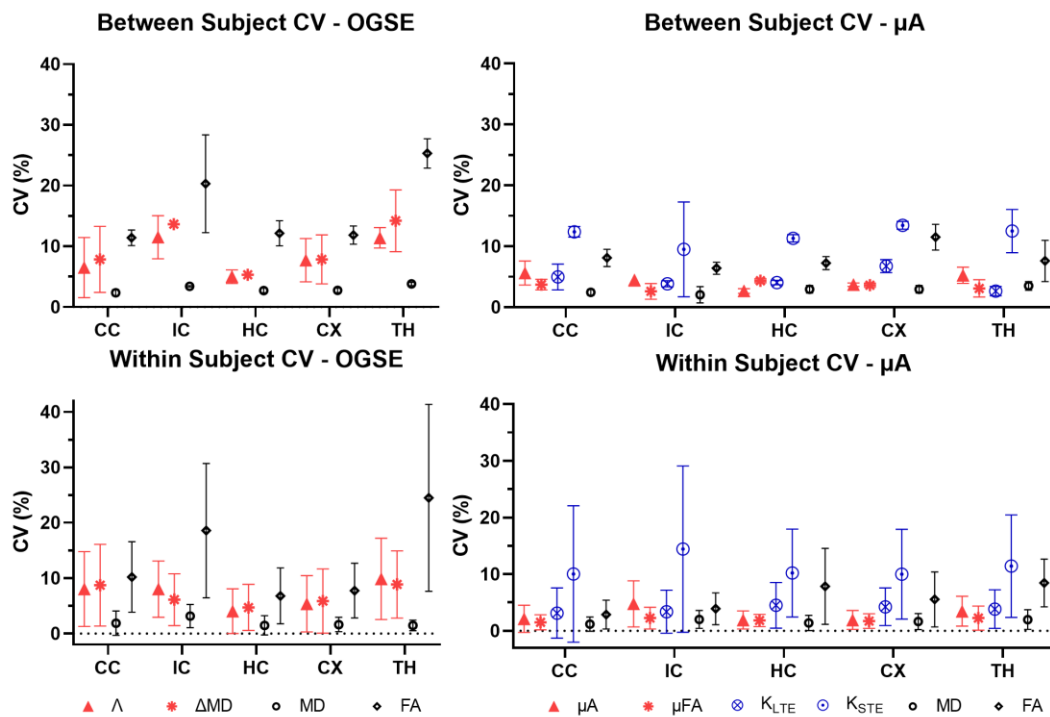
Figure 2.8 - *Mean between subject and within subject coefficients of variation (CV) for OGSE and µA metrics for each ROI. Values for the between subject condition represent the mean ± standard deviation over subjects (averaged over the test and retest timepoints). Values for the within subject condition represent the mean ± standard deviation between test and retest (averaged over all subjects). ROIs are abbreviated as*

follows: CC – corpus callosum; IC – internal capsule; HC – hippocampus; CX – cortex;

TH – thalamus.

2.3.4   Voxel-wise Analysis

Bland-Altman plots comparing whole brain test and retest voxels for all twelve subjects revealed negligible biases for all metrics (Figure 2.9). However, ΔMD, Λ, and K_{STE} showed greater variation in test and retest differences. The CV maps (Figure 2.10) show very high CVs in the CSF regions (except for the K_{STE} and FA CV maps). Histograms (Figure 2.11) show ΔMD and Λ have the same distribution. Overall, the between and within subject CVs are comparable for all metrics. μA, μFA, and K_{LTE} have comparable CVs with peaks at 10, 8, and 16 % respectively. ΔMD, Λ, and K_{STE} peak around 50 % and have very wide distributions. In comparison, the DTI metrics, MD and FA, peak at 8 % and 25 % respectively. Whole brain histograms and histograms for specific ROIs (Supplemental Figure 2.S2) show similar trends.
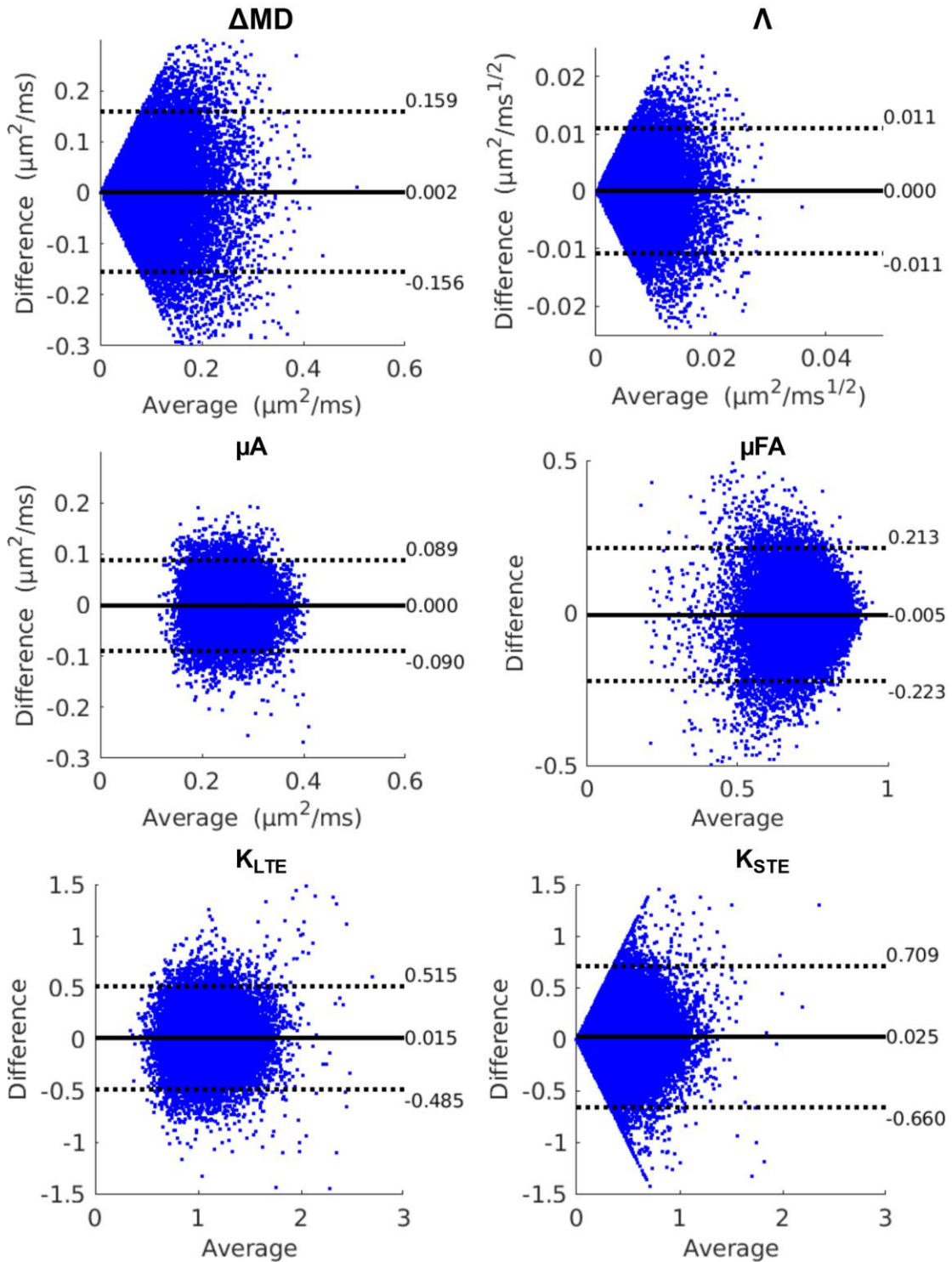
Figure 2.9 - *Bland-Altman plots depicting biases between test and retest scans for OGSE*

and μA metrics from the whole-brain voxelwise analysis for all subjects. The solid black

lines represent the mean bias, and the dotted black lines represent the ±1.96 standard deviation lines. The average of the test and retest voxels is plotted along the x-axis and the difference between the test and retest voxels is plotted along the y-axis.
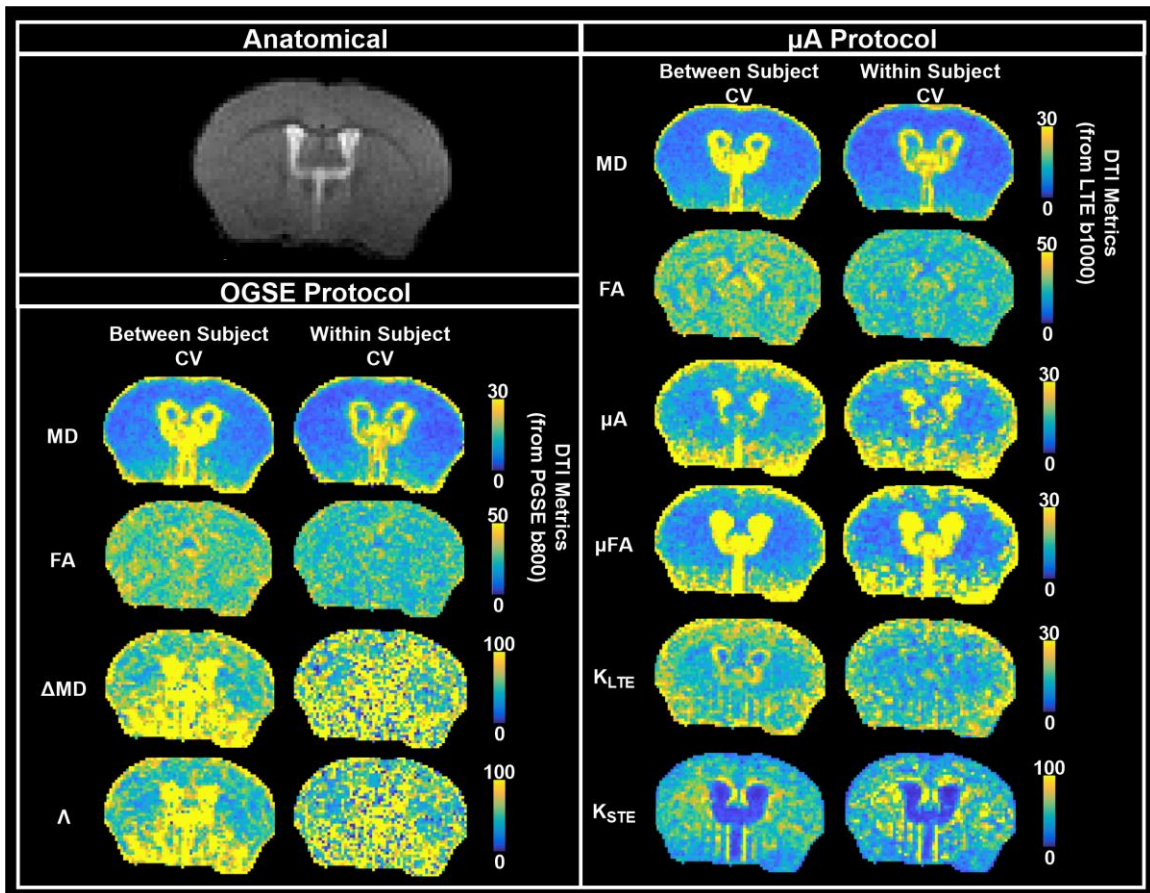
Figure 2.10 - *Whole brain average between subject and within subject CV maps. All diffusion data was registered to a single anatomical T2-weighted dataset (representative axial slice shown). Values for the between subject condition represent the mean CV within each voxel averaged over the test and retest timepoints. Values for the within subject condition represent the mean CV within each voxel averaged over all subjects. DTI metrics, MD and FA, acquired from both the OGSE and µA protocols, are shown as a reference. Note that the color bar scale varies between the maps.*
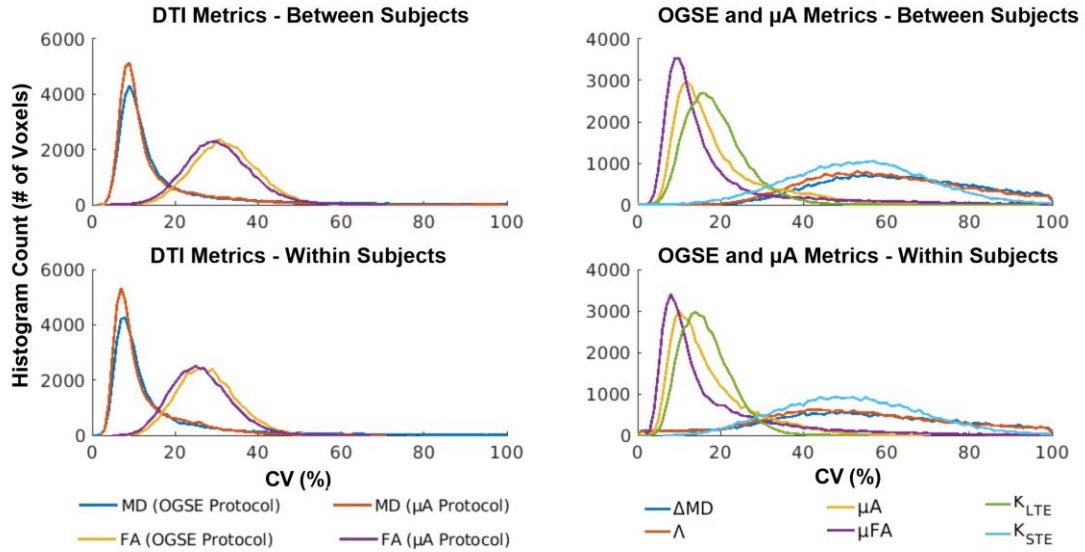
Figure 2.11 - *Distribution of between and within subject whole brain voxel-wise CVs for the OGSE and µA metrics. DTI metrics, acquired from both protocols, are shown as a reference.*

2.3.5 Sample sizes and minimum detectable effect

2.3.5.1 Between subjects

The between subject CVs, from the ROI analysis, were used to determine the minimum sample sizes required to detect statistically significant changes of 4, 6, 8, 10, and 12 % between subjects in each metric within each ROI. ΔMD required a sample size of 15 to detect a minimum change of 8 % in the three larger ROIs (the corpus callosum, hippocampus, and cortex). In comparison, the same changes could be detected in Λ with a sample size of 9 (Figure 2.12). µA and µFA required a sample size of 9 to detect a 6 % change in the three larger ROIs. With a sample size of 12, a minimum change of 8 % in K_{LTE} could be detected within all ROIs. K_{STE}, on the other hand, required much larger

sample sizes (at least 20 subjects per group are required to detect a 12 % change in the three larger ROIs).
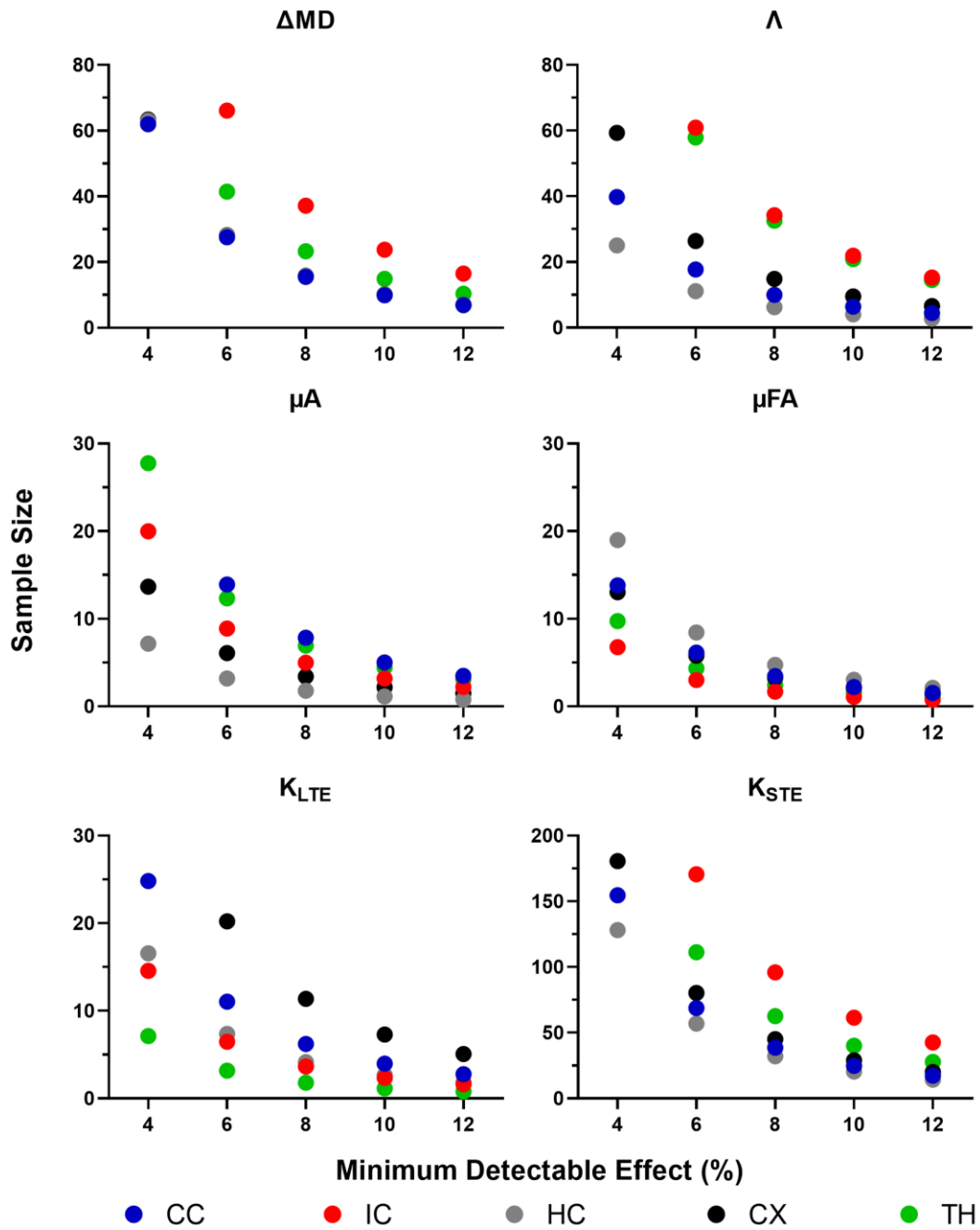
Figure 2.12 - *Sample size estimation using a between-subjects approach. Sample sizes required, calculated from ROI-based between-subject CVs, to detect a statistically significant effect within each ROI with a change in each metric of 4, 6, 8, 10, and 12 %. Note that the sample size range varies between plots and sample sizes exceeding the range are not shown. ROIs are abbreviated as follows: CC – corpus callosum; IC – internal capsule; HC – hippocampus; CX – cortex; TH – thalamus.*

2.3.5.2   Within subjects

The standard deviations of the differences between test-retest mean values across subjects (assuming paired t-tests) were used to determine the minimum sample sizes required to detect statistically significant changes of 4, 6, 8, 10, and 12 % within subjects in each metric within each ROI. In the larger ROIs, changes on the order of 8 – 10 % could be detected in Λ with 12 subjects per group, while ΔMD showed similar trends, requiring 15 subjects per group to detect changes of 8 – 10 % (Figure 2.13). μA was able to detect a minimum change of 4 % in the larger ROIs with 12 subjects per group, while the smaller ROIs required greater sample sizes. μFA was slightly more robust, being able to detect a 4 % change in the larger ROIs (with 9 subjects per group) and in all ROIs (with 14 subjects per group). K_{LTE} was able to detect moderate changes (6 %) with 12 subjects per group in all ROIs, whereas K_{STE} required at least 30 subjects to detect larger changes (12 %).
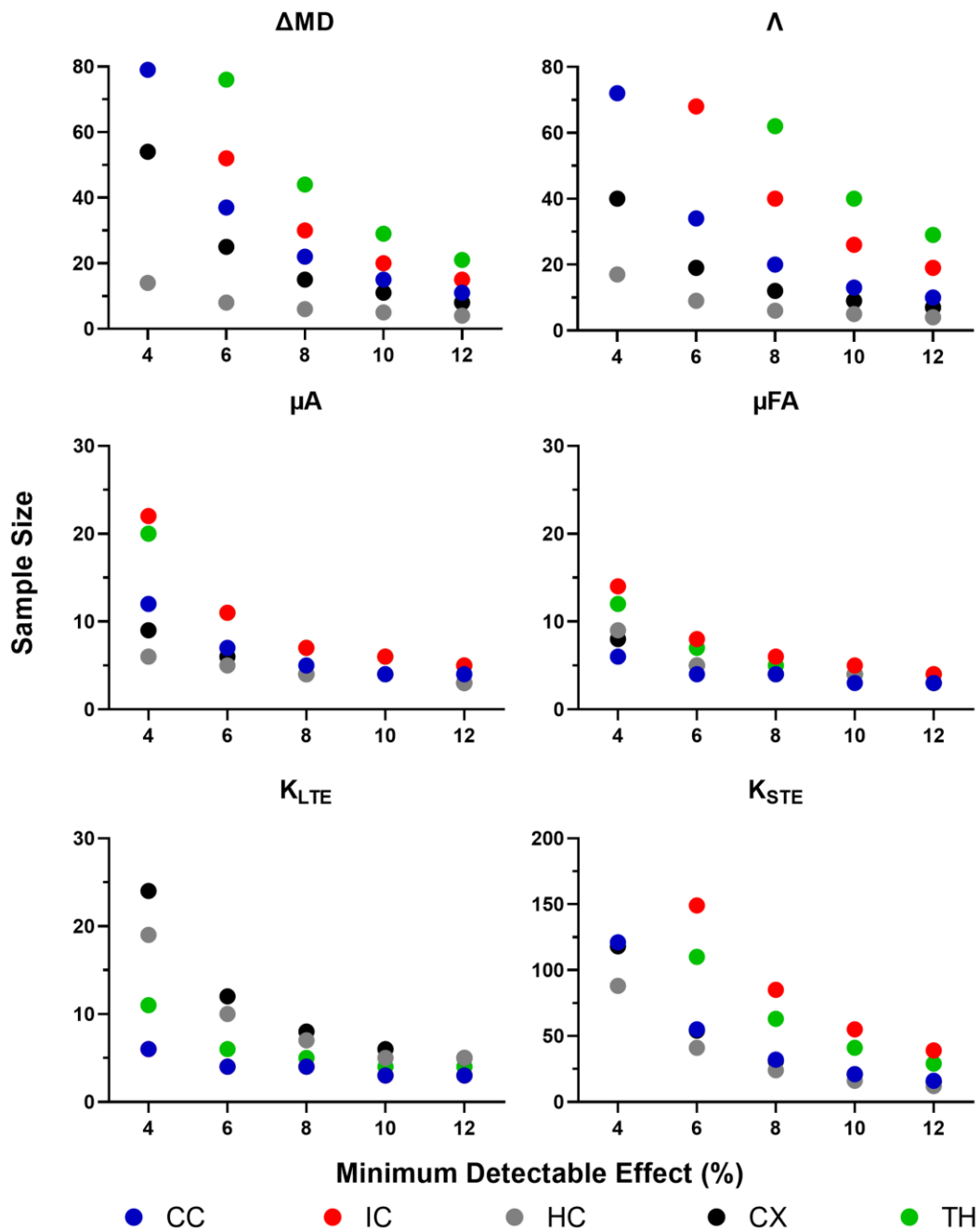
Figure 2.13 - *Sample size estimation using a within-subjects approach. Sample sizes required, calculated from the standard deviation of differences between test-retest mean values across subjects (assuming paired t-tests), to detect a statistically significant effect within each ROI with a change in each metric of 4, 6, 8, 10, and 12 %. Note that the*

sample size range varies between plots and sample sizes exceeding the range are not shown. ROIs are abbreviated as follows: CC – corpus callosum; IC – internal capsule; HC – hippocampus; CX – cortex; TH – thalamus.

2.4   DISCUSSION

This study explored the reproducibility of OGSE and µA metrics at 9.4 Tesla. No biases were found between repeat measurements with either ROI-based or voxel-wise analysis. µA, µFA, and K_{LTE} were shown to be reproducible in both the mean ROI analysis and the whole brain voxel-wise analysis, while ΔMD, Λ, and K_{STE} were reproducible in only the mean ROI analysis. µA and µFA showed the highest reproducibility of all the metrics, comparable to the DTI metric MD, and the least dispersion of CVs. The CVs observed for µFA in this work are consistent with CVs reported in a recent study by Arezza et al. (12) in human subjects at 3 T, where CVs ranged from 6 – 8 %. Overall, within subject CVs were lower than between subject CVs for both ROI-based and voxel-wise analysis, indicating less variability within subjects on a test-retest basis.

2.4.1   SNR Analysis

Although the MP40 volume coil provides uniform whole-brain SNR (as shown in Figure 2.2), the surface coil may be preferred for applications focusing on certain regions of the brain, such as the cortex and the corpus callosum. Although higher CVs are observed farther away from the surface coil for all metrics (Figure 2.10), the gradient of SNR change observed for the surface coil (Figure 2.2) does not seem to affect the voxel-wise CV maps to the same extent, which could be due to the denoising quality.

Furthermore, lowering the number of averages in the acquisition shows comparable ROI-based reproducibility (Supplemental Figure 2.S1), which points to the robustness of the denoising and outlier removal in the pipeline. This also suggests that the reproducibility of the dMRI metrics is more heavily impacted by physiological effects (such as between-subject heterogeneity) and partial volume effects, compared to SNR.

2.4.2   ROI-based Reproducibility

Our ΔMD maps (Figure 2.4) show contrast which is consistent with recent observations in both *in vivo* and *ex vivo* OGSE studies in mouse brains by other groups (201,233–235). Aggarwal et al. related the higher OGSE contrast in the dentate gyrus layer of the hippocampal formation to densely packed neurons in the region (233), which simulations have indicated increase the rate of change in MD with frequency (176). The very low values of ΔMD seen in certain regions of the gray matter are due to partial volume effects from CSF, as CSF exhibits negative values of ΔMD due to flow (170,183). ΔMD and Λ maps (Figure 2.4) show the same contrast, since the apparent diffusion dispersion rate is directly proportional to ΔMD. This relationship is also reflected in the ΔMD and Λ ROI-based CVs (Figure 2.8) and voxel-wise CV maps (Figure 2.10), which are very similar. While ΔMD requires less scan time than Λ, as it requires only a single OGSE and PGSE acquisition, acquiring multiple frequencies allows probing of whether diseases may affect the power law scaling of MD with respect to frequency ($f^{0.5}$ was assumed here). Further, Λ is expected to be more robust in terms of reproducibility as it includes data from all OGSE acquisitions (as shown in Figure 2.5). This is reflected in our results by the smaller sample sizes needed to detect the same statistically significant changes in Λ, compared to ΔMD (Figure 2.12 and Figure 2.13).

In the mean ROI analysis, the size and location of the ROIs influenced the reliability of the measurements. A greater distribution in the mean values for all metrics are observed in the internal capsule and thalamus (Figure 2.6), which are the smallest ROIs analyzed in this study. Similarly, higher CVs and a greater dispersion of CV values are observed in both smaller ROIs (Figure 2.8). This result leads to greater sample sizes being required to detect the same change in the smaller ROIs compared to the larger ROIs in some metrics (Figure 2.12). Thus, smaller ROIs lead to unreliable measurements due to less averaging and possibly a greater effect from slight registration inaccuracies. Both smaller ROIs are also positioned in the lower half of the brain, farther away from the surface coil. In addition to the location and the size of the ROIs, certain brain regions, such as the internal capsule, show higher between-subject anatomical variation (236), which would result in a higher between-subject CV. Furthermore, greater variability in terms of tissue microstructure, such as the greater variation of cell sizes and cell types in the thalamus (148), may also lead to higher CVs.

It is noteworthy that FA showed comparable reproducibility to Λ and μFA in the corpus callosum (i.e., white matter) and generally lower reproducibility in grey matter, which suggests sample sizes estimated using FA reproducibility would also be sufficient to investigate Λ and μFA. The lower reliability of FA in grey matter, compared to μFA, likely stems from its low value due to intravoxel dispersion of fiber orientations.

2.4.3   Voxel-wise Reproducibility

Voxel-wise analysis for specific ROIs (Supplemental Figure 2.S2) shows that in general, the 3 ROIs shown (the corpus callosum, hippocampus, and cortex) follow the same trends. The corpus callosum shows a slightly lower CV peak than the gray matter

regions for the more reproducible metrics (μA, μFA, and K_{LTE}). Overall, the within subject CV histograms have peaks at lower values than the between subject CV histograms, indicating less variability on a within subject test-retest basis. This is also noticeable in the between and within subject CV maps (Figure 2.10), with the within subject CV maps showing lower values overall.

One of the main reasons for the lack of reproducibility through voxel-wise analysis of ΔMD and Λ is likely CSF partial voluming. Since voxels with CSF can exhibit negative ΔMD and Λ values, whereas brain tissue shows positive ΔMD values, this leads to very high CVs (CVs > 60) in voxels impacted by CSF contamination, such as in regions with CSF in adjacent slices. This partial volume effect on ΔMD and Λ can be mitigated by using a higher resolution. However, this would also reduce SNR and longer scan times would be required to produce the same image quality. Voxel-wise analysis of ΔMD and Λ (from *in vivo* OGSE data) is not feasible given the resolution and scan time constraints. In contrast, ΔMD and Λ both show good reproducibility in the ROI analysis, where this partial volume effect is mitigated due to averaging. μA, μFA, and K_{LTE} also show greater CVs in regions with CSF, such as the ventricles, arising from the very small values of these metrics in CSF.

As K_{STE} values are intrinsically low in the brain (11,21), higher CVs and greater dispersion of CV values are observed, even in the ROI analysis. Since K_{STE} depends on the variance in mean diffusivity, low K_{STE} values point to a low variance in MD. This indicates similar sized cells across the brain, since a higher variance in cell size would lead to a higher variance in MD. In other words, the volume-weighted variance of cell size is low compared to the mean cell size. Unlike the other metrics explored in this

study, K_{STE} shows very low CVs in regions with CSF and in regions affected by CSF contamination (Figure 2.10), since K_{STE} values are very high in CSF (Figure 2.6). As the CSF STE signal as a function of b-value decays very rapidly and reaches the noise floor, the fitting detects a false variance (very high K_{STE}) if high b-value data is not excluded (21). The generally low reliability of K_{STE} is likely due to a combination of its low value and the well-known sensitivity of kurtosis fitting to both physiological and thermal noise (237). Notably, while ostensibly based on kurtosis fitting, μA and μFA do not suffer similar issues because no 2nd order kurtosis fitting is required to estimate these metrics due to term cancellations that occur when the kurtosis difference between LTE and STE is evaluated to estimate these metrics (12). Despite the low reliability, it is encouraging that the K_{STE} maps (Figure 2.4) exhibit contrast which is comparable to K_{STE} maps shown in a recent *in vivo* rodent study applying correlation tensor imaging (a DDE technique) (238).

2.4.4   Sample Size and Minimum Detectable Effect

Given the current test-retest study design, small changes (< 6 %) can be detected in μA, μFA, and K_{LTE}, both between and within subjects, with moderate sample sizes of 10 – 15. With all minimum detectable changes explored (Figure 2.12 and Figure 2.13), μFA was the most sensitive metric, followed by μA. ΔMD and Λ can detect moderate changes (> 6 %), given sample sizes of 12 - 15. K_{STE} cannot detect small changes with sample sizes relevant to preclinical neuroimaging studies, unless compromises in scan time or resolution are made to improve SNR compared to the scans performed here.

2.4.5   Limitations

It should be noted that the findings in this work are specific to the scan parameters used. Diffusion MRI is inherently a low SNR technique and high b-value acquisitions (from the µA protocol) and high oscillating gradient frequency acquisitions (from the OGSE protocol) result in even lower SNR. To acquire sufficient SNR, the voxel size was adjusted, with slice thickness set to 500 µm. Since our metrics are greatly impacted by partial volume effects (mostly from CSF), a higher resolution may provide more accurate and reproducible measurements. However, acquiring higher resolution with comparable SNR would require much greater scan time, which is not feasible for longitudinal *in vivo* neuroimaging studies, which are essential to characterize the progression of disease and injury recovery. Furthermore, a single channel transceive surface coil was used in this study and scan acceleration with parallel imaging was not possible. An option for obtaining more reliable ΔMD measures is to acquire only one PGSE and one OGSE scan, utilizing the same scan time of 45 minutes for the multifrequency OGSE protocol in this study. Thus, greater SNR and/or resolution can be achieved with more averaging. However, in doing so, one would lose the potential additional insight into microstructure organization and tissue integrity that multiple frequency analysis can provide if, for example, the $f^{0.5}$ power law scaling of MD changes in certain pathologies.

In the statistical analyses, it should be noted that for the within-subject calculation of CV, the standard deviation was determined from only two data points (the test and retest conditions). As a result, the standard deviation may not accurately represent the spread of data within the population, leading to an unknown bias in the resulting within-subject CV.

2.5   CONCLUSION

In conclusion, we have investigated the reproducibility of OGSE and µA metrics in a rodent model at an ultra-high field strength. We have shown that the µA, µFA, and K_{LTE} metrics (from the µA protocol) are reproducible in both ROI-based and voxel-wise analysis, while the ΔMD and Λ metrics (from the OGSE protocol) are only reproducible in ROI-based analysis. Given feasible sample sizes (10 – 15), µA, µFA, and K_{LTE} may provide sensitivity to subtle microstructural changes (4 - 8 %), while ΔMD and Λ may provide sensitivity to moderate changes (> 6 %). This work will provide insight into experiment design and sample size estimation for future longitudinal *in vivo* OGSE and µA microstructural dMRI studies at 9.4 T.

2.6   SUPPORTING INFORMATION
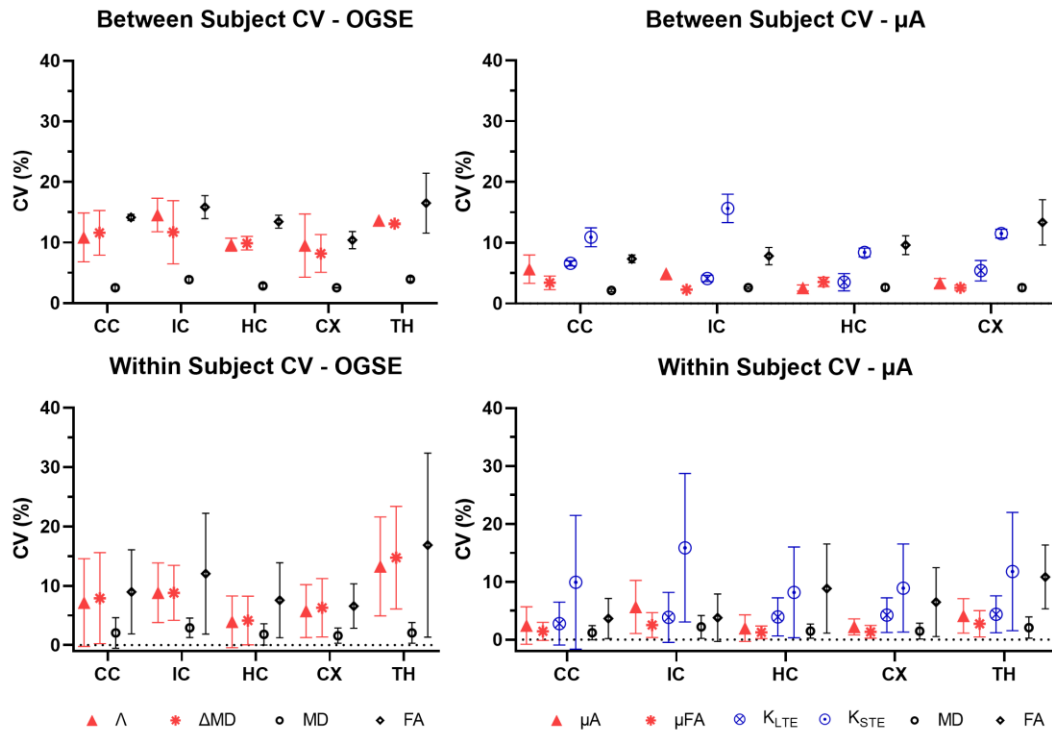
Supplemental Figure 2.S1 - *ROI-based mean between subject and within subject coefficients of variation (CV) analysis for OGSE and μA metrics, acquired with fewer averages. DTI metrics, MD and FA, acquired from both the OGSE and μA protocols, are shown as a reference. Values for the between subject condition represent the mean ± standard deviation over subjects (averaged over the test and retest timepoints). Values for the within subject condition represent the mean ± standard deviation between test and retest (averaged over the eight subjects). ROIs are abbreviated as follows: CC – corpus callosum; IC – internal capsule; HC – hippocampus; CX – cortex; TH – thalamus.*

Between Subject CV **Within Subject CV**

ΔMD   ΔMD

Λ   Λ

μA   μA

μFA   μFA

K_{LTE} K_{LTE}

K_{STE} K_{STE}

Percentage of Voxels (%)

CV (%)

—— Corpus callosum —— Hippocampus —— Cortex
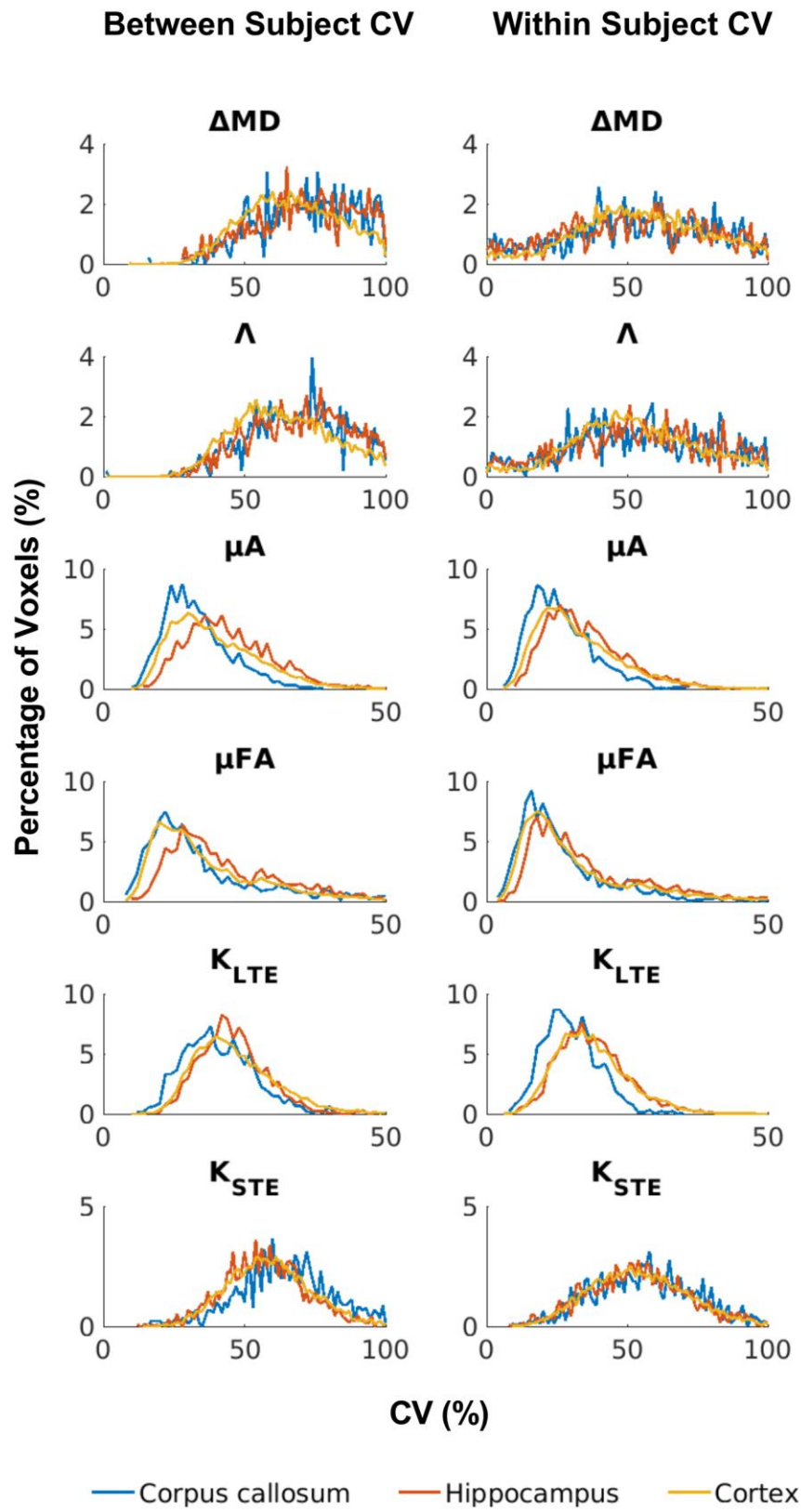
Supplemental Figure 2.S2 - *Distribution of voxel-wise between and within subject CVs within each ROI.*

Chapter 3

3   Test-retest reproducibility of *in vivo* magnetization transfer ratio and saturation index in mice at 9.4 Tesla

This chapter was published in *Journal of Magnetic Resonance Imaging,* volume 56, Rahman *et al.*, ***Test-retest reproducibility of in vivo magnetization transfer ratio and saturation index in mice at 9.4 Tesla*** (239), Copyright Wiley, 2022.

3.1   INTRODUCTION

Magnetization transfer (MT) imaging has been used extensively to investigate changes in myelin content and integrity in brain development, injury and white matter diseases, most notably in multiple sclerosis patients (153,240). MT imaging applications include both conventional contrast-weighted protocols (such as magnetization transfer ratio, MTR) and quantitative MT (qMT) methods (241).

MT is a physical process by which macromolecules and their closely associated water molecules cross-relax with protons in the free water pool (241). Based on this phenomenon, it is possible to quantify the protons bound to large molecules, which are not MR visible, due to their extremely short transverse relaxation time (T2). MT contrast can be generated by applying an off-resonance radiofrequency pre-pulse (MT pulse) to selectively saturate the spectrally broad macromolecular proton pool. This saturation then transfers to the free water proton pool via MT, resulting in a decrease in the observed free water signal. The magnitude of the MT effect can be characterized by the magnetization transfer ratio (MTR):

$$MTR = \frac{PDw - MTw}{PDw} \tag{3.1}$$

where PDw is the signal without an MT pulse applied, which is proton density weighted (PDw), and MTw is the signal with the MT pulse applied, which is MT weighted (MTw). Although MTR has been shown to correlate well with histological myelin content (153,154), it is also sensitive to the choice of sequence parameters, flip angle inhomogeneities, and longitudinal relaxation time (T1) (14). T1 also correlates strongly with myelin content, but is also sensitive to axon size (155) and iron content (156), mitigating the power of MTR as a measure of myelin. Quantitative MT has been used in many recent works to quantify myelin (242–244), as it reduces the confounding effects of scan parameters and quantifies specific tissue characteristics, such as the macromolecular pool size (241). However, qMT relies on complex modeling of the MR signal dependence on myelin, and requires more measurements and thus longer acquisition times compared to contrast-weighted MT protocols (241).

Magnetization transfer saturation (MTsat) imaging was developed to improve MTR, by decoupling MTR from T1 effects, while maintaining a feasible scan time (14). The shorter scan time compared to qMT enables longitudinal *in vivo* imaging and allows the addition of other imaging techniques required to characterize microstructure. A scalar map of MTsat can be acquired using two reference scans of proton density and T1 weighting (PDw and T1w respectively), and one MTw scan. MTsat, being more independent of system parameters and T1 weighting, and less susceptible to inhomogeneities of the receiver coil and the transmitted RF field, provides greater specificity and contrast compared to MTR (14,15). MTsat shows higher white matter

contrast in the brain than MTR (14), and has been shown to correlate more with disability metrics than MTR in patients with multiple sclerosis (18). Hagiwara et al. reported that MTsat may be more suited to measure myelin in the white matter, compared to the ratio of T1-weighted to T2-weighted images, which has also been proposed as a measure of myelin (245).

There is strong interest in applying MT to preclinical rodent neuroimaging studies at ultra-high field strengths ($\geq$ 7 T), demonstrated by MTR (246–249) and qMT studies (244,250–252). The feasibility of MTsat imaging in mice at 9.4 T has been shown previously (253) and MTsat has been explored in a feline model of demyelination at 3 T (254). While most MTsat studies have been performed at 3 T, recently, Olsson et al. reported an optimized whole-brain MTsat protocol at 7 T (255), which highlights the increasing interest in this method. Although previous *in vivo* MTsat studies have shown high reproducibility in humans at 3 T (180,256), the comparability of MTR and MTsat reproducibility has not been fully evaluated. This also leaves open the question of MTsat reproducibility in a preclinical setting, at an ultra-high field strength. As MTsat provides a time-efficient alternative to fully quantitative techniques but with increased specificity and contrast compared to MTR, investigation of MTsat in preclinical rodent imaging will likely be of interest to other research groups. The aim of this work was to assess test-retest reproducibility of *in vivo* MTR and MTsat in mice at 9.4 Tesla and provide estimates of required sample sizes, which is essential in planning preclinical neuroimaging studies involving models of disease/injury.

3.2   METHODS

3.2.1   Subjects

All animal procedures were approved by the University of Western Ontario Animal Use Subcommittee and were consistent with guidelines established by the Canadian Council on Animal Care. Twelve adult C57Bl/6 mice (six males and six females) were scanned twice 5 days apart. The sample size was chosen to reflect similar sample sizes used in other pre-clinical imaging studies (214,215,217). Before scanning, anesthesia was induced by placing the animals in an induction chamber with 4 % isoflurane and an oxygen flow rate of 1.5 L/min. Following induction, isoflurane was maintained during the imaging session at 1.8 % with an oxygen flow rate of 1.5 L/min through a custom-built nose cone. The mouse head was fixed in place using ear bars and a bite bar to prevent head motion. These mice were also part of a different longitudinal study with 3 additional imaging sessions following the test and retest scans, at the end of which they were euthanized for histology. The mice were anesthetized with ketamine/xylazine (2:1) and then underwent trans-cardiac perfusion with ice-cold saline, followed by 4% paraformaldehyde in phosphate-buffer saline (PBS).

3.2.2   *In vivo* MRI

In vivo MRI experiments were conducted on a hybrid system: Agilent 9.4 Tesla, 31-cm bore magnet (Agilent, Palo Alto, CA, USA), equipped with a 60 mm gradient coil set of 1 T/m strength (slew rate = 4100 T/m/s) (Agilent, Palo Alto, CA, USA) and Bruker Avance MRI III console with software package of Paravision-7 (Bruker BioSpin Corp, Billerica, MA). A single channel transceiver surface coil (20 mm x 25 mm), built in-house, was fixed in place directly above the mouse head to maximize signal-to-noise

ratio (SNR). A boost in SNR in the cortex when using this surface coil, compared to a commercially available 40-mm millipede (MP40) volume coil (Agilent, Palo Alto, CA, USA), has been reported previously (181).

The MT protocol required 50 minutes total scan time and comprised three FLASH-3D (fast low angle shot) scans, and one RF transmit field (B1) map scan to correct for local variations in flip angle. An MT-weighted scan, and reference T1-weighted and PD-weighted scans (MTw, T1w, and PDw respectively) were acquired by appropriate choice of the repetition time (TR) and the flip angle (α): TR/α = 8.5 ms/20° for the T1w scan and 25 ms/9° for the PDw and the MTw scans. MT-weighting was achieved by applying an off-resonance Gaussian-shaped RF pulse (12 ms duration, 385° nominal flip angle, 3.5 kHz frequency offset from water resonance, 5 μT RF peak amplitude) prior to the excitation. Other acquisition parameters were: TE = 2.75 ms; resolution = 150x150x400 μm^3; field of view (FOV) = 19.2 x 14.4 x 12 mm^3; read-out bandwidth = 125 kHz; 12 averages. The B1 map was acquired at a lower resolution of 600x600x400 um^3 and the following scan parameters: TE = 4 ms; α = 60°; short TR = 20 ms; long TR = 100 ms; 2 averages. Anatomical images were also acquired for each subject within each session using a 2D T2-weighted TurboRARE pulse sequence (150 μm in-plane resolution; 500 μm slice thickness; TE/TR = 40/5000 ms; 16 averages; total acquisition time = 22 min).

3.2.3   Image Processing

MTR and MTsat maps were generated using in-house MATLAB (ver. 2020b, Mathworks, Natick, MA) code. Gaussian filtering (full-width-half-maximum = 3 voxels) was first applied to the original images (MTw, PDw, and T1w images, and B1 maps) to

reduce noise, while retaining image contrast. The standard MTR maps were calculated using Equation 3.1. MTw, PDw, and T1w images were used to calculate MTsat maps, following the original method proposed by Helms et al. (14), and outlined by Hagiwara et al. (245) The following parameter estimates are influenced by local flip angle errors and are hence labeled by the subscript "app." The apparent longitudinal relaxation rate, R_{1app}, was calculated as follows:

$$R_{1app} = \frac{1}{2} \frac{S_{T1}\alpha_{T1}/TR_{T1} - S_{PD}\alpha_{PD}/TR_{PD}}{S_{PD}/\alpha_{PD} - S_{T1}/\alpha_{T1}} \tag{3.2}$$

where S_{T1} and S_{PD} denote signal intensities of T1w and PDw images, respectively; TR_{T1} and TR_{PD} denote TR of T1w and PDw images, respectively; and α_{T1} and α_{PD} denote excitation flip angles of T1w and PDw images, respectively. The apparent signal amplitude, A_{app}, was calculated as follows:

$$A_{app} = S_{PD}S_{T1} \frac{TR_{PD}\alpha_{T1}/\alpha_{PD} - TR_{T1}\alpha_{PD}/\alpha_{T1}}{S_{T1}TR_{PD}\alpha_{T1} - S_{PD}TR_{T1}\alpha_{PD}} \tag{3.3}$$

Using R_{1app} and A_{app}, the apparent MT saturation, $MTsat_{app}$, was calculated as follows:

$$MTsat_{app} = \left(\frac{A_{app}\alpha_{MT}}{S_{MT}} - 1\right) R_{1app}TR_{MT} - \alpha_{MT}^2/2 \tag{3.4}$$

where S_{MT}, TR_{MT}, and α_{MT} denote signal intensity, TR, and excitation flip angle of the MTw image, respectively.

$MTsat_{app}$ is inherently robust against differences in relaxation rates and inhomogeneities of RF transmit and receive field compared with conventional MTR imaging (14,15). Furthermore, B1 maps were used to correct for small residual higher-

order dependencies of the MT saturation on the local RF transmit field to further improve

spatial uniformity, as suggested by Weiskopf et al. (180):

$$\text{MTsat} = \frac{\text{MTsat}_{\text{app}} \cdot (1 - 0.4)}{1 - 0.4 \cdot \text{RF}_{\text{local}}} \tag{3.5}$$

where RF_{local} is the relative flip angle α compared to the nominal flip angle.

Brain masks were produced using the skull stripping tool from BrainSuite (ver.
19b, http://brainsuite.org/quickstart/cse/) (226). Image registration was performed using

affine and symmetric diffeomorphic transforms with ANTs software

(https://github.com/ANTsX/ANTs) (227). Region-of-interest (ROI) masks were acquired

from the labeled Allen Mouse Brain Atlas (228). One T2-weighted scan was performed

for each subject at each timepoint. As registration to an atlas is time-consuming, a T2-

weighted scan from only one subject at the test timepoint was chosen (the "chosen T2")

to be registered to the atlas. All other T2-weighted images from other subjects, at both

timepoints, were registered to the "chosen T2." MTR parameter maps were registered to

the corresponding anatomical images (from the same subject at the same timepoint). For

ROI-based analysis, the inverse transformations resulting from the preceding registration

steps (MTR → corresponding T2 → chosen T2 → atlas) were then used to bring the

labeled atlas to the corresponding MT space for each subject at each timepoint. The

inverse transformations, computed by ANTs for each registration step, are used to

perform the opposite operation (such as deforming an image in the atlas space and

producing an output in the chosen T2 space), and include inverse deformation fields and

inverse affine transforms. Binary masks for each ROI were generated by thresholding the

labeled atlas. Each mask was eroded by one voxel, except for the corpus callosum masks,

to minimize partial volume errors within a given ROI. The binary masks were visually inspected to ensure good registration quality.

Furthermore, to perform whole brain voxel-wise analysis of all subjects across both timepoints, the data was registered to a common template. MTR maps were first registered to one MTR map (the "chosen MTR"). All MTsat maps were then registered to the chosen MT space using a single transform: MTR $\rightarrow$ chosen MTR.

3.2.4   Data Availability

The test-retest dataset and in-house code to compute MTR and MTsat is available online: https://osf.io/5nwae/.

3.2.5   Data Analysis

3.2.5.1   *ROI-based and Voxel-wise Analysis*

ROI analysis was performed using two approaches: (1) analysis of unregistered data and (2) analysis of data registered to a common template. For the second approach, all MTR and MTsat maps were registered to a "chosen" MTR space, as described above.

The ROI analysis focused on five different tissue regions: corpus callosum (CC), internal capsule (IC), hippocampus (HC), cortex (CX), and thalamus (TH). For both ROI-based approaches, Bland-Altman and CV analyses were performed using the mean MTR and MTsat values from each ROI. Voxel-wise CV analysis was also performed with the registered data.

3.2.6   Statistical Analysis

The normalized contrast between white matter (WM) and gray matter (GM) regions was calculated as $(WM_{(MTR\ or\ MTsat)} - GM_{(MTR\ or\ MTsat)})/GM_{(MTR\ or\ MTsat)}$, where the WM MTR and MTsat values were the average of mean ROI-based CC and IC values, and the GM MTR and MTsat values were the average of mean ROI-based HC, CX, and TH values. For the test scans of the registered data, the normalized contrast was averaged across all subjects, and an unpaired two-tailed t-test was performed between MTR and MTsat contrast. For both registered and unregistered data, paired two-tailed t-tests were performed to test for significant differences between ROI-based test and retest mean measurements. As there were multiple ROIs, the Bonferroni-Dunn method was used to correct for multiple comparisons.

Measurement reproducibility was explored for both ROI-based analysis and whole brain voxel-wise analysis. To mitigate partial volume errors from cerebrospinal fluid (CSF) in ROI-based analysis, voxels with $MTR < 0.1$ were omitted in both test and retest images. In voxel-wise analysis, voxels with $MTR < 0.1$, as measured on the test images, were omitted. Bland-Altman analysis was performed for the ROI-based analyses to identify any biases between test and retest measurements. For both analysis techniques, the scan-rescan reproducibility was characterized using the coefficient of variation (CV). The CV reflects both the reproducibility and variability of these metrics, as well as provides insight into necessary sample sizes and minimum detectable effect size. CVs were calculated between subjects (bsCV) and within subjects (wsCV) to quantify the between subject and within subject reproducibility, respectively. The between subject CV was calculated separately for the test and retest timepoints as the standard deviation

divided by the mean value across subjects 1–12. These two CV values were then averaged for the mean between subject CV. The within subject CV was calculated separately for each subject as the standard deviation divided by the mean of the test and retest scans. The 12 within subject CVs were then averaged to determine the mean within subject CV. For both registered and unregistered data, one-way ANOVA was performed to test for significant differences between ROI-based CVs, and unpaired two-tailed t-tests were performed to test for significant differences between ROI-based MTR and MTsat CVs (using the Bonferroni-Dunn method to correct for multiple comparisons).

Sample size calculations were performed based on CVs from the ROI analysis of registered data. Minimum sample sizes required to detect defined biological effects (statistically significant changes of 6, 8, 10, 12 and 14 %), using both between and within subject approaches, were determined at a 95 % significance level ($\alpha = 0.05$) and power of 80 % ($1-\beta = 0.80$). The defined statistically significant changes were centered around 10 %, as most MT studies report changes in MTR between 15 – 30 % (248,257), while some studies report more subtle changes between 5 – 10 % (247,258). This is explained in greater detail in the Discussion. Thus, changes smaller than 10 % were considered "small" changes and changes larger than 10 % were considered "large" changes.

Following the procedure presented in van Belle (231), the between subject CVs were used to determine the sample size required per group to detect a defined biological effect between subjects in each ROI. Assuming paired t-tests, the standard deviations of the differences between test-retest mean values across subjects, were used to determine the sample size required to detect a defined biological effect within subjects in each ROI, using an online sample size calculator (UCSF Clinical & Translational Science Institute,

San Francisco, CA, https://sample-size.net/sample-size-study-paired-t-test/) (232). BA plots, CV calculations, and sample sizes required (using a between subjects approach) were generated using MATLAB (ver. 2020b, Mathworks, Natick, MA). All tests of statistical significance were performed using GraphPad Prism 9 (San Diego, CA). Results were considered statistically significant at $P \leq 0.05$.

3.3   RESULTS

3.3.1   Parameter Maps

Representative parameter maps are shown in Figure 3.1. MTsat revealed slightly greater contrast than MTR between gray matter and white matter, which was noticeable when comparing the corpus callosum and internal capsule (white matter regions) to the surrounding gray matter. The normalized contrast between gray matter and white matter regions, averaged over all subjects, in MTsat (0.376) was significantly higher ($P < 0.0001$) than in MTR (0.226).
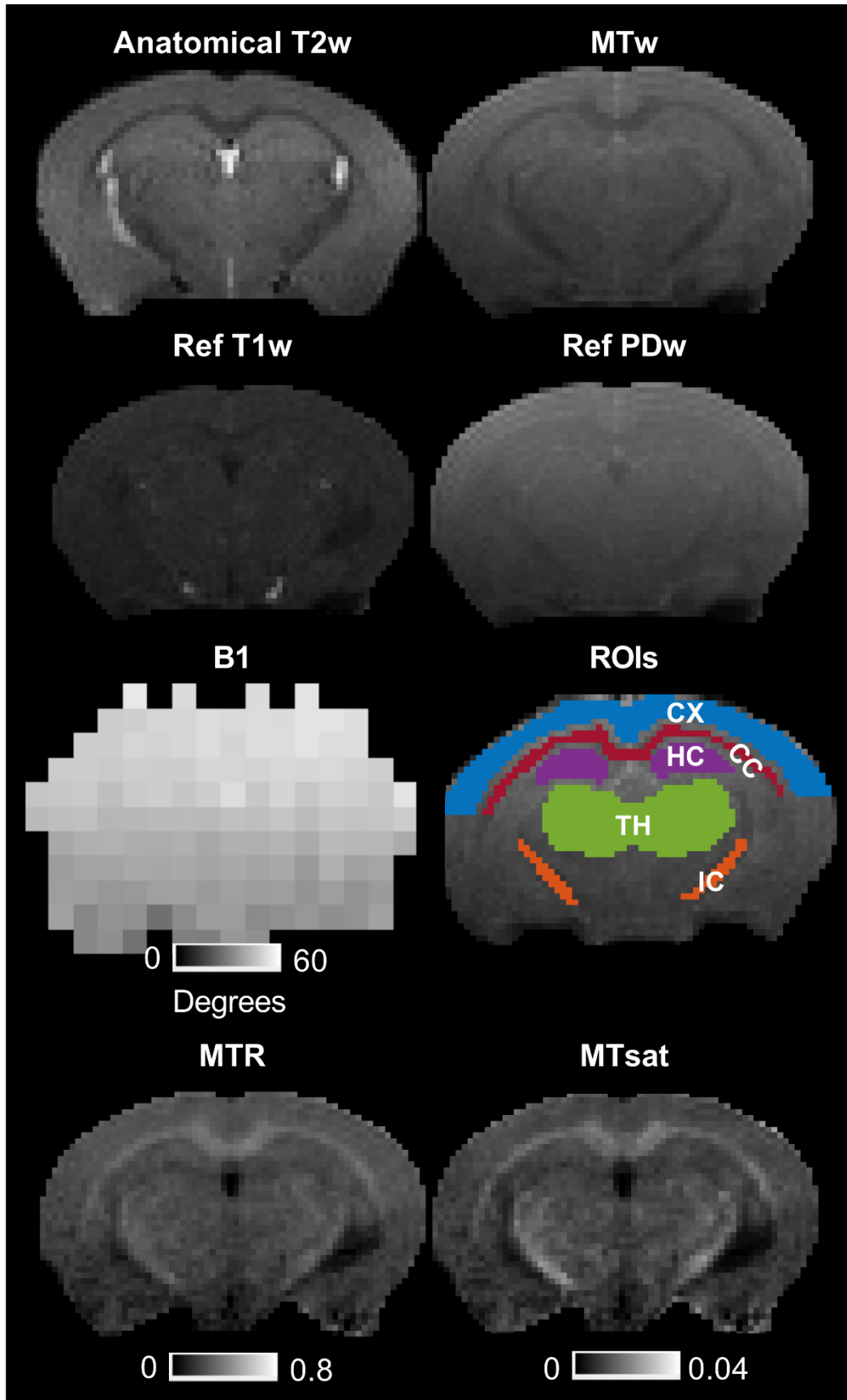
Figure 3.1 - *Example axial cross sections from a single subject. An anatomical T2-weighted image, an MT weighted (MTw) image, reference T1 weighted (T1w) and proton density weighted (PDw) images, a B1 map, and corresponding MTR and MTsat maps are shown. ROIs analyzed are overlaid on an MTw image and abbreviated as follows: CC – corpus callosum; IC – internal capsule; HC – hippocampus; CX – cortex; TH – thalamus.*

3.3.2   ROI-based Analysis

Violin plots, shown in Figure 3.2, depict the distribution of the mean values for each metric within each ROI for the 12 subjects for both registered and unregistered datasets. Across all ROIs, for both MTR and MTsat, no significant differences were found between mean test and retest values. For registered data, adjusted P-values for MTR were (P = 0.864 (CC); 0.315 (HC); 0.353 (CX); 0.285 (TH); 0.448 (IC)), while all adjusted P-values for MTsat were > 0.999 (paired two-tailed t-test). For unregistered data, adjusted P-values for MTR and MTsat were (P = 0.423 (CC); 0.273 (HC); > 0.999 (CX); 0.260 (TH); 0.586 (IC)) and (P = 0.954 (CC); 0.902 (HC); 0.957 (CX); 0.954 (TH); 0.954 (IC)), respectively. In general, the smaller ROIs (i.e., the internal capsule) showed greater distributions, while the larger ROIs (i.e., the cortex) showed much tighter distributions. For example, for registered data at the test timepoint, MTR and MTsat had a range of 0.059 and 0.0031, respectively, in the CX, and 0.075 and 0.0046, respectively, in the IC.
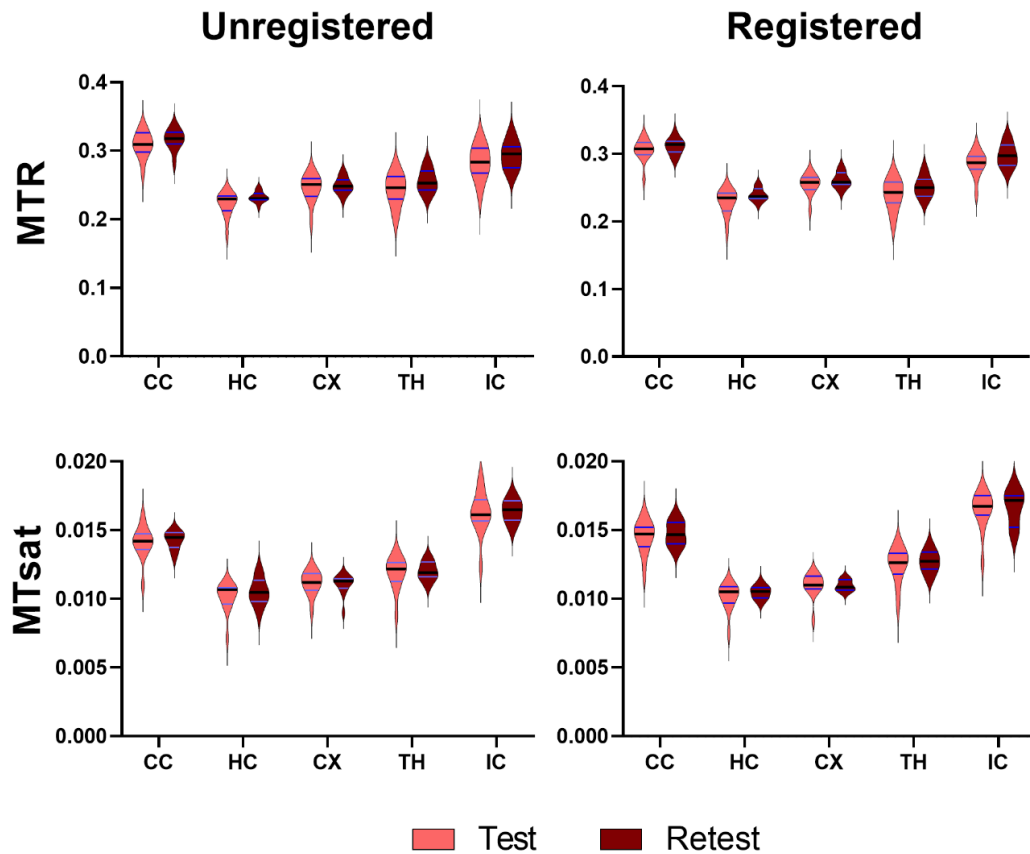
Figure 3.2 - *Violin plots showing the distribution of MTR and MTsat at the test and retest timepoints (five days apart) for 12 subjects in several brain regions. Unregistered data (left column) and data registered to a common template (right column) are shown. The dark black line represents the median and the red lines depict the interquartile range (25th to 75th percentile). The violin plots extend to the minimum and maximum values of each metric. ROIs are abbreviated as follows: CC – corpus callosum; IC – internal capsule; HC – hippocampus; CX – cortex; TH – thalamus.*

Bland-Altman (BA) plots, shown in Figure 3.3, revealed negligible biases, with mean biases of 0.009 and 0 for MTR and MTsat, respectively. Although not significant, MTR exhibited lower between and within subject CVs (2.9 – 8 %) compared

to MTsat (4.5 – 10 %), as shown in Figure 3.4. This range represents the minimum and maximum CVs obtained across all ROIs in the registered dataset. For registered data, adjusted P-values for bsCV and wsCV were (P = 0.680 (CX); > 0.999 (all other ROIs)) and (P = 0.080 (CX); > 0.999 (all other ROIs)), respectively (unpaired two-tailed t-test between MTR and MTsat CVs). For unregistered data, adjusted P-values for bsCV and wsCV were (P > 0.999 (all ROIs)) and (P = 0.162 (CC); 0.557 (CX); > 0.999 (all other ROIs)), respectively. In general, CVs were comparable across all ROIs, as no significant differences were found between ROI-based mean CVs (one-way ANOVA). For registered data, P-values were (P = 0.532 (bsCV-MTR); 0.255 (wsCV-MTR); 0.789 (bsCV-MTsat); 0.817 (wsCV-MTsat)). For unregistered data, P-values for were (P = 0.661 (bsCV-MTR); 0.353 (wsCV-MTR); 0.890 (bsCV-MTsat); 0.666 (wsCV-MTsat)).
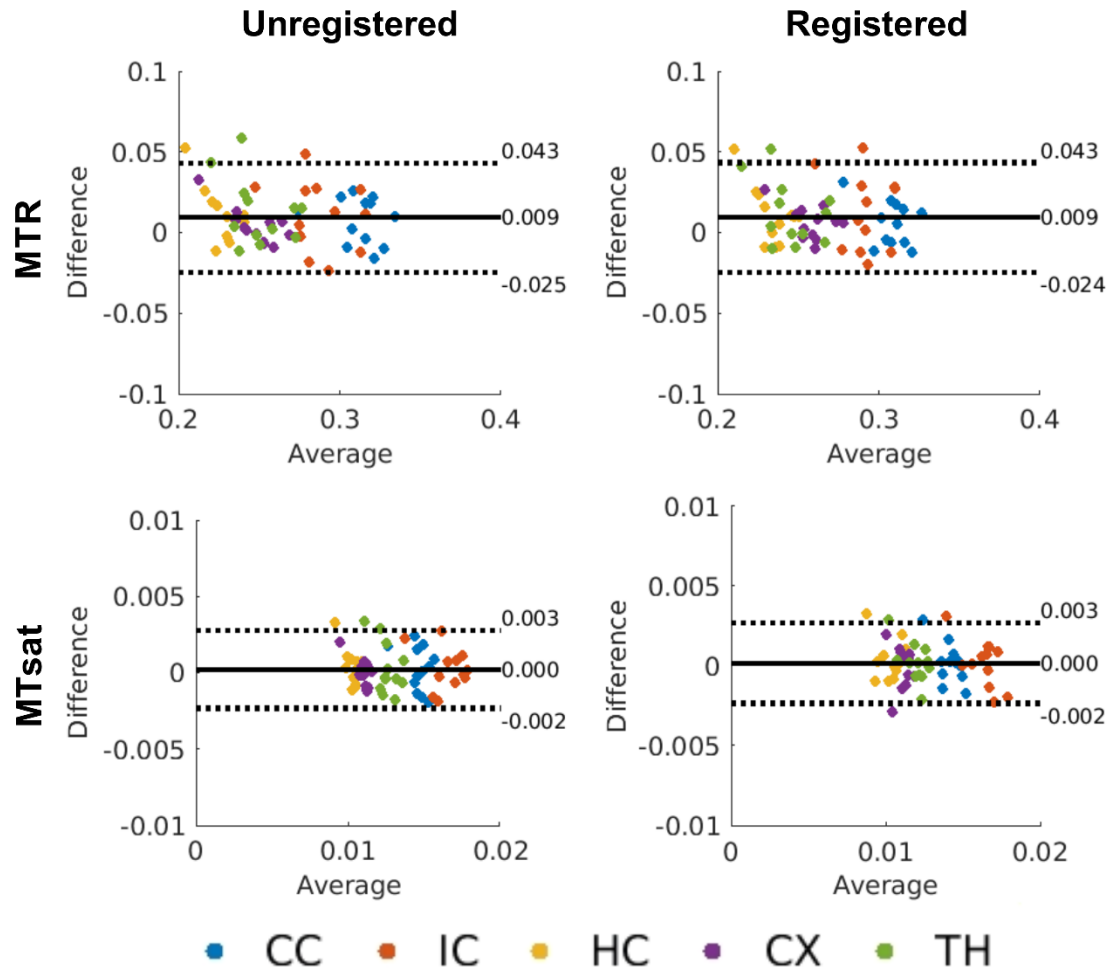
Figure 3.3 - *Bland-Altman plots depicting biases between test and retest scans for mean MTR and MTsat values (from the ROI-based analysis). Unregistered data (left column) and data registered to a common template (right column) are shown. The solid black lines represent the mean bias, and the dotted black lines represent the ±1.96 standard deviation lines. The average of the test and retest mean values is plotted along the x-axis and the difference between the test and retest mean values is plotted along the y-axis. ROIs in the legend are abbreviated as follows: CC – corpus callosum; IC – internal capsule; HC – hippocampus; CX – cortex; TH – thalamus.*
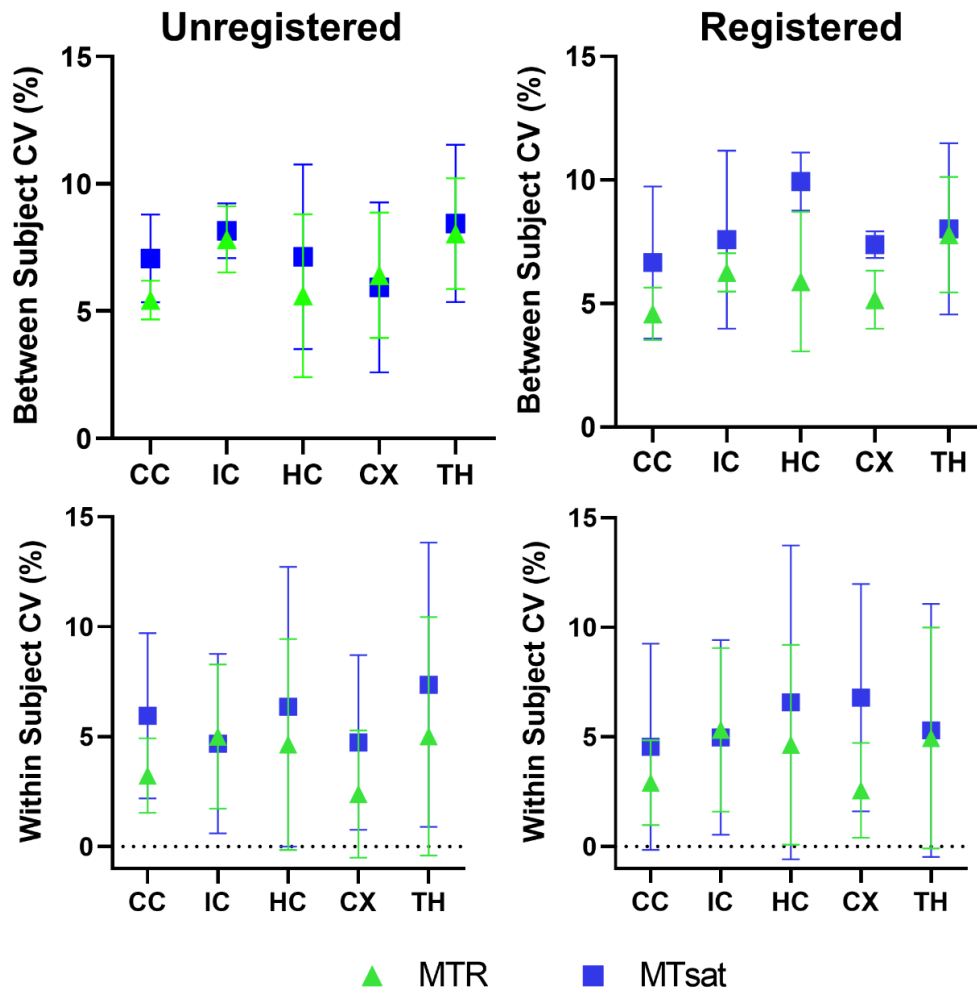
Figure 3.4 - *Mean between subject and within subject coefficients of variation (CV) for MTR and MTsat in each ROI. Reproducibility metrics for unregistered data (left column) and data registered to a common template (right column) are shown. Values for the between subject CV condition represent the mean ± standard deviation over subjects (averaged over the test and retest timepoints). Values for the within subject CV condition represent the mean ± standard deviation between test and retest (averaged over the 12 subjects). ROIs are abbreviated as follows: CC – corpus callosum; IC – internal capsule; HC – hippocampus; CX – cortex; TH – thalamus.*

3.3.3　Voxel-wise Analysis

The voxel-wise CV maps showed very high CVs in the cerebrospinal fluid (CSF), due to the low values of MTR (< 0.1) and MTsat (< 0.004) in the CSF (Figure 3.5). In the CSF, mean bsCV/wsCV were 44.5%/36.5% and 53.2%/39.8% for MTR and MTsat, respectively, while whole brain mean bsCV/wsCV (with a mask applied to omit CSF voxels) were significantly lower at 20.5%/11.8% and 26.2%/16.5% for MTR and MTsat, respectively. Throughout the whole brain, between and within subject CVs showed good reproducibility (CV $< 20\%$) with 67% of voxels and 87% of voxels falling within this range for MTR bsCV and wsCV, respectively. For MTsat, 54% and 80% of voxels were within this range for bsCV and wsCV, respectively. The wsCVs were significantly lower than the bsCVs for both MTR ($p < 0.0001$) and MTsat ($p < 0.0001$). For both wsCVs and bsCVs, voxelwise MTR and MTsat CVs had significantly different variances (F test). As shown in Figure 3.6, the MTsat histograms revealed a wider distribution (with standard deviations of 17.3 (bsCV) and 9.3 (wsCV)) compared to the MTR histograms (with standard deviations of 16.3 (bsCV) and 8.3 (wsCV)). As observed in the ROI-based CVs, MTR exhibited lower bsCVs ($p < 0.0001$) and wsCVs ($p < 0.0001$) (with peaks at 7 % and 6 %, respectively) compared to MTsat (with peaks at 15 % and 12 %, respectively), as shown in whole brain histograms (Figure 3.6).
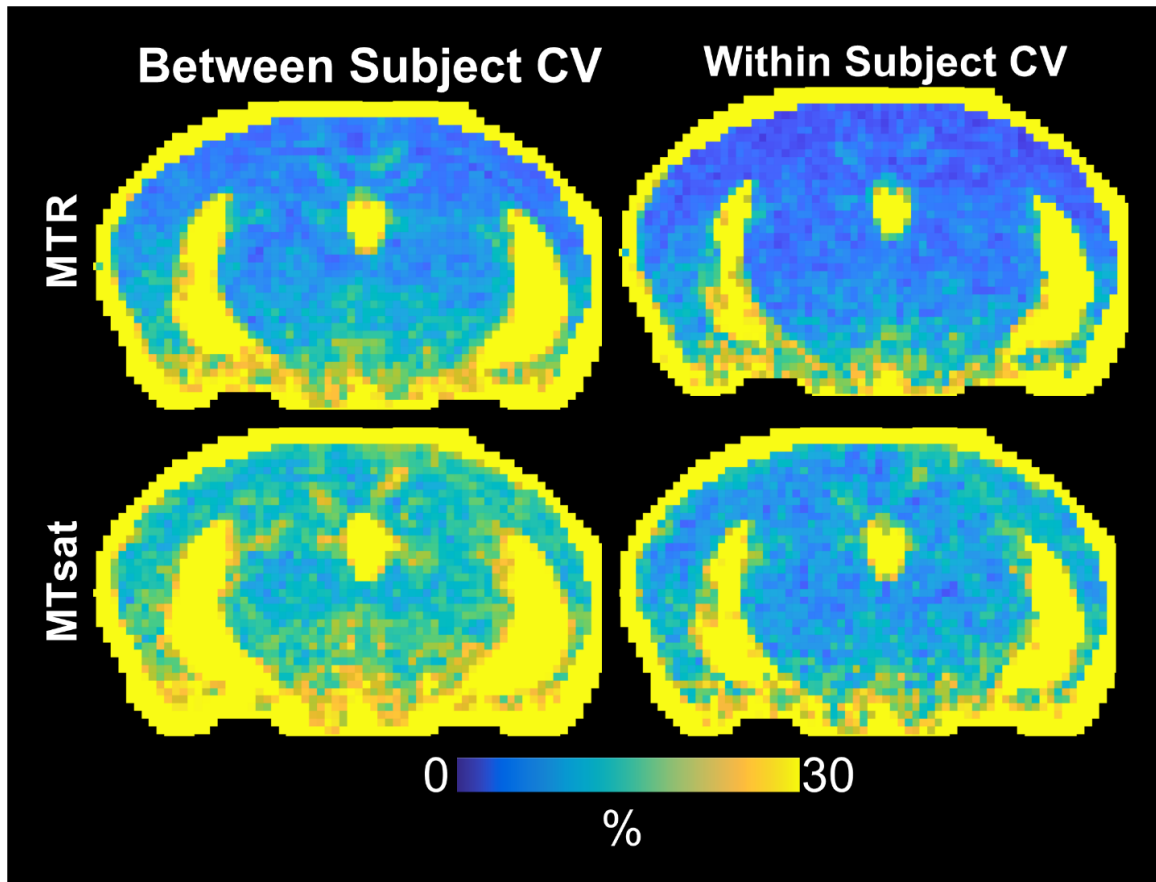
Figure 3.5 - *Voxelwise average between subject and within subject CV maps for MTR (top row) and MTsat (bottom row). Values for the between subject condition represent the mean CV within each voxel averaged over the test and retest timepoints. Values for the within subject condition represent the mean CV within each voxel averaged over all eight subjects. ROIs are abbreviated as follows: CC – corpus callosum; IC – internal capsule; HC – hippocampus; CX – cortex; TH – thalamus.*
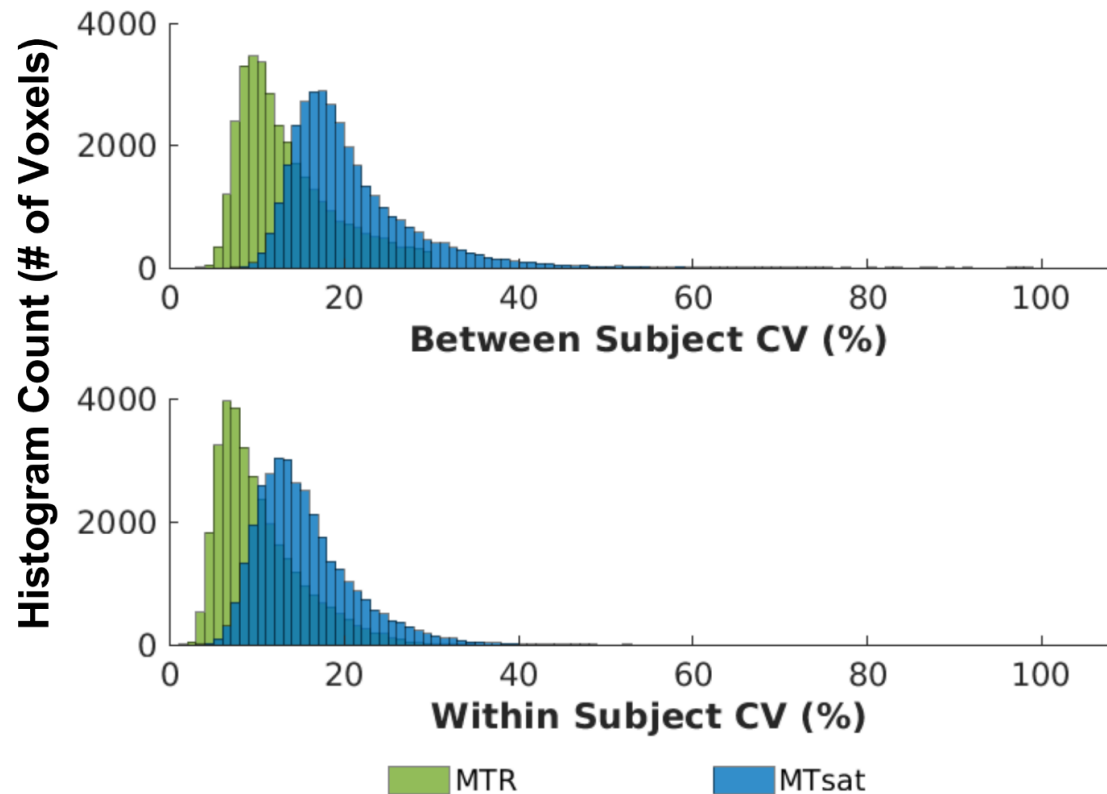
Figure 3.6 - *Distribution of whole brain voxel-wise between and within subject CVs for MTR and MTsat.*

3.3.4   Sample sizes and minimum detectable effect

3.3.4.1   *Between subjects*

To detect a minimum change of 8 % in all ROIs, MTR required a sample size of 15 (Figure 3.7a). In comparison, MTsat required a sample size of 25 to detect an 8 % change in all ROIs. The CC and CX required smaller sample sizes, with MTR requiring 12 subjects to detect a 6 % change, and MTsat requiring 15 subjects to detect an 8 % change.

3.3.4.2   *Within subjects*

As shown in Figure 3.7b, in the CC and CX, small changes (6 %) could be detected in MTR with 6 subjects per group, while MTsat could detect larger changes (8 – 12 %) with 12 subjects per group. For MTR, small changes (6 %) could be detected in the other ROIs (IC, HC, TH) with a feasible sample size of 15. MTsat could detect larger changes (8 % and greater) in all ROIs with 20 subjects per group.
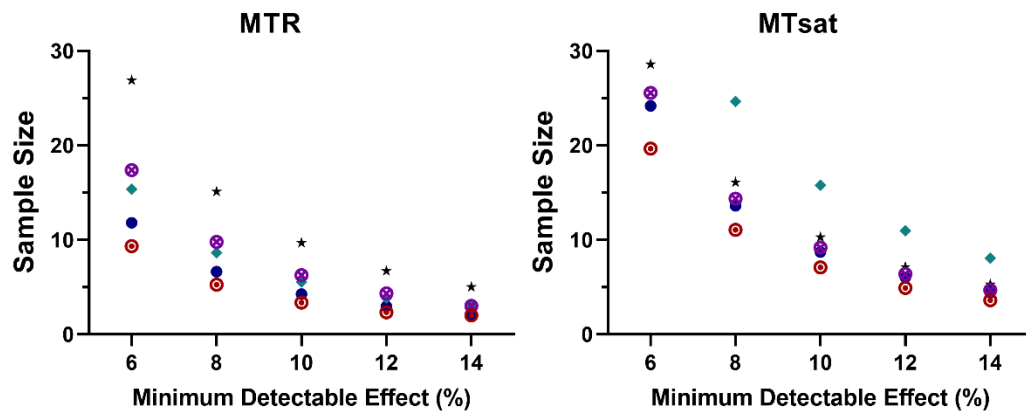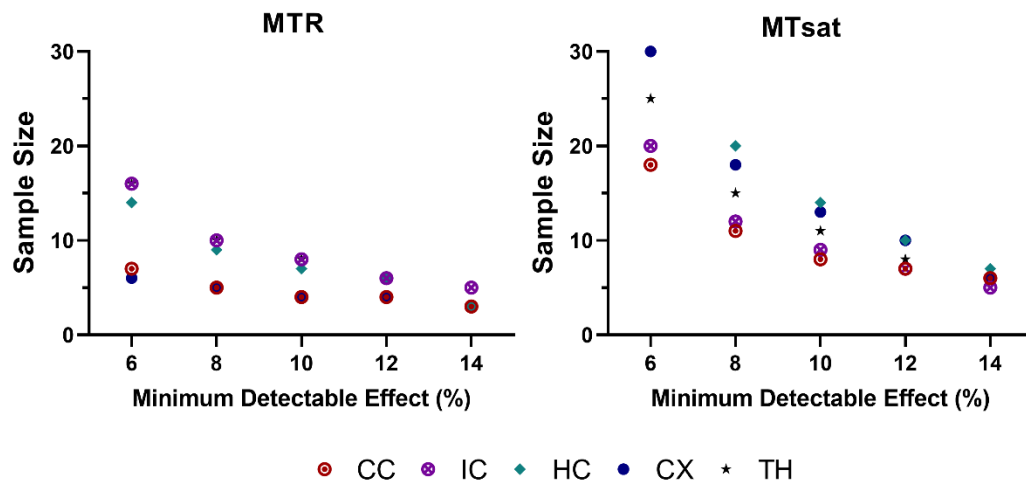
Figure 3.7 - *Sample size estimation using a between subjects (a) and within subjects approach (b) approach on data registered to a common template. Sample sizes required,*

calculated from ROI-based between-subject CVs, to detect a statistically significant effect within each ROI with a change in each metric of 6, 8, 10, 12, and 14 %. Note that the sample size range varies between plots and sample sizes exceeding the range are not shown. ROIs are abbreviated as follows: CC – corpus callosum; IC – internal capsule; HC – hippocampus; CX – cortex; TH – thalamus.

3.4   DISCUSSION

This study explored the reproducibility of MTR and MTsat at 9.4 T and will provide insight into experiment design and sample size estimation for future *in vivo* MTsat imaging studies. No biases were found between repeat measurements with ROI-based analysis. MTR and MTsat were shown to be reproducible in both the mean ROI analysis and the whole brain voxel-wise analysis, with MTsat CVs being slightly higher than MTR CVs (which was not significant in ROI analysis, but significant in voxel-wise analysis). Overall, within subject CVs were lower than between subject CVs for both ROI-based (not significant) and voxel-wise (significant) analysis, indicating less variability within subjects on a test-retest basis.

3.4.1   ROI-based Reproducibility

ROI-based reproducibility was investigated using an unregistered dataset and a dataset registered to a common template, as both unregistered and registered analysis techniques have been used in neuroimaging studies, and the difference between using either analysis technique remains sparsely explored. Recently, Klingenberg et al. reported that registration significantly increased the accuracy of a convolutional neural network (CNN) to detect Alzheimer's disease, compared to no registration (259). In our study, violin plots, BA plots, and ROI-based CV analysis revealed the same trends for both registered and unregistered ROI-based analysis approaches, which indicated that either

method can be used for MT analysis. However, we recommend using the registered analysis approach, as there is only one set of ROI masks to edit, making the analysis process more time efficient. The unregistered analysis approach will also introduce inter- and intra-rater variability, due to the large number of ROI masks being edited.

The MTR ROI CVs observed in this work are consistent with MTR CVs in human studies done by Welsch et al (260). and Hannila et al (261). MTsat CVs reported here are comparable to MTsat CVs in human studies at 3 T (180,256). Overall, MTsat exhibits slightly higher CVs than MTR, which may arise from noise propagation through the equations used to calculate MTsat, as described by Olsson et al. (255) A noticeable increase in MTsat CVs compared to MTR CVs, in the HC and CX, may be due to low MTsat values in these regions.

3.4.2 Voxel-wise Reproducibility

Voxel-wise CV trends were comparable to ROI-based CV trends. Voxel-wise CV maps revealed a more noticeable increase in CVs in the superior-inferior direction of the brain in MTR, compared to MTsat. This can be related to the inherent compensation of flip angle inhomogeneities in MTsat (14).

3.4.3 Sample Size and Minimum Detectable Effect

The CC consistently exhibited the smallest required sample sizes, which can be related to the lower variability of myelin content in the CC, compared to the gray matter ROIs (148). Interestingly, the CC and IC (the white matter regions) required similar sample sizes to detect the same changes in MTsat (using both between and within subject approaches), but not in MTR, which required larger sample sizes to detect changes in the

IC. This may stem from the better contrast seen between the IC and gray matter in MTsat, compared to MTR, which arises from MTsat being less susceptible to inhomogeneities of the transmitted field and more independent of T1-weighting (14,253).

Most MT studies report changes in MTR between 15 – 30 %, with some studies reporting more subtle changes between 5 – 10 %. In a cuprizone demyelination model in mice, MTR decreased by 15 % and 30 % at 4 weeks and 6 weeks of cuprizone administration, respectively (257). In an ischemic injury model in mice, MTR decreased by 30 % in the corpus callosum of injured mice compared to controls (248). In a closed head traumatic brain injury model in mice, MTR in the corpus callosum decreased by 10 % from baseline at 1-day post-injury (247). A post-mortem study revealed a 10 % decrease in MTR between normal-appearing white matter and multiple sclerosis lesions (153). In a recent multiple sclerosis study, MTR was able to differentiate between patients with and without cognitive impairment, showing a 7 % decrease in patients with cognitive impairment (258).

MTR can detect changes on the order of 15 - 30 % (such as the changes found in the cuprizone demyelination model) with small sample sizes (n = 6). With disease and injury models resulting in less drastic changes to myelin content, our findings suggest that MTR and MTsat can detect smaller changes with feasible preclinical sample sizes. Thiessen et al. (257) showed that when there's an 80% reduction in myelinated axon density, MTR only decreases by ~ 30 % (because it's thought that inflammation has a competing effect on MTR). So, a two-fold difference in myelination will result in at least a 15 % change in MTR. However, as MTsat provides greater specificity to myelin, a two-fold difference in myelination should translate to a larger percent change in MTsat.

3.4.4   Limitations

Although a volume coil is more appropriate for structural imaging as it provides stable signal-to-noise ratio throughout the brain, this study used a transceiver surface coil. The voxel-wise CV maps showed that between-subject and within-subject CVs were slightly higher towards the inferior region of the brain. However, the increase in CV was subtle and as shown in ROI-based analysis, the CVs of ROIs located in inferior regions of the brain (such as the IC) were comparable to the ROIs closer to the surface coil. Moreover, MTsat maps were comparable to MTsat maps acquired by Boretius et al. in the mouse brain at 9.4 T (253). This shows the feasibility of acquiring MTR and MTsat data using a surface coil, which may be useful in studies in which MT imaging is combined with other methods that require a surface coil or in inherently low SNR methods that would benefit from a surface coil, such as diffusion MRI. Recent preclinical investigations have included a combination of MT imaging and diffusion MRI (247,252). Moreover, the findings in this study will complement a recent test-retest reproducibility study in advanced diffusion MRI techniques in mice at 9.4 T (181).

Although the sample size was chosen to reflect similar sample sizes used in other pre-clinical imaging studies (214,215,217), the small number of subjects is another limitation in this work. Nevertheless, we believe that these results are valuable and useful for the MT imaging community. In the statistical analyses, it should be noted that for the within-subject calculation of CV, the standard deviation was determined from only two data points (the test and retest conditions). As a result, the standard deviation may not accurately represent the spread of data within the population, leading to an unknown bias in the resulting within-subject CV.

3.5   CONCLUSION

We demonstrated that MTR and MTsat were reproducible in both ROI-based analysis, which includes both registered and unregistered analysis techniques, and voxel-wise analysis. Importantly, MTsat exhibited comparable reproducibility to MTR, and could detect small changes ($< 10\%$) with sample sizes of 15 - 20, while providing better contrast and maintaining a feasible scan time.

Chapter 4

4 Tensor-valued and frequency-dependent diffusion MRI and magnetization transfer saturation MRI evolution during adult mouse brain maturation

This chapter is adapted from a manuscript currently in preparation titled ***Tensor-valued and frequency-dependent diffusion MRI and magnetization transfer saturation MRI evolution during adult mouse brain maturation*** (262), which is posted as a preprint on *arXiv*.

4.1   INTRODUCTION

Rodent models are a predominant study model in basic neuroscience research (263), with applications in ageing and Alzheimer's disease (264), traumatic brain injury (265), brain tumours (266), and other neuroscience research avenues. Most studies consider adulthood in rodents at 2-3 months of age, assuming a steady state condition of adulthood (23). However, Hammelrath et al. (23) and Mengler et al. (267) demonstrated that myelination continues to increase past 3 months of age in rodents, using T2-weighted MRI, diffusion MRI (dMRI), and histology. Many MRI studies investigated early postnatal neurodevelopment in rodents (236,268–276), but few have explored normal brain maturation after 3 months of age. This motivates further study of normal brain maturation in rodents to exclude confounds of cerebral developmental changes from interpretations of disease and injury mechanisms.

As neurobiological changes are challenging to track longitudinally using histology, dMRI provides a non-invasive means to capture changes in brain microstructure during development, aging, disease, and injury by probing the diffusion of water molecules (182). The most widely used dMRI technique is diffusion tensor imaging (DTI), which assumes the dMRI signal is entirely characterized by Gaussian diffusion (8) and utilizes a diffusion tensor model to estimate metrics including mean, axial, and radial diffusivity (MD, AD, and RD), and fractional anisotropy (FA). Diffusion kurtosis imaging (DKI) provides more information about the underlying tissue via the diffusion kurtosis, which quantifies the deviation from Gaussian diffusion (124). However, both DTI and DKI are unable to distinguish between microstructural changes and neuron fiber orientation dispersion (8,21), reducing their specificity to microstructural changes in brain regions with crossing fibers.

To reduce orientation dispersion effects on diffusion measurements, tensor-valued diffusion encoding (11–13), which varies the shape of the b-tensor (describes the strength of diffusion weighting along each direction) to vary the sensitivity to diffusion anisotropy, was developed. The utility of tensor-valued encoding stems from the fact that diffusion kurtosis characterizes the heterogeneity of sub-voxel sources of diffusion coefficient heterogeneity (124). Linear tensor encoding (LTE), which is the conventional method of encoding diffusion along a single diffusion direction at a time, is sensitive to sources of diffusion coefficient heterogeneity from both isotropic and anisotropic microstructural components, while spherical tensor encoding (STE), which encodes diffusion equally along all directions at the same time, is only sensitive to isotropic sources of sub-voxel diffusion heterogeneity. Accordingly, tensor-valued dMRI

distinguishes between different sources of kurtosis and allows for computation of microscopic fractional anisotropy (µFA), which reports water diffusion anisotropy independent of the neuron fiber orientation dispersion (21,141,190). Previous studies have shown that tensor-valued dMRI provides better sensitivity than conventional DTI in distinguishing between different types of brain tumours (21), assessment of multiple sclerosis lesions (16,17), and detecting white matter microstructure changes associated with HIV infection (193). The normalized signal intensity of powder-averaged (i.e., average over all diffusion directions) dMRI acquisitions of a multiple Gaussian component system can be represented by the cumulant expansion (124,141):

$$\ln\left(\frac{S}{S_o}\right) = -bD + \frac{1}{6}bD^2K \ ...$$ (4.1)

where S is the powder-averaged signal, S_o is the mean signal with no diffusion encoding, b is the b-value, D is the diffusivity, and K is the kurtosis of the powder-averaged signal. By fitting Equation 4.1 with the powder-averaged LTE and STE signals (S_{LTE} and S_{STE} respectively), the total kurtosis (K_{total}), which is the conventionally reported mean kurtosis measure in DKI, and isotropic kurtosis (K_{iso}), can be calculated, respectively. K_{iso} is a measure of the variance in the magnitude of diffusion tensors (i.e., MD), which can be related to cell size heterogeneity (21). Additionally, by subtracting K_{iso} from K_{total}, the kurtosis arising from diffusion anisotropy, K_{aniso}, can be calculated:

$$K_{total} = K_{iso} + K_{aniso}$$ (4.2)

Subsequently, µFA can be expressed in terms of K_{aniso} by (141):

$$\mu FA = \sqrt{\frac{3}{2}} \left(1 + \frac{6}{5} \frac{1}{K_{aniso}}\right)^{-\frac{1}{2}} \tag{4.3}$$

Conventional dMRI sequences are also limited to probing length scales on the order of 10-30 µm due to hardware constraints (9), as they rely on the pulsed gradient spin echo (PGSE) sequence to encode diffusion. To probe smaller length scales, the oscillating gradient spin echo (OGSE) sequence was developed to modify sensitivity to cellular length scales (10). OGSE dMRI has helped to identify neurite beading as a mechanism for contrast after ischemic stroke (30,31), and has shown increased sensitivity compared to conventional PGSE dMRI in the assessment of hypoxia-ischemia (201) in rodents, and in various pathologies in humans (202–204). By varying the frequency of the gradient waveform (i.e., frequency-dependent dMRI), which is inversely related to diffusion time, OGSE encoding allows different microstructural length scales to be probed. For increasing diffusion times (lower oscillating gradient frequencies), the molecules travel greater distances and interact with more barriers such as cell membranes, resulting in lower observed diffusivity values and higher FA values (145). Subsequently the difference in these DTI metrics between the highest and lowest frequencies applied (ΔMD, ΔAD, ΔRD, and ΔFA) can be used to examine their dispersion with frequency and provide greater insight into tissue microstructure (162,178). Additionally, evidence of a linear dependence of MD on the square root of frequency has been demonstrated in healthy and globally ischemic rodent brain tissue (169) and healthy human white matter (183,277). Therefore, the diffusion dispersion rate (Λ) can be calculated using a power-law model as:

$$MD_f = MD_0 + \Lambda f^{0.5} \tag{4.4}$$

where MD_f is the MD at OGSE frequency, f, and MD_0 is the MD at f = 0, which is the conventional PGSE sequence (162,178,183).

As myelination is an adaptive process that continues throughout adulthood, changes in myelin content throughout healthy brain maturation are important to consider when comparing to effects of disease/injury. As myelin is MR-invisible in diffusion-weighted scans, recent studies have applied both dMRI and myelin-sensitive methods for a more comprehensive view of microstructural changes (247,252,278). Sensitivity to myelin can be encoded in the MR signal by probing the magnetization transfer (MT) effect of bound water molecules by quantifying the MT ratio (MTR) (241). However, MTR has been shown to be sensitive to sequence parameters, flip angle inhomogeneities, and T1 effects (14,15). MT saturation (MTsat) imaging has been shown to reduce these sensitivities and increase specificity to changes in myelin content (14). Additionally, changes in DTI, DKI, and μFA metrics have been correlated with changes in myelin content and/or integrity of the myelin sheath (279–281), however, the biophysical nature of how myelination impacts these metrics remains unclear. Many studies have correlated an increase in total kurtosis with increased myelin content, however, whether this is the anisotropic or isotropic diffusion component (K_{aniso} and K_{iso}, respectively) remains to be determined.

In humans, a number of MRI studies have been conducted on brain maturation and aging across the entire lifespan, most involving large multi-center datasets (24,282,291–293,283–290). The studies have included structural MRI, DTI, DKI, NODDI (a biophysical dMRI model), and myelin-sensitive MR techniques, with quantitative and volumetric analyses. Lifespan patterns of quantitative and volumetric

analyses were widely reported to follow U-shaped or inverted U-shaped trajectories, including brain regional variations in these trajectories. For example, MD demonstrated a U-shape, while FA demonstrated an inverted U-shape, showing that brain maturation continues until middle age followed by a phase of degeneration at older ages. Most studies have reported on MD and FA, while only Latt et al. (292) and Das et al. (293) have reported on diffusion kurtosis changes over the human lifespan, and Cheung et al. (294) and Han et al. (125) have reported on diffusion kurtosis evolution in rats, up to 3 months and 13 months of age, respectively. K_{total} has been shown to follow the inverted U-shape trajectory through normal development in humans and rodents. However, the sources of kurtosis that drive these changes remains unclear, so it is necessary to disentangle how each kurtosis component is affected by neurobiological changes during ageing to examine what changes in K_{total} could indicate. Importantly, frequency-dependent and tensor-valued dMRI metrics, which provide improved sensitivity and specificity to microstructural changes, have not been explored in terms of normal brain maturation.

As microstructural MRI studies in rodents are becoming more prevalent in neuroscience research, our aim was to investigate how frequency-dependent and tensor-valued dMRI, and MT MRI metrics change over the course of brain maturation and disentangle what changes in these metrics may indicate on a neurobiological level. Understanding how these MRI metrics change over the course of normal development can potentially yield additional insights into the contrast mechanisms of these metrics and on the underlying mechanisms of changes in disease and injury models.

4.2   METHODS

Detailed information on the data acquisition and analysis pipeline used for this study, including the dataset, is openly available (295). Moreover, the test-retest reproducibility of the MRI metrics have been reported previously (181,239). Therefore, we will only summarize acquisition and analysis and refer the reader to the linked papers for full detailed methods.

4.2.1   Subjects

Data used for this study included 12 C57Bl/6 mice (6 males, 6 females) scanned at 3, 4, 5, and 8 months of age. We chose to exclude 'Day 3' and 'Week 1' data from Rahman et al. (295) to avoid possible effects from anesthesia on tissue microstructure. For this study we used data from 11 mice (6 males), as one female mouse did not receive a scan at all timepoints.

Before scanning, anesthesia was induced by placing the animals in an induction chamber with 4 % isoflurane and an oxygen flow rate of 1.5 L/min. Following induction, isoflurane was maintained during the imaging session at 1.8 % with an oxygen flow rate of 1.5 L/min through a custom-built nose cone. The mouse head was fixed in place using ear bars and a bite bar to prevent head motion. As these mice were part of a larger longitudinal study, they were anaesthetized 2 days after the first scan (at 3 months of age) by intra-peritoneum injection with Ketamine 80mg/kg and Xylazine 10mg/kg, diluted in saline. After the last timepoint, the mice were euthanized for histology. The mice were

anesthetized with ketamine/xylazine (2:1) and then underwent trans-cardiac perfusion with ice-cold saline, followed by 4% paraformaldehyde in phosphate-buffer saline (PBS).

4.2.2   Data Acquisition

MRI experiments were conducted on a 9.4 Tesla (T) Bruker small animal scanner equipped with a gradient coil insert of 1 T/m strength (slew rate = 4100 T/m/s). During each imaging session, frequency-dependent and tensor-valued dMRI, MT MRI, and anatomical data was acquired with a total scan time of 2 hours and 35 minutes. Anatomical images were acquired using a T2-weighted TurboRARE sequence with parameters: in-plane resolution 150 x 150 µm, slice thickness 500 µm, TE/TR = 40/5000 ms, 16 averages, total scan time of 22 minutes. The frequency-dependent dMRI protocol included a PGSE sequence (gradient duration = 11 ms and diffusion time = 13.8 ms) and OGSE sequences with frequencies of 50, 100, 145, and 190 Hz with a single b-value shell of 800 s/mm^2 (10 directions) (296) and parameters: in-plane resolution 175 x 200 µm, slice thickness 500 µm, TE/TR = 39.2/10000 ms, 5 averages, total scan time of 45 minutes. Frequency tuned bipolar (FTB) waveforms were used at 50 Hz to lower the TE of the acquisition (297). The tensor-valued dMRI protocol consisted of LTE and STE acquisitions with b-value shells of 1000 s/mm^2 (12 directions) and 2000 s/mm^2 (30 directions) with parameters: in-plane resolution 175 x 200 µm, slice thickness 500 µm, TE/TR = 26.8/10000 ms, 3 averages, total scan time of 45 minutes. The MT protocol included three FLASH-3D scans and one B1 map scan to correct for local variations in flip angle. The FLASH-3D scans consisted of an MT-weighted scan, and reference T1-

weighted and PD-weighted scans with parameters: in-plane resolution 150 x 150 µm, slice thickness 500 µm, 12 averages, total scan time of 43 minutes.

4.2.3   Data analysis

Complex-valued averages were combined using in-house MATLAB code which included frequency and signal drift correction (221) and Marchenko-Pastur denoising of complex-valued data (223). After averages were combined, data underwent correction for Gibbs ringing using Mrtrix3 (224), and eddy-current induced distortions using TOPUP (218) followed by EDDY (219) from FMIRB Software library (FSL, Oxford, UK) (225).

Scalar maps of magnetization transfer ratio (MTR) and MT saturation (Mtsat) were generated from the MT protocol as outlined by Rahman et al. (295). From the frequency-dependent dMRI data, Mrtrix3 was used to fit the diffusion tensor and acquire maps of MD, AD, RD, and FA. Quantitative values of ΔFA, ΔAD, and ΔRD were calculated as the mean of each metric within the region-of-interest (ROI) between the highest frequency (190 Hz) and the lowest frequency (0 Hz). Diffusion dispersion rate (Λ) maps were computed as outlined in Eq. 4. From the tensor-valued dMRI data, maps of K_{total} and K_{iso} were generated by fitting Eq. 1 to the signal from LTE and STE acquisitions, respectively. K_{aniso} and µFA maps were generated using Eq.'s 2 and 3, respectively.

4.2.4   Region-of-interest (ROI) analysis

Quantitative MRI parameters were investigated in three regions of interest: global white matter (WM), global deep grey matter (DGM), and the cortex (CX). Masks for

these three ROIs were generated from the labelled Turone mouse brain atlas (298), which was downsampled to the resolution of the T2-weighted images. To ensure accurate registration of scalar maps to the atlas, a T2 template, an FA template, and an MT-weighted template was created based on images from all scanning sessions using ANTs software (227). There are 3 steps to warp individual scalar maps to the down sampled atlas space: (1) Individual FA and MT-weighted maps are registered to their respective templates, (2) the FA and MT templates are registered to the T2 template, and (3) the T2 template is registered to the downsampled atlas. Each registration step involves affine transformation followed by symmetric diffeomorphic transformation using ANTs software. Output deformation fields and affine transforms from each of the three steps were used to warp the individual scalar maps to the atlas space, resulting in only a single interpolation during registration, to obtain quantitative values for each dMRI metric.

4.2.5   Statistical Analysis

To investigate if the MRI metrics changed significantly over time, repeated measures MANOVAs were performed for each metric, over the multiple ROIs (WM, DGM, and CX), to examine differences between timepoints. Metrics with a significant MANOVA were followed up by separate univariate ANOVAs within each ROI, and significant ANOVAs were followed up by Tukey HSD test for post hoc pair-wise comparison to determine differences in metrics within an ROI across time. As previous literature has shown U-shaped trajectories over the healthy brain lifespan (24,38,286,287,290,299), for each ROI and metric, both linear and quadratic models were fit to the data. Furthermore, we performed an extra sum of squares F test to determine

whether the data was significantly better fit by a quadratic model as compared to a linear model. Similarly, to examine if the developmental trajectories of male and female mice were significantly different, an extra sum of squares F test was used to determine if both data sets could be accurately fit using a single quadratic fit. Statistical analysis was done in MATLAB and GraphPad Prism version 9.5.1.

4.3   RESULTS

4.3.1   MRI Metrics over Time

Figure 4.1 shows representative parameter maps for one mouse at 3 months of age. K_{aniso} shows the same contrast as µFA and enhanced WM contrast compared to K_{total}. Λ shows selective enhancement of distinct regions in the brain with densely packed neurons, such as the dentate gyrus (part of the hippocampal formation). MTsat reveals
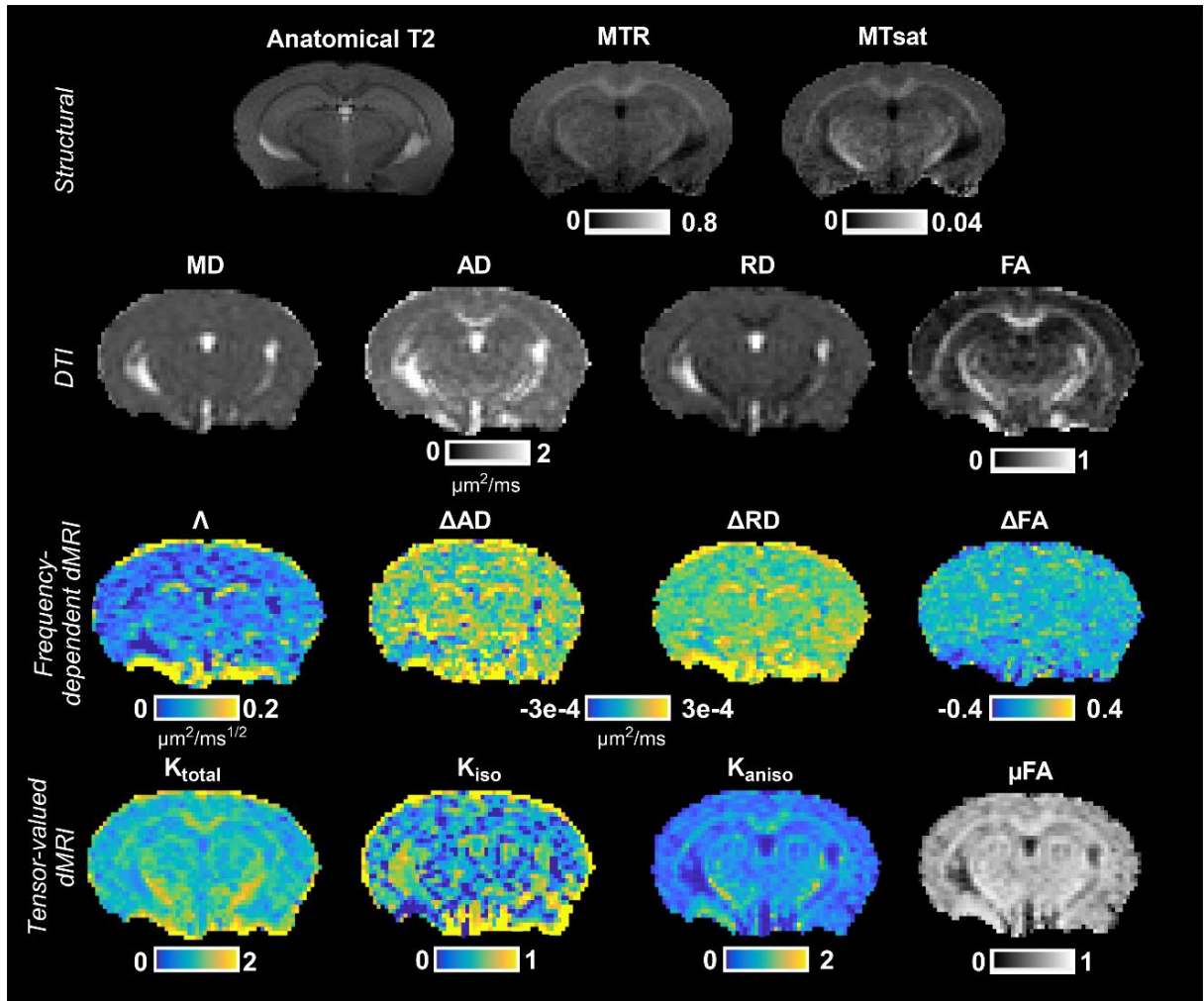
slightly greater contrast than MTR between gray matter and white matter, which is noticeable when comparing the corpus callosum and internal capsule (white matter regions) to the surrounding gray matter.

Figure 4.1 - *Representative axial parameter maps from one mouse at 3 months of age. Structural maps include a T2-weighted map, MTR (magnetization transfer ratio), and*

MTsat (magnetization transfer saturation). Conventional DTI metrics are shown for reference (MD, AD, RD, and FA). Maps from the frequency-dependent dMRI protocol include Λ (the diffusion dispersion rate), ΔAD, ΔRD, and ΔFA, which show the difference between the DTI metrics at 190 Hz and 0 Hz. Maps from the tensor-valued dMRI protocol include K_{total}, K_{iso}, K_{aniso}, and μFA.

Figure 4.2 shows each metric at each timepoint for 3 key ROIs: WM, DGM, and CX. Of the DTI metrics, MD and AD are relatively stable over time, while the significant decreases in RD agree with the significant increases in FA, over all 3 ROIs. Among the frequency-dependent metrics, Λ shows a significant decrease in WM between 4 to 5 months of age. However, ΔAD, ΔRD, and ΔFA do not show any significant changes in follow-up post hoc testing. K_{total} shows significant increases over time for all ROIs, from 3 to 8 months. This is paired with increasing trends of K_{iso}, significant in WM and DGM, and increasing trends in MTsat, while K_{aniso} and μFA remain stable over time. Interestingly, while μFA remains stable, FA shows a significantly increasing trend over time.
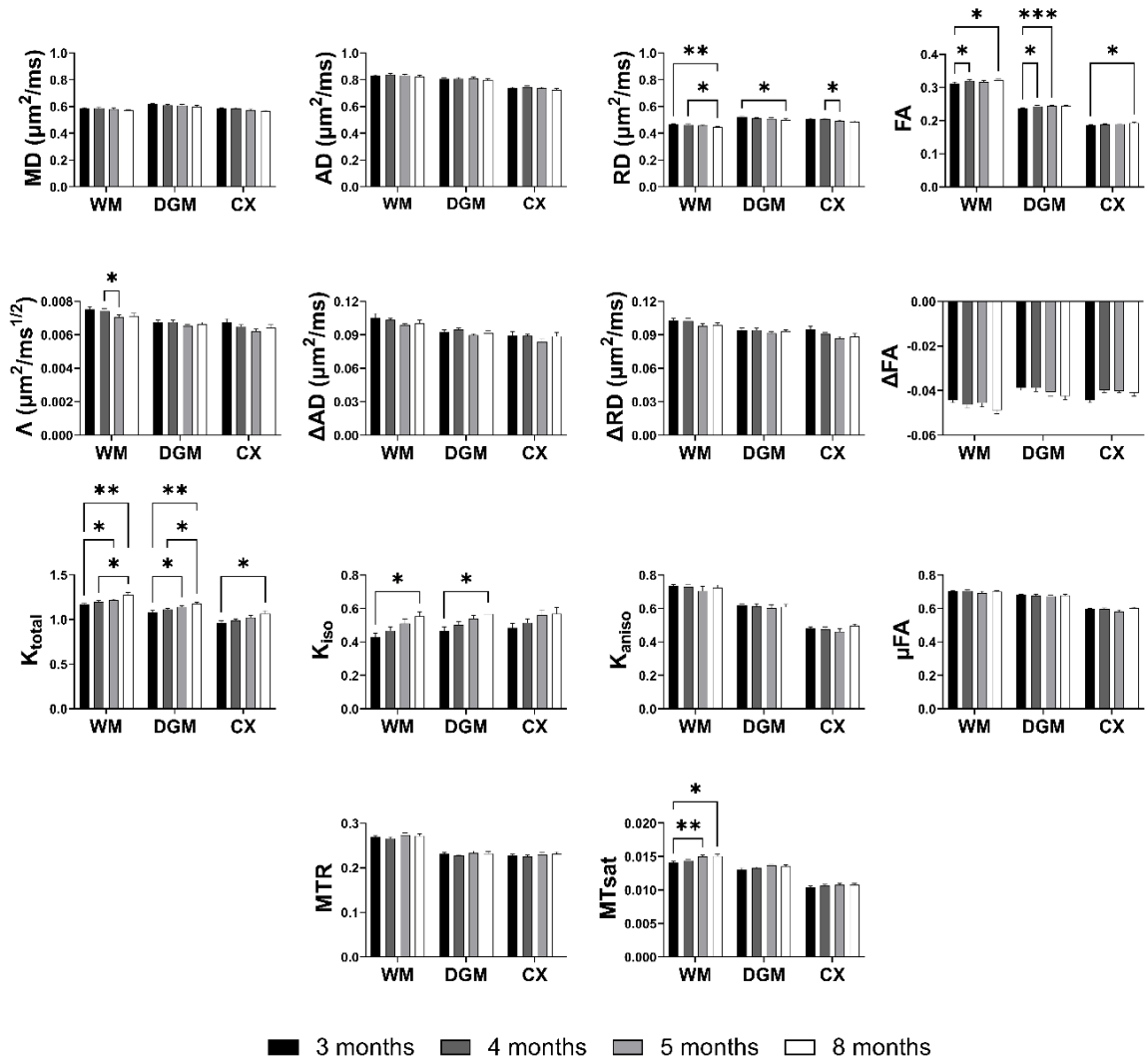
Figure 4.2 - *Quantitative MRI parameter evolution during healthy ageing in white matter (WM), deep gray matter (DGM), and the cortex (CX). Data represents mean values of each metric and error bars represent the standard deviation among n=11 mice. Asterisks represent results from post hoc pair-wise comparison (* p<0.05, ** p<0.01, *** p<0.001).*

Supplemental Figure 4.S1 shows each metric at each timepoint for smaller ROIs including 4 white matter ROIs (corpus callosum, internal capsule, external capsule, and fornix) and 4 gray matter ROIs (hippocampus, hypothalamus, thalamus, and amygdala). The trends are similar to the global WM and DGM ROIs, with the corpus callosum and internal capsule showing decreases in RD and increases in MTsat. A trend of increasing K_{total} is found in the corpus callosum, internal capsule, hippocampus, thalamus, and amygdala, while increasing K_{iso} is only observed in the hippocampus, and K_{aniso} and µFA remain stable over time.

4.3.2 Linear and Quadratic Fits to the Data

Linear and quadratic fits of all metrics over time, in WM, DGM, and CX are shown in Figure 4.3, with coefficients of determination for each fit and F test results comparing quadratic and linear fits in Tables 1-3. Most metrics show a maximum or minimum in the quadratic fits around 5-6 months of age. Significant linear fits ($p < 0.05$) were obtained for MTsat (WM), MD (WM, CX), RD (all ROIs), FA (CX), K_{total} (all ROIs), K_{iso} (WM, DGM), Λ (WM) and ΔFA (WM, DGM). Significant quadratic fits were also obtained for most cases with significant linear fits. In addition to cases with significant linear fits, significant quadratic fits were also obtained for FA (CX and

DGM), K_{iso} (all ROIs), Λ (WM and CX), and ΔRD (CX). Although MD did not show any significant changes in Figure 4.2, MD does show a significant linear and quadratic fit over time with a trend of decreasing MD, in WM and CX. For most cases the non-linear fit is not significantly better than the linear fit, except for FA in DGM, ΔRD in cortex, and ΔFA in cortex.
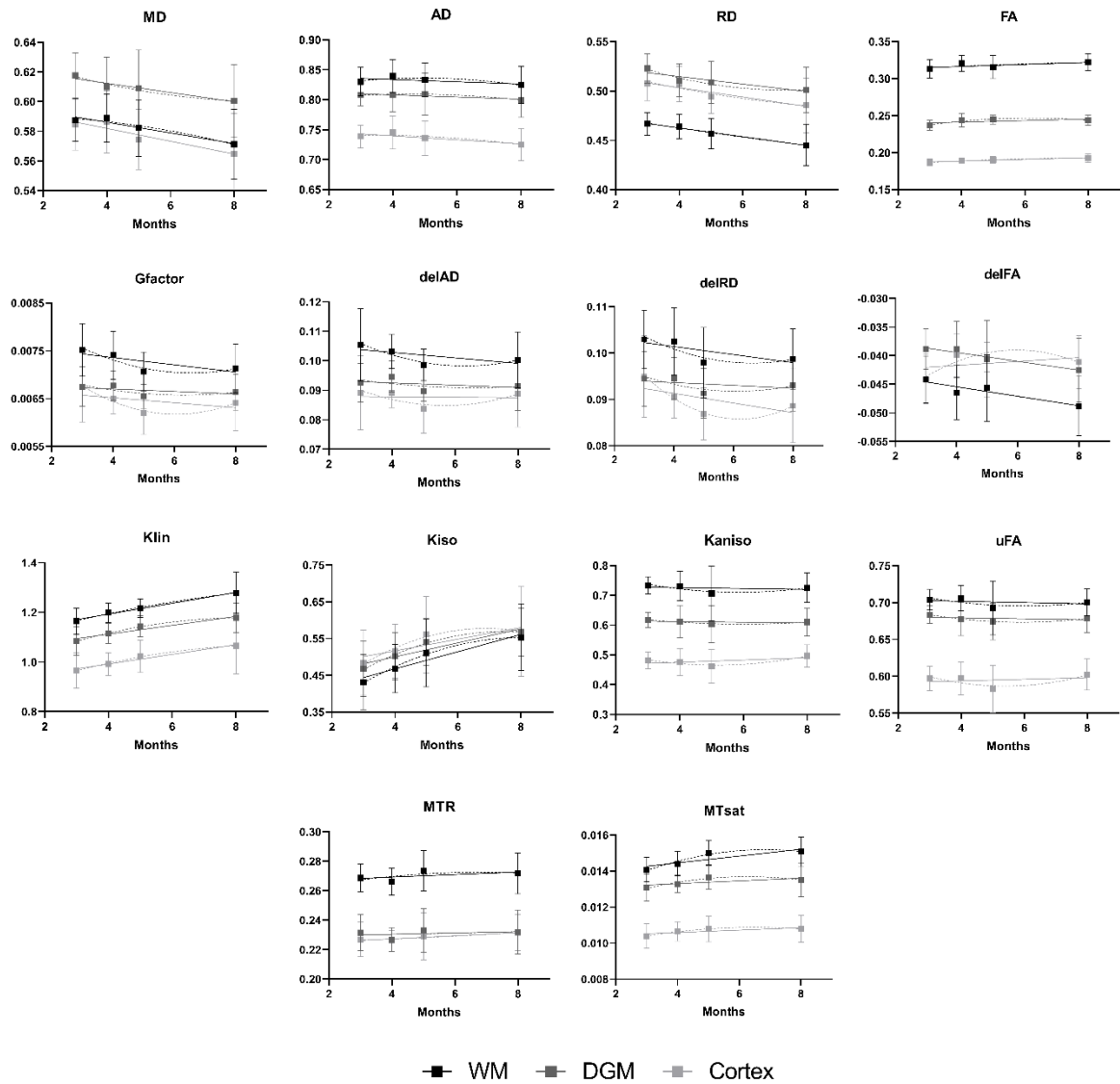
Figure 4.3 - *Linear and quadratic fits of the metrics with age for WM (white matter), DGM (deep gray matter), and CX (cortex). The solid lines represent linear fits, and the dotted lines represent quadratic fits. For linear and quadratic fits, the coefficient of determination, R^2, is reported in Table 1 and Table 2, respectively. Table 3 reports p-values comparing regression models to assess whether the data supports a quadratic model versus a linear model for all metrics in all 3 ROIs.*

Table 4-1: Coefficients of determination, R2, and p-values for linear fits to the data over age in WM (white matter), DGM (deep gray matter), and CX (cortex). Highlighted cells show significant fits with p < 0.05.

Metric	ROIs					
	WM		DGM		Cortex	
	R^2	P-value	R^2	P-value	R^2	P-value
MD	0.1239	0.01408 *	0.07240	0.05145	0.1308	0.01302 *
RD	0.2386	4.891E-05 ***	0.1266	0.009886 **	0.1674	0.004804 **
AD	0.01691	0.3572	0.01480	0.3577	0.05840	0.1047
FA	0.04212	0.2022	0.05977	0.1304	0.1922	0.001683 *
Λ	0.07728	0.04176 *	0.01977	0.3359	0.03104	0.2510
ΔAD	0.04070	0.1274	0.01379	0.4022	0.0002007	0.8842
ΔRD	0.05451	0.09165	0.01150	0.4855	0.07185	0.0936
ΔFA	0.09463	0.03164 *	0.07508	0.04812 *	0.02454	0.3519
K_{total}	0.3684	1.38E-05 ****	0.3133	2.79E-05 ****	0.1934	0.0017 **
K_{iso}	0.2378	0.001117 **	0.2279	0.00064 ***	0.08732	0.05140
K_{aniso}	0.002294	0.7397	0.002151	0.7783	0.02638	0.2795
µFA	0.005026	0.6689	0.003499	0.7144	0.007399	0.5332

Metric						
MTR	0.01870	0.4274	0.04585	0.8168	0.02877	0.2749
MTsat	0.1993	0.001111 **	0.03896	0.1684	0.03643	0.1545

Table 4-2: Coefficients of determination, R2, and p-values for quadratic fits to the data over age in WM (white matter), DGM (deep gray matter), and CX (cortex). Highlighted cells show significant fits with p < 0.05.

Metric	ROIs					
	WM		DGM		Cortex	
	R^2	P-value	R^2	P-value	R^2	P-value
MD	0.1263	0.04770 *	0.07531	0.149471	0.1308	0.04733 *
RD	0.2388	0.002441 **	0.1458	0.02448 *	0.1697	0.01722 *
AD	0.0.03110	0.461225	0.02052	0.501572	0.06381	0.224762
FA	0.04311	0.43848	0.1476	0.03199 *	0.2008	0.004257 **
Λ	0.1204	0.02213 *	0.04087	0.307299	0.1157	0.03186 *
ΔAD	0.08250	0.051128	0.02098	0.632942	0.03695	0.254895
ΔRD	0.07981	0.093223	0.03655	0.324595	0.1696	0.009456 **
ΔFA	0.09464	0.097398	0.07508	0.14487	0.1333	0.13293
K_{total}	0.3711	8.23E-05 ****	0.3347	7.78E-05 ****	0.1999	0.005298 **
K_{iso}	0.2552	0.001893 **	0.2584	0.0007960 ***	0.09781	0.04666 *
K_{aniso}	0.02334	0.2742	0.01029	0.5906	0.07684	0.08512

μFA	0.02271	0.2763	0.02782	0.3225	0.06467	0.1044
MTR	0.02473	0.5108	0.004614	0.9413	0.02894	0.5457
MTsat	0.2629	0.0007330 ***	0.08520	0.1077	0.05879	0.2117

Table 4-3: P-values from extra sum of squares F test for each metric in WM, DGM, and Cortex showing if the non-linear fit is significantly better than linear fit. Highlighted cells show significantly better non-linear fits with p < 0.05.

	ROIs		
Metric	WM	DGM	Cortex
MD	0.7389	0.7215	0.9993
RD	0.9139	0.3422	0.7392
AD	0.4428	0.6271	0.6288
FA	0.8385	0.0462*	0.5108
Λ	0.1638	0.3478	0.0543
ΔAD	0.1792	0.5863	0.2810
ΔRD	0.2946	0.3076	0.0337*
ΔFA	0.9835	0.9932	0.0287*
K_{total}	0.6796	0.2570	0.5669
K_{iso}	0.3335	0.2014	0.2744
K_{aniso}	0.3528	0.5647	0.1420

μFA	0.3940	0.3171	0.1208
MTR	0.6173	0.9729	0.9330
MTsat	0.0670	0.1576	0.3295

4.3.3   Sex-dependent Differences over Time

Data was separated by sex to examine sex-based differences for all metrics in WM, CX, and DGM (Figure 4.4). Most metrics show significantly different fits between males and females. For the diffusivity metrics (MD, AD, RD), the females show an inverted U-shape trajectory, while the males consistently show a decreasing trend. Among the frequency-dependent metrics, ΔAD and ΔFA show the same fits for both sexes, while Λ shows a U-shape trajectory for females and an inverted U-shape for males in the CX, driven by the ΔRD trajectories. K_{total} and K_{iso} both show a U-shape trajectory for males and an inverted U-shape trajectory for females. Interestingly, K_{iso} and K_{aniso} show opposing trends for males and females. As expected, K_{aniso} and μFA show similar trends to each other for both sexes. MTR and MTsat also show the same fits for both sexes, with MTsat showing an increasing trend up to 5 months and remaining stable until 8 months.
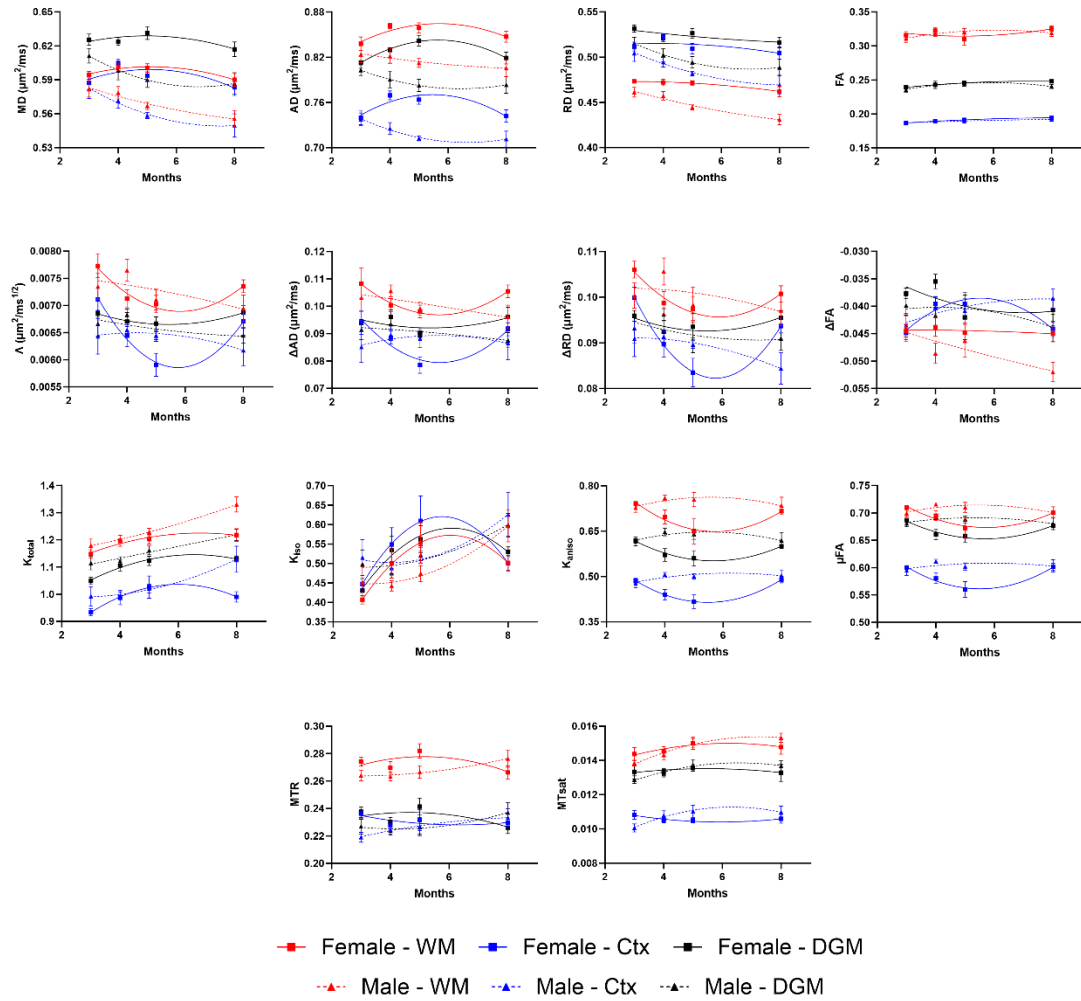
Figure 4.4 - *Plots showing quadratic fits to the data, separated by sex, for each metric in WM (white matter), DGM (deep gray matter), and CX (cortex). For those plots with separate fits for male and female, there was a significant difference in the fitting parameters, and for those with a single line, a single fit could accurately represent both datasets.*

4.3.4   Linear Regression of Kurtosis with Myelin-Specific Metrics

To explore how kurtosis relates to the myelin-specific metrics over time, Figure 4.5 shows linear regressions of the kurtosis metrics with MTR and MTsat over all timepoints and mice, for each ROI. K_{total} and K_{iso} show similar trends, with positive correlations with MTR and MTsat in the WM and CX. Although K_{aniso} does not show any correlations with MTsat, negative correlations are found for K_{aniso} and MTR for all ROIs.
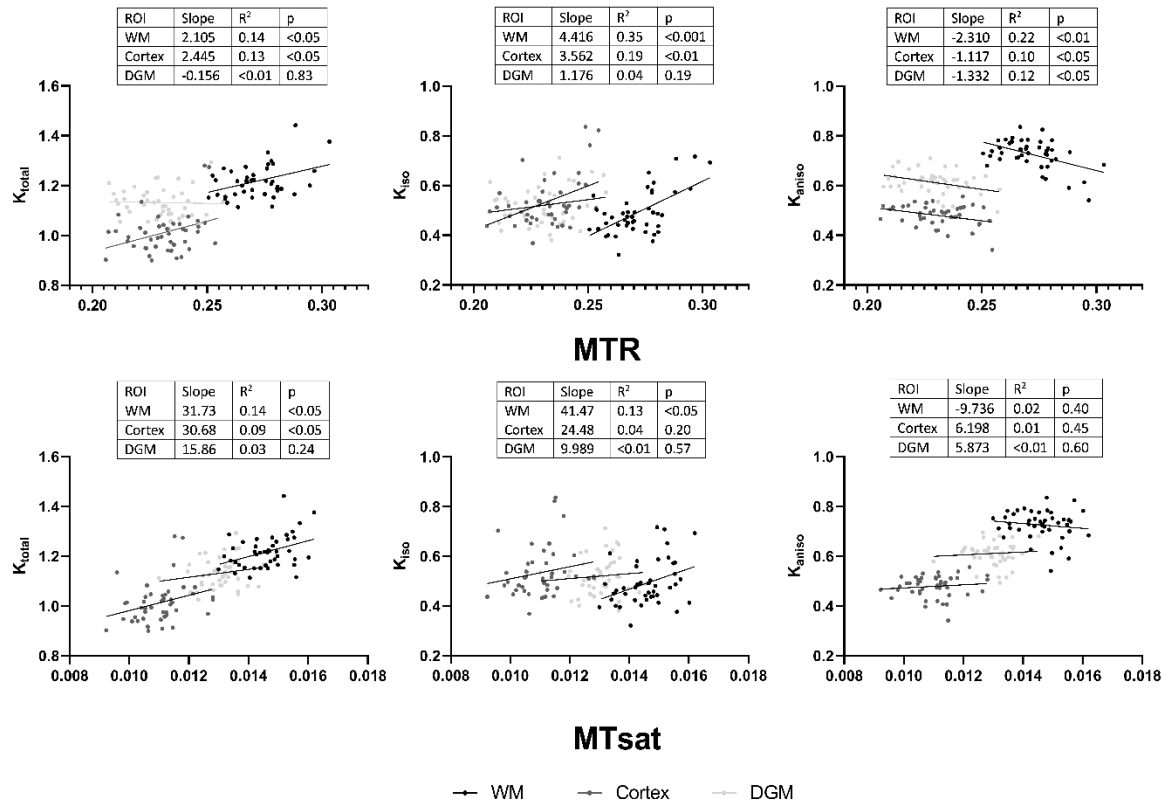
Figure 4.5 - *Plots illustrating linear fits of the kurtosis metrics (K_{total}, K_{iso}, and K_{aniso}) to the myelin-specific metrics (MTR and MTsat) in WM (white matter), DGM (deep gray*

matter), and CX (cortex) over all timepoints. The slope, R^2, and p-value are reported for each fit.

To explore the linear relationship of kurtosis metrics to myelin-specific metrics from gray to white matter, Figure 4.6 shows the linear fits of the kurtosis metrics with MTR and MTsat over all ROIs. Interestingly, K_{aniso} shows a positive correlation with both MTR and MTsat, in contrast to Figure 4.5. The positive correlation of K_{total} with MTR and MTsat is driven by the trend in K_{aniso}, as K_{iso} does not show any correlation with MTR and MTsat over all ROIs.
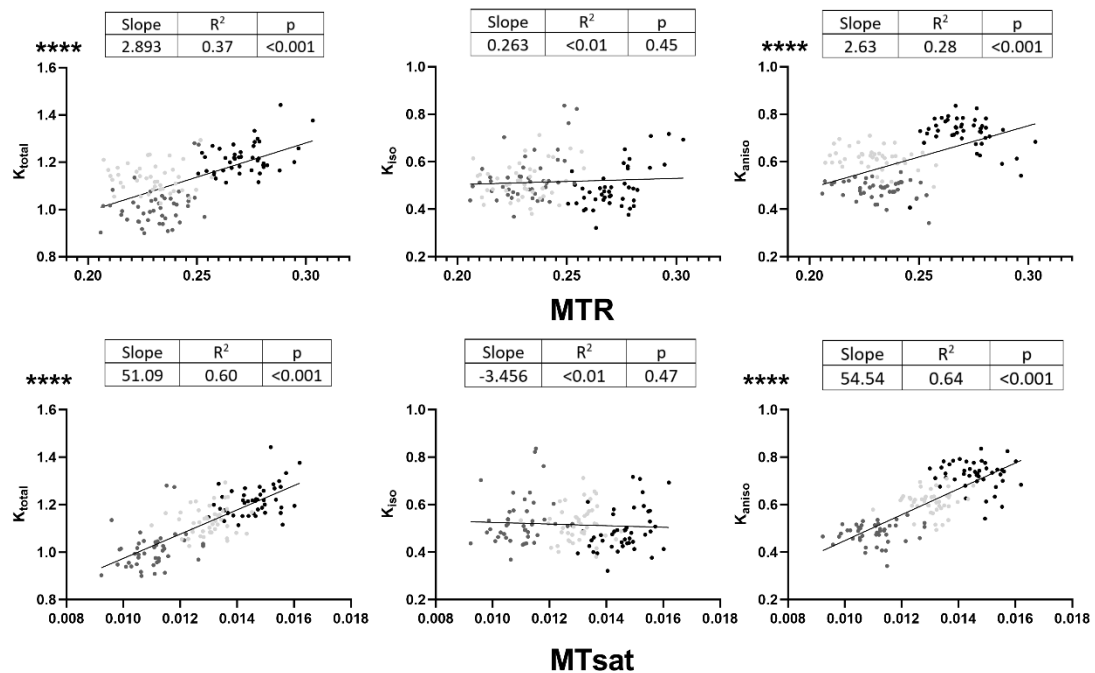
Figure 4.6 - *Plots illustrating linear fits of the kurtosis metrics (K_{total}, K_{iso}, and K_{aniso}) to the myelin-specific metrics (MTR and MTsat) for all ROIs together (WM, DGM, and Cortex) over all timepoints. The slope, R^2, and p-value are reported for each fit.*

4.4   DISCUSSION

Here we explored healthy mouse brain maturation using frequency-dependent and tensor-valued dMRI and MT MRI to probe smaller spatial scales, orientation-independent diffusion and various kurtosis sources, and myelin content, respectively. Our protocols were applied longitudinally in mice between 3 – 8 months of age to better understand the contrast mechanisms of these advanced MRI metrics and how they evolve over the course of healthy brain maturation. As microstructural MRI is becoming more prevalent in the neuroscience community, there is a need to assess the evolution of these metrics in healthy rodents, which may provide insights into the underlying mechanisms of changes in these metrics in disease and injury models. Although there have been several human lifespan imaging studies, healthy rodent brain maturation studies are sparse. This study builds on previous rodent studies (23,125,267,294), including more timepoints and a more comprehensive set of advanced imaging protocols to probe the evolving microstructure in the maturing brain. Importantly, this is the first study to characterize the evolution of frequency-dependent and tensor-valued dMRI metrics longitudinally during brain maturation. Additionally, we show here changes in total kurtosis over time may be dominated by isotropic sources, which suggests that total kurtosis is unlikely to be sensitive to how myelination affects water diffusion anisotropy over the course of normal brain development but may rather be sensitive to myelin formation/remodeling and glial cell diversification. For studies that only calculate total kurtosis (likely as most only use LTE acquisitions), we suggest caution in attributing neurobiological changes to changes in total kurtosis as we show here no changes in anisotropic sources of kurtosis in the presence of increasing myelin content.

4.4.1   MRI Metrics over Time

The trends observed in our DTI metrics are comparable to previous human and rodent studies investigating normal brain development (23,24,38,267,289,290,299). As MD and AD do not show any significant change with post hoc analyses (although they show significant time effects and a decreasing trend with age), the significant increases in FA in WM, DGM, and CX are driven by the significant decreases in RD in these three regions between 3 – 8 months (Figure 4.2). Hammelrath et al. reported that in most white matter ROIs, FA continuously increased in agreement with increased intensity on myelin staining, in mice studied until 6 months of age (23). Mengler et al. found a pronounced increase in myelinated fibers, using histology, in the cortex between 3 – 6 months of age in rats (267). They interpreted that the drop in MD and RD with age was likely due to myelination. Myelination results in reduced RD, as radial water diffusivity becomes more restricted, which consequently leads to reduced MD (300). In addition, myelination, as well as neurogenesis (301), decreases the extracellular free water compartment in favour of the intracellular compartment, which can also lower MD (302). Interestingly, in a histological study, Mortera et al. found a significant trend of widespread and progressive neuronal loss that began as early as 3 months of age in rats (15-20 % decrease in neuron counts between 3 – 5 months of age in the cortex and olfactory bulb), when neuronal numbers are maximal in all structures, which indicates that age-related decline in the brain begins as soon as the end of adolescence (301). Neuronal loss would result in increased MD, and counteract the decreased MD due to myelination, which may explain why no significant changes are observed in MD after post hoc analyses (Figure 4.2). Additionally, Mortera et al. reported that brain mass increased in all structures over time

despite a decline in numbers of neurons, which implies that the average size of the surviving cells, neuronal and/or non-neuronal, may be increasing during aging and/or there is increased extracellular fluid.

Among the metrics from the frequency-dependent dMRI protocol, there is a significant decrease in Λ, the diffusion dispersion rate, between 4 – 5 months of age in WM (Figure 4.2). As Λ shows similar contrast to ΔMD (181), we can refer to previous ΔMD studies to interpret changes in Λ. Aggarwal et al. reported elevated ΔMD contrast in mouse brain regions with high neuron packing, such as in the dentate gyrus of the hippocampus (233). This elevated contrast in the dentate gyrus can also be seen in the Λ map in Figure 4.1. In a phantom study, Parsons et al. related elevated ΔMD to the presence of larger spherical structures (174), and in a simulation study, Xu et al. related elevated ΔMD with higher nuclear volume fraction (303). In another study, Aggarwal et al. found consistent decrease in ΔMD in the CA1 Pyramidal Layer of the hippocampus in healthy mice during the first two months after birth and related this to a progressive increase in pyramidal cell soma size with age (304). Thus, the decrease in Λ observed in Figure 4.2 can be interpreted as a reduction in axonal packing, which is also supported by the neuron loss finding of Mortera et al. (301) and may be related to synaptic pruning during development (305), and an increase in soma cell size. The other frequency-dependent metrics here do not show any significant changes after post hoc analyses, possibly due to higher inter-subject variation in these metrics, although ΔRD did show a significant time effect, with decreasing trends in WM and CX. Aggarwal et al. found significantly higher ΔRD in the mouse corpus callosum in a cuprizone demyelination model (233), so the decreasing trend of ΔRD here may be due to continued myelination.

K_{total} shows significant increases over time for WM, DGM, and CX, from 3 to 8 months. This is comparable to previous DKI studies in healthy brain maturation (125,293,294), and previous literature has related K_{total} increases to myelination and dense packing of axon fibers in white matter and more densely packed structures like cells or membranes and dendritic architectural modifications in gray matter. However, these interpretations involving fibre microstructure would be expected to coincide with changes in anisotropic components of kurtosis, which was not seen here. By investigating both isotropic and anisotropic kurtosis components in this study, we observe that during healthy brain development, changes in K_{total} are driven by changes in K_{iso} (significant in WM and DGM). This is paired with increasing trends in MTsat, which indicates increasing myelination, while K_{aniso} and μFA remain relatively stable over time. MTR does not show any significant trends over time, which could be due to the reduced myelin-sensitivity of MTR, while MTsat has improved specificity to myelin (14). Moreover, the contrast between gray and white matter regions, averaged over all mice in this dataset, was previously shown to be significantly higher in MTsat, compared to MTR (239). As there is a trend of increasing K_{total}, K_{iso}, and MTsat, the relationship of the kurtosis metrics and the myelin-specific metrics is further explored in Figure 4.5 and Figure 4.6.

The mean μFA values are much higher than mean FA values (by ~0.4), indicating there is orientation dispersion of axons within our ROIs. It is interesting to note that although μFA remains stable, FA is increasing over time, which may be due to fibers becoming more aligned through development. As fibers become more aligned, FA is expected to increase, as macroscopic water diffusion anisotropy increases, but μFA is not

expected to change, as it disentangles effects of fiber orientation dispersion from microstructure (21,141). As µFA remains unchanged over time, this indicates that axon integrity is not compromised over this period. Moreover, as there are no changes in µFA despite increases in MTsat, this suggests myelination in the mature brain is not a main contributor to microscopic diffusion anisotropy and anisotropic kurtosis in axons. In a study investigating axon diameters and myelin content in fixed rat spinal cord, a moderate negative correlation was observed between µFA and MWF (myelin water fraction), while FA was positively correlated with MWF (281). This is comparable to our study as increasing FA is paired with increasing MTsat. Shemesh explains that the negative correlation between µFA and MWF would reflect indirectly the approximately constant g-ratio in healthy tissue, rather than enhanced restriction, and as axon diameter increases with myelination, µFA decreases (281). Additionally, unlike FA, compartments of proportionally different sizes can give rise to the same µFA. However, µFA reported in the rat spinal cord study was derived from Double Oscillating Diffusion Encoding (DODE) protocols, which can probe smaller spatial scales. Thus, the µFA calculated from our b-tensor encoding protocol may not be sensitive to changes in axon diameter, as the larger the diffusion time, the longer path will be probed in the unrestricted dimension (parallel to the axon length), and the µFA will be larger and less reflective of axon diameter, and consequently, myelination.

The increase in K_{iso} reflects increased cell size and density heterogeneity, as it indicates a heterogeneous microenvironment with compartments having a wide variation of diffusivities within the voxel (184,306). We hypothesize that the increased cell size/density heterogeneity may be due to (1) differentiation and maturation of

oligodendrocytes (OLs) and/or (2) increased number and increased diversity of glial cells. Oligodendrocyte precursor cells (OPCs) divide and generate myelinating oligodendrocytes (OLs) throughout postnatal and adult life. Although most OPC proliferation, OL differentiation, and myelin development occurs before 3 months of age, after postnatal 3 months (the age of our mice at the start of this study), OPCs continue to proliferate, OLs continue to differentiate, and adaptive myelination continues, at a lower stable rate (307). He et al. showed increased K_{iso} in LPC (L-α-Lysophosphatidylcholine) treated regions in the mouse brain (208). LPC is known to kill mature OLs, so increased K_{iso} could be due to re-population of mature OLs by OPCs, which has been seen 3-7 days post-LPC treatment (308). The increase in K_{iso} may reflect oligodendrocyte proliferation and maturation, and thus myelin formation, which is supported by the increase observed in MTsat. Elevated K_{iso} may also be related to the increasing release of myelin debris over the course of normal aging, which is effectively cleared by activated microglia (309), also known to play a role in 'myelin remodeling'. K_{iso} may be sensitive to microglia activation associated with normal brain development, which would result in diversification of cell morphology. Cell size and density of astrocytes increasing at different rates in different regions of the brain may also result in increased K_{iso} (310,311). In the rat cerebral cortex, Sabbatini et al. reported that the size and number of astrocytes increased progressively from 3 to 24 months old (311). Age-associated increases in astrocytic hypertrophy and microglial activation were found to be prominent in white matter (310), which may explain why we observe the largest increase of K_{iso} in WM. It is likely that changes in K_{iso} are reflective of these various microstructural changes to some degree, as increases in K_{iso} in GM may suggest glial cell diversification whereas the

larger increase in WM may suggest a combination of glial cell diversification including OL proliferation/maturation.

4.4.2   Linear and Quadratic Fits to the Data

Quadratic fits of the metrics with age (Figure 4.3) reveal a maximum or minimum for most metrics around 5-6 months of age. This is comparable with the mean kurtosis peak of 6 months in rats reported by Han et al. (125). Although most metrics that show a significant linear fit (Table 4-1) also show a significant quadratic fit (Table 4-2), the quadratic fit is not significantly better than the linear fit in most cases (Table 4-3). Investigating more subjects and timepoints after the minimum/maximum had been reached would likely have improved the quadratic fits. The largest variability is also observed around the maximum/minimum period, likely due to individual mice reaching their maxima/minima at slightly different times.(24,286,287,290,291) Among the frequency-dependent metrics, significant quadratic fits were found for Λ and ΔRD. Interestingly, a significant linear trend of decreasing ΔFA is found in WM and DGM. To our knowledge, previous literature has not discussed values of ΔFA, and our results show that ΔFA may be a relevant frequency-dependent metric to explore. Significant linear and quadratic fits were found for K_{total} and K_{iso}, but not for K_{aniso}, which indicates that K_{aniso} is not sensitive to age-related changes during normal brain maturation.

The linear and quadratic fits shown here are comparable to previous studies in both humans (24,38,286,287,289–293) and rodents (125), investigating DTI, DKI, and myelin-specific metrics. In a human lifespan study, peak age calculated with the quadratic model revealed peak ages in the range of 30-50 years depending on brain

region and metric (290). 30 human years is equivalent to about 6 mouse months and 50 human years is equivalent to about 15 mouse months (312). This is consistent with our results, as we start to observe peaks around the 5-6 month timepoint. Most DTI studies indicate a U-shaped relationship between the diffusivity metrics and age in most ROIs, with FA exhibiting an inverted U-shaped relationship. An inverted U-shape trend of myelin-specific metrics with age has been reported (286,287,290,313–315), and this quadratic association is attributed to the process of myelination from youth through middle age, followed by demyelination in later years.

4.4.3   Sex-dependent Differences over Time

Sex-dependent differences over time are observed in most of the dMRI metrics (Figure 4.4), while MTsat shows the same fits for both sexes. This suggests that the diffusion metrics are more sensitive to differences between sexes, as they are sensitive to other factors beyond myelination. Interestingly, the overall shape of the fits for the metrics do not change between ROIs (WM, CX, DGM), possibly as the ROIs are quite large. MD, AD, and RD show opposing trends for both sexes, with males following a U-shape trajectory. Among human lifespan studies, Kiely et al. (290) reported that sex effects were limited to very few ROIs, while Grydeland et al. (286) and Lebel et al. (24,38) found no sex effects. Although these studies included both sexes, some studies contained disproportionately more males, while others contained almost equal proportions, but it is unknown what percentage of males and females were considered for each age range, which may have introduced bias into the results. According to a review, most DTI human lifespan studies have not explicitly measured sex differences over time

(299). Previous DTI studies (imaged at a single cross-sectional timepoint) have found higher FA and lower MD in males (the lower MD is consistent with our results), tied to hormonal levels, although contradictory and null findings have also been reported (316). The frequency-dependent metrics show the same fit for males and females for most cases in Figure 4.4. Tetreault et al. were the first to explore sex differences in the human corpus callosum using frequency-dependent dMRI (194). They reported greater ΔRD in the genu of males, which could reflect larger axon diameters than females. However, this study combined data from all ages (20-73 years old) when reporting this difference, so analyzing age ranges separately may change the results.

Kurtosis metrics and µFA also show opposing trends for both sexes, with females showing an inverted U-shape for K_{total} and K_{iso} and a U-shape trajectory for K_{aniso} and µFA. This further supports our finding that K_{total} changes over time are driven by changes in K_{iso}. Previous µFA studies have not explored sex differences, as most studies have been proof-of-concept. The differences in K_{iso} trajectories between sexes may be related to differences in glial cell number and morphology and/or oligodendrocyte cell diversity between males and females. Mouton et al. reported that female mice have significantly higher numbers of microglia and astrocytes than males (consistently as measured from 3-24 months) in the hippocampus (317). Previous studies have found that female microglia are more developmentally mature than male microglia and females have higher expression of inflammatory, phagocytic, and immune genes than males (318). Thus, females could have lower levels of cell proliferation due to increased phagocytosis of progenitor cells, which may explain the overall lower trend of K_{total} and K_{iso} in the female trajectory. The differences seen in the male and female trajectories in Figure 4.4 highlight

the importance of including both sexes in research and considering sex-dependent analyses. However, these differences may be amplified by the oldest age lying only barely outside the peak of the U-shape, and may be consistent with a later peak in males (that is not captured here) compared to females. Combined with the small sample size in this study, it is challenging to fully interpret the sex dependent trajectories, which will require larger sample sizes and age ranges, and further histological analyses.

4.4.4   Linear Regression of Kurtosis with Myelin-Specific Metrics

Figure 4.5 illustrates the linear relationship of kurtosis metrics with myelin-specific metrics in each ROI independently. K_{aniso} does not show any correlations with MTsat (Figure 4.5). The negative correlations of K_{aniso} with MTR may include biases, as MTR is sensitive to T1-weighting and various sequence parameters. This indicates that K_{aniso} (and µFA via Eq. 3) is not sensitive to myelination, which agrees with the results in Figure 4.2. Although previous studies found changes in µFA with demyelination in the cuprizone demyelination model (208) and multiple sclerosis patients (17), we anticipate that subsequent damage to axons and/or neuroinflammation may have caused resultant changes in µFA and K_{iso} as well, which supports our reasoning that myelination may not be a key contributor to axonal anisotropy. Figure 4.5 shows that increases in K_{total} over the course of development, which have been shown by others in humans (292,293) and rodents (125,294), are largely due to increases in isotropic kurtosis rather than anisotropic kurtosis. Furthermore, the results highlight the importance of using both LTE and STE acquisitions as K_{total} accounts for kurtosis from both anisotropic and isotropic sources,

and most studies only explore the total kurtosis. We show here changes in total kurtosis over time may be predominated by isotropic sources, which suggests that total kurtosis is unlikely to be sensitive to how myelination affects water diffusion anisotropy over the course of normal brain development (as these changes would be reflected in anisotropic sources of kurtosis).

Figure 4.6 illustrates the linear fits of kurtosis metrics with myelin-specific metrics in all ROIs combined, to focus on linear relationships over the ROIs. As K_{aniso} shows positive correlations with both MTR and MTsat (Figure 4.6), and K_{iso} does not show any correlations here, this indicates that K_{aniso} is sensitive to microstructural differences that distinguish different brain regions, while K_{iso} is not. **Figure 4.5 and Figure 4.6 highlight that changes in total kurtosis found over time (in normal brain development) are driven by isotropic kurtosis, while differences in total kurtosis found between brain regions are driven by anisotropic kurtosis.** This indicates that while the main differences between white and gray matter regions stem from fiber content and alignment, leading to differences in anisotropic kurtosis, the main differences over time are not related to changes in axonal content. Age and region dependent kurtosis changes have been reported in previous DKI studies (125,292–294,319–321), but these studies only focused on the total kurtosis.

4.4.5   Limitations

Although conducted using a longitudinal study design and state-of-the-art methods, our investigation has limitations. Firstly, we do not calculate microscopic kurtosis (µK), which is another source of total kurtosis and ignoring it can impact the

accuracy of other kurtosis sources. µK is the weighted sum of different microscopic sources of non-Gaussian diffusion, which include restricted diffusion inside compartments, microstructural disorder due to the presence of microscopic hindrances to water molecules (such as membranes and axon caliber variations), and exchange between components (164,238). Recently, µK was shown to be a primary driver of total kurtosis upon ischemia in mice (322) and was mapped in human brain tissue for the first time (323), revealing that this component is non-negligible. Moreover, Novello et al. showed that assuming the multiple Gaussian component approximation for kurtosis source estimation (ignoring µK) introduces significant bias in the estimation of other kurtosis sources (323). Additionally, for our frequency-dependent dMRI protocol, our highest OGSE frequency (190 Hz) was determined by hardware constraints, and reaching even higher frequencies would allow us to probe smaller spatial scales. Although our MTsat protocol improves myelin specificity compared to MTR, a more recent technique, inhomogeneous magnetization transfer (ihMT), may be better suited for our study. ihMT, which was developed based on MT MRI, is more specific to myelin than MTsat, due to its direct sensitivity to the phospholipids in myelin (324,325). In this study, we only explored one phase of the mouse brain lifespan, the brain maturation phase, while the degeneration phase remains to be investigated. Including more timepoints after 8 months would allow for a more robust and complete picture of the mouse brain lifespan trajectory. However, the time period used in this study (between 3-8 months of age) is a widely used time period for longitudinal rodent neuroimaging studies and will provide insight into healthy rodent brain development to help disentangle normal and pathological microstructural changes. It is also important to note that the developmental

trajectory described here is for wild type C57Bl/6 mice and may be altered in other mouse lines.

4.5   CONCLUSION

In conclusion, we investigated the evolution of advanced dMRI and MT MRI metrics longitudinally in healthy mouse brain maturation, as the study of normal brain maturation will help exclude confounds of cerebral developmental changes from interpretations of disease and injury mechanisms. Overall, the trends observed in our DTI and MTsat metrics are comparable to previous human and rodent studies investigating normal brain development. Neurobiological changes that result in changes to isotropic kurtosis remain understudied, however, we suggest here that isotropic kurtosis sources drive changes in total kurtosis during normal brain maturation. Our results suggest myelination is not a main contributor to microscopic diffusion anisotropy and anisotropic kurtosis in axons. For studies that only calculate total kurtosis, we suggest caution in attributing neurobiological changes to changes in total kurtosis as we show here no changes in anisotropic sources of kurtosis in the presence of myelination.

4.6 SUPPORTING INFORMATION
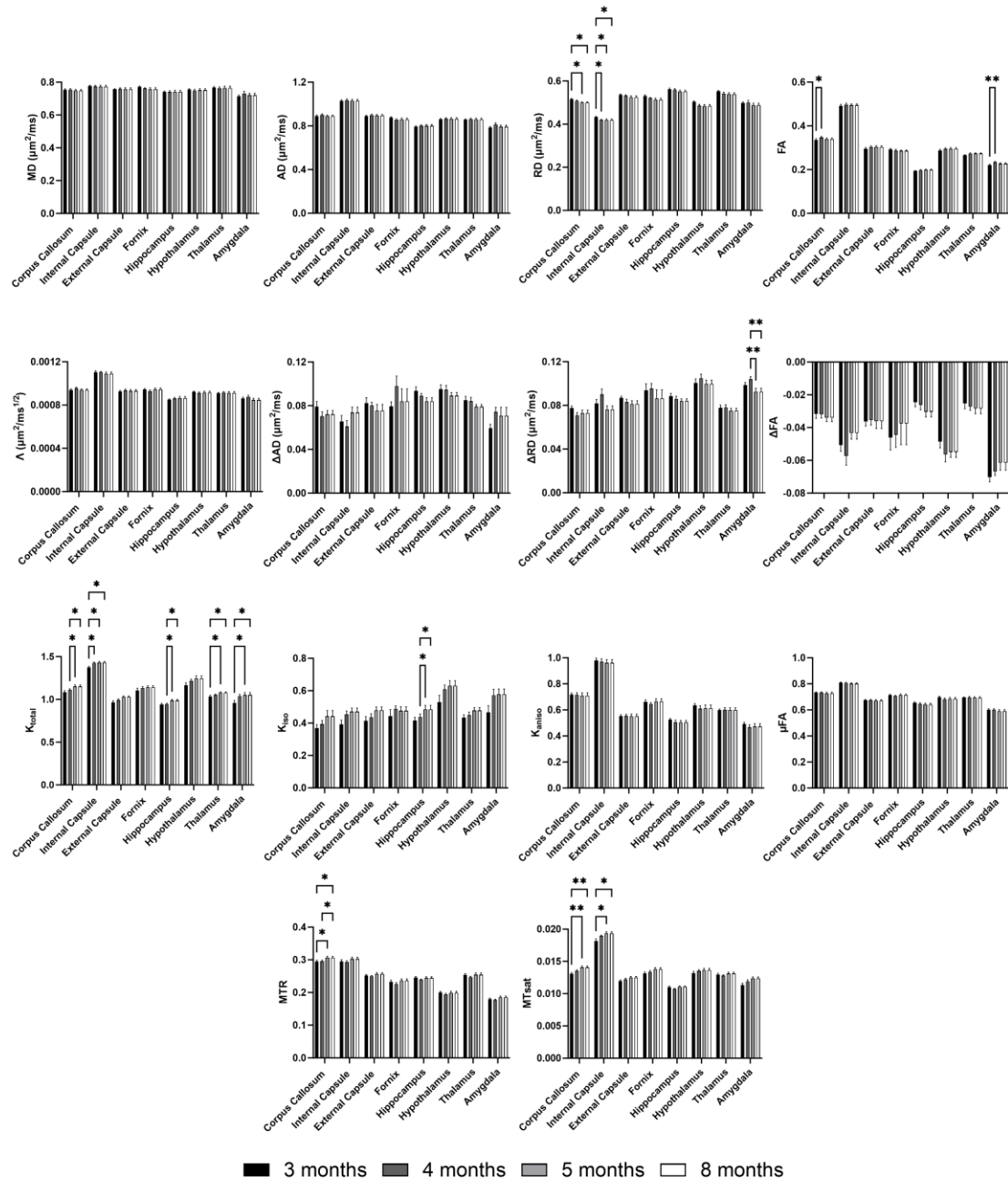
Supplemental Figure 4.S1 - *Quantitative MRI parameter evolution during healthy ageing in smaller ROIs including 4 white matter ROIs (corpus callosum, internal capsule, external capsule, and fornix) and 4 gray matter ROIs (hippocampus,*

hypothalamus, thalamus, and amygdala). Data represents mean values of each metric and error bars represent the standard deviation among n=11 mice. Asterisks represent results from post hoc pair-wise comparison (* p<0.05, ** p<0.01, *** p<0.001).

Chapter 5

5   Microstructural MRI evolution during adult mouse brain concussion recovery

5.1   INTRODUCTION

Mild traumatic brain injury (mTBI), also known as concussion, is a significant public health concern, with approximately 200,000 cases reported annually in Canada (47). mTBI is defined as acute neurophysiologic brain dysfunction resulting from impact contact forces or sudden acceleration/deceleration causing a transient alteration of consciousness and/or a period of anterograde (and possibly retrograde) amnesia (55). The overwhelming majority (75 - 90%) of traumatic brain injuries (TBIs) are mild (326) with the acknowledgment that the incidence of mTBI is likely grossly underestimated because many patients with mTBI do not seek medical treatment (327). Moreover, while symptom resolution in most concussion patients occurs within 3 months post-injury, 15 % of individuals with a single mTBI demonstrate long-term cognitive impairment (56–58). A more recent review by McInnes et al. (49) found that the 15 % estimate is an underestimation, and approximately half of individuals with a single mTBI demonstrate long-term cognitive impairment. The pathological mechanisms underlying this incongruence remain largely unknown, presenting a need to continue efforts to better understand the transition from early phase to late phase disorder after mTBI.

Diagnosis of mTBI relies on patient-reported symptomatology, such as headaches, fatigue, depression, and cognitive impairments. However, this subjective assessment can be imprecise and unreliable. While structural MRI and CT show

sensitivity to TBIs, they often show normal findings in mTBI cases (50,51). Additionally, CT and MR findings are poor indicators of persistent symptoms in patients with mTBI (52). Biomarkers for diagnosing and assessing the severity of mTBI are not yet established, although techniques like diffusion tensor imaging (DTI) and magnetic resonance spectroscopy (MRS) are promising (53,54).

Diffusion MRI (dMRI) provides a non-invasive means to capture changes in brain microstructure during development, aging, disease, and injury by probing the diffusion of water molecules (182). Diffusion tensor imaging (DTI), the most widely used dMRI technique, is sensitive to the coherence of fibrous structures that can detect diffuse axonal injury in TBI patients (328,329) and experimental studies (135,136,247). Although DTI has arguably had the greatest influence to-date of neuroimaging modalities in mTBI (330), previous studies have reported inconsistent DTI findings across studies (22). In the late period following TBI, the most common DTI finding is reduced fractional anisotropy (FA) that is proportional to the injury severity, reported 1 – 6 years post-injury (330–332). Overall, DTI studies demonstrate diffusion restrictions, resulting in lower mean diffusivity (MD) and higher FA, along white matter tracts in the acute setting that typically pseudo-normalize in the sub-acute period (121). There is not yet a consensus as to what these changes mean in terms of specific underlying neuropathology nor is there consensus on how they relate to functional impairment. Magnetization transfer (MT) MRI has also been applied to mTBI, and the magnetization transfer ratio (MTR) offers sensitivity to myelin content and integrity to detect axonal injury and demyelination, as well as recovery and remyelination, consequent to mTBI (247,333). Although inconsistent MTR findings have been reported, with one study reporting no changes in

the acute stage (24 hours) and chronic stage (90 days) post-mTBI (334), most MTR studies indicate decreased MTR, histologically verified as demyelination (247,335) and correlating with cognitive dysfunction (336). While an mTBI study found that MTR values normalized 30 days post-injury (247), a TBI study reported decreased MTR even 1-year post-injury (336). As DTI and MTR MRI have limitations reducing their sensitivity and specificity to microstructural changes, we apply a microstructural MRI protocol, in addition to DTI and MTR metrics as references, including: 1) frequency-dependent dMRI; 2) tensor-valued dMRI; 3) magnetization transfer saturation (MTsat) MRI. This is the first application of any of these advanced MRI techniques to mTBI. Each of these 3 advanced techniques, and the limitations they overcome, are described below.

Firstly, conventional dMRI sequences are limited to probing length scales on the order of 10-30 µm due to hardware constraints (9), as they rely on the pulsed gradient spin echo (PGSE) sequence to encode diffusion. To probe smaller length scales, the oscillating gradient spin echo (OGSE) sequence was developed to modify sensitivity to cellular length scales (10). By varying the frequency of the diffusion gradient waveform (i.e., frequency-dependent dMRI), which is inversely related to diffusion time, OGSE encoding allows different microstructural length scales to be probed. Subsequently the difference in DTI metrics between the highest and lowest frequencies applied, such as ΔMD, can be used to examine their dispersion with frequency and provide greater insight into tissue microstructure (162,178). Additionally, evidence of a linear dependence of MD on the square root of frequency has been demonstrated in healthy and globally

ischemic rodent brain tissue (169) and healthy human white matter (183,277). Therefore, the diffusion dispersion rate (Λ) can be calculated using a power-law model as:

$$MD_f = MD_0 + \Lambda f^{0.5} \tag{5.1}$$

where MD_f is the MD at OGSE frequency, f, and MD_0 is the MD at f = 0, which is the conventional PGSE sequence (162,178,183). Frequency-dependent dMRI has helped to identify neurite beading as a mechanism for contrast after ischemic stroke (19,20), and has shown increased sensitivity compared to conventional PGSE dMRI in the assessment of hypoxia-ischemia (201) in rodents, and in various pathologies in humans (202–204).

Secondly, DTI is confounded by neuron fiber orientation dispersion (8,21), reducing its specificity to microstructural changes in brain regions with crossing fibers, and assumes the dMRI signal is entirely characterized by Gaussian diffusion (8), providing a vague and limited model of neuroanatomy. To reduce orientation dispersion effects on diffusion measurements, tensor-valued diffusion encoding (11–13), which varies the shape of the b-tensor (describes the strength of diffusion weighting along each direction) to vary the sensitivity to diffusion anisotropy, was developed. Previous studies have shown that tensor-valued dMRI provides better sensitivity than conventional DTI in distinguishing between different types of brain tumours (21) and assessment of multiple sclerosis lesions (16,17). Tensor-valued dMRI distinguishes between different sources of kurtosis (kurtosis quantifies the deviation away from Gaussian diffusion) and allows for computation of microscopic fractional anisotropy (μFA), which is analogous to the standard FA metric and reports water diffusion anisotropy independent of the neuron fiber orientation dispersion (21,141,190). In tensor-valued dMRI, the total diffusional

kurtosis (K_{total}), reported as the mean kurtosis in conventional diffusion kurtosis imaging (DKI) (124), can be disentangled into isotropic and anisotropic kurtosis (K_{iso} and K_{aniso}, respectively). K_{iso} is a measure of the variance in compartment-specific diffusivities which can be related to cell size heterogeneity (21) and K_{aniso} arises from microscopic diffusion anisotropy. μFA can be expressed in terms of K_{aniso}:

$$\mu FA = \sqrt{\frac{3}{2}}\left(1 + \frac{6}{5}\frac{1}{K_{aniso}}\right)^{-\frac{1}{2}} \qquad (5.2)$$

Last but not least, MTR has been shown to be sensitive to sequence parameters, flip angle inhomogeneities, and T1 effects (14,15). MT saturation (MTsat) imaging reduces these sensitivities and increases specificity to changes in myelin content in a comparable scan time (14). MTsat shows higher white matter contrast in the brain than MTR (14), and has been shown to correlate more with disability metrics than MTR in patients with multiple sclerosis (18).

To explore the pathophysiology and the evolution of microstructural MR metrics at the mild end of the spectrum of mTBIs, we implemented possibly one of the mildest single impact models in the literature. Our results exhibit greater sensitivity of microstructural MR metrics, compared to standard DTI, to changes following injury at both subacute and chronic stages. Of particular interest, we identify evidence of a sexually dimorphic response to mTBI, reinforcing that sex matters in mTBI as females are still underrepresented in clinical and preclinical mTBI research.

5.2   METHODS

Detailed information on the data acquisition and analysis pipeline used for this study is openly available (295) and included as Appendix A. Moreover, the test-retest reproducibility of the MRI metrics have been reported previously in Chapters 2 and 3 (181,239). Therefore, we will only summarize acquisition and analysis and refer the reader to the previous chapters for full detailed methods.

5.2.1   Subjects

The sham and concussed cohorts each consisted of 12 C57Bl/6 mice (6 males, 6 females), with a total of 24 mice aged 10-12 weeks at the start of the study. The mice were scanned longitudinally at Baseline (before mTBI), 1-month post-mTBI, 2-months post-mTBI, and 5-months post-mTBI, as shown in Figure 5.1. One female sham mouse was not scanned at the 5-month timepoint, as it expired before this timepoint due to natural causes. Imaging was also performed at the acute stage after mTBI, at 2 days post-mTBI and 1-week post-mTBI. However, this data was excluded from analysis to avoid possible effects from anesthesia on tissue microstructure (337,338). In a DTI mTBI study, Hoogenboom et al. observed considerable DTI changes in sham animals between baseline and 48 hours post-sham procedure (339), which was the most anesthesia-intense timeframe in the study. In a repeated isoflurane study in mice, behavioral deficits and reduced axial diffusivity in the corpus callosum were found up to 90 days after isoflurane exposure (340).

Before scanning, anesthesia was induced by placing the animals in an induction chamber with 4 % isoflurane and an oxygen flow rate of 1.5 L/min. Following induction,

isoflurane was maintained during the imaging session at 1.8 % with an oxygen flow rate of 1.5 L/min through a custom-built nose cone. The mouse head was fixed in place using ear bars and a bite bar to prevent head motion. After the last timepoint, the mice were euthanized for histology. The mice were anesthetized with ketamine/xylazine (2:1) and then underwent trans-cardiac perfusion with ice-cold saline, followed by 4% paraformaldehyde in phosphate-buffer saline (PBS).
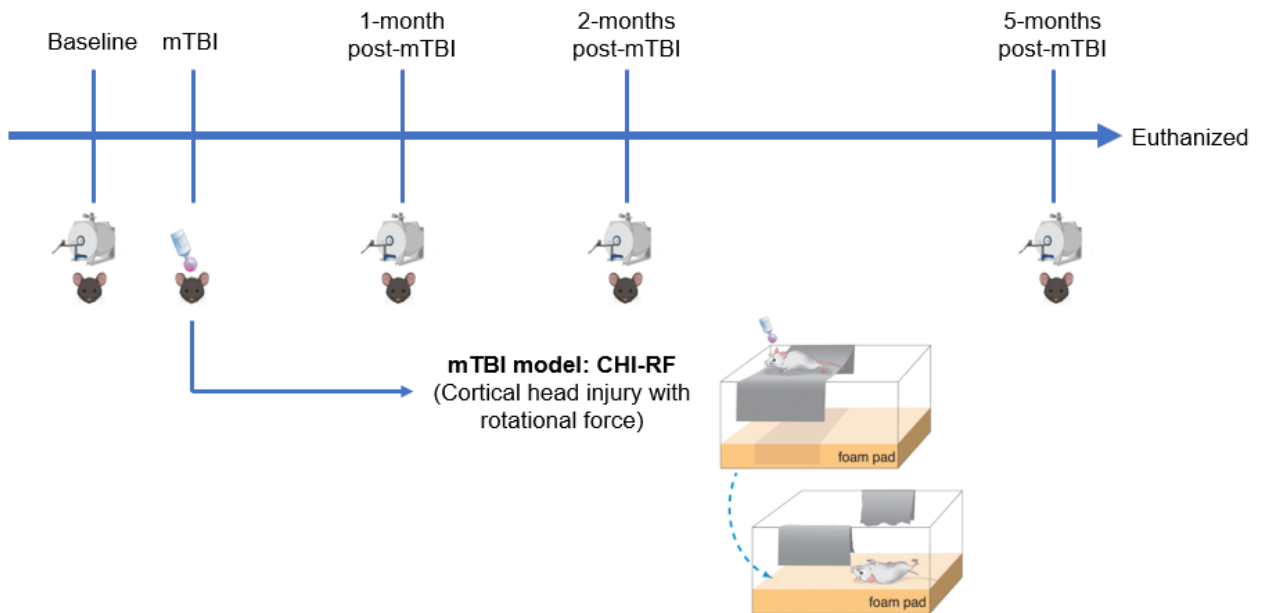
Figure 5.1 - *Overview of study design. At Baseline, all mice were 12–14 weeks old. A single mild impact was delivered to the concussed cohort 2 days after baseline imaging, following the CHI-RF (cortical head injury with rotational force) model. In the CHI-RF model, the mouse is placed on a piece of pre-pierced clear plastic and following impact, undergoes a 180° rotation and falls onto a foam pad or soft towel. After the 5-month*

scan, all mice were euthanized. Injury graphic adapted from Bodnar et al. (open access)
(341).

5.2.2   Mild Traumatic Brain Injury Model

For the concussed cohort, a closed head single mild impact model, involving both linear and rotational forces, was implemented 2 days after the Baseline scan. This emerging mTBI model is termed "Closed head injury with rotational force" or CHI-RF. The goal of this model is to match the stretch and strain in the rodent brain during mTBI to that experienced by the human brain, as measured in contact sports (342). The mouse is placed on a custom-made acrylic box, topped with a piece of pre-pierced clear plastic (facilitating the fall). Following impact, the mouse undergoes a 180° rotation and falls onto a foam pad or soft towel, as depicted in Figure 5.1. The parameters of our CHI-RF impact were: impact speed (3.5 m/s), tissue depth (8 mm) and dwell time (500 ms, the amount of time the impactor tip will remain in contact with the brain surface).

Animals were anaesthetized by intra-peritoneum injection with Ketamine 80mg/kg and Xylazine 10mg/kg, diluted in saline, and placed in a Kopf stereotaxic frame for positioning under a traumatic brain injury device (TBI 0310, Precision Systems and Instrumentation, LLC), which consists of an air-driven custom impactor, centered on Bregma, as shown in Figure 5.2. Sham mice also underwent the same anesthetic procedure. In rodents, the Bregma is widely used as the origin reference point for stereotaxic coordinates and refers to the crossing point of the coronal and the sagittal sutures (343). The custom impactor is a 4 mm-diameter pliant silicone tip. The sham cohort underwent a sham procedure, 2 days after the baseline scan, and were subjected to equal amounts of anesthesia as the concussed cohort.
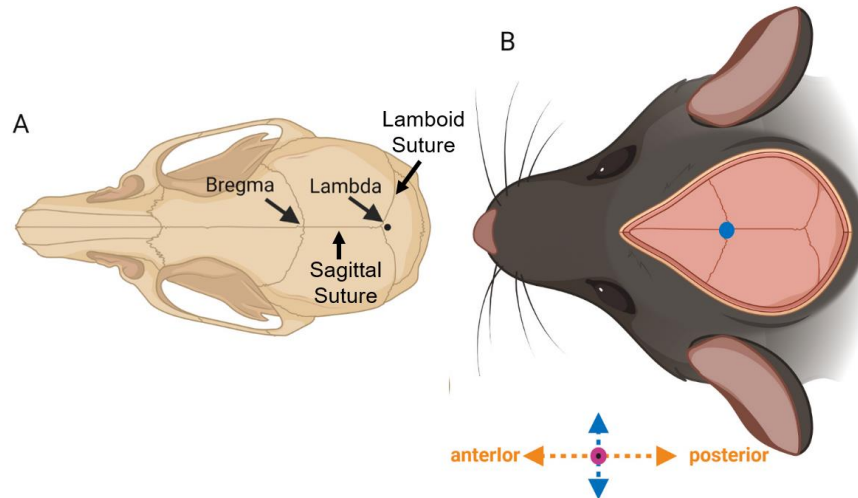
Figure 5.2 - *Dorsal view of the rodent skull diagram with sutures and detailed points of measurement of the Bregma and the Lambda. A) The Bregma is measured on the crossing point between the coronal and the sagittal sutures. The Lambda landmark is defined "as the point of intersection of the best-fit lines passing through the sagittal suture and the left and right portions of the lambdoid suture". B) Skull landmarks on surgery view, with the blue dot indicating Bregma and location of the single mild impact. Image adapted from Cecyn & Abrahao (open access) (343).*

These injury depths and speeds are similar to the injury parameters used by others studying mTBI in mice (214,344,345), although these studies investigated models of repetitive mTBI. Single impact models in the literature use relatively greater injury parameters (247,346,347). Thus, to the best of our knowledge, this study may be implementing one of the mildest single impact models in literature.

5.2.3 Data Acquisition

MRI experiments were conducted on a 9.4 Tesla (T) Bruker small animal scanner equipped with a gradient coil insert of 1 T/m strength (slew rate = 4100 T/m/s). During

each imaging session, frequency-dependent and tensor-valued dMRI, MT MRI, and anatomical data was acquired with a total scan time of 2 hours and 35 minutes. Anatomical images were acquired using a T2-weighted TurboRARE sequence with parameters: in-plane resolution 150 x 150 µm, slice thickness 500 µm, TE/TR = 40/5000 ms, 16 averages, total scan time of 22 minutes. The frequency-dependent dMRI protocol included a PGSE sequence (gradient duration = 11 ms and diffusion time = 13.8 ms) and OGSE sequences with frequencies of 50, 100, 145, and 190 Hz with a single b-value shell of 800 s/mm^2 (10 directions) (348) and parameters: in-plane resolution 175 x 200 µm, slice thickness 500 µm, TE/TR = 39.2/10000 ms, 5 averages, total scan time of 45 minutes. Frequency tuned bipolar (FTB) waveforms were used at 50 Hz to lower the TE of the acquisition (297). The tensor-valued dMRI protocol consisted of LTE and STE acquisitions with b-value shells of 1000 s/mm^2 (12 directions) and 2000 s/mm^2 (30 directions) with parameters: in-plane resolution 175 x 200 µm, slice thickness 500 µm, TE/TR = 26.8/10000 ms, 3 averages, total scan time of 45 minutes. The MT protocol included three FLASH-3D scans and one B1 map scan to correct for local variations in flip angle. The FLASH-3D scans consisted of an MT-weighted scan, and reference T1-weighted and PD-weighted scans with parameters: in-plane resolution 150 x 150 µm, slice thickness 500 µm, 12 averages, total scan time of 43 minutes.

5.2.4   Data analysis

Complex-valued averages were combined using in-house MATLAB code which included frequency and signal drift correction (221) and Marchenko-Pastur denoising of complex-valued data (223). After averages were combined, data underwent correction for

Gibbs ringing using MRtrix3 (224), and eddy-current induced distortions using TOPUP (218) followed by EDDY (219) from FMIRB Software library (FSL, Oxford, UK) (225).

Scalar maps of magnetization transfer ratio (MTR) and MT saturation (MTsat) were generated from the MT protocol as outlined by Rahman et al. (295). From the frequency-dependent dMRI data, MRtrix3 was used to fit the diffusion tensor and acquire maps of MD, AD, RD, and FA. Quantitative values of ΔFA, ΔAD, and ΔRD were calculated as the mean of each metric within the region-of-interest (ROI) between the highest frequency (190 Hz) and the lowest frequency (0 Hz). Diffusion dispersion rate (Λ) maps were computed as outlined in Eq. 1. From the tensor-valued dMRI data, maps of K_{total}, K_{iso}, and μFA were generated as described in Chapter 4.

5.2.5 Region-of-interest (ROI) analysis

Quantitative MRI parameters were investigated in 3 gray matter and 3 white matter regions of interest (ROIs): hippocampus (HC), prefrontal cortex (PFC), olfactory region (OLF), corpus callosum (CC), internal capsule (IC), and cerebral peduncle (CP). We defined the PFC to include cortex from the orbital area to 1 mm caudal to the bregma, which included the secondary motor cortex; the anterior cingular area, the prelimbic area, the infralimbic area and the agranular insular area as defined by Carlen (349). The olfactory region included the olfactory bulb, anterior olfactory cortex, taenia tecta, and olfactory tubercle. The white matter tracts (CC, IC, and CP) are perpendicular to each other and were thus chosen to account for differences in injury based on the axis of the tracts. Masks for all ROIs were generated from the labelled Turone mouse brain atlas (298), which was downsampled to the resolution of the T2-weighted images. To ensure accurate registration of scalar maps to the atlas, a T2 template, an FA template, and an

MT-weighted template was created based on images from all scanning sessions using ANTs software (227). There are 3 steps to warp individual scalar maps to the downsampled atlas space: (1) Individual FA and MT-weighted maps are registered to their respective templates, (2) the FA and MT templates are registered to the T2 template, and (3) the T2 template is registered to the downsampled atlas. Each registration step involves affine transformation followed by symmetric diffeomorphic transformation using ANTs software. Output deformation fields and affine transforms from each of the three steps were used to warp the individual scalar maps to the atlas space, resulting in only a single interpolation during registration, to obtain quantitative values for each dMRI metric.

5.2.6   Statistical Analysis

Statistical analysis was done in MATLAB version R2020b and graphs were created in GraphPad Prism version 9.5.1. To investigate if the MRI metrics changed significantly over time, repeated measures MANOVAs were performed for each metric, over all ROIs, to examine differences between timepoints, and account for multiple regions being examined in each mouse. Metrics with a significant group effect ($p < 0.05$) from MANOVA were followed up by separate univariate repeated measures ANOVAs within each ROI. Significant group by time interaction effects (Greenhouse-Geisser corrected) from the ANOVAs were followed up by repeated measures ANOVA and Tukey HSD test for post hoc pair-wise comparison within each group separately, to determine within-subject differences in metrics within an ROI across time.

To perform sex-dependent analysis, significant group by sex interaction effects from the initial MANOVA, for each metric, were followed up by analyzing the male and

female group separately for each ROI. Repeated measures ANOVAs were performed in the male and female group, separately. Significant group by time interaction effects (Greenhouse-Geisser corrected) from the ANOVAs were followed up by repeated measures ANOVA and Tukey HSD test for post hoc pair-wise comparison within the concussed and sham groups separately, to determine within-subject differences in metrics within an ROI across time.

5.3   RESULTS

Table 5-1 shows the results of group effects and group by sex interaction effects from the initial MANOVA for each metric. RD shows a significant group effect, while AD shows a significant group by sex interaction effect. All tensor-valued dMRI metrics (K_{total}, K_{iso}, K_{aniso}, and µFA) reveal significant group and group by sex interaction effects. MTR shows both group and group by sex interaction effects, while MTsat only shows a group by sex interaction effect. The frequency-dependent dMRI metrics did not show any significant results from the initial MANOVA. Table 5-2 shows results of group by time interaction effects from repeated measures ANOVAs, for each ROI, for all metrics that demonstrated a significant group effect from the initial MANOVA. The only significant group by time effects are observed in K_{aniso} and µFA in the olfactory region, and MTR in the cerebral peduncle.

Table 5-1: MANOVA results for each metric over all ROIs showing group effects and group by sex interaction effects. Highlighted cells show significant p-values (p < 0.05).

Metric	Group effect (P-value)	Group*Sex effect (P-value)

MD	0.0944	0.8083
AD	0.5322	0.0131 *
RD	0.0324 *	0.4055
FA	0.6358	0.1889
Λ	0.0610	0.0644
ΔAD	0.2847	0.3503
ΔRD	0.3261	0.1310
ΔFA	0.3068	0.1256
K_{total}	0.0047 **	1.662×10^{-6} ***
K_{iso}	1.846×10^{-4} ***	5.200×10^{-10} ***
K_{aniso}	1.441×10^{-4} ***	5.350×10^{-8} ***
µFA	4.074×10^{-5} ***	1.739×10^{-7} ***
MTR	6.646×10^{-5} ***	1.339×10^{-6} ***
MTsat	0.5493	2.390×10^{-9} ***

Table 5-2: Repeated measures ANOVA results showing group by time interaction effects, for each ROI, for all metrics that demonstrated a significant group effect from the initial MANOVA. Highlighted cells show significant p-values ($p < 0.05$).

Group*Time Effect (P-value)		
ROIs		

Metrics	HC	PFC	OLF	CC	IC	CP
RD	0.1497	0.2024	0.1062	0.2337	0.3920	0.3400
K_{total}	0.1337	0.4688	0.2408	0.2063	0.3946	0.4911
K_{iso}	0.0946	0.2025	0.1134	0.1826	0.4050	0.2070
K_{aniso}	0.1636	0.3610	0.0020	0.3880	0.3304	0.2045
µFA	0.0937	0.1811	7.275×10^{-4}	0.2775	0.2489	0.1624
MTR	0.1789	0.2457	0.4182	0.2256	0.4956	0.0448

Figure 5.3 shows all MRI metrics at all timepoints and ROIs for both sham and concussed cohorts. The significant group by time effects in K_{aniso}, µFA, and MTR are shown, including the results of follow-up post hoc pairwise comparisons over time within each group. No significant pairwise comparisons were found for MTR. Only in the concussed group, both K_{aniso} and µFA significantly increase in the olfactory region from Baseline to 5-months post-mTBI, with a 32% increase in K_{aniso} and 15% increase in µFA. Of the frequency-dependent metrics, Λ and ΔAD in the concussed cohort reveal an increasing trend over time in PFC and OLF, compared to the shams, although not significant.
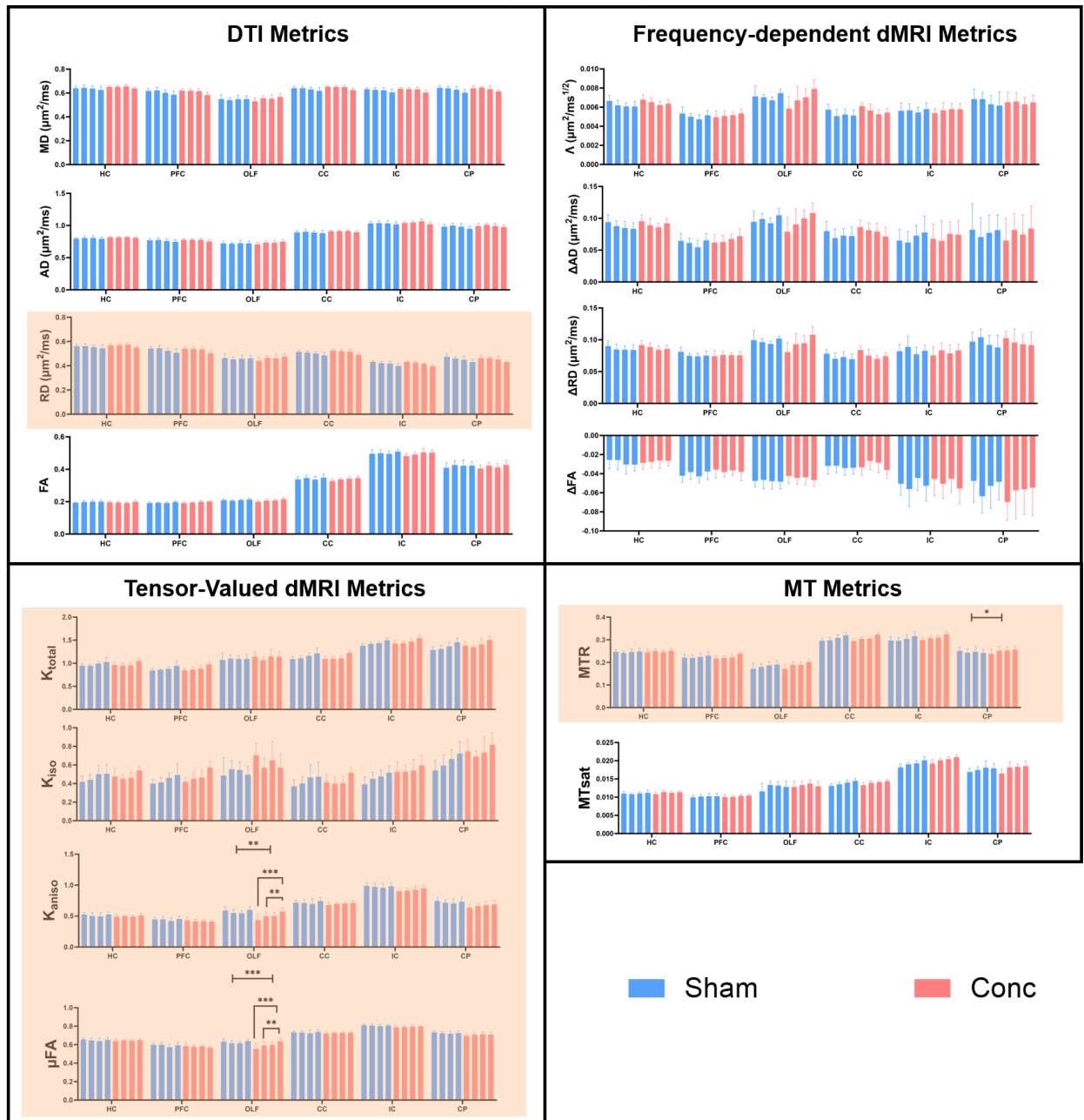
Figure 5.3 - *Quantitative MRI parameter in sham and concussed cohorts in the following ROIs: hippocampus (HC); prefrontal cortex (PFC); olfactory region (OLF); corpus callosum (CC); internal capsule (IC); cerebral peduncle (CP). Data represents mean values of each metric and error bars represent the standard deviation over all mice in the*

cohort. Within each cohort, the four bars from left to right represent the following timepoints: Baseline; 1-month post-mTBI; 2-months post-mTBI; 5-months post-mTBI. The shaded background represents metrics with significant group effects. Asterisks represent statistically significant results (* p<0.05, ** p<0.01, *** p<0.001), with capped lines showing significant group by time effects and n zig-zag lines showing significant post-hoc pairwise comparisons.

Group by time interaction effects from repeated measures ANOVAs, for males and females separately, are reported in Tables 5.3 (females) and 5.4 (males), for all metrics that demonstrated a significant group by sex interaction effect from the initial MANOVA. Interestingly, no group by time interaction effects are found in males. In females, all reported metrics show significant group by time effects in various ROIs. Both MTR and MTsat show significant effects in HC and CP, while only MTR shows significant results in PFC and OLF. K_{aniso} and μFA show significant effects in the same regions: HC, OLF, CC, IC. K_{iso} shows significant results in all ROIs, except CP. AD shows significant group by time effects only in HC and CC.

Table 5-3: Repeated measures ANOVA results showing group by time interaction effects for each ROI in females, for all metrics that demonstrated a significant group by sex interaction effect from the MANOVA. Highlighted cells show significant p-values (p < 0.05).

	Group*Time Effect (P-value)					
	ROIs					
Metrics	HC	PFC	OLF	CC	IC	CP

AD	0.0203 *	0.3324	0.4860	0.0119 *	0.3994	0.8928
K_{total}	0.0143 *	0.0202 *	0.1354	0.0059 **	0.0430 *	0.2373
K_{iso}	0.0036 **	0.0184 *	0.0317 *	0.0077 **	0.0152 *	0.1448
K_{aniso}	0.0064 **	0.3303	2.058×10^{-4} ***	0.0315 *	0.0334 *	0.2481
µFA	0.0109 *	0.1411	1.595×10^{-4} ***	0.0294 *	0.0209 *	0.1785
MTR	0.0058 **	0.0241 *	0.0041 **	0.0795	0.0512	0.0131 *
MTsat	0.0012 **	0.0573	0.3303	0.0927	0.2628	0.0254 *

Table 5-4: Repeated measures ANOVA results showing group by time interaction effects for each ROI in males, for all metrics that demonstrated a significant group by sex interaction effect from the initial MANOVA.

	Group*Time Effect (P-value)					
	ROIs					
Metrics	HC	PFC	OLF	CC	IC	CP
AD	0.2999	0.3822	0.1685	0.5238	0.6140	0.6212
K_{total}	0.6737	0.6735	0.6717	0.6804	0.4429	0.8836
K_{iso}	0.6033	0.3108	0.4806	0.7216	0.3467	0.7532

K_{aniso}	0.7169	0.2315	0.2990	0.9207	0.3042	0.5921
μFA	0.7269	0.2085	0.3278	0.8860	0.2902	0.7253
MTR	0.6229	0.7966	0.3439	0.6821	0.7120	0.6980
MTsat	0.4452	0.2930	0.0069	0.0752	0.2943	0.5446

Figure 5.4 shows MRI metrics, with a significant group by sex interaction effect from the initial MANOVA, for females and males separately. In females, post hoc pairwise comparisons over time are shown, within sham and concussed cohorts, following up the significant group by time effects reported in Table 5-3. For concussed females, MTsat (HC) shows an initial 13% increase at 1-month post-mTBI, followed by a 5% decrease at 2-months post-mTBI (compared to 1-month). The initial MTsat increase is not resolved by 5-months post-mTBI, and MTsat remains 11% higher than at Baseline. MTR (HC) shows a similar trend (although not significant). MTR shows significant increases from Baseline to 5-months post-mTBI in PFC (13%) and OLF (27%), while MTsat shows similar (not significant) trends. On the other hand, MTsat shows significant increases post-mTBI in CP (22% increase at 5-months), with MTR showing similar (not significant) trends. In concussed females, there is an increase in K_{total} at 5-months post-mTBI, compared to 1-month post-mTBI, in HC (13%), PFC (13%), CC (12%), and IC (7%). K_{total} increases in sham females are more gradual across time, from Baseline to 5-months, as seen in CC (6%) and IC (8%). K_{total} increases in concussed females in HC and CC are paired with increases in K_{iso}, K_{aniso}, and μFA in those regions. K_{total} increases in the PFC are only paired with K_{iso} increases. K_{aniso} and μFA increases are also observed in

OLF from Baseline to 5-months post-mTBI, although this increase is not significant for K_{total}.
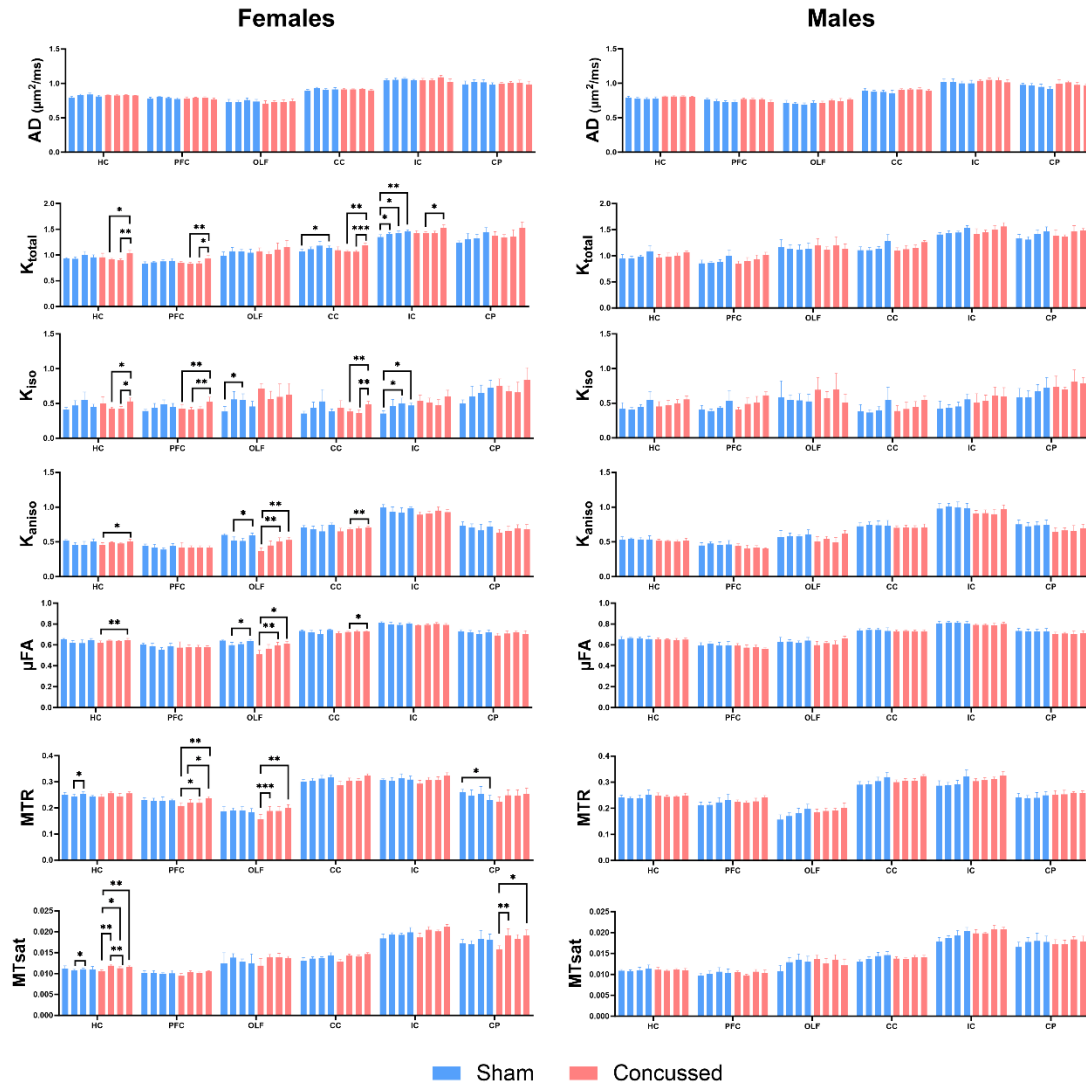
Figure 5.4 - *Quantitative MRI parameters in sham and concussed cohorts, within each sex, in the following ROIs: hippocampus (HC); prefrontal cortex (PFC); olfactory region (OLF); corpus callosum (CC); internal capsule (IC); cerebral peduncle (CP). Results from female and male mice are presented in the left and right columns, respectively. Data represents mean values of each metric and error bars represent the standard deviation*

within each cohort. Within each cohort, the four bars from left to right represent the following timepoints: Baseline; 1-month post-mTBI; 2-months post-mTBI; 5-months post-mTBI. Asterisks represent results from post hoc pair wise comparisons (* p<0.05, ** p<0.01, *** p<0.001).

5.4   DISCUSSION

In this study, we investigated mouse brain concussion recovery at subacute and chronic timepoints after a single closed head impact with rotational force, utilizing frequency-dependent and tensor-valued dMRI and MT MRI to probe smaller spatial scales, orientation-independent diffusion and various kurtosis sources, and myelin content, respectively. We performed sex-dependent analysis to disentangle male and female contributions to the whole group results, as there is a gap in the literature with respect to how the female brain responds to mTBI. We demonstrate that tensor-valued dMRI and MT metrics are more sensitive to microstructural changes in the sub-acute and chronic stages following mTBI, compared to DTI. Of particular interest, the tensor-valued dMRI and MT metrics exhibited a sex-dependent response to mTBI. Notably, this is the first time that frequency-dependent and tensor-valued dMRI are applied to mTBI.

A unique feature of the present study was the utilization of a closed-head model of mTBI. This circumvents some of the issues associated with the more invasive controlled cortical impact (CCI) and fluid percussion (FP) models, in which the brain itself is directly impacted, by surgically removing part of the skull, producing significant and focal physical damage that commonly extends into the hippocampus (350). The CHI-RF (closed head injury with rotational force) model, as used in this study, produces diffuse injury characterized by activation of inflammatory reactions and axonal damage,

replicating many aspects of the neuropathology of human mTBI without overt focal damage (351). Thus, we did not observe any gross anatomical changes here post-mTBI, as well as any qualitative changes in any of the MR metric maps, as confirmed by visual inspection.

5.4.1   DTI of mTBI

Most mTBI animal imaging studies investigate the acute stage post-mTBI, within the first month (136,137,247,352). DTI findings in mTBI all point to restricted diffusion in the early acute injury window, with subsequent pseudo-normalization sometimes within 3 - 7 days post injury (121). Pseudo-normalization of DTI metrics may be one reason why we are not observing changes in DTI metrics here. In a CCI model, decreased FA and AD was evident in the corpus callosum within several hours after injury (137). While AD pseudo-normalized beyond 4 days, RD increased compared to control levels in the similar window, with FA remaining low regardless of the time after injury. In the same injury model, prominent decreases in MD in the cortex immediately below the injury were demonstrated at two hours post injury, with values normalizing or increasing compared to controls at 7 days post injury (123). In a repetitive mTBI model, FA was increased at 48 hours post-injury compared to 4 weeks and 10 weeks post-injury in the corpus callosum and hippocampus (214). In human mTBI, DTI findings have been considerably more mixed (353). Differences in the injury classification, the injury-to-imaging time, and the heterogeneity in brain regions affected have complicated a single interpretation of the reported effects.

5.4.2   Evolution of MR Metrics and Underlying Biological Interpretations

Increases in Λ can be related to axonal beading, as increased ΔMD was related to a combination of neuronal beading and axonal swelling after ischemic stroke (19,20). No significant changes in Λ here, although an increasing trend is observed in the concussed cohort in the PFC and OLF (Figure 5.3), indicates that there likely is not substantial sub-acute or chronic axonal beading. Histologically observed axonal beading in a repetitive mTBI model was reported at acute, subacute, and chronic (up to 10 weeks) timepoints post-injury (214). As expected, there is much less damage with this single mild impact model. The frequency-dependent metrics also demonstrated a lower test-retest reproducibility than tensor-valued metrics in Chapter 2 (181), and this greater variability may be another reason the frequency-dependent metrics are not exhibiting significant effects.

No decrease in µFA suggests a lack of neurodegeneration and axon loss with this mild impact model. Variation in µFA in the brain has been related to axonal content (354) and increased µFA has been related to the presence of elongated cells (21). Monte Carlo simulations suggest K_{aniso} and µFA reduce with axon beading and µFA increases with greater intracellular volume fraction (355,356). Here, the increase in µFA and K_{aniso}, observed in concussed mice at the whole group level, as well as for concussed females, may be related to a greater number of elongated cells and greater intracellular volume fraction. This may arise from the infiltration of activated microglia in their hypertrophied and elongated state (357,358). In a rat TBI model, increased total kurtosis at the acute stage (1-week post-mTBI) was associated with reactive astrogliosis (123). Although the

effect of astrogliosis on µFA and K_{aniso} is unknown, we hypothesize that the highly branched processes of reactive astrocytes may contribute to increased µFA and K_{aniso}. Although a repetitive mTBI model showed persistent microgliosis 3-months post-mTBI (359), it is unknown whether a single mTBI can lead to persistent microgliosis or astrogliosis. The increase in µFA and K_{aniso} may also be associated with synaptic remodeling.

Increasing K_{iso} for concussed females at the chronic timepoint (5-months post-mTBI) may be related to the infiltration of glial cells and/or differentiation and maturation of oligodendrocytes, as increased K_{iso} reflects increased cell size and density heterogeneity (21,184). These mechanisms may arise as a chronic response to the initial injury or from delayed normal brain maturation after the injury. Specifically, in the internal capsule, the gradually increasing total kurtosis over time in sham females compared to the chronic (delayed) increase in total kurtosis in concussed females may indicate delayed normal brain development after injury.

The increase observed in MTR and MTsat in concussed females may be a combined effect of myelin remodeling (360), as a response to impaired synaptic plasticity and myelin abnormalities, and remyelination, which may be forms of plasticity after mTBI (361). In a weight drop model of mTBI in rats, Tu et al. observed significantly reduced MTR at 10 days post-mTBI, related to demyelination, which resolved by 20 days post-mTBI (247). In our milder model of mTBI, demyelination may not be triggered, or demyelination may occur at acute timepoints that were not included in our analysis. In a controlled cortical impact model in mice, with the brain being directly impacted, histologically evaluated demyelination was reported from 7 days to 3 months post-injury

and electron microscopy revealed various myelin sheath abnormalities within the corpus callosum at 3 months post-mTBI (362). Mouse models of single impact closed skull mTBI have demonstrated demyelination that is associated with evidence of remyelination, including oligodendrocyte progenitor cell proliferation and generation of new oligodendrocytes (101,107). In one of these models, Mierzwa et al. (101) reported that the frequency of demyelinated intact axons did not correlate with the presence of degenerating axons, which suggests that myelin remodeling can occur along intact axons through demyelination and remyelination. So, demyelination can occur without the presence of neurodegeneration. This phenomenon may explain our results as we observe an increase in MTR and MTsat, which indicates myelin remodeling and/or remyelination, but no evidence of neurodegeneration. In a contact sports concussion study, myelin water fraction (MWF), another MR measure of myelin content, was found to be increased in the brains of players compared with the brains of controls, suggesting acute/chronic MWF alterations in players from previous injuries (363). Increases in MWF were also demonstrated in the brains of players 3 months after the players sustained an mTBI. The full clinical significance of increased myelin and whether this reflects axon neuropathology or disorderly remyelination leading to hypermyelination has yet to be determined.

In a juvenile rat mTBI model, the dentate gyrus region of the hippocampus in females showed a significant reduction in synaptic plasticity (as investigated with electrophysiology) at 1 day, which persisted to 28 days following injury (350). In male rats, the deficit was maximal in hippocampal subfields 7 days post-injury; however, these deficits did not persist to 28 days post-injury. These data indicate that mTBI can produce

more immediate and persistent impairments in synaptic plasticity in the female brain. The cellular and molecular mechanisms underlying the mTBI-induced synaptic plasticity deficits are yet to be fully elucidated. There are many possible mechanisms that may contribute to the observed impaired synaptic plasticity, including acute and chronic inflammatory processes, decreases in blood–brain barrier integrity (364), dendritic spine remodeling (365), and changes in metabolic pathways (69).

5.4.3   Brain Region-Specific Notes

Interestingly, the only white matter tract with MTR/MTsat changes is the cerebral peduncle (CP). This tract is positioned anterior-posterior in the mouse brain, and thus may undergo more axonal stretching and shearing than the corpus callosum (CC) and internal capsule (IC) during the rotational acceleration of the CHI-RF model. The olfactory region (OLF) is the only region with significant post hoc pairwise comparisons in the whole group analysis. Although olfactory dysfunction is one of the most common symptoms in TBI patients and often an early signal for neurodegenerative disorders (366–368), there are very few studies that show the association between olfactory dysfunction and mTBI. A repetitive mTBI model showed a significant change of olfactory dysfunction-related behaviors in injured compared to control mice, as well as axonal damage in olfactory-bulb-associated areas 5 days post-mTBI (369). The prefrontal cortex (PFC) region includes the site of injury and thus changes are expected in this region. The hippocampus shows changes in all tensor-valued and MT metrics in concussed females. The hippocampus is particularly vulnerable to brain injury, with demonstrable neuronal degeneration (370,371). Previous work showed that demyelination in the hippocampus and associated spatial learning impairments peaked between 1 and 2 weeks after m TBI

(372), which may be why we are not observing a decrease in MT metrics 1-month post-injury in the hippocampus.

5.4.4   Sexual Dimorphism in mTBI Response

Overall, sex dependent changes observed here suggest either a chronic response to mTBI or delayed development in female concussed mice, while the male concussed mice do not exhibit a response. Females remain underrepresented in mTBI research, where fewer women than men are recruited to clinical trials and male rodents have predominantly been used as an experimental injury model (373). The sexually dimorphic findings identified here suggest more research into sex-dependent changes post-mTBI are needed. In a recent review on sex differences in TBI, Gupte et al. (373) found that most human studies report worse outcomes in women than men, whereas most animal studies report better outcomes in females than males. However, closer examination shows that multiple factors including injury severity, sample size, and experimental injury model may differentially interact with sex to affect TBI outcomes. Interestingly, in humans, most mTBI studies reported worse outcomes for females, whereas most moderate/severe TBI studies reported better outcomes for females. Among animal studies of mTBI, only 17% showed better outcomes in females than males, whereas in moderate/severe TBI a larger proportion (55%) showed better outcomes in females.

One of the most compelling and widely studied hypotheses of the cause of sex differences in TBI is that the injury response is modulated by sex hormones, as recently reviewed by Spani et al. (374). Whereas women experience cyclic production of estrogen and progesterone until menopause, testosterone production in men declines incrementally over time and is markedly reduced in older men. Whether better outcomes in female

animals are due to the neuroprotective effects of estrogen and/or progesterone has been extensively examined, with studies indicating that estradiol can produce quite favorable results in treating the central nervous system injuries in animal models (375,376).

There are also structural differences between sexes that may give rise to sex-dependent differences in injury response. At the ultrastructural level, axons of cultured neurons isolated from females were consistently smaller and contained fewer microtubules than those from males (377). This finding is also corroborated by electron microscopy analysis of the rat corpus callosum showing female axon diameters to be smaller than male axons (378,379), and by axon diameter mapping using diffusion MRI showing female mean axon diameters within the human corpus callosum to be smaller than male axons (380). Interestingly, it has even been speculated that this size difference may be due to greater number of microtubules in male axons than female axons (381). Also, following a stretch-induced injury *in vitro*, axons from females exhibited greater swelling and loss of calcium signaling compared with those from males (377). Mechanical vulnerability to dynamic injuries may be increased for smaller axons on average. This has precedence in animal models of TBI, where white matter axons with smaller diameters have been shown to undergo more acute dysfunction, slower recovery of function and/or greater degeneration than large diameter axons (382). Thus, under the same level of mechanical loading during head impact, axons in female brains may be more susceptible to damage than axons in male brains due to fundamental differences in axon ultrastructure.

Another factor that may give rise to sex-dependent differences is neck musculature (383). The male mice in this study were noticeably larger in size than their

female counterparts, with visibly larger neck girth. Nutt et al. (384) reported that male rugby athletes who self-reported higher rates of a previous concussion demonstrated greater strength imbalances of their neck musculature. Males also had stronger neck musculature compared to age-matched females, with these strength differences becoming increasingly significant with age. Recent research has demonstrated that linear and rotational head acceleration, as well as the magnitude of force upon impact, is influenced by neck biomechanics, and increased neck strength and girth are associated with reduced linear and rotational head acceleration during impact (385). Thus, the lower neck strength and girth of female mice in this study may cause increased linear and rotational head acceleration and thus greater observed changes post-mTBI.

5.4.5   Limitations

This study is not without its limitations and has many avenues for improvement. Scanning of sham and concussed cohorts was not interleaved. All sham mice were scanned first, and all concussed mice were scanned the following year due to delays in procuring a cortical impactor associated with the COVID-19 pandemic. This may have resulted in slightly different genomes between the sham and concussed mice, although all mice were acquired from the same vendor. Also, as the whole group analysis did not show significant group effects in DTI metrics, except for RD, between sham and concussed cohorts, and there is no evidence of axon loss, our CHI-RF model may have been too mild. In repeated mTBI models, reduced FA and increased RD was found 1-month post-injury in the corpus callosum (25,217). In a more severe single mTBI model, elevated RD and MD, and reduced FA, was reported at 1-month post-injury in the corpus callosum (137). It is likely that due to our model being too mild, we are not sensitive to

group by time effects in RD, and group effects in other DTI metrics. Ideally, our impact should be strong enough to elicit a response from the male mice as well, to allow for a more comprehensive investigation of sex-dependent differences. Due to neuromodulatory effects of anesthesia (337) potentially confounding results in the acute stage, at 2 days and 1-week post-mTBI, and the focus of our work on brain maturation, we did not include acute stage data in our analysis here. Anesthesia may confound both behavioral measures and the biochemical dynamics of the injury cascade and is a major caveat in mTBI research (330). Future closed head mTBI models can consider delivering impacts to unanesthetized animals, as has been demonstrated in a mouse study (367). Imaging without the use of anesthesia can also be considered by habituating mice to awake MRI, as recently demonstrated (386). Studies designed to specifically disentangle anesthetic effects is an important area for future research. It is also important to note that the developmental trajectory described here is for wild type C57Bl/6 mice and may be altered in other mouse lines. Other mouse lines, such as transgenic mice carrying humanized wildtype microtubule-associated protein tau (387) and amyloid precursor protein (388), would also result in greater translatability to humans. Future work should include investigating more timepoints in the acute and chronic stage for a comprehensive view of the time course of MR metric evolution after injury. Application of mTBI at different mouse ages including in juvenile and aged mice would help elucidate how mTBIs impact younger and aged populations, as most mTBI research is focused on adults. In a recent study in juvenile male mice, mTBI led to significant region-specific DTI microstructural alterations, distant from the site of impact, that correlated with

cognitive and spatial memory impairments at 12 months after a single concussive injury (389).

There are also several technical limitations to consider in this study. Although our MTsat protocol improves myelin specificity compared to MTR, a more recent technique, inhomogeneous magnetization transfer (ihMT), may be better suited for our study. ihMT, which was developed based on MT MRI, is more specific to myelin than MTsat, due to its direct sensitivity to the phospholipids in myelin. For our frequency-dependent dMRI protocol, our highest OGSE frequency (190 Hz) was determined by hardware constraints, and reaching even higher frequencies would allow us to probe smaller spatial scales. This may have limited our frequency-dependent dMRI findings here. In our tensor-valued dMRI protocol, we do not consider microscopic kurtosis (μK), which is another source of total kurtosis and ignoring it can impact the accuracy of other kurtosis sources (323). μK is the weighted sum of different microscopic sources of non-Gaussian diffusion, which include restricted diffusion inside compartments, microstructural disorder due to the presence of microscopic hindrances to water molecules (such as membranes and axon caliber variations), and exchange between components (164,238). Recently, μK was shown to be a primary driver of total kurtosis upon ischemia in mice (322) and was mapped in human brain tissue for the first time (323), revealing that this component is non-negligible.

5.5   CONCLUSION

In this study, we investigated mouse brain concussion recovery at subacute and chronic timepoints after a single closed head impact with rotational force, utilizing frequency-dependent and tensor-valued dMRI and MT MRI. We demonstrate that tensor-

valued dMRI and MT metrics are more sensitive to microstructural changes in the subacute and chronic stages following mTBI, compared to DTI. We hope the sexually dimorphic pattern of response identified here will motivate more research in sex-dependent changes after mTBI.

Chapter 6

6   Conclusions

While each Chapter of this thesis describes chapter-specific limitations, there are several broad limitations that affected most of the work. Following the discussion of limitations, the overall conclusions, future directions, and impact of the thesis will be discussed.

6.1   Limitations and Suggestions

6.1.1   Anesthetic Effects

The neuromodulatory effects of anesthesia (337,338) could have potentially confounded our results, but all scans analyzed in Chapters 4 and 5 were acquired at least 1 month after the last anesthesia session, which gave time for recovery. Notably, acute timepoints (2 days and 1-week) were not included in the analysis in Chapters 4/5, but evidence of parameter changes in the sham cohort at acute time-points is present, as depicted in Figure 6.1 in the cerebral peduncle, as an example. Although anesthesia can result in negative effects during development, such as apoptotic neurodegeneration, deficits in hippocampal synaptic functions, and persistent behavioral and cognitive impairments (337,338), few studies have investigated neural and behavioral deficits that may extend into adulthood (390,391). In a DTI mTBI study, Hoogenboom et al. observed considerable DTI changes in sham animals between baseline and 48 hours post-sham procedure (339), which was the most anesthesia-intense timeframe in the study. In a repeated isoflurane study in mice, behavioral deficits and reduced axial diffusivity in the corpus callosum were found up to 90 days after isoflurane exposure (340). Repeated

isoflurane anesthesia exposure impacted burrowing behavior and reduced exploratory behavior in adult mice, though these differences became negligible 8 days after anesthesia (392). Lindhardt et al. applied diffusion kurtosis imaging in awake and sedated mice for a single imaging session and demonstrated MR metric modulations between the cohorts (393).

Our study was not designed to disentangle anesthetic effects. Future closed head mTBI models can consider delivering impacts to unanesthetized animals, as has been demonstrated in a mouse study (367). Imaging without the use of anesthesia can also be considered by habituating mice to awake MRI, as recently demonstrated (386). Studies designed to specifically disentangle anesthetic effects is an important area for future research, to better understand to what degree sedation affects the MR signal and the acute and chronic implications. A study focused on disentangling anesthetic effects can include two cohorts of mice, an awake mouse cohort (unanesthetized) and an anesthetized mouse cohort, imaged longitudinally to identify acute and chronic effects of anesthesia applied during imaging. Furthermore, investigating various doses of anesthesia would help elucidate how the dosage relates to microstructural alterations.
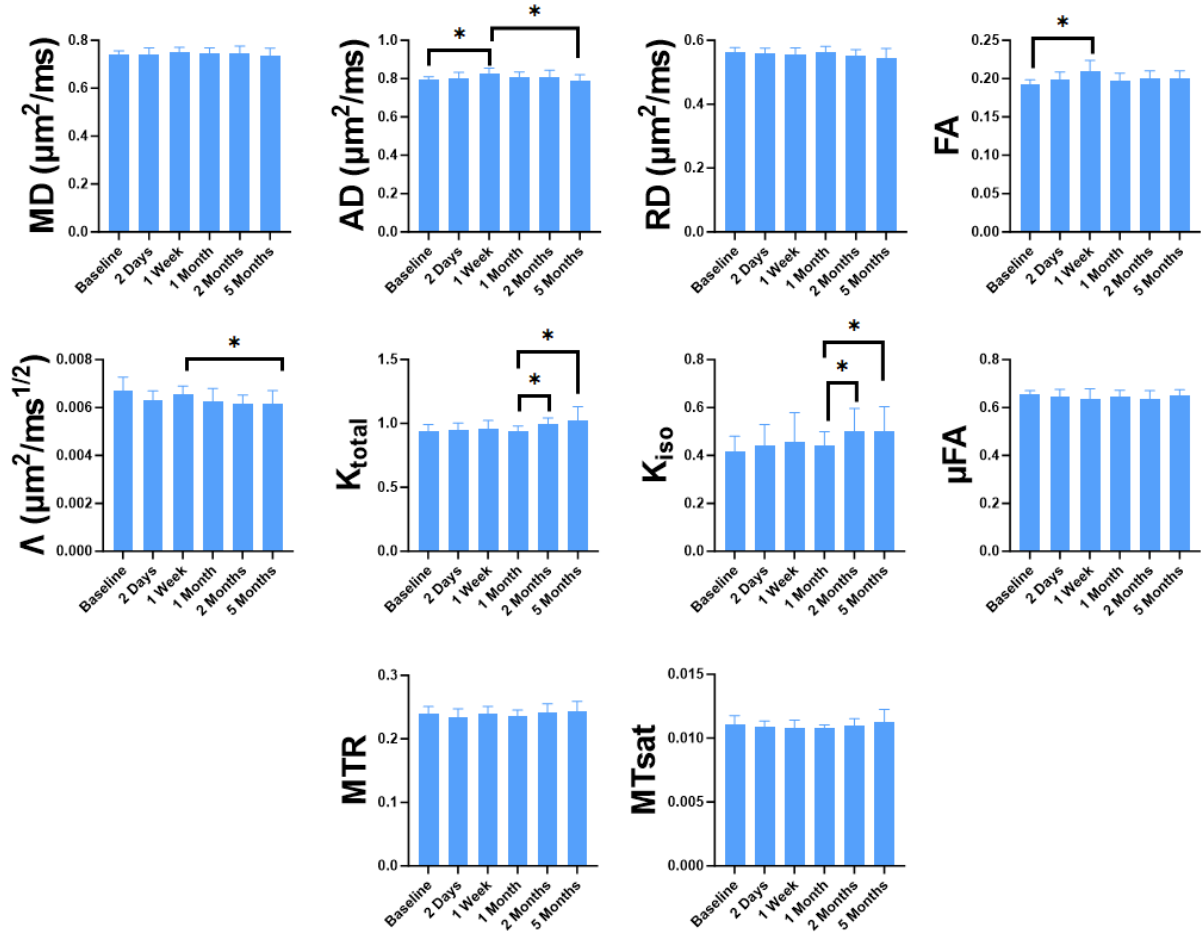
Figure 6.1 - *Quantitative MRI parameters in the sham cohort in the cerebral peduncle (a white matter tract). Data represents mean values and error bars represent the standard deviation over all mice in the cohort. At acute timepoints, an increase in AD and FA is observed after repeated measures ANOVA. Asterisks represent statistically significant differences between timepoints (* p < 0.05).*

6.1.2   Imaging Timepoints

Although healthy brain maturation was assessed over a period of 5 months (Chapter 4) and concussion recovery was assessed at both subacute and chronic stages (Chapter 5), evaluating more timepoints would provide a more comprehensive view of

MR metric evolution. In healthy mice (Chapter 4), imaging at more timepoints during developing, maturing, and ageing periods would give us a picture of the entire mouse lifespan. This may help us identify more contrast mechanisms driving changes in MR metrics and the results would be applicable to a wider range of preclinical research in mice. In the mTBI study (Chapter 5), adding more chronic timepoints would allow us to identify when and if the MR metrics normalize, as the present study did not show normalization of tensor-valued dMRI and MT metrics in concussed females by the last imaging timepoint. This suggests that there are still ongoing microstructural changes, due to mTBI, occurring after the last imaging timepoint.

6.1.3   Sex-Dependent Analysis

Although the reproducibility and sample sizes required for the MR metrics used in this thesis were characterized in Chapters 2 and 3, a greater sample size would be beneficial for sex-dependent analysis, increasing the power to disentangle sex-dependent effects. Including other sex-dependent factors in the study would have facilitated our understanding of the causes of the sexually dimorphic MR metric evolution observed in Chapters 4 and 5. One example is the measurement of sex hormone levels to explore whether differences in hormone levels correlated with differences in imaging results. Future animal studies of sex differences in TBI should also consider the potential for hidden confounds, such as differential response to anesthetics, sex differences in body and/or skull size, and sex differences in motivation to perform behavioral tasks (373).

6.2   Conclusions

Although concussion has become a significant public health concern, current clinical neuroimaging techniques lack the sensitivity and specificity required to reliably detect signs of concussion, as large-scale changes are absent (22). This results in an inability to predict who will recover completely, who will have long-term impairments, or when it is safe to return to play in contact sports. Diffusion tensor imaging has arguably had the greatest influence to-date of neuroimaging modalities in mTBI (330), but previous studies have reported inconsistent DTI findings across studies (22), as standard diffusion MRI lacks the specificity to identify unique microstructural environments (e.g., cannot distinguish between loss of structural integrity and fiber orientation) and represents and inherently vague and limited model of neuroanatomy (8). This thesis explores the application of microstructural MR methods, that go beyond DTI to improve sensitivity and specificity, to a preclinical model of mTBI and adult brain maturation. This work characterizes the reproducibility of the microstructural MR metrics applied, establishes that these metrics are capable of detecting microstructural changes throughout adult mouse brain maturation and concussion recovery, and represents the first application of these advanced MR techniques in either healthy brain aging or mTBI.

Chapters 2 and 3 present test-retest reproducibility studies of advanced diffusion MRI and magnetization transfer MRI metrics, respectively. Both chapters describe the implementation of the MRI methods used in this thesis, characterize both ROI-based and voxel-wise test-retest reproducibility of the *in vivo* MRI metrics, and report sample sizes required to detect a variety of effect sizes. This is the first test-retest assessment of these advanced MR protocols at ultra-high field strength, which will be useful in planning

future preclinical neuroimaging studies involving models of disease/injury. Presented in Chapter 2, most of the tensor-valued dMRI metrics are reproducible in both ROI-based and voxel-wise analysis, while the frequency-dependent dMRI metrics are only reproducible in ROI-based analysis. ROI-based coefficients of variation (CVs) revealed high reproducibility for most metrics (CVs < 15%), while voxel-wise CV maps revealed high reproducibility for tensor-valued metrics (CVs ~ 10%), but low reproducibility for frequency-dependent metrics (CVs ~ 50%). Given feasible sample sizes (10 - 15), tensor-valued and frequency-dependent dMRI metrics may provide sensitivity to subtle microstructural changes (4 - 8%) and moderate changes (> 6%), respectively. Presented in Chapter 3, MTR and MTsat were reproducible in both ROI-based and voxel-wise analysis. MTsat exhibited comparable reproducibility to MTR and could detect small changes (< 10%) with sample sizes of 15–20, while providing better contrast and maintaining a feasible scan time.

Research investigating healthy rodent brain maturation remains limited, which warrants further study of normal brain maturation in rodents to exclude confounds of developmental changes from interpretations of disease mechanisms. Chapter 4 investigates healthy rodent brain maturation in mice scanned longitudinally at 3, 4, 5, and 8 months of age, and provides a discussion of what the evolution of MR metrics suggests on a neurobiological level. This work shows that there are continuing microstructural changes in the brain, even after 3 months of age, when mice are considered adults. The linear and quadratic fits observed over time are comparable to previous studies in both humans (24,38,286,287,289–293) and rodents (125), investigating DTI, DKI, and myelin-specific metrics. In a human lifespan study, peak age calculated with the quadratic model

revealed peak ages in the range of 30-50 years depending on brain region and metric (290). 30 human years is equivalent to about 6 mouse months and 50 human years is equivalent to about 15 mouse months (312). This is consistent with our results, as we start to observe peaks around the 5-6 month timepoint. Most DTI studies indicate a U-shaped relationship between the diffusivity metrics and age in most ROIs, with FA exhibiting an inverted U-shaped relationship. An inverted U-shape trend of myelin-specific metrics with age has been reported (286,287,290,313–315), and this quadratic association is attributed to the process of myelination from youth through middle age, followed by demyelination in later years.

Overall, the trends observed in conventional dMRI and MT metrics are comparable to previous studies on normal brain development (23,24,38), while the trajectories of our more advanced dMRI metrics provide novel insight. Particularly, total kurtosis increases over time were driven by increases in isotropic kurtosis, which may be related to glial cell diversification and/or oligodendrocyte differentiation and maturation. Based on the developmental trajectories of tensor-valued dMRI and MT metrics, our results suggest myelination during brain maturation is not a main contributor to microscopic diffusion anisotropy and anisotropic kurtosis in axons. Through this work, for studies that only calculate total kurtosis, we suggest caution in attributing neurobiological changes to changes in total kurtosis as we show constant anisotropic kurtosis in the presence of increasing myelin content. These findings can be translated to understanding human brain maturation as well. As K_{iso} and K_{aniso} have not been explored in the context of human brain maturation, and our observed K_{total} shows similar trends to human brain maturation, it is likely that K_{iso} and K_{aniso} in the human brain may follow the

same trajectory that we observe here, and our interpretations for the increase in isotropic kurtosis can likely be extrapolated to humans.

Chapter 5 explores the evolution of microstructural MR metrics in a closed head, single impact, mouse model of concussion at 1-month, 2-months, and 5-months post-mTBI. Tensor-valued dMRI and MT metrics exhibited greater sensitivity to microstructural changes in the subacute and chronic stages following mTBI, compared to DTI, with a chronic increase in tensor-valued metrics and a more gradual increase in MT metrics in concussed females. These changes suggest delayed normal brain development and/or myelin and synaptic remodeling as forms of brain plasticity in concussed females. The sexually dimorphic pattern of response identified here motivates more research in sex-dependent changes after mTBI, as females remain underrepresented in both clinical and preclinical mTBI research.

6.3   Future Directions

Future studies should consider application of mTBI at different mouse ages including in juvenile and aged mice, which would help characterize the time-course of injury response in younger and aged populations, as most mTBI research is focused on adults. In a recent study in juvenile male mice, DTI alterations, distant from the site of impact, correlated with cognitive and spatial memory impairments, even at 12 months after a single concussive injury (389). Future studies would benefit from quantitative histological analysis that can be correlated with MR results to accurately identify the contract mechanisms underlying the MR changes. Specifically, histological analysis can be performed for glial cells (oligodendrocytes, microglia, and astrocytes), myelin content, and axonal beading and injury. Additionally, our institute has recently acquired a light

sheet microscope which facilitates acquisition of whole mouse brain 3D images. Histological images acquired in this format can also be more readily registered to their MR counterparts to ensure the same ROIs are investigated in histology and MRI (394). Performing Monte Carlo simulations of diffusion (20,356) to reflect the biophysical alterations hypothesized in this thesis would also help verify or contradict our hypotheses and elucidate what is contributing to dMRI contrast. Harnessing biophysical multi-compartment modeling in dMRI is another avenue for future research, as biophysical models possess greater specificity through access to more meaningful and specific parameters of the tissue microstructure, such as neurite fraction (395). For example, the CODIVIDE (constrained diffusional variance decomposition) model can be applied to tensor-valued dMRI data (396). Additionally, as tensor-valued diffusion MRI can be applied in clinical scanners in under 3 minutes (12,184), the changes observed in tensor-valued metrics in this thesis motivate the application of this method in investigations of clinical mTBI.

As both our brain maturation and concussion recovery studies reveal increases in isotropic kurtosis, which is a measure of cell size/density heterogeneity, isotropic kurtosis can be leveraged to evaluate disease models where changes to cell size/density are expected. K_{iso} would be a strong candidate to evaluate brain tumour models, where changes in cell size and density are substantial. K_{iso} has previously been mapped in brain tumours as a proof-of-concept (21) but has not been used to explore the detection of brain tumour progression and differentiation. As glial cell loss may be a feature of schizophrenia (397) and have significant roles in the progression of Alzheimer's disease (398), K_{iso} can be utilized to non-invasively characterize the changes to glial cells in these

models. K_{iso} can also be applied to models of demyelination and remyelination to further investigate the sensitivity of K_{iso} to oligodendrocyte differentiation and maturation. Increased K_{iso} was reported in LPC (L-α-Lysophosphatidylcholine) treated regions in the mouse brain, which introduces focal demyelination (399). The increased K_{iso} was hypothesized to be due to repopulation of mature oligodendrocytes by oligodendrocyte progenitor cells. However, this study did not include histological analysis, which would verify the hypotheses for K_{iso} changes in future studies. Exploring the time-dependence of K_{iso} is an interesting avenue for future research, as it may provide new insight and capture contrast from smaller cells.

In Chapter 5, no behavioral measures were acquired to determine if the injury model used did in fact produce an mTBI, although preliminary histological analysis did show diffuse axonal damage at 2-days post-injury. The varied responses on an individual level could possibly be explained in part by behavioral analysis of the subjects. Behavioral sex-dependent analysis correlated with MR results would also provide a window into the sex-dependent functional outcomes associated with underlying microstructural brain changes. While the controlled cortical impact was landmarked and standardized for each mTBI in this thesis, no metrics were obtained quantifying kinematic properties such as rotation and translation of the head. Although kinematic analysis was done on different mice during the development of this injury model (400), this analysis was not done on the mice used in this study. Performing kinematic analysis and imaging on the same mice would allow us to correlate the strain experienced in different regions of the brain to the changes in MR parameters. Finally, the concussion injury may have been too mild, as males did not show any changes with DTI metrics or advanced dMRI methods, females only had

detectable changes with advanced dMRI methods. Future work would benefit from a stronger model (while verifying that gross anatomical changes are not present) to elicit detectable changes with microstructural MR methods to better understand the contrast mechanisms of these advanced metrics and non-invasively characterize the time-course post-injury.

The mouse brain maturation study in this thesis inspires the concept of stratification based on 'brain age' for neuroscience experiments, as there is variability in the time that individual subjects reach their peak and in the trajectory of MR metrics for each subject. This grouping can differ for males and females, as this work shows evidence for different trajectories for both sexes. Thus, a possible outlook for future neuroscience research may be grouping subjects based on 'brain age,' instead of actual age in years, which may present a more accurate means of studying brain injury, disease, development, and aging. This grouping idea is similar to grouping children based on growth charts for height and weight (401). Stratification based on 'brain age' can be defined with access to very large datasets, to study brain development in early childhood (402,403), and throughout the human lifespan with the LIFESPAN dataset which pools together data from ages 3 – 96 (283), the brain chart resource which aggregates data from over 100,000 participants and is an interactive open resource to benchmark brain morphology derived from future samples as well (284), and the Human Connectome Project with multiple aging and development datasets (404), to name a few. Brain charts are an essential step towards robust quantification of individual variation benchmarked to normative trajectories, and thus identifying early deviations from normative trajectories, which may lead to neuropathology such as dementia.

6.4   Clinical Relevance

Along with diffusion MRI research, imaging studies have also investigated changes in blood flow (arterial spin labeling MRI) (405), neuroinflammation (PET) (406), connectivity (functional MRI) (407), metabolic activity (MRS) (408) after concussion, and changes have been identified in all these metrics, but clinical translation is still limited. We are now at a point in concussion research where it is imperative that we start using results from different imaging metrics, together, to interpret and understand what is happening after concussion, and why. Thus, it is critical to continue paving the path to clinical translation for more advanced imaging techniques. With a better understanding of these mechanisms, therapies can be optimized. For example, MRS provides a way to measure the chemical content of MR-visible nuclei, allowing for evaluation of brain metabolism and the biochemical pathways involved, but cannot interrogate changes in microstructure that altered brain metabolism can lead to. Harnessing microstructural MRI along with MRS can provide a more comprehensive view of altered brain metabolism and the resulting microstructural changes, and vice versa.

By longitudinally tracking changes in brain microstructure post-concussion, animal studies can shed light on the long-term effects of concussive injuries. Understanding the chronic consequences of concussion is crucial for implementing appropriate follow-up care and rehabilitation strategies. The findings in Chapter 5 point to delayed normal brain development and/or myelin and synaptic remodeling as forms of brain plasticity in concussed females, detectable even 5 months post-mTBI, elicited by possibly one of the mildest cortical impacts in the literature. This work identifies tensor-

valued dMRI and myelin-sensitive MRI as promising candidates for mTBI diagnosis and prognosis in the clinic. Both tensor-valued dMRI and myelin-sensitive MRI have been applied before in clinical populations (354,409,410) and are clinically feasible. Applying these microstructural MR techniques in human mTBI may help provide evidence for the period of rest required for brain recovery, which will be a better indicator of patient recovery than the currently used marker of symptom recovery.

Multi-modal neuroimaging techniques can provide a wealth of information about complex features that contribute to underlying neurobiological processes. Through strong inter-disciplinary collaborations, this avenue of research could be used to quantitatively monitor and stratify neurological phenotypes, develop diagnostic and prognostic biomarkers of neuronal integrity and health, and optimize neuroplasticity and potential recovery strategies. Moreover, as the medical field shifts towards personalized medicine, there should be a parallel shift towards real-time patient specific data analysis, using microstructural MRI and other imaging modalities, allowing for more evidence-based and personalized concussion management protocols and treatment options.

6.5   Significance and Impact

Overall, this thesis explores the capabilities of microstructural MRI in a preclinical model of mTBI and healthy brain maturation, advancing our understanding of the contrast mechanisms of microstructural MRI metrics and the evolution of these metrics during brain maturation and concussion recovery. This thesis characterizes the reproducibility of the microstructural MR metrics applied and provides preclinical sample sizes required to detect relevant effect sizes, which had not been done before at an ultra-

high field strength. This work will inform future preclinical investigations of neuronal health, disease, and injury using these MR metrics. This thesis reinforces that there are continuing microstructural changes in the brain, even after 3 months of age, when mice are considered adults. We observe for the first time that total kurtosis increases over time are driven by increases in isotropic kurtosis during brain maturation, which may be related to glial cell diversification and/or oligodendrocyte differentiation and maturation. Through this work, for studies that only calculate total kurtosis, we suggest caution in attributing neurobiological changes to changes in total kurtosis as we show constant anisotropic kurtosis in the presence of increasing myelin content. We provide for the first time, *in vivo* evidence of changes post-mTBI detectable with microstructural MR methods in subacute and chronic stages, while the standard DTI metrics did not show changes. The sexually dimorphic patterns observed in this thesis, both during brain maturation and concussion recovery, may motivate more sex-dependent mTBI research, as females remain underrepresented in mTBI research. This thesis indicates that these microstructural MR techniques have potential to be further optimized and applied to better understand concussion neuropathology and its time-course, and to be further applied in clinical settings to study human mTBI.

Appendices

Appendix A: A longitudinal microstructural MRI dataset in healthy C57Bl/6 mice at 9.4 Tesla

This Appendix was published in *Scientific Data,* volume 10, Rahman *et al.*, ***A longitudinal microstructural MRI dataset in healthy C57Bl/6 mice at 9.4 Tesla*** (295), Copyright CC-BY, 2023.

Background & Summary

Multimodal microstructural MRI has shown increased sensitivity and specificity to microstructural changes in various brain disease and injury models in the preclinical setting. Here, we present an *in vivo* longitudinal imaging dataset in the healthy mouse brain, which includes structural T2-weighted, magnetization transfer (MT), and advanced diffusion MRI (dMRI) data. There were no hardware or software changes during data acquisition, and all protocols for a single timepoint in each mouse were acquired in the same session. Each of 12 C57Bl/6 mice were scanned at 6 different timepoints, between 3 - 8 months of age (Figure A.1). Importantly, this dataset provides imaging data in the same mice over time, which provides greater statistical power compared to cross-sectional studies, to detect changes in brain maturation, as myelination continues to increase between three and six months (23).
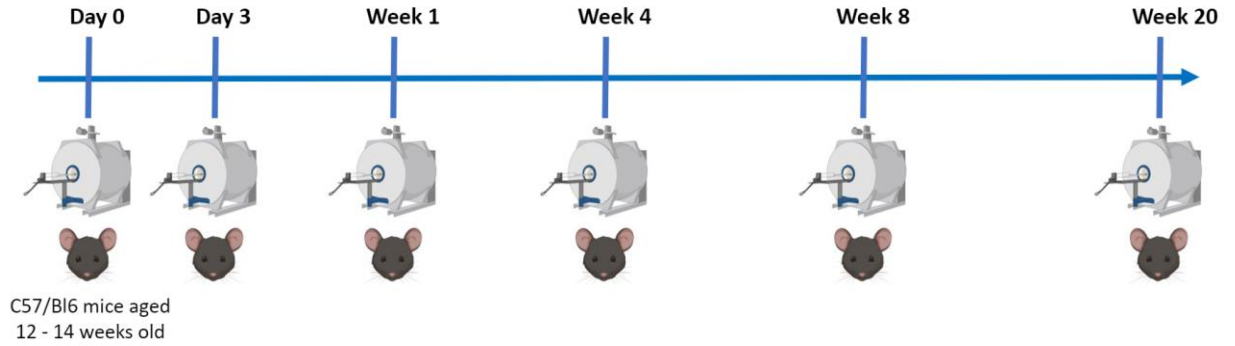
Figure A.1 - *Overview of study design. At Day 0, all mice were 12 – 14 weeks old. Each C57Bl/6 mouse (n = 12, six males and six females) was scanned at 6 different timepoints, comprising a total of 72 MRI sessions. After Week 20, four of the mice (two males and two females) underwent ex vivo imaging.*

We envision utility of this dataset in the microstructural MRI field to develop and test methods that model temporal brain dynamics, registration and preprocessing pipelines, and biophysical models of brain microstructure. Sex and age-dependent differences can be investigated, as the dataset includes an equal number of male and female age-matched mice. *In vivo* to *ex vivo* changes, arising from perfusion and fixation processes, can be explored, as a subset of *ex vivo* data has been included. The data were acquired with the goals of forming a control dataset and investigating microstructural changes in the healthy mouse brain. Analysis of test-retest reproducibility of the MRI metrics, using a subset of the data, have been published elsewhere (181,239). To optimize potential applications of this dataset, we provide dMRI pulse sequences and protocols, source data (DICOM format), code to process source data, unprocessed and preprocessed data (NIFTI format), and quantitative MRI metric maps. We have made this dataset publicly available as other groups may not have access to all resources required to

undertake a longitudinal MRI study. This includes hardware, software (specifically custom pulse sequences to implement advanced dMRI protocols), and time/personnel required. MT imaging has been used extensively to investigate changes in myelin content and integrity (153,240). The MT imaging protocol applied here enables computation of the widely used MT ratio (MTR), and the more recently developed MT saturation index (MTsat) (14). As MTR is confounded by T1 effects, flip angle inhomogeneities, and choice of sequence parameters, MTsat was developed to reduce T1 dependence and improve specificity to myelin, while maintaining a feasible scan time. MTsat shows higher white matter contrast in the brain than MTR (14,239), and has been shown to correlate more with disability metrics than MTR in patients with multiple sclerosis (18).

Developing advanced dMRI techniques, beyond the conventional diffusion tensor imaging (DTI) model, is currently of broad interest, as DTI lacks the specificity to identify unique microstructural environments (8). The advanced dMRI methods applied here include oscillating gradient spin echo (OGSE) dMRI (9,170), implemented by varying the oscillating gradient frequency, and microscopic anisotropy (μA) dMRI (12,141,189,193), implemented via tensor valued diffusion encoding. In addition to advanced dMRI metrics, traditional DTI metrics are also provided. OGSE dMRI provides additional insight, compared to conventional dMRI, by increasing sensitivity to smaller spatial scales. This is a robust dataset to explore the frequency dependence of OGSE dMRI metrics, which may provide insight into the relevant mesoscopic structures affecting water diffusion (178). Evidence of a linear dependence of mean diffusivity on the square root of OGSE frequency has been demonstrated in healthy and globally ischaemic rodent brain tissue (169) and in healthy human white matter (183). In contrast

to the widely used fractional anisotropy metric (FA) (8), which confounds true microstructural changes with fiber orientation dispersion, the microscopic anisotropy (µA) metric quantifies water diffusion anisotropy independent of orientation dispersion (141,184,185). Importantly, µA dMRI can provide estimates of cell shape (21,141,185–188,190,191). Additionally, diffusional kurtosis estimated from the µA protocol includes linear kurtosis (arising from the linear tensor encoding (LTE) acquisitions) and isotropic kurtosis (arising from the spherical tensor encoding (STE) acquisitions), which can be related to cell size heterogeneity (21).

As myelin is MR-invisible in diffusion-weighted scans, recent studies have applied both dMRI and MT methods for a more comprehensive view of microstructural changes (247,252,278). Thus, there may be interest in investigating longitudinal changes by jointly assessing MT and dMRI data, and additionally testing biophysical models using the combined OGSE, µA, and MT data.

Methods

Subjects

All animal procedures were approved by the University of Western Ontario Animal Care Committee and were consistent with guidelines established by the Canadian Council on Animal Care. Twelve adult C57Bl/6 mice (six male and six female) were scanned at six timepoints. They were between 12 - 14 weeks old at the first timepoint (Figure A.1). Before scanning, anesthesia was induced by placing the animals in an induction chamber with 4 % isoflurane and an oxygen flow rate of 1.5 L/min. Following induction, isoflurane was maintained during the imaging session at 1.8 % with an oxygen

flow rate of 1.5 L/min through a custom-built nose cone. At the end of the study, the mice were euthanized. The mice were anesthetized with ketamine/xylazine (2:1) and then underwent trans-cardiac perfusion with ice-cold saline, followed by 4% paraformaldehyde in phosphate-buffer saline (PBS).

In vivo MRI Acquisition

In vivo MRI experiments were performed on a 9.4 Tesla (T) Bruker small animal scanner, running ParaVision 6.0.1, equipped with a gradient coil set of 1 T/m strength (slew rate = 4100 T/m/s). A single channel transceive surface coil (20 mm x 25 mm), built in-house, was fixed in place directly above the mouse head to maximize signal-to-noise ratio (SNR). The mouse holder (which included ear bars and a bite bar), nose cone, and surface coil were fixed onto a support, which was placed into the scanner (Figure A.2a). This ensured consistent positioning of the mouse head in the scanner at each session. For all protocols, 30 slices, with a slice thickness of 400 µm (anatomical scans) or 500 µm (diffusion-weighted scans), were required for full brain acquisition. Anatomical images were acquired at each session for each subject using a T2-weighted TurboRARE sequence. A brief overview of the protocols is given in Table A-1.
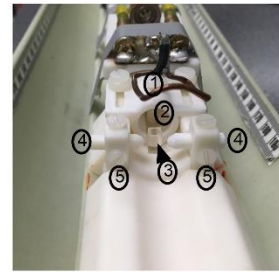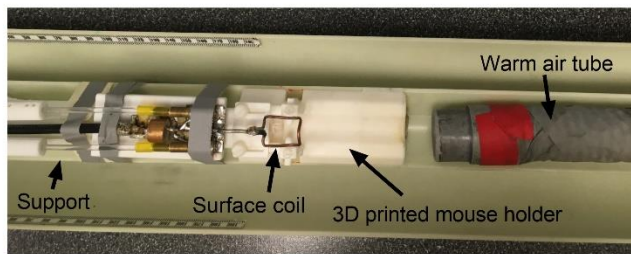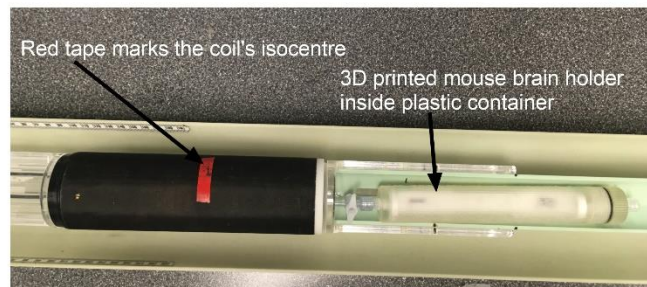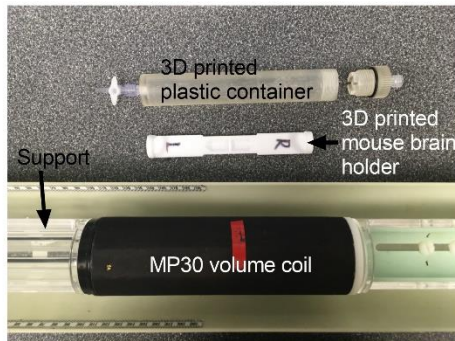
Figure A.2 - *Schematic of experimental setup for in vivo and ex vivo imaging sessions. a) In vivo setup showing the 3D printed mouse holder and surface coil securely attached to a support. The cross-section of the mouse holder depicts how the mouse is secured in place with a nose cone, bite bar, and ear bars. b) Ex vivo setup showing the 3D printed mouse brain holder, which can hold two extracted brains, and the 3D printed plastic container, which holds the mouse holder and is filled with Christo-lube. Both the mouse brain holder and container were custom designed to fit in the MP30 volume coil. The MP30 volume coil is securely attached to the support, with the isocenter marked in red.*

Table A-1: Brief sequence details for *in vivo* imaging. For a full list of parameters, the exported protocols are included in the repository.

Sequence	FoV (mm³)	Slice Thickness (μm)	In-plane Resolution (μm²)	TE/TR (ms)	α (°)	Averages	Scan Time (min.)	Notes	
T2 weighted TurboRARE	19.2x14.4x15	500	150x150	40/5000	90	16	22		
MT Imaging FLASH-3D	19.2x14.4x12	400	150x150	2.75/25	9	12	18	MT pulse on (MTw)	
	19.2x14.4x12	400	150x150	2.75/25	9	12	18	Reference PD-weighted scan (PDw) MT pulse off	
	19.2x14.4x12	400	150x150	2.75/8.5	20	12	6	Reference T1-weighted scan (T1w) MT pulse off	
	19.2x14.4x12	400	300x300	3/(TR_1 = 20, TR_2 = 100)	60	1	1	B1 map	
OGSE dMRI Single-shot EPI	19.2x14.4x15	500	175x200	39.2/10000	90	5	45	b-value (s/mm²)	# of directions
								0	10
								800	10
μA dMRI Single-shot EPI	19.2x14.4x15	500	175x200	26.8/10000	90	3	45	b-value (s/mm²)	# of directions
								0	8
								1000	12 LTE + 12 STE
								2000	30 LTE + 30 STE

OGSE and µA dMRI

Each dMRI protocol was acquired with single-shot spin echo echo-planar-imaging (EPI) readout with partial Fourier imaging in the phase encode direction with 80% of k-space being sampled. For each dMRI protocol, a single reverse phase encoded $b = 0$ s/mm^2 volume was acquired at the end of the diffusion sequence for subsequent use in TOPUP (218) and EDDY (219), from FMRIB Software Library (FSL, Oxford, UK) (225), to correct for susceptibility and eddy current induced distortions.

The OGSE dMRI protocol included a PGSE sequence (with gradient duration = 11 ms and diffusion time = 13.8 ms) and four OGSE sequences with oscillating gradient frequencies of 50 Hz, 100 Hz, 145 Hz, and 190 Hz at $b = 800$ s/mm^2 (10 directions for each frequency). The lowest OGSE frequency (50 Hz) uses the newly introduced frequency tuned bipolar (FTB) waveforms to reduce TE of the acquisition (297). The µA sequence was implemented with linear (LTE) and spherical tensor (STE) encodings, as shown in Table A-1, at $b = 2000$ s/mm^2 (30 directions for each of LTE and STE) and $b = 1000$ s/mm^2 (12 directions). Details about gradient waveforms and gradient modulation power spectra for the OGSE and µA protocols implemented here are presented in Rahman et al. (181).

MT Imaging

The MT protocol required 50 minutes total scan time and comprised three FLASH-3D (fast low angle shot) scans, and one RF transmit field (B1) map scan acquired using the actual flip-angle imaging (AFI) method (411) to correct for local variations in flip angle. An MT-weighted scan, and reference T1-weighted and PD-

weighted scans (MTw, T1w, and PDw respectively) were acquired by appropriate choice of the repetition time (TR) and the flip angle (α). MT-weighting was achieved by applying an off-resonance Gaussian-shaped RF pulse (12 ms duration, 385° nominal flip angle, 3.5 kHz frequency offset from water resonance, 5 µT RF peak amplitude) prior to the excitation.

Ex vivo MRI Acquisition

Ex vivo MRI experiments were performed on a subset of four mice (two male and two female) after the last *in vivo* scan. The mouse IDs of *ex vivo* data are: NR1_F (female), NR2_F (female), NR7_M (male), and NR8_M (male). NR1_F and NR2_F were scanned with the skull attached to the brain to minimize chances of tissue deformation, while NR7_M and NR8_M were scanned with the skull removed.

Ex vivo imaging was also performed on the 9.4 Tesla (T) Bruker small animal scanner, running ParaVision 6.0.1, equipped with a gradient coil set of 1 T/m strength (slew rate = 4100 T/m/s). A 3D printed mouse brain holder, holding two mouse brains at a time, was placed into a 3D printed plastic container and submerged with lubricant (Christo-lube MCG 1009; Engineered Custom Lubricants) to avoid magnetic susceptibility-related distortion artifacts (Figure A.2b). The mouse brain holder and container were custom designed to fit in the MP30 volume coil. The container was then slid into the volume coil (fixed on a support) and taped onto the support. The design of the mouse brain holder and container ensured that the mouse brain was positioned at the isocenter of the volume coil and the design of the support ensured consistent positioning of the mouse brain in the scanner at each session. For all protocols, 30 slices, with a slice

thickness of 400 µm (anatomical scans) or 500 µm (diffusion-weighted scans), were required for full brain acquisition. Anatomical images were acquired for each brain using a T2-weighted TurboRARE sequence. Due to field-of-view (FOV) constraints, one brain was imaged at a single session (although the mouse holder was designed to hold two brains). A brief overview of the protocols is given in Table A-2. The total *ex vivo* scan time for each brain was 15 hours.

Table A-2: Brief sequence details for *ex vivo* imaging. For a full list of parameters, the exported protocols are included in the repository.

Sequence	FoV (mm^3)	Slice Thick-ness (µm)	In-plane Resolution (µm^2)	TE/TR (ms)	α (°)	Averages	Scan Time	Notes	
T2 weighted TurboRARE	19.2x14.4x17.5	500	100x100	30/5000	90	48	1h12min		
MT Imaging FLASH-3D	19.2x14.4x12	400	100x100	3.06/30	9	36	1h42min	MT pulse on (MTw)	
	19.2x14.4x12	400	100x100	3.06/30	9	36	1h42min	Reference PD-weighted scan (PDw) MT pulse off	
	19.2x14.4x12	400	100x100	3.06/12	20	36	40min	Reference T1-weighted scan (T1w) MT pulse off	
	19.2x14.4x12	400	300x300	3/(TR$_1$ = 20, TR$_2$ = 100)	60	1	1 min	B1 map	
OGSE dMRI Multishot EPI	19.5x15x15	500	130x150	36.4/15000	90	14	6h25min	b-value (s/mm^2)	# of directions
								0	10

								1600	10
(2 segments)									
µA dMRI Multishot EPI (2 segments)	19.5x15x15	500	130x150	28.9/10000	90	10	3h34min	b-value (s/mm^2)	# of directions
								0	4
								1320	6 LTE + 6 STE
								2640	9 LTE + 9 STE
								4000	15 LTE + 15 STE

OGSE and µA dMRI

Each dMRI protocol was acquired with multi-shot spin echo echo-planar-imaging (EPI) readout with 2 shots and partial Fourier imaging in the phase encode direction with 75% of k-space being sampled. Reverse phase-encoded volumes were not acquired for *ex vivo* data.

The OGSE dMRI protocol included a PGSE sequence (with gradient duration = 11 ms and diffusion time = 13.8 ms) and four OGSE sequences with oscillating gradient frequencies of 50 Hz, 80 Hz, 115 Hz, and 150 Hz at b = 1600 s/mm^2 (10 directions for each frequency), with the lowest OGSE frequency using the FTB waveform. The µA sequence was implemented with linear (LTE) and spherical tensor (STE) encodings, as shown in Table A-2, at b = 1320 s/mm^2 (6 directions for each of LTE and STE), b = 2640 s/mm^2 (9 directions), and b = 4000 s/mm^2 (15 directions).

MT Imaging

MT-weighting was achieved by applying an off-resonance Gaussian-shaped RF pulse, with the same parameters for *in vivo* imaging, prior to the excitation.

Data Analysis Pipeline

The data analysis pipeline was built using Snakemake (412) (described in greater detail in the Usage Notes section). A Snakemake workflow defines data analysis in terms of rules that are specified in the "Snakefile." Figure A.3 outlines the data analysis steps from DICOM to scalar map generation.
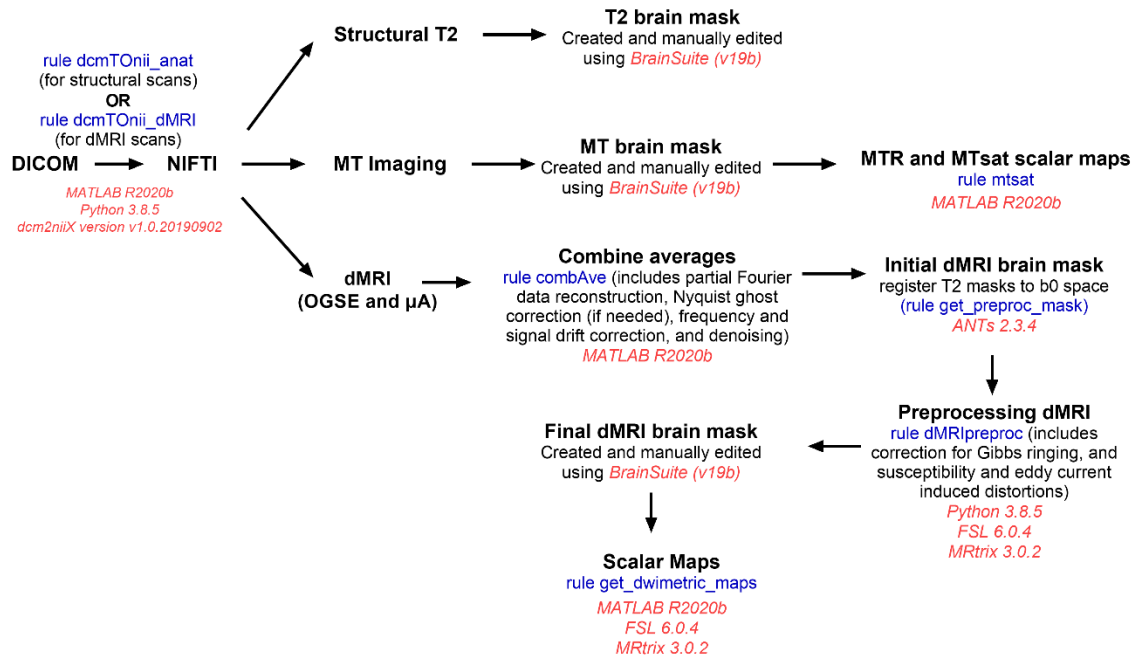
Figure A.3 - *Flowchart outlining data analysis steps from DICOM to scalar map generation. The "rules" listed are those used in the Snakemake pipeline, using Snakemake 3.13.3. The software dependencies and versions of each analysis step are included.*

OGSE and µA dMRI Recon and Preprocessing

For the dMRI protocols, averages were acquired separately on the scanner and the complex-valued averages were combined using in-house MATLAB code which included reconstruction of partial Fourier data using POCS (Projection onto Convex Sets) (220), correction for frequency and signal drift associated with gradient coil heating (221), and Marchenko-Pastur denoising of complex-valued data (223). If averages were not collected separately, this step can simply be skipped. Importantly, the pipeline can be used for both complex-valued and magnitude data. After the averages were combined, images were preprocessed using Gibbs ringing correction from the MRtrix3 package (224), followed by TOPUP (218) and EDDY (219) from FMRIB Software Library (FSL, Oxford, UK) (225). Using the data collected with reverse phase-encode blips, the susceptibility-induced off-resonance field was estimated using TOPUP. Then, EDDY was run to correct for eddy current induced distortions (volume-by-volume), perform motion correction, and apply the results from TOPUP.

Brain Masks

Brain masks, for each protocol, were produced using the skull stripping tool from BrainSuite (v. 19b) (226) and manually edited, as needed. For dMRI data, an initial brain mask (after dMRI averages were combined) was created by registering the T2 brain masks to a $b = 0$ s/mm^2 volume, using ANTs software (227). This initial brain mask was required for EDDY in the dMRI preprocessing step. After dMRI preprocessing, a final brain mask was produced and manually edited using BrainSuite. Brain masks for images from the T2, MT, and dMRI protocols have been included in the repository.

Scalar Map Generation

Scalar maps are shown in Figure A.4 (*in vivo*) and Figure A.5 (*ex vivo*). Table A-3 summarizes the scalar maps provided in the repository. Although briefly described here, more details describing the scalar maps are presented in previous reproducibility studies of the data that examined the two earliest time points (181,239).
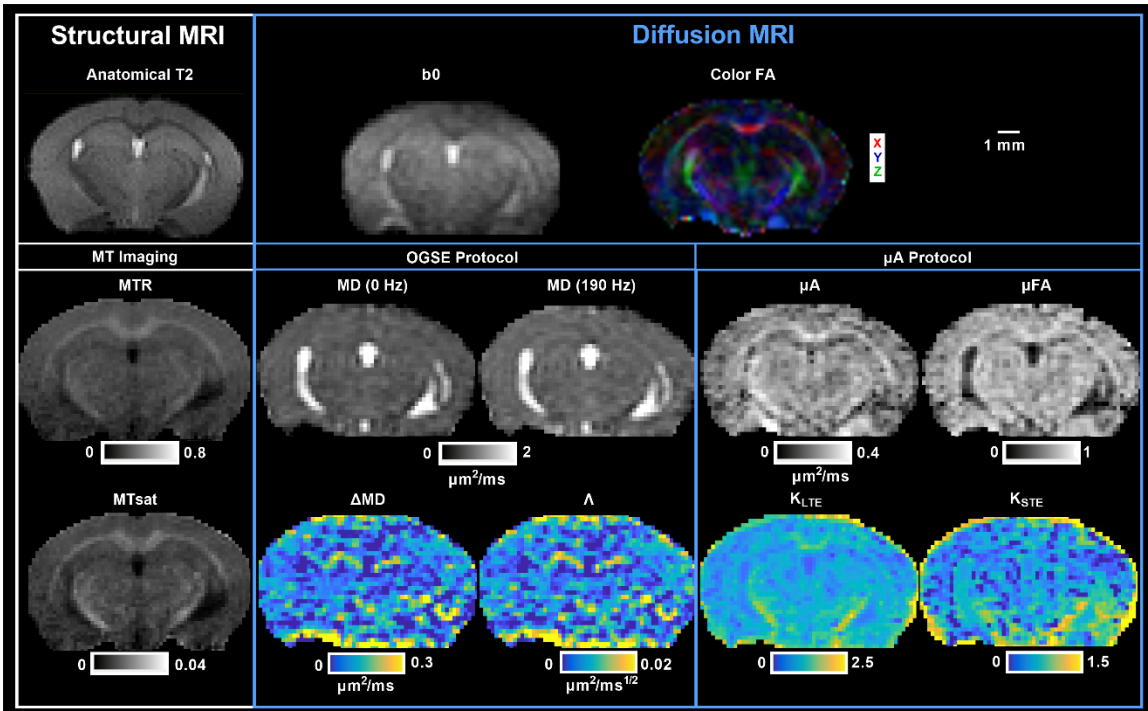
Figure A.4 - *In vivo scalar maps. Other DTI metric maps (such as axial and radial diffusivity) are not shown here but have been included in the repository. MTR: magnetization transfer ratio; MTsat: magnetization transfer saturation; FA: fractional anisotropy; MD: mean diffusivity; ΔMD: mean diffusivity difference between MD (190 Hz) and MD (0 Hz); Λ: diffusion dispersion rate; μA: microscopic anisotropy; μFA: microscopic fractional anisotropy; K_{LTE}: linear kurtosis acquired from LTE volumes; K_{STE}: isotropic kurtosis acquired from STE volumes.*
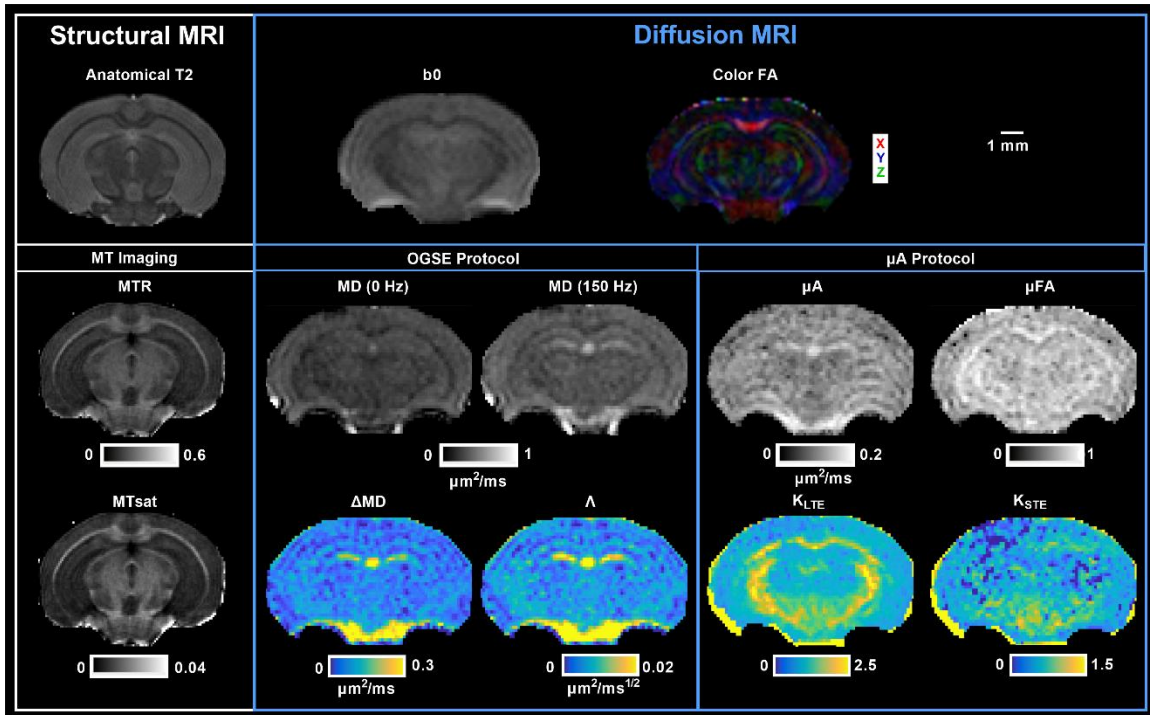
Figure A.5 - *Ex vivo scalar maps. Other DTI metric maps (such as axial and radial diffusivity) are not shown here but have been included in the repository. MTR: magnetization transfer ratio; MTsat: magnetization transfer saturation; FA: fractional anisotropy; MD: mean diffusivity; ΔMD: mean diffusivity difference between MD (190 Hz) and MD (0 Hz); Λ: diffusion dispersion rate; µA: microscopic anisotropy; µFA: microscopic fractional anisotropy; K_{LTE}: linear kurtosis acquired from LTE volumes; K_{STE}: isotropic kurtosis acquired from STE volumes.*

Table A-3: Brief description of scalar maps provided in the repository.

Imaging Protocol	MRI Metrics (Scalar Maps)	Equation	Interpretation
MT	Magnetization transfer ratio (MTR)	$$MTR = \frac{PDw - MTw}{PDw}$$	MTR has been shown to correlate well with histological myelin content (153,154).

			However, MTR is also sensitive to the choice of sequence parameters, flip angle inhomogeneities, and longitudinal relaxation time (T1) (14).
	Magnetization transfer saturation index (MTsat)	The apparent MTsat is calculated as: $$MTsat_{app} = \left(\frac{A_{app}\,\alpha_{MT}}{S_{MT}} - 1\right) R_{1app} TR_{MT} - \alpha_{MT}^2/2$$ A_{app}: apparent signal amplitude; α_{MT}: excitation flip angle of the MTw image; S_{MT}: signal intensity of MTw image; R_{1app}: apparent longitudinal relaxation rate; TR_{MT}: TR of MTw image MTsat was calculated from $MTsat_{app}$, after correcting for small residual higher order dependencies of the MT saturation on the local RF transmit field to further improve spatial uniformity: $$MTsat = \frac{MTsat_{app} \cdot (1 - 0.4)}{1 - 0.4 \cdot RF_{local}}$$ RF_{local}: relative flip angle α compared to the nominal flip angle For more details on the calculations of A_{app} and R_{1app}, see Helms et al.(14)	MTsat reduces T1 dependence and improves specificity to myelin, compared to MTR, while maintaining a feasible scan time (14).
OGSE dMRI	DTI Metrics at each frequency: • Axial Diffusivity	DTI assumes Gaussian diffusion and models diffusion as an ellipsoid with three eigenvectors and corresponding eigenvalues ($\lambda_1, \lambda_2, \lambda_3$).	DTI metrics reflect white matter tissue properties such as myelination or fiber

	(AD) • Radial Diffusivity (RD) • Mean Diffusivity (AD) • Fractional Anisotropy (FA)	$$AD = \lambda_1$$ $$RD = \frac{\lambda_2 + \lambda_3}{2}$$ $$MD = \frac{\lambda_1 + \lambda_2 + \lambda_3}{3}$$ $$FA = \sqrt{\frac{3}{2}} \frac{\sqrt{(\lambda_1 - MD)^2 + (\lambda_2 - MD)^2 + (\lambda_3 - MD)^2}}{\sqrt{\lambda_1{}^2 + \lambda_2{}^2 + \lambda_3{}^2}}$$	density. However, the effects of orientation dispersion dominate such contrast and more sophisticated models are necessary to separate the effects (8).
	Mean diffusivity difference (ΔMD)	$$\Delta MD = MD_f - MD_0$$ MD_f: OGSE MD at a frequency f MD_0: MD at $f = 0$ f: OGSE frequency	Here, ΔMD maps provided are ΔMD between OGSE-190 Hz and PGSE-0 Hz. ΔMD has shown increased sensitivity, compared to MD alone, in the assessment of hypoxia-ischemia in rodents (201), and in various pathologies in humans (202–204). Notably, ΔMD has helped to identify neurite beading as a mechanism for dMRI contrast after ischemic stroke (19,20).
	Diffusion dispersion rate (Λ)	$$MD_f = MD_0 + \Lambda f^{0.5}$$	By acquiring diffusion data at multiple frequencies, the power law relationship between MD and frequency can be explored via the "diffusion

			dispersion rate", Λ (162,178).
μA dMRI	DTI Metrics (acquired with b1000 LTE volumes): AD, RD, MD, FA		
	Microscopic anisotropy (μA)	$$\mu A = \sqrt{\dfrac{\ln \left(\dfrac{S_{LTE}}{S_{STE}}\right)}{b^2}}$$ S_{LTE}: powder-averaged LTE signal S_{STE}: powder-averaged STE signal	In contrast to the widely used FA metric, which confounds true microstructural changes with fiber orientation dispersion (8), the microscopic anisotropy (μA) metric quantifies water diffusion anisotropy independent of orientation dispersion (141,189). μA is defined here based on the difference in signal between LTE and STE dMRI acquisitions. Preliminary studies in humans have found that μA provides better sensitivity than the conventional FA in distinguishing between different types of brain tumours (21), and the assessment of multiple sclerosis lesions (16,17).

Microscopic fractional anisotropy (μFA)	$\mu FA = \sqrt{\dfrac{3}{2}\dfrac{\mu A^2}{\mu A^2 + 0.2 MD^2}}$	μFA is the normalized counterpart of μA and can be expressed in terms of μA.
Linear Diffusion Kurtosis (K_{LTE})	K_{LTE} was calculated by fitting the LTE signal to the diffusion kurtosis model using a joint non-negative least squares method, assuming MD is the same between LTE and STE acquisitions: $$\ln\left(\frac{S_{LTE}}{S_o}\right) = -bMD + \frac{1}{6}b^2 MD^2 K_{LTE}$$ S_o: mean signal with no diffusion encoding	K_{LTE} arises from the LTE acquisitions, which depends on the variance of both isotropic and anisotropic diffusivity.
Isotropic diffusion kurtosis (K_{STE})	K_{STE} was calculated as described above: $$\ln\left(\frac{S_{STE}}{S_o}\right) = -bMD + \frac{1}{6}b^2 MD^2 K_{STE}$$	K_{STE} arises from the STE acquisitions, which depends only on the variance of isotropic diffusivity. K_{STE} is a measure of the variance in the magnitude of diffusion tensors or the mean diffusivity, which can be related to cell size heterogeneity (21). Recently, He et al. have shown that K_{STE} may be particularly sensitive to deep gray matter lesions (208).

Scalar maps of MTR and MTsat were generated from the MT protocol. MTw, PDw, and T1w images were used to calculate MTsat maps, following the original method proposed by Helms et al. (14) and outlined by Hagiwara et al. (413) and Rahman et al. (239) Furthermore, B1 maps are available to correct for small residual higher-order

dependencies of the MT saturation on the local RF transmit field to further improve spatial uniformity, as suggested by Weiskopf et al. (180).

From the OGSE data, maps of MD at each frequency were generated using MRtrix3 (224). The mean diffusivity difference, ΔMD, was calculated as the difference between MD acquired at the highest frequency (190 Hz (*in vivo*) or 150 Hz (*ex vivo*)) and MD acquired at the lowest frequency (0 Hz). To characterize the power law relationship between MD and OGSE frequency (f),(178) the slope of linear regression of MD with $f^{0.5}$, the diffusion dispersion rate (Λ), was calculated. From the µA data, maps of microscopic anisotropy (µA), microscopic fractional anisotropy (µFA), and diffusion kurtosis arising from LTE and STE acquisitions (K_{LTE} and K_{STE} respectively) were generated by fitting the powder-averaged STE and LTE signals versus b-value to the diffusion kurtosis model (12). The powder-averaged signal, in diffusion MRI, refers to the average signal intensity over all directions in a specific b-shell (141). As a reference for the OGSE and µA metrics, DTI metrics have been included in the repository.

Data Records

The datasets, exported MRI protocols, Snakemake pipeline, and in-house MATLAB code are available in the Federated Research Data Repository (FRDR) at https://doi.org/10.20383/103.0594 (414).

Datasets are arranged in 'Data' as *mouseID_sex/timepoint/MRI_contrast*. For dMRI data, preprocessed data and scalar maps are arranged in 'DiffusionDataPreproc' with the same structure of *mouseID_sex/timepoint/MRI_contrast*.

Table A-4: Structural T2-weighted dataset

Folder	Filename	Filename Extensions
Data	**T2-weighted scan:** *mouseID_sex*/*timepoint*/T2_TurboRARE_AX150150500_A16/ T2_TurboRARE_AX150150500_A16 *(in vivo)* *mouseID_sex*/*ex_vivo*/ T2_TurboRARE_AX100100500_A48/ T2_TurboRARE_AX100100500_A48 *(ex vivo)*	.dcm .nii.gz .json _method.json
Data	**Brain mask:** *mouseID_sex*/*timepoint*/T2_TurboRARE_AX150150500_A16/ T2_TurboRARE_AX150150500_A16_mask *(in vivo)* *mouseID_sex*/*ex_vivo*/ T2_TurboRARE_AX100100500_A48/ T2_TurboRARE_AX100100500_A48_mask *(ex vivo)*	.nii.gz
Data	**T2-weighted scan with brain mask applied:** *mouseID_sex*/*timepoint*/T2_TurboRARE_AX150150500_A16/ T2_TurboRARE_AX150150500_A16_Wmask *(in vivo)* *mouseID_sex*/*ex_vivo*/ T2_TurboRARE_AX100100500_A48/ T2_TurboRARE_AX100100500_A48_Wmask *(ex vivo)*	.nii.gz

Table A-5: MT Imaging dataset

Folder	Filename	Filename Extensions
Data	**MTw scan:** *mouseID_sex*/*timepoint*/MTon_GRE_3D_150x400_12A_5uT_385FA_3500Hz/ MTon_GRE_3D_150x400_12A_5uT_385FA_3500Hz *(in vivo)* *mouseID_sex*/*ex_vivo*/ MTon_GRE_3D_100x400_36A_5uT_385FA_3500Hz/ MTon_GRE_3D_100x400_36A_5uT_385FA_3500Hz *(ex vivo)*	.dcm .nii.gz .json _method.json _visu_pars.json
Data	**PDw scan:** *mouseID_sex*/*timepoint*/MToff_PD_GRE_3D_150x400_12A/MToff	.dcm .nii.gz

		PD_GRE_3D_150x400_12A *(in vivo)*	.json
		mouseID_sex/*ex_vivo*/ MToff_PD_GRE_3D_100x400_36A/ MToff_PD_GRE_3D_100x400_36A *(ex vivo)*	_method.json
			_visu_pars.js on
Data	**T1w scan:**		.dcm
			.nii.gz
	mouseID_sex/*timepoint*/ MToff_T1_GRE_3D_150x400_12A/MToff_T1_GRE_3D_150x400_12A *(in vivo)*	.json
			_method.json
	mouseID_sex/*ex_vivo*/ MToff_T1_GRE_3D_100x400_36A/ MToff_T1_GRE_3D_100x400_36A *(ex vivo)*	_visu_pars.js on
Data	**B1 map data (2 volumes acquired from 2 TRs):**		.dcm
			.nii.gz
	mouseID_sex/*timepoint*/rpAFI_mouse_2/rpAFI_mouse_2 *(in vivo* and *ex vivo)*	.json
			_method.json
			_visu_pars.js on
Data	**B1 map (from the scanner):**		.dcm
			.nii.gz
	mouseID_sex/*timepoint*/rpAFI_mouse_1/rpAFI_mouse_1 *(in vivo* and *ex vivo)*	.json
			_method.json
			_visu_pars.js on
Data	**B1 map (resampled to match MTw scan's resolution):**		.nii.gz
	mouseID_sex/*timepoint*/rpAFI_mouse_1/rpAFI_mouse_1_vol2_RS *(in vivo* and *ex vivo)*		
Data	**Text file detailing which B1 map slices have artifacts (0 for slices with the banding artifact and 1 for slices without artifacts):**		.csv

	mouseID_sex/*timepoint*/rpAFI_mouse_1/rpAFI_mouse_1 *(in vivo* and *ex vivo)*	
Data	**Brain mask:** *mouseID_sex*/*timepoint*/MTon_GRE_3D_150x400_12A_5uT_385FA_3500Hz/MTon_GRE_3D_150x400_12A_5uT_385FA_3500Hz_mask *(in vivo)* *mouseID_sex*/*ex_vivo*/ MTon_GRE_3D_100x400_36A_5uT_385FA_3500Hz/ MTon_GRE_3D_100x400_36A_5uT_385FA_3500Hz_mask *(ex vivo)*	.nii.gz
Data	**MTR – scalar map:** *mouseID_sex*/*timepoint*/MTon_GRE_3D_150x400_12A_5uT_385FA_3500Hz/MTon_GRE_3D_150x400_12A_5uT_385FA_3500Hz_mtr *(in vivo)* *mouseID_sex*/*ex_vivo*/ MTon_GRE_3D_100x400_36A_5uT_385FA_3500Hz/ MTon_GRE_3D_100x400_36A_5uT_385FA_3500Hz_mtr *(ex vivo)*	.nii.gz
Data	**MTsat – scalar map:** *mouseID_sex*/*timepoint*/MTon_GRE_3D_150x400_12A_5uT_385FA_3500Hz/MTon_GRE_3D_150x400_12A_5uT_385FA_3500Hz_mtsat *(in vivo)* *mouseID_sex*/*ex_vivo*/ MTon_GRE_3D_100x400_36A_5uT_385FA_3500Hz/ MTon_GRE_3D_100x400_36A_5uT_385FA_3500Hz_mtsat *(ex vivo)*	.nii.gz

Table A-6: OGSE dMRI dataset

Folder	Filename	Filename Extensions
Data	**OGSE dMRI scan (complex-valued data):** *mouseID_sex*/*timepoint*/OGSE_5Shapes_1A_5Rep_TR10/OGSE_5Shapes_1A_5Rep_TR10 *(in vivo)* *mouseID_sex*/*ex_vivo*/OGSE_res130150500/OGSE_res130150500 *(ex vivo)*	.dcm _real.nii.gz _imaginary.nii.gz _real.json

		_imaginary.json
		_method.json
		_visu_pars.json
		.bmat
		.bvec
		.bval
Data	**OGSE dMRI scan (after averages are combined):**	.nii.gz
	mouseID_sex/*timepoint*/OGSE_5Shapes_1A_5Rep_TR10/OGSE_5Shapes_1A_5Rep_TR10_aveComb *(in vivo)*	.bmat
		.bvec
	mouseID_sex/*ex_vivo*/OGSE_res130150500/OGSE_res130150500_aveComb *(ex vivo)*	.bval
Data	**b0 scan acquired with reverse PE (complex-valued data):**	.dcm
	mouseID_sex/*timepoint*/OGSE_5Shapes_1A_5Rep_TR10_b0_reversePE/OGSE_5Shapes_1A_5Rep_TR10_b0_reversePE_aveComb *(in vivo)*	_real.nii.gz
		_imaginary.nii.gz
	*(*not acquired for *ex vivo)*	_real.json
		_imaginary.json
		_method.json
		_visu_pars.json
		.bmat
		.bvec
		.bval
Data	**b0 scan acquired with reverse PE (after averages are combined):**	.nii.gz
		.bmat

	mouseID_sex/*timepoint*/OGSE_5Shapes_1A_5Rep_TR10_b0_ reversePE/OGSE_5Shapes_1A_5Rep_TR10_b0_reversePE_a veComb *(in vivo)*	.bvec .bval
Data	**Mean b0 volume extracted from dataset after averages are combined (with normal PE):** *mouseID_sex*/*timepoint*/OGSE_5Shapes_1A_5Rep_TR10/OG SE_5Shapes_1A_5Rep_TR10_aveComb_mean_b0 *(in vivo)*	.nii.gz
DiffusionDat aPreproc	**Preprocessed Dataset split into separate frequencies (in vivo):** **PGSE or 0 Hz:** *mouseID_sex*/*timepoint*/OGSE_5Shapes_1A_5Rep_TR10/OG SE_5Shapes_1A_5Rep_TR10_aveComb_preproc_f000 **50Hz OGSE:** *mouseID_sex*/*timepoint*/OGSE_5Shapes_1A_5Rep_TR10/OG SE_5Shapes_1A_5Rep_TR10_aveComb_preproc_f050 **100 Hz OGSE:** *mouseID_sex*/*timepoint*/OGSE_5Shapes_1A_5Rep_TR10/OG SE_5Shapes_1A_5Rep_TR10_aveComb_preproc_f100 **145 Hz OGSE:** *mouseID_sex*/*timepoint*/OGSE_5Shapes_1A_5Rep_TR10/OG SE_5Shapes_1A_5Rep_TR10_aveComb_preproc_f145 **190 Hz OGSE:** *mouseID_sex*/*timepoint*/OGSE_5Shapes_1A_5Rep_TR10/OG SE_5Shapes_1A_5Rep_TR10_aveComb_preproc_f190 **Preprocessed Dataset split into separate frequencies (ex vivo):** **PGSE or 0 Hz:** *mouseID_sex*/*timepoint*/OGSE_res130150500/OGSE_ res130150500_aveComb_preproc_f000 **50Hz OGSE:**	.nii.gz .bvec .bval

	mouseID_sex/*timepoint*/OGSE_ res130150500/OGSE_ res130150500_aveComb_preproc_f050	
	80 Hz OGSE:	
	mouseID_sex/*timepoint*/OGSE_ res130150500/OGSE_ res130150500_aveComb_preproc_f080	
	115 Hz OGSE:	
	mouseID_sex/*timepoint*/OGSE_ res130150500/OGSE_ res130150500_aveComb_preproc_f115	
	150 Hz OGSE:	
	mouseID_sex/*timepoint*/OGSE_ res130150500/OGSE_ res130150500_aveComb_preproc_f150	
DiffusionDataPreproc	**Scalar Maps generated for each frequency (*in vivo* and *ex vivo*)**	.nii.gz
	For example, for PGSE or 0 Hz (*in vivo*):	
	Axial Diffusivity (AD):	
	mouseID_sex/*timepoint*/OGSE_5Shapes_1A_5Rep_TR10/OGSE_5Shapes_1A_5Rep_TR10_aveComb_preproc_f000_AD	
	Radial Diffusivity (RD):	
	mouseID_sex/*timepoint*/OGSE_5Shapes_1A_5Rep_TR10/OGSE_5Shapes_1A_5Rep_TR10_aveComb_preproc_f000_RD	
	Mean Diffusivity (MD):	
	mouseID_sex/*timepoint*/OGSE_5Shapes_1A_5Rep_TR10/OGSE_5Shapes_1A_5Rep_TR10_aveComb_preproc_f000_MD	
	Fractional Anisotropy (FA):	
	mouseID_sex/*timepoint*/OGSE_5Shapes_1A_5Rep_TR10/OGSE_5Shapes_1A_5Rep_TR10_aveComb_preproc_f000_FA	
	Color Fractional Anisotropy (Color FA):	
	mouseID_sex/*timepoint*/OGSE_5Shapes_1A_5Rep_TR10/OGSE_5Shapes_1A_5Rep_TR10_aveComb_preproc_f000_FAvec	

	Voxelwise Diffusion Dispersion Rate (Λ): *mouseID_sex*/*timepoint*/OGSE_5Shapes_1A_5Rep_TR10/OGSE_5Shapes_1A_5Rep_TR10_aveComb_preproc_f000_MD_Gfactor	
DiffusionDataPreproc	**Other Scalar Maps** **Mean Diffusivity Difference (between 190 Hz OGSE and PGSE (0 Hz)):** *mouseID_sex*/*timepoint*/OGSE_5Shapes_1A_5Rep_TR10/OGSE_5Shapes_1A_5Rep_TR10_aveComb_preproc_delMD *(in vivo)* *mouseID_sex*/*timepoint*/OGSE_res130150500/OGSE_res130150500_aveComb_preproc_delMD *(ex vivo)*	.nii.gz

As the same brain mask is used for both dMRI datasets, the brain mask has been included in the µA dMRI dataset.

Table A-7: µA dMRI dataset

Folder	Filename	Filename Extensions
Data	**µA dMRI scan (complex-valued data):** *mouseID_sex*/*timepoint*/uFA_2Shapes_1A_3Rep_TR10/uFA_2Shapes_1A_3Rep_TR10 *(in vivo)* *mouseID_sex*/*timepoint*/uFA_res130150500/uFA_res130150500 *(ex vivo)*	.dcm _real.nii.gz _imaginary.nii.gz _real.json _imaginary.json _method.json _visu_pars.json .bmat .bvec

		.bval
Data	**μA dMRI scan (after averages are combined):** *mouseID_sex*/*timepoint*/uFA_2Shapes_1A_3Rep_TR10/ uFA_2Shapes_1A_3Rep_TR10_aveComb *(in vivo)* *mouseID_sex*/*timepoint*/uFA_res130150500/ uFA_res130150500 *(ex vivo)*	.nii.gz .bmat .bvec .bval
Data	**b0 scan acquired with reverse PE (complex-valued data):** *mouseID_sex*/*timepoint*/uFA_2Shapes_1A_3Rep_TR10_b0_ reversePE/ uFA_2Shapes_1A_3Rep_TR10_b0_reversePE *(in vivo)* *(*not acquired for *ex vivo)*	.dcm _real.nii.gz _imaginary.nii.gz _real.json _imaginary.json _method.json _visu_pars.json .bmat .bvec .bval
Data	**b0 scan acquired with reverse PE (after averages are combined):** *mouseID_sex*/*timepoint*/uFA_2Shapes_1A_3Rep_TR10_b0_ reversePE/ uFA_2Shapes_1A_3Rep_TR10_b0_reversePE_aveComb *(in vivo)*	.nii.gz .bmat .bvec .bval
Data	**Mean b0 volume extracted from dataset after averages are combined (normal PE):** *mouseID_sex*/*timepoint*/uFA_2Shapes_1A_3Rep_TR10/uFA _2Shapes_1A_3Rep_TR10_aveComb_mean_b0 *(in vivo)*	.nii.gz
DiffusionDat aPreproc	**Preprocessed Dataset:**	.nii.gz

	mouseID_sex/*timepoint*/uFA_2Shapes_1A_3Rep_TR10/uFA_2Shapes_1A_3Rep_TR10_aveComb_preproc *(in vivo)*	.bvec .bval
	mouseID_sex/*timepoint*/uFA_res130150500/uFA_res130150500_aveComb_preproc *(ex vivo)*	.isiso
DiffusionDataPreproc	**Scalar maps (*in vivo*):** (for *ex vivo* scalar maps, replace 'uFA_2Shapes_1A_3Rep_TR10/uFA_2Shapes_1A_3Rep_TR10' with 'uFA_res130150500/uFA_res130150500') **Axial Diffusivity (AD) – acquired with b1000 LTE volumes:** *mouseID_sex*/*timepoint*/uFA_2Shapes_1A_3Rep_TR10/uFA_2Shapes_1A_3Rep_TR10_aveComb_preproc_AD **Radial Diffusivity (RD) – acquired with b1000 LTE volumes:** *mouseID_sex*/*timepoint*/uFA_2Shapes_1A_3Rep_TR10/uFA_2Shapes_1A_3Rep_TR10_aveComb_preproc_RD **Mean Diffusivity (MD) – acquired with b1000 LTE volumes:** *mouseID_sex*/*timepoint*/uFA_2Shapes_1A_3Rep_TR10/uFA_2Shapes_1A_3Rep_TR10_aveComb_preproc_MD **Fractional Anisotropy (FA) – acquired with b1000 LTE volumes:** *mouseID_sex*/*timepoint*/uFA_2Shapes_1A_3Rep_TR10/uFA_2Shapes_1A_3Rep_TR10_aveComb_preproc_FA **Fractional Anisotropy (FA) – acquired with b2000 LTE volumes:** *mouseID_sex*/*timepoint*/uFA_2Shapes_1A_3Rep_TR10/uFA_2Shapes_1A_3Rep_TR10_aveComb_preproc_b2000_FA **Color Fractional Anisotropy (FA) – acquired with b1000 LTE volumes:** *mouseID_sex*/*timepoint*/uFA_2Shapes_1A_3Rep_TR10/uFA_2Shapes_1A_3Rep_TR10_aveComb_preproc_b1000_FAve	.nii.gz

	c	
	Color Fractional Anisotropy (FA) – acquired with b2000 LTE volumes: *mouseID_sex*/*timepoint*/uFA_2Shapes_1A_3Rep_TR10/uFA_2Shapes_1A_3Rep_TR10_aveComb_preproc_b2000_FAvec **Microscopic Anisotropy (µA):** *mouseID_sex*/*timepoint*/uFA_2Shapes_1A_3Rep_TR10/uFA_2Shapes_1A_3Rep_TR10_aveComb_preproc_uA **Microscopic Fractional Anisotropy (µFA):** *mouseID_sex*/*timepoint*/uFA_2Shapes_1A_3Rep_TR10/uFA_2Shapes_1A_3Rep_TR10_aveComb_preproc_uFA **Linear Kurtosis – acquired from LTE volumes (KLTE):** *mouseID_sex*/*timepoint*/uFA_2Shapes_1A_3Rep_TR10/uFA_2Shapes_1A_3Rep_TR10_aveComb_preproc_Klin **Isotropic Kurtosis – acquired from STE volumes (KSTE):** *mouseID_sex*/*timepoint*/uFA_2Shapes_1A_3Rep_TR10/uFA_2Shapes_1A_3Rep_TR10_aveComb_preproc_Kiso	
DiffusionDataPreproc	**Initial brain mask (for use in EDDY in the preprocessing step):** *mouseID_sex*/*timepoint*/uFA_2Shapes_1A_3Rep_TR10/uFA_2Shapes_1A_3Rep_TR10_aveComb_preproc_mask *(in vivo)* *mouseID_sex*/*timepoint*/uFA_res130150500/uFA_res130150500_aveComb_preproc_mask *(ex vivo)*	.nii.gz
DiffusionDataPreproc	**Final brain mask:** *mouseID_sex*/*timepoint*/uFA_2Shapes_1A_3Rep_TR10/uFA_2Shapes_1A_3Rep_TR10_aveComb_preproc_mask_after *(in vivo)* *mouseID_sex*/*timepoint*/uFA_res130150500/uFA_res130150500_aveComb_preproc_mask_after *(ex vivo)*	.nii.gz

DiffusionDat aPreproc	**Mean b0 volume extracted from dataset after preprocessing:** *mouseID_sex*/*timepoint*/uFA_2Shapes_1A_3Rep_TR10/uFA _2Shapes_1A_3Rep_TR10_aveComb_preproc_mean_b0 *(in vivo)*	.nii.gz

Table A-8: Templates and Atlas for Registration

Folder	Filename	Filename Extensions
Registration	**Turone Atlas (as downloaded from https://www.nitrc.org/projects/tmbta_2019/):** atlas/TMBTA_Brain_Template **Turone Atlas Labels (as downloaded from https://www.nitrc.org/projects/tmbta_2019/):** atlas/TMBTA_Brain_Labels	.nii
Registration	**Downsampled Turone Atlas (to be used for registration):** atlas/TMBTA_Brain_Template_reorient_smoothed0_2_RS_Ga ussian **Downsampled Turone Atlas Labels:** atlas/TMBTA_Brain_Labels_reorient_RS_Gaussian	.nii.gz
Registration	**Study-specific templates:** ANTStemplate_T2/T2_template (T2-weighted template) ANTStemplate_MT/MT_template (MTw template) ANTStemplate_FA/FA_template (FA template)	.nii.gz
Registration	**Registration transforms (Affine transform to register individual images to template space):** In each template folder: template_*contrast_mouseID_sex_timepoint****GenericAffine where *'contrast'* is 'T2,' 'b2000_FA,' or 'MTon' and *** are 3	.mat

	numbers outputted by the ANTs template building command	
	For example: template_T2_NR1_F_1week600GenericAffine	
Registration	**Registration transforms (Symmetric diffeomorphic transform to register individual images to template space):** In each template folder: template_*contrast_mouseID_sex_timepoint****Warp template_*contrast_mouseID_sex_timepoint****InverseWarp	.nii.gz
Registration	**Registration transforms (between templates):** **FA template to T2 template:** FAtemplate_to_T2template/FA_T2_SynMI0_005_transform0 GenericAffine.mat (affine transform) FAtemplate_to_T2template/FA_T2_SynMI0_005_transform1 Warp.nii.gz (symmetric diffeomorphic transform) FAtemplate_to_T2template/FA_T2_SynMI0_005_transform1I nverseWarp.nii.gz (inverse symmetric diffeomorphic transform) **MTw template to T2 template:** MTtemplate_to_T2template/ MT_T2_SynCI0.005_transform0GenericAffine.mat (affine transform) MTtemplate_to_T2template/ MT_T2_SynCI0.005__transform1Warp.nii.gz (symmetric diffeomorphic transform) MTtemplate_to_T2template/ MT_T2_SynCI0.005__transform1InverseWarp.nii.gz (inverse symmetric diffeomorphic transform)	
Registration	**Registration transforms (from T2 template to the downsampled atlas):** T2template_to_atlas/T2_atlas_SynMI0_00005_transform0Gen	

| | ericAffine.mat (affine transform)

 T2template_to_atlas/T2_atlas_SynMI0_00005_transform1War p.nii.gz (symmetric diffeomorphic transform) | |

Imaging Protocols

To optimize utility of the protocols, imaging protocols were exported from a Bruker ParaVision 6.0.1 system (OGSE and µA dMRI protocols), which was used for data collection, and are included. The files can be imported into the Bruker ParaVision system to run all protocols. ParaVision 6.0.1 compiled binaries for the custom diffusion MRI pulse sequences are available at doi.org/10.17605/OSF.IO/5EUSW, while the other scans used vendor-provided sequences. Imaging protocols and compiled binaries for a Bruker ParaVision 7.0.0 system are also included, for convenience. The diffusion MRI pulse sequence source code is available upon reasonable request.

Technical Validation

As 3D printed custom designed parts and the surface/volume coil were fixed onto a support, which was placed into the scanner, this ensured consistent positioning of the mouse head in the scanner at each session and prevented motion artifacts. Raw and preprocessed dMRI data were visually inspected to ensure good preprocessing results, as shown previously (181) and in Figure A.6a (*in vivo*) and Figure A.6b (*ex vivo*).
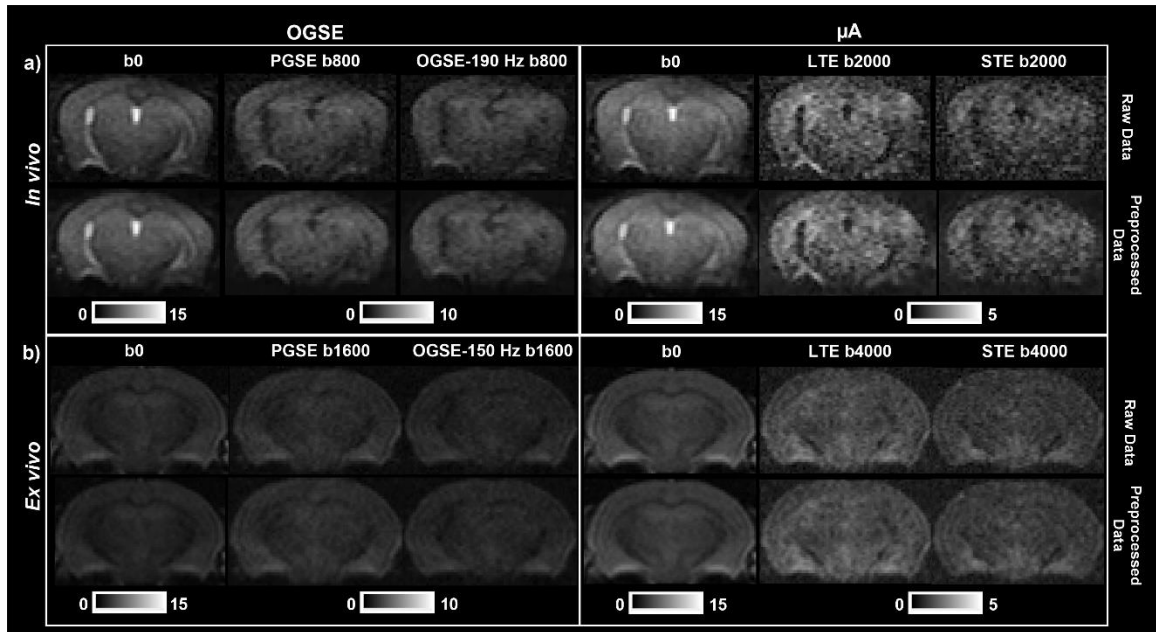
Figure A.6 - *In vivo (a) and ex vivo (b) raw and preprocessed dMRI data. Raw data (after combining averages) is shown in the top row and preprocessed data is shown in the bottom row. Representative b = 0 s/mm² images are shown for both the OGSE and µA protocols. From the OGSE protocol, representative diffusion weighted images from a single diffusion gradient direction are shown from PGSE and OGSE with the highest frequency used in this study (190 Hz (in vivo) and 150 Hz (ex vivo)), at b = 800 s/mm² (in vivo) and b = 1600 s/mm² (ex vivo). From the µA protocol, diffusion weighted images from a single diffusion gradient direction are shown from the LTE and STE sequences, at b = 2000 s/mm² (in vivo) and b = 4000 s/mm² (ex vivo). Adapted from Rahman et al. (181).*

The only artifact observed in the *in vivo* data was a banding artifact in the rostral region of the brain in most of the B1 maps, which were acquired as part of the MT protocol. Thus, the MTsat maps included in the repository were generated without applying the B1 correction. Users have the option to turn the B1 correction on or off. If

the B1 correction is on, the correction will be applied only to the slices which showed no banding artifact in the B1 map. Although the B1 maps have an artifact and the correction cannot be applied to all brain slices, inhomogeneities in the transmitted RF field are inherently compensated to some degree when calculating MTsat (14). The B1 maps were acquired to correct for small residual higher-order dependencies of the MT saturation on the local RF transmit field to further improve spatial uniformity, as suggested by Weiskpof et al. (180). Thus, the B1 correction is a finetuning for MTsat maps rather than a substantial part of the calculation, and the MTsat maps can still be analyzed without the correction.

For *ex vivo* data, as mouse IDs NR7_M and NR8_M were scanned with the skull removed, slight deformation of the tissue is observed at the superior edges of the brain. Mouse IDs NR1_F and NR2_F show banding artifacts in the caudal region of the brain in the B1 maps.

Test-retest Reproducibility

Test-retest analysis is an additional tool for technical validation. Test-retest comparisons have been performed using data from two timepoints: Day 3 and Week 1 (181,239). Bland-Altman plots and coefficients of variation (CVs) revealed that most of the μA dMRI metrics are reproducible in both ROI-based and voxelwise analysis, while the OGSE dMRI metrics are only reproducible in ROI-based analysis. MTR and MTsat show high reproducibility (CVs < 10%) in both voxelwise and ROI-based analyses. The previous test-retest analysis also shows that given feasible preclinical sample sizes (10 – 15), the MRI metrics may provide sensitivity to subtle microstructural changes (6 – 8%).

Signal-to-noise ratio measurements

For dMRI data, SNR maps were calculated by dividing the powder-averaged magnitude signal (of the combined averages) by the noise. Noise was calculated from each of the real and imaginary components of the complex-valued data as the standard deviation of the background signal from a single average of a single direction divided by $\sqrt{(\text{number of averages}) \cdot (\text{number of directions})}$, and averaged over the real and imaginary components. For MT data, SNR maps were calculated by dividing the magnitude signal by the standard deviation of background signal.

To maximize SNR, a surface coil, built in-house, was used for *in vivo* imaging. As expected with a surface coil, a gradient of SNR change can be seen in the superior-inferior direction of the brain, compared to the commercially available MP30 volume coil, which was used for *ex vivo* imaging (Figure A.7). This gradient of SNR change does not seem to affect voxel-wise CV maps to the same extent, as shown in Rahman et al. (181), which could be due to the denoising quality.
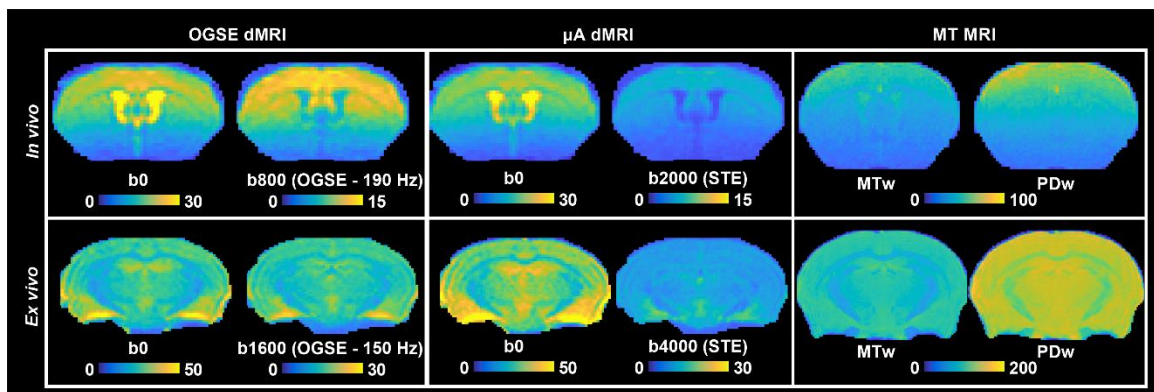
Figure A.7 - *SNR maps of in vivo and ex vivo images. SNR maps for a single b = 0 s/mm² image are shown for all dMRI protocols, and SNR maps for the powder average of the*

highest b-values are shown for all protocols (b = 800 s/mm^2 for OGSE-190 Hz (in vivo),

b = 2000 s/mm^2 for μA-STE (in vivo), b = 1600 s/mm^2 for OGSE-150 Hz (ex vivo), and b

= 4000 s/mm^2 for μA-STE (ex vivo)). SNR maps for MTw and PDw scans are shown for

MT MRI. Adapted from Rahman et al.(181).

Usage Notes

Data Analysis Pipeline - Snakemake

The data preprocessing and analysis pipeline was built using Snakemake (412), a

reproducible and adaptable Python-based workflow management system. Snakemake

itself is easily deployable via the Conda package manager (https://conda.io). Instructions

and further information can be found at https://snakemake.github.io.

The workflow, called the "Snakefile," contains all data analysis steps such as

DICOM to NIFTI conversion, preprocessing data, and scalar map generation. This

involves FSL (225), MRtrix3 (224), and ANTs (227) commands, as well as MATLAB

functions and bash scripts. Users can easily modify and add rules to the pipeline.

Example Snakemake Usage

Below are example Snakemake commands, which can be run from the command

line, to process dicoms to preprocessed data and scalar maps. These instructions have

also been included in the README of the code directory. The Snakemake rules used are

listed directly below each command. The filepaths and filenames, which the user must

change, are in italics, and any number of files can be converted at once. Importantly,

most of the code assumes that the dicom or NIFTI filename matches the name of the

folder that it is in. All brain masks (for each MRI contrast) have been provided in the repository and the user should copy the masks to their respective folders, as the code assumes that these masks exist. Alternatively, the user can edit the code to run without masks.

Anatomical Data

To convert the anatomical dicoms (which include T2 and all MT related dicoms) to NIFTI format, the following Snakemake command can be used:

$ snakemake   --cores   1 *filepath/{mouse#1_sex/timepoint,mouse#2_sex/timepoint,mouse#3_sex/timepoint}/dicom _foldername/dicom_filename*.json

[Rules: dcmTOnii_anat]

For example, a real use case of the above command, with the actual filepaths and filenames to acquire T2-weighted NIFTIs may be:

$ snakemake   --cores   1 Data/{NR1_F/Day0,NR1_F/Day3,NR2_F/Day0}/T2_TurboRARE_AX150150500_A16/ T2_TurboRARE_AX150150500_A16.json

Before acquiring MT metric maps, users must make a brain mask using the MT-weighted images (with software such as BrainSuite) and save the mask as "MTon_GRE_3D_150x400_12A_5uT_385FA_3500Hz_mask.nii.gz" in the folder "MTon_GRE_3D_150x400_12A_5uT_385FA_3500Hz." As brain masks are also

provided in the repository, users can also copy the mask, instead of creating a new one. To generate MT metric maps (MTR and MTsat), the following Snakemake command can be used:

$ snakemake --cores 1 *filepath/{mouse#1_sex* */timepoint,mouse#2_sex* */timepoint,mouse#3_sex* */timepoint}/* MTon_GRE_3D_150x400_12A_5uT_385FA_3500Hz/MTon_GRE_3D_150x400_12A_ 5uT_385FA_3500Hz_mtsat.nii.gz

[Rules: mtsat]

Diffusion MRI Data

To convert a number of dicoms to combined averages (in NIFTI format, with partial Fourier reconstruction, correction for frequency and signal drift, and denoising) and generate the initial dMRI brain mask (needed for preprocessing), the following Snakemake command can be used:$ snakemake --cores 1 *filepath/{mouse#1_sex* */timepoint,mouse#2_sex* */timepoint,mouse#3_sex* */timepoint}/dMRI_filename/dMRI_filename*_aveComb_preproc_mask.nii.gz

[Rules: dcmTOnii_dMRI, combAve, get_preproc_mask]

The above command assumes that T2-weighted brain masks exist as "T2_TurboRARE_AX150150500_A16_mask.nii.gz" in the folder "T2_TurboRARE_AX150150500_A16," as this mask is registered to dMRI space to create the initial dMRI brain mask. As the data acquired with reverse phase-encoding do not require an initial mask, since they are combined with the larger datasets

("uFA_2Shapes_1A_3Rep_TR10" and "OGSE_5Shapes_1A_5Rep_TR10"), the command to convert dicoms with reverse phase-encoding to combined averages is:

$ snakemake --cores 1 *filepath/{mouse#1_sex /timepoint,mouse#2_sex /timepoint,mouse#3_sex /timepoint}/dMRI_filename/dMRI_filename_*aveComb.nii.gz

[Rules: dcmTOnii_dMRI, combAve]

After combined averages and initial dMRI brain masks are generated, preprocessing can be run by this command:

$ snakemake --cores 1 DiffusionDataPreproc/{*mouse#1_sex /timepoint,mouse#2_sex /timepoint,mouse#3_sex*

*/timepoint}/dMRI_filename/dMRI_filename_*aveComb_preproc.nii.gz

[Rules: dMRIpreproc]

Note that the code assumes that the original NIFTI files are located in the "Data" folder and that FSL is being run from a singularity container. The user can change the code in "dMRIpreproc.sh" located in the folder "code_scidata_paper/dMRIpreproc" to align with their FSL environment. The above command will work with or without reverse phase-encoded data.

After the dMRI preprocessing step, final dMRI brain masks can be created, or the user can use the masks provided in the repository ("*dMRI_filename_*aveComb_preproc_mask_after.nii.gz"). The code assumes that the masks are named as they are in the repository. Alternatively, the user can acquire dMRI

scalar maps without using brain masks by editing the code in the Snakefile. To acquire dMRI scalar maps, the following command can be run:

$ snakemake --cores 1 *filepath/{mouse#1_sex /timepoint,mouse#2_sex /timepoint,mouse#3_sex /timepoint}/dMRI_filename/dMRI_filename_*aveComb_preproc_mean_b0_Wmask.nii.gz

[Rules: get_dwimetric_maps]

The above command will generate scalar maps as well as a non-diffusion weighted (b0) NIFTI, averaged over all non-diffusion weighted volumes. This mean b0 NIFTI may be used to facilitate registration.

Image Registration

The dMRI and MT data were not registered to a template or to the anatomical T2-weighted images to avoid errors from interpolation and registration inaccuracies, and as other researchers may prefer using their own registration pipelines. However, for flexible utility of the dataset, the anatomical T2-weighted images, study-specific templates, a downsampled atlas, and registration transforms have been included in the repository, so registration of the dMRI and MT data to anatomical space or an atlas is possible. Currently, the registration pipeline has been tested only with the *in vivo* dataset. Users may use the robust registration pipeline, based on ANTs commands, included in the Snakefile or tweak them accordingly. ANTs is an open source software package which comprises tools for image registration, template building and segmentation (227). ANTs was chosen due to its flexibility and the robust performance of default ANTs registration

parameters. Moreover, the nonlinear deformation algorithm used in ANTs was top ranked in a comparative study (415).

The Turone atlas (298), downsampled to the resolution of the *in vivo* T2-weighted images, was used for registration (Figure A.8a). Three study-specific templates, based on all images from all sessions, were created to facilitate the registration process, which included a T2 template, an FA template, and an MT-weighted template. Individual images can be registered to the downsampled atlas in three steps, as shown in Figure A.8b and A.8c: 1) the FA maps and MT-weighted images are registered to the FA template and MT-weighted template, respectively; 2) the FA template and MT-weighted template are registered to the T2 template; 3) the T2 template is registered to the downsampled atlas. Each registration step involves an affine transformation, followed by a symmetric diffeomorphic transformation using ANTs' Symmetric Normalization (SyN) algorithm. The registration transforms resulting from the previous three registration steps can be used to warp all dMRI metric maps and MT metric maps (MTR and MTsat) to the downsampled atlas space. Registration of all images to the atlas allows for voxel-wise analysis and atlas-based region-of-interest analysis. For region-of-interest analysis, atlas labels can be downloaded from https://www.nitrc.org/projects/tmbta_2019/ (298). Example ANTs commands, used for template-building and generating registration transforms, have been included in the text file 'ANTs_Registration_Commands.txt.' All other code to warp metric maps to the downsampled atlas space have been included in the Snakefile.
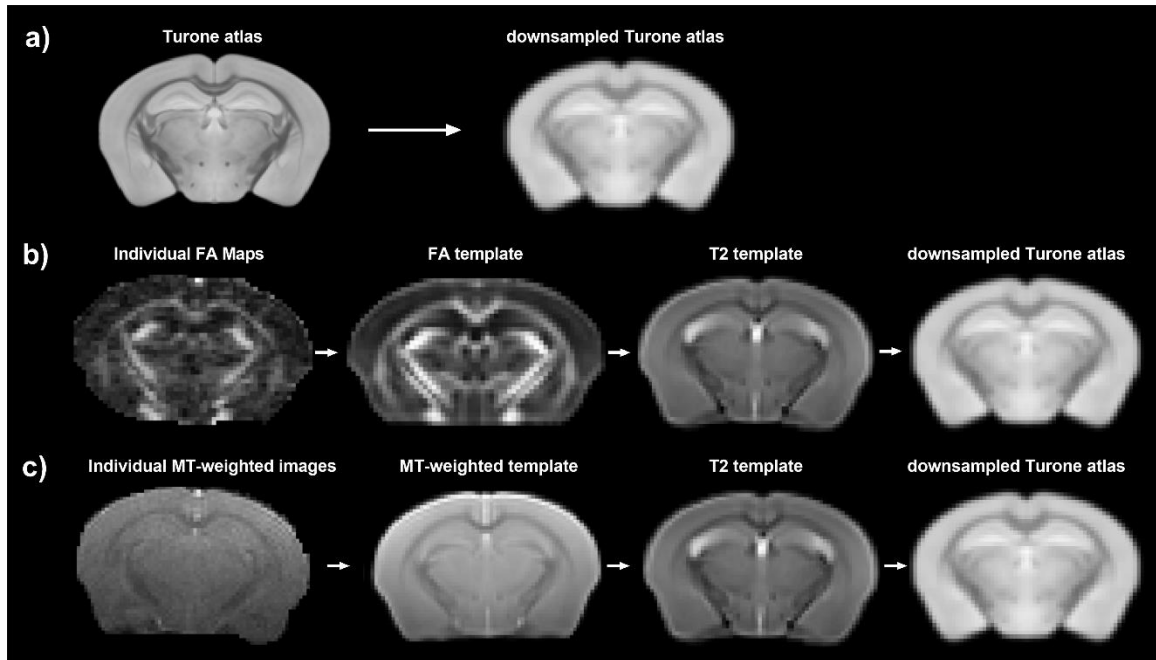
Figure A.8 - *Schematic of registration steps. a) The Turone atlas (60 μm isotropic resolution) was downsampled to the resolution of the T2-weighted images. b) Registration steps to register individual FA maps to the downsampled atlas space. c) Registration steps to register individual MT-weighted images to the downsampled atlas space. The registration transforms resulting from part b) and c) can be used to warp dMRI and MT metric maps to the downsampled atlas space.*

Code Availability

As mentioned previously, all code required to process dicoms to the final scalar maps are available: https://doi.org/10.20383/103.0594 (414). The code is also available publicly through GitLab: https://gitlab.com/cfmm/pipelines/mouse_dmri_MT_dicomTOscalarMaps. This includes a Snakemake pipeline, which includes FSL, MRtrix3, and ANTs commands, and MATLAB functions. The custom dMRI pulse sequences used in this work are available

as binary methods: https://osf.io/5eusw/, and the source code is available upon reasonable

request (416).

Appendix B: Permissions for Use of Copyrighted Content

Chapter 1

Figure1.2
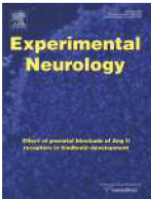
Partial interruption of axonal transport due to microtubule breakage accounts for the formation of periodic varicosities after traumatic axonal injury

Author:
Min D. Tang-Schomer,Victoria E. Johnson,Peter W. Baas,William Stewart,Douglas H. Smith

Publication: Experimental Neurology

Publisher: Elsevier

Date: January 2012

Copyright © 2011 Elsevier Inc. All rights reserved.

Review Order

Please review the order details and the associated terms and conditions.

No royalties will be charged for this reuse request although you are required to obtain a license and comply with the license terms and conditions. To obtain the license, click the Accept button below.

Licensed Content

Licensed Content Publisher	Elsevier
Licensed Content Publication	Experimental Neurology
Licensed Content Title	Partial interruption of axonal transport due to microtubule breakage accounts for the formation of periodic varicosities after traumatic axonal injury
Licensed Content Author	Min D. Tang-Schomer,Victoria E. Johnson,Peter W. Baas,William Stewart,Douglas H. Smith
Licensed Content Date	January 2012
Licensed Content Volume	233
Licensed Content Issue	1
Licensed Content Pages	9

Order Details

Type of Use	reuse in a thesis/dissertation
Portion	figures/tables/illustrations
Number of figures/tables/illustrations	7
Format	both print and electronic
Are you the author of this Elsevier article?	No
Will you be translating?	No

📄 About Your Work ✏️

Title of new work	Microstructural MRI Evolution During Adult Mouse Brain Maturation and Concussion Recovery
Institution name	Western University
Expected presentation date	May 2024

📁 Additional Data

Portions	Figure 7

📍 Requestor Location ✏️

Requestor Location	Ms. Naila Rahman 1 Grosvenor St. Apt. 1220 London, ON N6A 1Y2 Canada Attn: Western University

📋 Tax Details

Publisher Tax ID	GB 494 6272 12

☑ I agree to these terms and conditions.

☐ I understand this license is for reuse only and that no content is provided.

Total: 0.00 CAD

BACK   DECLINE   SAVE QUOTE   ACCEPT

Please click accept only once.

Figure 1.5

Figure 1.9

Figure 1.10

Chapter 3

JOHN WILEY AND SONS LICENSE
TERMS AND CONDITIONS

Jan 16, 2024

This Agreement between Ms. Naila Rahman ("You") and John Wiley and Sons ("John Wiley and Sons") consists of your license details and the terms and conditions provided by John Wiley and Sons and Copyright Clearance Center.

License Number	5710830838850
License date	Jan 16, 2024
Licensed Content Publisher	John Wiley and Sons
Licensed Content Publication	Journal of Magnetic Resonance Imaging
Licensed Content Title	Test–Retest Reproducibility of In Vivo Magnetization Transfer Ratio and Saturation Index in Mice at 9.4 Tesla
Licensed Content Author	Naila Rahman, Jordan Ramnarine, Kathy Xu, et al
Licensed Content Date	Feb 14, 2022
Licensed Content Volume	56
Licensed Content Issue	3
Licensed Content Pages	11
Type of use	Dissertation/Thesis

Requestor type	Author of this Wiley article
Format	Print and electronic
Portion	Full article
Will you be translating?	No
Title of new work	Microstructural MRI Evolution During Adult Mouse Brain Maturation and Concussion Recovery
Institution name	Western University
Expected presentation date	May 2024

References

1.   Kerr JND, Denk W. Imaging in vivo: Watching the brain in action. Nat Rev Neurosci. 2008;9(3):195–205.

2.   Garcia-Alloza M, Bacskai BJ. Techniques for brain imaging in vivo. NeuroMolecular Med. 2004;6(1):65–78.

3.   Weiskopf N, Edwards LJ, Helms G, Mohammadi S, Kirilina E. Quantitative magnetic resonance imaging of brain anatomy and in vivo histology. Nat Rev Phys. 2021;3(8):570–88.

4.   Granziera C, Wuerfel J, Barkhof F, Calabrese M, De Stefano N, Enzinger C, et al. Quantitative magnetic resonance imaging towards clinical application in multiple sclerosis. Brain. 2021;144(5):1296–311.

5.   Keenan KE, Biller JR, Delfino JG, Boss MA, Does MD, Evelhoch JL, et al. Recommendations towards standards for quantitative MRI (qMRI) and outstanding needs. J Magn Reson Imaging. 2019;49(7):e26–39.

6.   Adler CH, Beach TG, Zhang N, Shill HA, Driver-Dunckley E, Mehta SH, et al. Clinical Diagnostic Accuracy of Early/Advanced Parkinson Disease: An Updated Clinicopathologic Study. Neurol Clin Pract. 2021;11(4):E414–21.

7.   Le Bihan D. Looking into the functional architecture of the brain with diffusion MRI. Nat Rev Neurosci. 2003;4(6):469–80.

8.   Jones DK, Knösche TR, Turner R. White matter integrity, fiber count, and other fallacies: The do's and don'ts of diffusion MRI. Neuroimage. 2013;73:239–54.

9.   Xu J. Probing neural tissues at small scales: Recent progress of oscillating gradient spin echo (OGSE) neuroimaging in humans. J Neurosci Methods. 2021;349(April 2020):109024.

10.   Schachter M, Does MD, Anderson AW, Gore JC. Measurements of Restricted Diffusion Using an Oscillating Gradient Spin-Echo Sequence. J Magn Reson. 2000;147(2):232–7.

11.   Westin CF, Knutsson H, Pasternak O, Szczepankiewicz F, Özarslan E, van Westen D, et al. Q-space trajectory imaging for multidimensional diffusion MRI of the human brain. Neuroimage. 2016;135:345–62.

12.   Arezza NJJ, Tse DHY, Baron CA. Rapid microscopic fractional anisotropy imaging via an optimized linear regression formulation. Magn Reson Imaging. 2021;80(April):132–43.

13.   Szczepankiewicz F, Westin CF, Nilsson M. Gradient waveform design for tensor-valued encoding in diffusion MRI. J Magn Reson. 2021;348.

14.   Helms G, Dathe H, Kallenberg K, Dechent P. High-resolution maps of magnetization transfer with inherent correction for RF inhomogeneity and T1 relaxation obtained from 3D FLASH MRI. Magn Reson Med. 2008;60(6):1396–

407.

15. Helms G, Dathe H, Dechent P. Modeling the influence of TR and excitation flip angle on the Magnetization Transfer Ratio (MTR) in human brain Obtained from 3D spoiled gradient echo MRI. Magn Reson Med. 2010;64(1):177–85.

16. Yang G, Tian Q, Leuze C, Wintermark M, McNab J. Double Diffusion Encoding MRI for the Clinic. Magn Reson Med. 2018;80(2):507–20.

17. Andersen KW, Lasič S, Lundell H, Nilsson M, Topgaard D, Sellebjerg F, et al. Disentangling white-matter damage from physiological fibre orientation dispersion in multiple sclerosis. Brain Commun. 2020;2(2).

18. Lema A, Bishop C, Malik O, Mattoscio M, Ali R, Nicholas R, et al. A Comparison of Magnetization Transfer Methods to Assess Brain and Cervical Cord Microstructure in Multiple Sclerosis. J Neuroimaging. 2017;27(2):221–6.

19. Budde MD, Frank JA. Neurite beading is sufficient to decrease the apparent diffusion coefficient after ischemic stroke. Proc Natl Acad Sci U S A. 2010;107(32):14472–7.

20. Baron CA, Kate M, Gioia L, Butcher K, Emery D, Budde M, et al. Reduction of Diffusion-Weighted Imaging Contrast of Acute Ischemic Stroke at Short Diffusion Times. Stroke. 2015;46(8):2136–41.

21. Szczepankiewicz F, Lasič S, van Westen D, Sundgren PC, Englund E, Westin CF, et al. Quantification of microscopic diffusion anisotropy disentangles effects of orientation dispersion from microstructure: Applications in healthy volunteers and in brain tumors. Neuroimage. 2015;104:241–52.

22. Eierud C, Craddock RC, Fletcher S, Aulakh M, King-Casas B, Kuehl D, et al. Neuroimaging after mild traumatic brain injury: Review and meta-analysis. NeuroImage Clin. 2014;4:283–94.

23. Hammelrath L, Škokić S, Khmelinskii A, Hess A, van der Knaap N, Staring M, et al. Morphological maturation of the mouse brain: An in vivo MRI and histology investigation. Neuroimage. 2016;125:144–52.

24. Lebel C, Walker L, Leemans A, Phillips L, Beaulieu C. Microstructural maturation of the human brain from childhood to adulthood. Neuroimage. 2008;40(3):1044–55.

25. Yu F, Shukla DK, Armstrong RC, Marion CM, Radomski KL, Selwyn RG, et al. Repetitive Model of Mild Traumatic Brain Injury Produces Cortical Abnormalities Detectable by Magnetic Resonance Diffusion Imaging, Histopathology, and Behavior. J Neurotrauma. 2017;34(7):1364–81.

26. waxman SG. Clinical Neuroanatomy; twenty-seventh edition. Neurology Secrets: Sixth Edition. 2013. 195–200 p.

27. Crossman AR, Neary D. Neuroanatomy : an illustrated colour text / Alan R. Crossman, David Neary. 2020. 185 p.

28. von Bartheld CS. Myths and truths about the cellular composition of the human

brain: A review of influential concepts. J Chem Neuroanat. 2018;93(August 2017):2–15.

29. von Bartheld CS, Bahney J, Herculano-Houzel S. The search for true numbers of neurons and glial cells in the human brain: A review of 150 years of cell counting. J Comp Neurol. 2016;524(18):3865–95.

30. Salas IH, Burgado J, Allen NJ. Glia: victims or villains of the aging brain? Neurobiol Dis. 2020;143(July).

31. Nishiyama A, Shimizu T, Sherafat A, Richardson WD. Life-long oligodendrocyte development and plasticity. Semin Cell Dev Biol. 2021;116(February):25–37.

32. Arain M, Johal L. Maturation of the adolescent brain. 2013;449–61.

33. Tian L, Ma L. Microstructural Changes of the Human Brain from Early to. Front Hum Neurosci. 2017;11(August):1–12.

34. Dow-Edwards D, MacMaster FP, Peterson BS, Niesink R, Andersen S, Braams BR. Experience during adolescence shapes brain development: From synapses and networks to normal and pathological behavior. Neurotoxicol Teratol. 2019;76(September):106834.

35. Laube C, van den Bos W, Fandakova Y. The relationship between pubertal hormones and brain plasticity: Implications for cognitive training in adolescence. Dev Cogn Neurosci. 2020;42(May 2019):100753.

36. Fuhrmann D, Knoll LJ, Blakemore SJ. Adolescence as a Sensitive Period of Brain Development. Trends Cogn Sci. 2015;19(10):558–66.

37. Tamnes CK, Østby Y, Fjell AM, Westlye T, Due-tønnessen P, Walhovd KB. Brain Maturation in Adolescence and Young Adulthood : Regional Age-Related Changes in Cortical Thickness and White Matter Volume and Microstructure. 2010;i(March).

38. Lebel C, Gee M, Camicioli R, Wieler M, Martin W, Beaulieu C. Diffusion tensor imaging of white matter tract evolution over the lifespan. Neuroimage. 2012;60(1):340–52.

39. Yakovlev P, Lecours A. The myelogenetic cycles of regional maturation of the brain. Reg Dev ofthe Brain Early Life. 1967;3–70.

40. Benes FM. Myelination of cortical-hippocampal relays during late adolescence. Schizophr Bull. 1989;15(4):585–93.

41. Sims RE, Butcher JB, Parri HR, Glazewski S. Astrocyte and Neuronal Plasticity in the Somatosensory System. Neural Plast. 2015;2015.

42. Ikegami A, Haruwaka K, Wake H. Microglia: Lifelong modulator of neural circuits. Neuropathology. 2019;39(3):173–80.

43. Baraban M, Mensch S, Lyons DA. Adaptive myelination from fish to man. Brain Res. 2016;1641:149–61.

44. Sams EC. Oligodendrocytes in the aging brain. Neuronal Signal. 2021;5(3):1–24.

45. Pajevic S, Basser PJ, Fields RD. Role of myelin plasticity in oscillations and synchrony of neuronal activity. Neuroscience. 2014;276:135–47.

46. García-Marqués J, Núñez-Llaves R, López-Mascaraque L. NG2-glia from pallial progenitors produce the largest clonal clusters of the brain: Time frame of clonal generation in cortex and olfactory bulb. J Neurosci. 2014;34(6):2305–13.

47. Tator C. Subcommittee of Sports-related Concussion Evidence 1855. 2019.

48. McCrory P, Meeuwisse W, Dvořák J, Aubry M, Bailes J, Broglio S, et al. Consensus statement on concussion in sport—the 5th international conference on concussion in sport held in Berlin, October 2016. Br J Sports Med. 2017;51(11):838–47.

49. McInnes K, Friesen CL, MacKenzie DE, Westwood DA, Boe SG. Mild Traumatic Brain Injury (mTBI) and chronic cognitive impairment: A scoping review. PLoS One. 2017;12(4).

50. Belanger HG, Vanderploeg RD, Curtiss G, Warden DL. Recent neuroimaging techniques in mild traumatic brain injury. J Neuropsychiatry Clin Neurosci. 2007;19(1):5–20.

51. Hoge C, McGurk D, Thomas J, Cox A, Engel C, Castro C. Mild Traumatic Brain Injury in U.S. Soldiers Returning from Iraq Charles. N Engl J Med. 2008;358(5):453–63.

52. Niogi SN, Mukherjee P, Ghajar J, Johnson CE, Kolster R, Lee H, et al. Structural dissociation of attentional control and memory in adults with and without mild traumatic brain injury. Brain. 2008;131(12):3209–21.

53. Müller K, Townend W, Biasca N, Undén J, Waterloo K, Romner B, et al. S100B serum level predicts computed tomography findings after minor head injury. J Trauma - Inj Infect Crit Care. 2007;62(6):1452–6.

54. Topolovec-Vranic J, Pollmann-Mudryj MA, Ouchterlony D, Klein D, Spence J, Romaschin A, et al. The value of serum biomarkers in prediction models of outcome after mild traumatic brain injury. J Trauma - Inj Infect Crit Care. 2011;71(5 SUPPL.1).

55. Katz DI, Cohen SI, Alexander MP. Mild traumatic brain injury. 1st ed. Vol. 127, Handbook of Clinical Neurology. Elsevier B.V.; 2015. 131–156 p.

56. Sterr A, Herron KA, Hayward C, Montaldi D. Are mild head injuries as mild as we think? Neurobehavioral concomitants of chronic post-concussion syndrome. BMC Neurol. 2006;6:1–10.

57. Spinos P, Sakellaropoulos G, Georgiopoulos M, Stavridi K, Apostolopoulou K, Ellul J, et al. Postconcussion syndrome after mild traumatic brain injury in Western Greece. J Trauma - Inj Infect Crit Care. 2010;69(4):789–93.

58. Rutherford WH, Merrett JD, McDonald JR. Symptoms at one year following concussion from minor head injuries. Injury. 1979;10(3):225–30.

59. Choe M, Giza C. Diagnosis and Management of Acute Concussion. Semin Neurol.

2015;35(1):29–41.

60. SCAT3. Br J Sport Med. 2013;47(5):259–62.

61. Schatz P, Pardini JE, Lovell MR, Collins MW, Podell K. Sensitivity and specificity of the ImPACT Test Battery for concussion in athletes. Arch Clin Neuropsychol. 2006;21(1):91–9.

62. Kuhn AW, Solomon GS. Supervision and computerized neurocognitive baseline test performance in high school athletes: An initial investigation. J Athl Train. 2014;49(6):800–5.

63. Collie A, Darby DG, Falleti MG, Silbert BS, Maruff P. Determining the extent of cognitive change after coronary surgery: A review of statistical procedures. Ann Thorac Surg. 2002;73(6):2005–11.

64. Collie A, Maruff P, Makdissi M, McCrory P, McStephen M, Darby D. CogSport: Reliability and correlation with conventional cognitive tests used in postconcussion medical evaluations. Clin J Sport Med. 2003;13(1):28–32.

65. Sadowski-Cron C, Schneider J, Senn P, Radanov BP, Ballinari P, Zimmermann H. Patients with mild traumatic brain injury: Immediate and long-term outcome compared to intra-cranial injuries on CT scan. Brain Inj. 2006;20(11):1131–7.

66. Yuh EL, Cooper SR, Ferguson AR, Manley GT. Quantitative CT improves outcome prediction in acute traumatic brain injury. J Neurotrauma. 2012;29(5):735–46.

67. Ashikaga R, Araki Y, Ishida O. MRI of head injury using FLAIR. Neuroradiology. 1997;39(4):239–42.

68. Schneider KJ, Iverson GL, Emery CA, McCrory P, Herring SA, Meeuwisse WH. The effects of rest and treatment following sport-related concussion: A systematic review of the literature. Br J Sports Med. 2013;47(5):304–7.

69. Giza CC, Hovda DA. The Neurometabolic Cascade of Concussion. J Athl Train. 2001;36(3):228–35.

70. Romeu-Mejia R, Giza CC, Goldman JT. CONCUSSION Concussion Pathophysiology and Injury Biomechanics. Curr Rev Musculoskelet Med. 2019;(Cdc):105–16.

71. Mayevsky A, Chance B. Repetitive patterns of metabolic changes during cortical spreading depression of the awake rat. Brain Res. 1974;65:529–33.

72. Yoshino A, Hovda DA, Kawamata T, Katayama Y, Becker DP. Dynamic changes in local cerebral glucose utilization following cerebral concussion in rats: evidence of a hyper- and subsequent hypometabolic state. Brain Res. 1991;561(1):106–19.

73. Osteen CL, Moore AH, Prins ML, Hovda DA. Age-dependency of 45calcium accumulation following lateral fluid percussion: Acute and delayed patterns. J Neurotrauma. 2001;18(2):141–62.

74. Bergsneider M, Hovda DA, Lee SM, Kelly DF, McArthur DL, Vespa PM, et al. Dissociation of cerebral glucose metabolism and level of consciousness during the

period of metabolic depression following human traumatic brain injury. J Neurotrauma. 2000;17(5):389–401.

75. Wang Y, Nelson LD, Laroche AA, Pfaller AY, Nencka AS, Koch KM, et al. Cerebral Blood Flow Alterations in Acute Sport-Related Concussion. J Neurotrauma. 2016;33(13):1227–36.

76. Fehily B, Fitzgerald M. Repeated mild traumatic brain injury: Potential mechanisms of damage. Cell Transplant. 2017;26(7):1131–55.

77. Johnson VE, Stewart W, Smith DH. Axonal pathology in traumatic brain injury. Exp Neurol. 2013;246:35–43.

78. Smith DH, Meaney DF, Shull WH. Diffuse axonal injury in head trauma. J Head Trauma Rehabil. 2003;18(4):307–16.

79. Hawkins BE, Krishnamurthy S, Castillo-Carranza DL, Sengupta U, Prough DS, Jackson GR, et al. Rapid accumulation of endogenous Tau oligomers in a rat model of traumatic brain injury: Possible link between traumatic brain injury and sporadic tauopathies. J Biol Chem. 2013;288(23):17042–50.

80. Baugh CM, Robbins CA, Stern RA, McKee AC. Current understanding of chronic traumatic encephalopathy. Curr Treat Options Neurol. 2014;16(9).

81. Smith DH, Meaney DF. PROGRESS IN CLINICAL NEUROSCIENCE n Axonal Damage in Traumatic Brain Injury. Neurosci. 2000;6(6):483–95.

82. Singleton RH, Zhu J, Stone JR, Povlishock JT. Traumatically induced axotomy adjacent to the soma does not result in acute neuronal death. J Neurosci. 2002;22(3):791–802.

83. Tang-Schomer MD, Johnson VE, Baas PW, Stewart W, Smith DH. Partial interruption of axonal transport due to microtubule breakage accounts for the formation of periodic varicosities after traumatic axonal injury. Exp Neurol. 2012;233(1):364–72.

84. Fu M, Zuo Y. Experience-dependent structural plasticity in the cortex. Trends Neurosci. 2011;34(4):177–87.

85. Aungst SL, Kabadi S V., Thompson SM, Stoica BA, Faden AI. Repeated mild traumatic brain injury causes chronic neuroinflammation, changes in hippocampal synaptic plasticity, and associated cognitive deficits. J Cereb Blood Flow Metab. 2014;34(7):1223–32.

86. Sofroniew M V., Vinters H V. Astrocytes: Biology and pathology. Acta Neuropathol. 2010;119(1):7–35.

87. Burda JE, Bernstein AM, Sofroniew M V. Astrocyte roles in traumatic brain injury. Exp Neurol. 2016;275:305–15.

88. Myer DJ, Gurkoff GG, Lee SM, Hovda DA, Sofroniew M V. Essential protective roles of reactive astrocytes in traumatic brain injury. Brain. 2006;129(10):2761–72.

89. Sofroniew M V. Molecular dissection of reactive astrogliosis and glial scar

formation. Trends Neurosci. 2009;32(12):638–47.

90. Villapol S, Loane DJ, Burns MP. Sexual dimorphism in the inflammatory response to traumatic brain injury. Glia. 2017;65(9):1423–38.

91. Gehrmann J, Matsumoto Y, Kreutzberg GW. Microglia: Intrinsic immuneffector cell of the brain. Brain Res Rev. 1995;20(3):269–87.

92. Zheng RZ, Lee KY, Qi ZX, Wang Z, Xu ZY, Wu XH, et al. Neuroinflammation Following Traumatic Brain Injury: Take It Seriously or Not. Front Immunol. 2022;13(March):1–13.

93. Loane DJ, Kumar A, Stoica BA, Cabatbat R, Faden AI. Progressive neurodegeneration after experimental brain trauma: Association with chronic microglial activation. J Neuropathol Exp Neurol. 2014;73(1):14–29.

94. Morganti-Kossmann MC, Rancan M, Stahel PF, Kossmann T. Inflammatory response in acute traumatic brain injury: A double-edged sword. Curr Opin Crit Care. 2002;8(2):101–5.

95. Mouzon BC, Bachmeier C, Ferro A, Ojo JO, Crynen G, Acker CM, et al. Chronic neuropathological and neurobehavioral changes in a repetitive mild traumatic brain injury model. Ann Neurol. 2014;75(2):241–54.

96. Brody DL, Benetatos J, Bennett RE, Klemenhagen KC, Mac Donald CL. The pathophysiology of repetitive concussive traumatic brain injury in experimental models; new developments and open questions. Mol Cell Neurosci. 2015;66(PB):91–8.

97. Freire MAM, Rocha GS, Bittencourt LO, Falcao D, Lima RR, Cavalcanti JRLP. Cellular and Molecular Pathophysiology of Traumatic Brain Injury: What Have We Learned So Far? Biology (Basel). 2023;12(8):1–27.

98. Shlosberg D, Benifla M, Kaufer D, Friedman A. Blood-brain barrier breakdown as a therapeutic target in traumatic brain injury. Nat Rev Neurol. 2010;6(7):393–403.

99. Weissberg I, Veksler R, Kamintsky L, Saar-Ashkenazy R, Milikovsky DZ, Shelef I, et al. Imaging blood-brain barrier dysfunction in football players. JAMA Neurol. 2014;71(11):1453–5.

100. Zagorchev L, Meyer C, Stehle T, Wenzel F, Young S, Peters J, et al. Differences in regional brain volumes two months and one year after mild traumatic brain injury. J Neurotrauma. 2016;33(1):29–34.

101. Mierzwa AJ, Marion CM, Sullivan GM, McDaniel DP, Armstrong RC. Components of myelin damage and repair in the progression of white matter pathology after mild traumatic brain injury. J Neuropathol Exp Neurol. 2015;74(3):218–32.

102. Ming CL, Akle V, Zheng W, Kitlen J, O'Steen B, Larner SF, et al. Extensive degradation of myelin basic protein isoforms by calpain following traumatic brain injury. J Neurochem. 2006;98(3):700–12.

103. Goes A Van Der, Brouwer J, Hoekstra K, Roos D. Reactive oxygen species are

required for the phagocytosis of myelin by macrophages. 1998;67–75.

104. Rhodes KE, Raivich G, Fawcett JW. The injury response of oligodendrocyte precursor cells is induced by platelets, macrophages and inflammation-associated cytokines. 2006;140:87–100.

105. Bramlett HM, Dietrich WD. Quantitative structural changes in white and gray matter 1 year following traumatic brain injury in rats. 2002;607–14.

106. Rodriguez-paez A, Brunschwig JP, Bramlett HM. Light and electron microscopic assessment of progressive atrophy following moderate traumatic brain injury in the rat. 2005;603–16.

107. Sullivan GM, Mierzwa AJ, Kijpaisalratana N, Tang H, Wang Y, Song S, et al. Oligodendrocyte Lineage and Subventricular Zone Response to Traumatic Axonal Injury in the Corpus Callosum. 2013;72(12):1106–25.

108. Nishimura DG. Principles of Magnetic Resonance Imaging. Lulu; 2010.

109. Bernstein M, King K, Xhou X. Handbook of MRI Pulse Sequences. Elsevier; 2004.

110. Jelescu IO, Fieremans E. Sensitivity and specificity of diffusion MRI to neuroinflammatory processes. 1st ed. Vol. 9, Advances in Magnetic Resonance Technology and Applications. Elsevier Inc.; 2023. 31–50 p.

111. Brown R. XXVII. A brief account of microscopical observations made in the months of June, July and August 1827, on the particles contained in the pollen of plants; and on the general existence of active molecules in organic and inorganic bodies. Philos Mag. 1828;4(21):161–173.

112. Einstein A. Investigations on the theory of the Brownian movement. Dover Publ. 1956;

113. Stejskal EO, Tanner JE. Spin diffusion measurements: Spin echoes in the presence of a time-dependent field gradient. J Chem Phys. 1965;42(1):288–92.

114. Hahn EL. Spin echoes. Phys Rev. 1950;80(4):580–94.

115. Patterson DM, Padhani AR, Collins DJ. Technology Insight: Water diffusion MRI - A potential new biomarker of response to cancer therapy. Nat Clin Pract Oncol. 2008;5(4):220–33.

116. Turner R, Le Bihan D. Single-shot diffusion imaging at 2.0 tesla. J Magn Reson. 1990;86(3):445–52.

117. M.K. S, R. T, P. M. Echo-planar imaging: Magnetic resonance imaging in a fraction of a second. Science (80-). 1991;254(5028):43–50.

118. Paschal CB, Morris HD. K-Space in the Clinic. J Magn Reson Imaging. 2004;19(2):145–59.

119. O'Donnell LJ, Westin C-F. An introduction to diffusion tensor image analysis. Neurosurg Clin N Am. 2011;22(2):185–viii.

120. Lo Buono V, Palmeri R, Corallo F, Allone C, Pria D, Bramanti P, et al. Diffusion

tensor imaging of white matter degeneration in early stage of Alzheimer's disease: a review. Int J Neurosci. 2020;130(3):243–50.

121. Budde MD, Skinner NP. Diffusion MRI in acute nervous system injury. J Magn Reson. 2018;292:137–48.

122. Sotak CH. The role of diffusion tensor imaging in the evaluation of ischemic brain - A review. NMR Biomed. 2002;15(7–8):561–9.

123. Zhuo J, Xu S, Hazelton J, Mullins R, Simon J. Diffusion Kurtosis as an In Vivo Imaging Marker for Reactive Astrogliosis in Traumatic Brain Injury. Nueroimage. 2012;59(1):467–77.

124. Jensen JH, Helpern JA, Ramani A, Lu H, Kaczynski K. Diffusional kurtosis imaging: The quantification of non-Gaussian water diffusion by means of magnetic resonance imaging. Magn Reson Med. 2005;53(6):1432–40.

125. Han XF, Geng ZJ, Zhu QF, Song ZH, Lv H Di. Diffusion kurtosis imaging: An efficient tool for evaluating age-related changes in rat brains. Brain Behav. 2021;11(11):1–9.

126. Raja R, Sinha N, Saini J, Mahadevan A, Rao KN, Swaminathan A. Assessment of tissue heterogeneity using diffusion tensor and diffusion kurtosis imaging for grading gliomas. Neuroradiology. 2016;58(12):1217–31.

127. Tugan Muftuler L, Meier TB, Keith M, Budde MD, Huber DL, McCrea MA. Serial Diffusion Kurtosis Magnetic Resonance Imaging Study during Acute, Subacute, and Recovery Periods after Sport-Related Concussion. J Neurotrauma. 2020;37(19):2081–92.

128. Batista C, Gomes GF, Candelario-jalil E, Fiebich BL, Oliveira A. Lipopolysaccharide-Induced Neuroinflammation as a Bridge to Understand Neurodegeneration. Int J Mol Sci. 2019;20(2293).

129. Lodygensky G, West T, Stump M, DM H, Inder T, Neil J. In vivo MRI analysis of an inflammatory injury in the developing brain. Brain Behav Immun. 2010;24(5):759–67.

130. Guan X, Liu S, Liang M, Li G, Dong J, Zhou Q. Diffusion kurtosis imaging to evaluate the effect and mechanism of tetramethylpyrazine on cognitive impairment induced by lipopolysaccharide in rats. Brain Imaging Behav. 2021;15(5):2492–501.

131. Guglielmetti C, Veraart J, Roelant E, Mai Z, Daans J, Van Audekerke J, et al. Diffusion kurtosis imaging probes cortical alterations and white matter pathology following cuprizone induced demyelination and spontaneous remyelination. Neuroimage. 2016;125:363–77.

132. Jelescu IO, Zurek M, Winters K V, Veraart J, Kim NS, Babb JS, et al. In vivo quantification of demyelination and recovery using compartment-specific diffusion MRI metrics validated by electron microscopy. Neuroimage. 2016;132:104–14.

133. Wang Y, Wang Q, Haldar JP, Yeh FC, Xie M, Sun P, et al. Quantification of increased cellularity during inflammatory demyelination. Brain.

2011;134(12):3587–98.

134. Falangola MF, Guilfoyle DN, Tabesh A, Hui ES, Nie X, Jensen JH, et al. Histological correlation of diffusional kurtosis and white matter modeling metrics in cuprizone-induced corpus callosum demyelination. NMR Biomed. 2014;27(8):948–57.

135. van de Looij Y, Mauconduit F, Beaumont M, Valable S, Farion R, Francony G, et al. Diffusion tensor imaging of diffuse axonal injury in a rat brain trauma model. NMR Biomed. 2012;25(1):93–103.

136. Bennett RE, Mac Donald CL, Brody DL. Diffusion tensor imaging detects axonal injury in a mouse model of repetitive closed-skull traumatic brain injury. Neurosci Lett. 2012;513(2):160–5.

137. Mac Donald CL, Dikranian K, Bayly P, Holtzman D, Brody D. Diffusion tensor imaging reliably detects experimental traumatic axonal injury and indicates approximate time of injury. J Neurosci. 2007;27(44):11869–76.

138. Hutchinson EB, Schwerin SC, Avram A V., Juliano SL, Pierpaoli C. Diffusion MRI and the detection of alterations following traumatic brain injury. J Neurosci Res. 2018;96(4):612–25.

139. Hui E, Du F, Huang S, Shen Q, Duong T. Spatiotemporal dynamics of diffusional kurtosis, mean diffusivity and perfusion changes in experimental stroke. Brain Res. 2012;1451:100–9.

140. Hui E, Fieremans E, Jensen J, Tabesh A, Feng W, Bonilha L, et al. Stroke Assessment with Diffusional Kurtosis Imaging. Stroke. 2012;43(11).

141. Lasič S, Szczepankiewicz F, Eriksson S, Nilsson M, Topgaard D. Microanisotropy imaging: Quantification of microscopic diffusion anisotropy and orientational order parameter by diffusion MRI with magic-angle spinning of the q-vector. Front Phys. 2014;2(February):1–14.

142. Figley CR, Uddin MN, Wong K, Kornelsen J, Puig J, Figley TD. Potential Pitfalls of Using Fractional Anisotropy, Axial Diffusivity, and Radial Diffusivity as Biomarkers of Cerebral White Matter Microstructure. Front Neurosci. 2022;15(January):1–7.

143. Pierpaoli C, Barnett A, Pajevic S, Chen R, Penix LR, Virta A, et al. Water diffusion changes in wallerian degeneration and their dependence on white matter architecture. Neuroimage. 2001;13(6):1174–85.

144. Beaulieu C, Allen PS. Water diffusion in the giant axon of the squid: Implications for diffusion-weighted MRI of the nervous system. Magn Reson Med. 1994;32(5):579–83.

145. Beaulieu C, Allen PS. An In Vitro Evaluation of the Effects of Local Magnetic-Susceptibility-Induced Gradients on Anisotropic Water Diffusion in Nerve. Magn Reson Med. 1996;36(1):39–44.

146. Joost S, Schweiger F, Pfeiffer F, Ertl C, Keiler J, Frank M, et al. Cuprizone Intoxication Results in Myelin Vacuole Formation. Front Cell Neurosci.

2022;16(February).

147. Davis BM, Salinas-Navarro M, Cordeiro MF, Moons L, Groef L De. Characterizing microglia activation: A spatial statistics approach to maximize information extraction. Sci Rep. 2017;7(1):1–12.

148. Erö C, Gewaltig MO, Keller D, Markram H. A cell atlas for the mouse brain. Front Neuroinform. 2018;12(November):1–16.

149. Kongsui R, Beynon SB, Johnson SJ, Walker FR. Quantitative assessment of microglial morphology and density reveals remarkable consistency in the distribution and morphology of cells within the healthy prefrontal cortex of the rat. J Neuroinflammation. 2014;11(1):1–9.

150. Degl'Innocenti E, Dell'Anno MT. Human and mouse cortical astrocytes: a comparative view from development to morphological and functional characterization. Front Neuroanat. 2023;17(April):1–10.

151. Valério-Gomes B, Guimarães DM, Szczupak D, Lent R. The absolute number of oligodendrocytes in the adult mouse brain. Front Neuroanat. 2018;12(October):1–19.

152. Haase A. Snapshot FLASH MRI. Applications to T1, T2, and Chemical-Shift Imaging. Magn Reson Med. 1990;13:77–89.

153. Schmierer K, Scaravilli F, Altmann DR, Barker GJ, Miller DH. Magnetization transfer ratio and myelin in postmortem multiple sclerosis brain. Ann Neurol. 2004;56(3):407–15.

154. Mottershead JP, Schmierer K, Clemence M, Thornton JS, Scaravilli F, Barker GJ, et al. High field MRI correlates of myelin content and axonal density in multiple sclerosis: A post-mortem study of the spinal cord. J Neurol. 2003;250(11):1293–301.

155. Harkins KD, Xu J, Dula AN, Li K, Valentine WM, Gochberg DF, et al. The microstructural correlates of T1 in white matter. Magn Reson Med. 2016;75(3):1341–5.

156. Stüber C, Morawski M, Schäfer A, Labadie C, Wähnert M, Leuze C, et al. Myelin and iron concentration in the human brain: A quantitative study of MRI contrast. Neuroimage. 2014;93(P1):95–106.

157. Eriksson S, Lasič S, Nilsson M, Westin CF, Topgaard D. NMR diffusion-encoding with axial symmetry and variable anisotropy: Distinguishing between prolate and oblate microscopic diffusion tensors with unknown orientation distribution. J Chem Phys. 2015;142(10).

158. Westin CF, Szczepankiewicz F, Pasternak O, Özarslan E, Topgaard D, Knutsson H, et al. Measurement tensors in diffusion MRI: Generalizing the concept of diffusion encoding. MICCAI. 2014;LNCS 8675(PART 3):209–16.

159. Le Bihan D, Breton E, Lallemand D, Grenier P, Cabanis E, Laval-Jeantet M. MR Imaging of Intravoxel Incoherent Motions: Application to Diffusion and Perfusion in Neurologic Disorders. Radiology. 1986;161:401–7.

160. Topgaard D. Multidimensional diffusion MRI. J Magn Reson. 2017;275:98–113.

161. Jespersen SN, Olesen JL, Ianuş A, Shemesh N. Effects of nongaussian diffusion on "isotropic diffusion" measurements: An ex-vivo microimaging and simulation study. J Magn Reson. 2019;300:84–94.

162. Burcaw LM, Fieremans E, Novikov DS. Mesoscopic structure of neuronal tracts from time-dependent diffusion. Neuroimage. 2015;114:18–37.

163. Lundell H, Nilsson M, Dyrby TB, Parker GJM, Cristinacce PLH, Zhou FL, et al. Multidimensional diffusion MRI with spectrally modulated gradients reveals unprecedented microstructural detail. Sci Rep. 2019;9(1):1–12.

164. Henriques RN, Jespersen SN, Shemesh N. Correlation tensor magnetic resonance imaging. Neuroimage. 2020;211(August 2019).

165. Kiselev VG. The cumulant expansion: an overarching mathematical framework for understanding diffusion NMR. In: Diffusion MRI. 2010. p. 152–68.

166. Jones D. Diffusion MRI. Oxford: Oxford University Press; 2010.

167. Stepišnik J. Analysis of NMR self-diffusion measurements by a density matrix calculation. Phys B&C. 1981;104(3):350–64.

168. Afzali M, Pieciak T, Jones DK, Schneider JE, Özarslan E. Cumulant expansion with localization: A new representation of the diffusion MRI signal. Front Neuroimaging. 2022;1.

169. Does MD, Parsons EC, Gore JC. Oscillating gradient measurements of water diffusion in normal and globally ischemic rat brain. Magn Reson Med. 2003;49(2):206–15.

170. Baron CA, Beaulieu C. Oscillating gradient spin-echo (OGSE) diffusion tensor imaging of the human brain. Magn Reson Med. 2014;72(3):726–36.

171. Novikov DS, Fieremans E, Jespersen SN, Kiselev VG. Quantifying brain microstructure with diffusion MRI: Theory and parameter estimation. NMR Biomed. 2019;32(4):1–53.

172. Parsons EC, Does MD, Gore JC. Modified oscillating gradient pulses for direct sampling of the diffusion spectrum suitable for imaging sequences. Magn Reson Imaging. 2003;21(3–4):279–85.

173. Van AT, Holdsworth SJ, Bammer R. In vivo investigation of restricted diffusion in the human brain with optimized oscillating diffusion gradient encoding. Magn Reson Med. 2014;71(1):83–94.

174. Parsons EC, Does MD, Gore JC. Temporal diffusion spectroscopy: Theory and implementation in restricted systems using oscillating gradients. Magn Reson Med. 2006;55(1):75–84.

175. Reynaud O. Time-dependent diffusion MRI in cancer: Tissue modeling and applications. Front Phys. 2017;5(NOV):1–16.

176. Xu J, Does MD, Gore JC. Dependence of temporal diffusion spectra on microstructural properties of biological tissues. Magn Reson Imaging.

2011;29(3):380–90.

177. Novikov DS, Kiselev VG. Surface-to-volume ratio with oscillating gradients. J Magn Reson. 2011;210(1):141–5.

178. Novikov DS, Jensen JH, Helpern JA, Fieremans E. Revealing mesoscopic structural universality with diffusion. Proc Natl Acad Sci U S A. 2014;111(14):5088–93.

179. Helms G, Dathe H, Dechent P. Quantitative FLASH MRI at 3T Using a Rational Approximation of the Ernst Equation. 2008;672:667–72.

180. Weiskopf N, Suckling J, Williams G, Correia M. MM, Inkster B, Tait R, et al. Quantitative multi-parameter mapping of R1, PD*, MT, and R2* at 3T: A multi-center validation. Front Neurosci. 2013;7(7 JUN):1–11.

181. Rahman N, Xu K, Omer M, Budde MD, Brown A, Baron CA. Test-retest reproducibility of in vivo oscillating gradient and microscopic anisotropy diffusion MRI in mice at 9.4 Tesla. PLoS One. 2021;16(11):e0255711.

182. Alexander DC, Dyrby TB, Nilsson M, Zhang H. Imaging brain microstructure with diffusion MRI: practicality and applications. NMR Biomed. 2019;32(4):1–26.

183. Arbabi A, Kai J, Khan AR, Baron CA. Diffusion dispersion imaging: Mapping oscillating gradient spin-echo frequency dependence in the human brain. Magn Reson Med. 2020;83(6):2197–208.

184. Nilsson M, Szczepankiewicz F, Brabec J, Taylor M, Westin CF, Golby A, et al. Tensor-valued diffusion MRI in under 3 minutes: an initial survey of microscopic anisotropy and tissue heterogeneity in intracranial tumors. Magn Reson Med. 2020;83(2):608–20.

185. Mitra PP. Multiple wave-vector extensions of the NMR pulsed-field-gradient spin-echo diffusion measurement. Am Phys Soc. 1995;51(21):74–8.

186. Ianuş A, Drobnjak I, Alexander DC. Model-based estimation of microscopic anisotropy using diffusion MRI: A simulation study. NMR Biomed. 2016;29(5):672–85.

187. Özarslan E. Compartment shape anisotropy (CSA) revealed by double pulsed field gradient MR. J Magn Reson. 2009;199(1):56–67.

188. Cheng Y, Cory DG. Multiple scattering by NMR. J Am Chem Soc. 1999;121(34):7935–6.

189. Shemesh N, Jespersen SN, Alexander DC, Cohen Y, Drobnjak I, Dyrby TB, et al. Conventions and nomenclature for double diffusion encoding NMR and MRI. Magn Reson Med. 2016;75(1):82–7.

190. Jespersen SN, Lundell H, Sønderby CK, Dyrby TB. Orientationally invariant metrics of apparent compartment eccentricity from double pulsed field gradient diffusion experiments. NMR Biomed. 2013;26(12):1647–62.

191. Shemesh N, Cohen Y. Microscopic and compartment shape anisotropies in gray and white matter revealed by angular bipolar double-PFG MR. Magn Reson Med.

2011;65(5):1216–27.

192. Xu J, Jiang X, Devan SP, Arlinghaus LR, McKinley ET, Xie J, et al. MRI-cytometry: Mapping nonparametric cell size distributions using diffusion MRI. Magn Reson Med. 2021;85(2):748–61.

193. Ianuş A, Jespersen SN, Serradas Duarte T, Alexander DC, Drobnjak I, Shemesh N. Accurate estimation of microscopic diffusion anisotropy and its time dependence in the mouse brain. Neuroimage. 2018;183(November 2017):934–49.

194. Tétreault P, Harkins KD, Baron CA, Stobbe R, Does MD, Beaulieu C. Diffusion time dependency along the human corpus callosum and exploration of age and sex differences as assessed by oscillating gradient spin-echo diffusion tensor imaging. Neuroimage. 2020;210(January).

195. Harkins KD, Beaulieu C, Xu J, Gore JC, Does MD. A simple estimate of axon size with diffusion MRI. Neuroimage. 2021;227(December 2020):117619.

196. Bongers A, Hau E, Shen H. Short Diffusion Time Diffusion-Weighted Imaging With Oscillating Gradient Preparation as an Early Magnetic Resonance Imaging Biomarker for Radiation Therapy Response Monitoring in Glioblastoma: A Preclinical Feasibility Study. Int J Radiat Oncol Biol Phys. 2018;102(4):1014–23.

197. Drobnjak I, Zhang H, Ianuş A, Kaden E, Alexander DC. PGSE, OGSE, and sensitivity to axon diameter in diffusion MRI: Insight from a simulation study. Magn Reson Med. 2016;75(2):688–700.

198. Kakkar LS, Bennett OF, Siow B, Richardson S, Ianuş A, Quick T, et al. Low frequency oscillating gradient spin-echo sequences improve sensitivity to axon diameter: An experimental study in viable nerve tissue. Neuroimage. 2018;182(January 2017):314–28.

199. Siow B, Drobnjak I, Ianus A, Christie I, Lythgoe M, Alexander D. Axon radius estimation with Oscillating Gradient Spin Echo (OGSE) Diffusion MRI. Diffus Fundam. 2013;18(1):1–6.

200. Nilsson M, Lasič S, Drobnjak I, Topgaard D, Westin CF. Resolution limit of cylinder diameter estimation by diffusion MRI: The impact of gradient waveform and orientation dispersion. NMR Biomed. 2017;30(7):1–13.

201. Wu D, Martin LJ, Northington FJ, Zhang J. Oscillating gradient diffusion MRI reveals unique microstructural information in normal and hypoxia-ischemia injured mouse brains. Magn Reson Med. 2014;72(5):1366–74.

202. Maekawa T, Hori M, Murata K, Feiweier T, Kamiya K, Andica C, et al. Differentiation of high-grade and low-grade intra-axial brain tumors by time-dependent diffusion MRI. Magn Reson Imaging. 2020;72(December 2019):34–41.

203. Mazzoli V, Moulin K, Kogan F, Hargreaves BA, Gold GE. Diffusion Tensor Imaging of Skeletal Muscle Contraction Using Oscillating Gradient Spin Echo. Front Neurol. 2021;12(February):1–10.

204. Gao F, Shen X, Zhang H, Ba R, Ma X, Lai C, et al. Feasibility of oscillating and pulsed gradient diffusion MRI to assess neonatal hypoxia-ischemia on clinical

systems. J Cereb Blood Flow Metab. 2020;

205. Shemesh N, Barazany D, Sadan O, Bar L, Zur Y, Barhum Y, et al. Mapping apparent eccentricity and residual ensemble anisotropy in the gray matter using angular double-pulsed-field-gradient MRI. Magn Reson Med. 2012;68(3):794–806.

206. Shemesh N, Rosenberg JT, Dumez JN, Muniz JA, Grant SC, Frydman L. Metabolic properties in stroked rats revealed by relaxation-enhanced magnetic resonance spectroscopy at ultrahigh fields. Nat Commun. 2014;5:1–8.

207. Henriques RN, Jespersen SN, Shemesh N. Microscopic anisotropy misestimation in spherical-mean single diffusion encoding MRI. Magn Reson Med. 2019;81(5):3245–61.

208. He Y, Aznar S, Siebner HR, Dyrby TB. In vivo tensor-valued diffusion MRI of focal demyelination in white and deep grey matter of rodents. NeuroImage Clin. 2021;30:102675.

209. Novikov DS. The present and the future of microstructure MRI: From a paradigm shift to normal science. J Neurosci Methods. 2021;351(October 2020):108947.

210. Shahim P, Holleran L, Kim JH, Brody DL. Test-retest reliability of high spatial resolution diffusion tensor and diffusion kurtosis imaging. Sci Rep. 2017;7(1):1–14.

211. Grech-Sollars M, Hales PW, Miyazaki K, Raschke F, Rodriguez D, Wilson M, et al. Multi-centre reproducibility of diffusion MRI parameters for clinical sequences in the brain. NMR Biomed. 2015;28(4):468–85.

212. Kasa LW, Haast RAM, Kuehn TK, Mushtaha FN, Baron CA, Peters T, et al. Evaluating High Spatial Resolution Diffusion Kurtosis Imaging at 3T: Reproducibility and Quality of Fit. J Magn Reson Imaging. 2021;53(4):1175–87.

213. Albi A, Pasternak O, Minati L, Marizzoni M, Bartrés-Faz D, Bargalló N, et al. Free water elimination improves test–retest reproducibility of diffusion tensor imaging indices in the brain: A longitudinal multisite study of healthy elderly subjects. Hum Brain Mapp. 2017;38(1):12–26.

214. Xu X, Cowan M, Beraldo F, Schranz A, McCunn P, Geremia N, et al. Repetitive mild traumatic brain injury in mice triggers a slowly developing cascade of long-term and persistent behavioral deficits and pathological changes. Acta Neuropathol Commun. 2021;9(1):1–27.

215. Gazdzinski LM, Mellerup M, Wang T, Adel SAA, Lerch JP, Sled JG, et al. White Matter Changes Caused by Mild Traumatic Brain Injury in Mice Evaluated Using Neurite Orientation Dispersion and Density Imaging. J Neurotrauma. 2020;37(16):1818–28.

216. McCunn P, Gilbert KM, Zeman P, Li AX, Strong MJ, Khan AR, et al. Reproducibility of Neurite Orientation Dispersion and Density Imaging (NODDI) in rats at 9.4 Tesla. PLoS One. 2019;14(4):1–14.

217. Wright DK, Brady RD, Kamnaksh A, Trezise J, Sun M, McDonald SJ, et al.

Repeated mild traumatic brain injuries induce persistent changes in plasma protein and magnetic resonance imaging biomarkers in the rat. Sci Rep. 2019;9(1):1–13.

218. Andersson JLR, Skare S, Ashburner J. How to correct susceptibility distortions in spin-echo echo-planar images: Application to diffusion tensor imaging. Neuroimage. 2003;20(2):870–88.

219. Andersson JLR, Sotiropoulos SN. An integrated approach to correction for off-resonance effects and subject movement in diffusion MR imaging. Neuroimage. 2016;125:1063–78.

220. Haacke EM, Lindskog ED, Lin W. A fast, iterative, partial-fourier technique capable of local phase recovery. J Magn Reson. 1991;92(1):126–45.

221. Vos SB, Tax CMW, Luijten PR, Ourselin S, Leemans A, Froeling M. The importance of correcting for signal drift in diffusion MRI. Magn Reson Med. 2017;77(1):285–99.

222. Borsos KB, Tse DHY, Dubovan PI, Baron CA. Frequency tuned bipolar oscillating gradients for mapping diffusion kurtosis dispersion in the human brain. arXiv. 2021;

223. Veraart J, Novikov DS, Christiaens D, Ades-aron B, Sijbers J, Fieremans E. Denoising of diffusion MRI using random matrix theory. Neuroimage. 2016;142:394–406.

224. Tournier JD, Smith R, Raffelt D, Tabbara R, Dhollander T, Pietsch M, et al. MRtrix3: A fast, flexible and open software framework for medical image processing and visualisation. Neuroimage. 2019;202(January):116137.

225. Smith SM, Jenkinson M, Woolrich MW, Beckmann CF, Behrens TEJ, Johansen-Berg H, et al. Advances in functional and structural MR image analysis and implementation as FSL. Neuroimage. 2004;23(SUPPL. 1):208–19.

226. Shattuck DW, Leahy RM. Brainsuite: An automated cortical surface identification tool. Lect Notes Comput Sci (including Subser Lect Notes Artif Intell Lect Notes Bioinformatics). 2000;1935:50–61.

227. Avants BB, Tustison NJ, Song G, Cook PA, Klein A, Gee JC. A reproducible evaluation of ANTs similarity metric performance in brain image registration. Neuroimage. 2011;54(3):2033–44.

228. Lein ES, Hawrylycz MJ, Ao N, Ayres M, Bensinger A. Genome-wide atlas of gene expression in the adult mouse brain. Nat Artic. 2007;445(11):168–76.

229. Basser P, Mattiello J, LeBihan D. Estimation of the effective self-diffusion tensor from the NMR spin echo. J Magn Reson B. 1994;103(3):247–54.

230. Baron CA, Rahman N. Test-retest of oscillating gradient and microscopic anisotropy diffusion MRI in mice at 9.4 Tesla. 2021.

231. van Belle G. Sample Size. In: Statistical Rules of Thumb. 2nd Ed. Hoboken: John Wiley and Sons; 2018. p. 27–51.

232. Kohn M, Senyak J. Sample Size Calculators. UCSF CTSI. [Internet]. 2021 [cited

2021 Jun 19]. Available from: https://www.sample-size.net/

233. Aggarwal M, Jones M V., Calabresi PA, Mori S, Zhang J. Probing mouse brain microstructure using oscillating gradient diffusion MRI. Magn Reson Med. 2012;67(1):98–109.

234. Aggarwal M, Smith MD, Calabresi PA. Diffusion-time dependence of diffusional kurtosis in the mouse brain. Magn Reson Med. 2020;84(3):1564–78.

235. Wu D, Li Q, Northington FJ, Zhang J. Oscillating gradient diffusion kurtosis imaging of normal and injured mouse brains. NMR Biomed. 2018;31(6):1–9.

236. Chuang N, Mori S, Yamamoto A, Jiang H, Ye X, Xu X, et al. An MRI-based atlas and database of the developing mouse brain. Neuroimage. 2011;54(1):80–9.

237. Veraart J, Van Hecke W, Sijbers J. Constrained maximum likelihood estimation of the diffusion kurtosis tensor using a Rician noise model. Magn Reson Med. 2011;66(3):678–86.

238. Henriques RN, Jespersen SN, Shemesh N. Evidence for microscopic kurtosis in neural tissue revealed by Correlation Tensor MRI. 2021;1–54.

239. Rahman N, Ramnarine J, Xu K, Brown A, Baron C. Test-retest reproducibility of in vivo magnetization transfer ratio and saturation index in mice at 9.4 Tesla. J Magn Reson Imaging. 2022;56(3):893–903.

240. Gass A, Barker GJ, Kidd D, Thorpe JW, MacManus D, Brennan A, et al. Correlation of magnetization transfer ration with clinical disability in multiple sclerosis. Ann Neurol. 1994;36(1):62–7.

241. Sled JG. Modelling and interpretation of magnetization transfer imaging in the brain. Neuroimage. 2018;182(December 2017):128–35.

242. Sui YV, Bertisch H, Lee H-H, Storey P, Babb JS, Goff DC, et al. Quantitative Macromolecular Proton Fraction Mapping Reveals Altered Cortical Myelin Profile in Schizophrenia Spectrum Disorders. Cereb Cortex Commun. 2021;2(2):1–12.

243. Clarke MA, Lakhani DA, Wen S, Gao S, Smith SA, Dortch R, et al. Perilesional neurodegenerative injury in multiple sclerosis: Relation to focal lesions and impact on disability. Mult Scler Relat Disord. 2021;49(January):102738.

244. Khodanovich M, Pishchelko A, Glazacheva V, Pan E, Akulov A, Svetlik M, et al. Quantitative Imaging of White and Gray Matter Remyelination in the Cuprizone Demyelination Model Using the Macromolecular Proton Fraction. Cells. 2019;8(10).

245. Hagiwara A, Hori M, Kamagata K, Warntjes M, Matsuyoshi D, Nakazawa M, et al. Myelin Measurement: Comparison Between Simultaneous Tissue Relaxometry, Magnetization Transfer Saturation Index, and T 1 w/T 2 w Ratio Methods. Sci Rep. 2018;

246. Giorgetti E, Obrecht M, Ronco M, Panesar M, Lambert C, Accart N, et al. Magnetic Resonance Imaging as a Biomarker in Rodent Peripheral Nerve Injury Models Reveals an Age-Related Impairment of Nerve Regeneration. Sci Rep.

2019;9(1):1–18.

247. Tu TW, Williams RA, Lescher JD, Jikaria N, Turtzo LC, Frank JA. Radiological-pathological correlation of diffusion tensor and magnetization transfer imaging in a closed head traumatic brain injury model. Ann Neurol. 2016;79(6):907–20.

248. Fatemi A, Wilson MA, Phillips AW, McMahon MT, Zhang J, Smith SA, et al. In vivo magnetization transfer MRI shows dysmyelination in an ischemic mouse model of periventricular leukomalacia. J Cereb Blood Flow Metab. 2011;31(10):2009–18.

249. Pohmann R, Shajan G, Balla DZ. Contrast at high field: Relaxation times, magnetization transfer and phase in the rat brain at 16.4 T. Magn Reson Med. 2011;66(6):1572–81.

250. Xu J, Li K, Zu Z, Li X, Gochberg DF, Gore JC. Quantitative magnetization transfer imaging of rodent glioma using selective inversion recovery. NMR Biomed. 2014;27(3):253–60.

251. Li K, Li H, Zhang XY, Stokes AM, Jiang X, Kang H, et al. Influence of water compartmentation and heterogeneous relaxation on quantitative magnetization transfer imaging in rodent brain tumors. Magn Reson Med. 2016;76(2):635–44.

252. Wu TL, Byun NE, Wang F, Mishra A, Janve VA, Chen LM, et al. Longitudinal assessment of recovery after spinal cord injury with behavioral measures and diffusion, quantitative magnetization transfer and functional magnetic resonance imaging. NMR Biomed. 2020;33(4):1–14.

253. Boretius S, Dechent P, Frahm J, Helms G. Magnetization Transfer Mapping of Myelinated Fiber Tracts in Living Mice at 9. 4 T. Proc Int Symp Magn Reson Med. 2010;1252(2009):2009.

254. Field AS, Samsonov A, Alexander AL, Mossahebi P, Duncan ID. Conventional and quantitative MRI in a novel feline model of demyelination and endogenous remyelination. J Magn Reson Imaging. 2019;49(5):1304–11.

255. Olsson H, Andersen M, Wirestam R, Helms G. Mapping magnetization transfer saturation (MTsat) in human brain at 7T: Protocol optimization under specific absorption rate constraints. Magn Reson Med. 2021;(April):1–15.

256. Leutritz T, Seif M, Helms G, Samson RS, Curt A, Freund P, et al. Multiparameter mapping of relaxation (R1, R2*), proton density and magnetization transfer saturation at 3 T: A multicenter dual-vendor reproducibility and repeatability study. Hum Brain Mapp. 2020;41(15):4232–47.

257. Thiessen JD, Zhang Y, Zhang H, Wang L, Buist R, Del Bigio MR, et al. Quantitative MRI and ultrastructural examination of the cuprizone mouse model of demyelination. NMR Biomed. 2013;26(11):1562–81.

258. Campanholo K, Pitombeira M, Rimkus C, Mendes M, Apóstolos-Pereira S, Busatto Filho G, et al. Myelin imaging measures as predictors of cognitive impairment in MS patients: A hybrid PET-MRI study. Mult Scler Relat Disord. 2021;(July):103331.

259. Klingenberg M, Stark D, Eitel F, Ritter K. MRI Image Registration Considerably Improves CNN-Based Disease. Vol. 2. Springer International Publishing; 2021. 44–52 p.

260. Welsch GH, Apprich S, Zbyn S, Mamisch TC, Mlynarik V, Scheffler K, et al. Biochemical (T2, T2* and magnetisation transfer ratio) MRI of knee cartilage: Feasibility at ultra-high field (7T) compared with high field (3T) strength. Eur Radiol. 2011;21(6):1136–43.

261. Hannila I, Susanna Räinä S, Tervonen O, Ojala R, Nieminen MT. Topographical variation of T2 relaxation time in the young adult knee cartilage at 1.5 T. Osteoarthr Cartil. 2009;17(12):1570–5.

262. Rahman N, Hamilton J, Xu K, Brown A, Baron CA. Tensor-valued and frequency-dependent diffusion MRI and magnetization transfer saturation MRI evolution during adult mouse brain maturation. arXiv. 2023;

263. Manger PR, Cort J, Ebrahim N, Goodman A, Henning J, Karolia M, et al. Is 21st century neuroscience too focussed on the rat/mouse model of brain function and dysfunction? Front Neuroanat. 2008;2(NOV):1–7.

264. Bilkei-Gorzo A. Genetic mouse models of brain ageing and Alzheimer's disease. Pharmacol Ther. 2014;142(2):244–57.

265. Zhang YP, Cai J, Shields LBE, Liu N, Xu XM, Shields CB. Traumatic Brain Injury Using Mouse Models. Transl Stroke Res. 2014;5(4):454–71.

266. Fomchenko EI, Holland EC. Mouse models of brain tumors and their applications in preclinical trials. Clin Cancer Res. 2006;12(18):5288–97.

267. Mengler L, Khmelinskii A, Diedenhofen M, Po C, Staring M, Lelieveldt BPF, et al. Brain maturation of the adolescent rat cortex and striatum: Changes in volume and myelination. Neuroimage. 2014;84:35–44.

268. Huang H, Yamamoto A, Hossain MA, Younes L, Mori S. Quantitative cortical mapping of fractional anisotropy in developing rat brains. J Neurosci. 2008;28(6):1427–33.

269. Calabrese E, Johnson GA. Diffusion tensor magnetic resonance histology reveals microstructural changes in the developing rat brain. Neuroimage. 2013;79:329–39.

270. Calabrese E, Badea A, Watson C, Johnson GA. A quantitative magnetic resonance histology atlas of postnatal rat brain development with regional estimates of growth and variability. Neuroimage. 2013;71:196–206.

271. Bockhorst KH, Narayana PA, Liu R, Ahobila-Vijjula P, Ramu J, Kamel M, et al. Early postnatal development of rat brain: In vivo diffusion tensor imaging. J Neurosci Res. 2008;86(7):1520–8.

272. Aggarwal M, Zhang J, Miller MI, Sidman RL, Mori S. Magnetic resonance imaging and micro-computed tomography combined atlas of developing and adult mouse brains for stereotaxic surgery. Neuroscience. 2009;162(4):1339–50.

273. Verma R, Mori S, Shen D, Yarowsky P, Zhang J, Davatzikos C. Spatiotemporal

maturation patterns of murine brian quantified by diffusion tensor MRI and deformation-based morphometry. Proc Natl Acad Sci U S A. 2005;102(19):6978–83.

274. Zhang J, Miller MI, Plachez C, Richards LJ, Yarowsky P, Van Zijl P, et al. Mapping postnatal mouse brain development with diffusion tensor microimaging. Neuroimage. 2005;26(4):1042–51.

275. Mori S, Itoh R, Zhang J, Kaufmann WE, Van Zijl PCM, Solaiyappan M, et al. Diffusion tensor imaging of the developing mouse brain. Magn Reson Med. 2001;46(1):18–23.

276. Baloch S, Verma R, Huang H, Khurd P, Clark S, Yarowsky P, et al. Quantification of brain maturation and growth patterns in C57BL/6J mice via computational neuroanatomy of diffusion tensor images. Cereb Cortex. 2009;19(3):675–87.

277. Dai E, Zhu A, Yang GK, Quah K, Tan ET, Fiveland E, et al. Frequency-dependent diffusion kurtosis imaging in the human brain using an oscillating gradient spin echo sequence and a high-performance head-only gradient. Neuroimage. 2023;279(March):120328.

278. Tu TW, Lescher JD, Williams RA, Jikaria N, Turtzo LC, Frank JA. Abnormal injury response in spontaneous mild ventriculomegaly wistar rat brains: A pathological correlation study of diffusion tensor and magnetization transfer imaging in mild traumatic brain injury. J Neurotrauma. 2017;34(1):248–56.

279. Lazari A, Lipp I. Can MRI measure myelin? Systematic review, qualitative assessment, and meta-analysis of studies validating microstructural imaging with myelin histology. Neuroimage. 2021;230(September 2020):117744.

280. Zhou Z, Tong Q, Zhang L, Ding Q, Lu H, Jonkman LE, et al. Evaluation of the diffusion MRI white matter tract integrity model using myelin histology and Monte-Carlo simulations. Neuroimage. 2020;223(September):117313.

281. Shemesh N. Axon diameters and myelin content modulate microscopic fractional anisotropy at short diffusion times in fixed rat spinal cord. Front Phys. 2018;6(JUN):1–15.

282. Coupé P, Catheline G, Lanuza E, Manjón JV. Towards a unified analysis of brain maturation and aging across the entire lifespan: A MRI analysis. Hum Brain Mapp. 2017;38(11):5501–18.

283. Pomponio R, Erus G, Habes M, Doshi J, Srinivasan D, Mamourian E, et al. Harmonization of large MRI datasets for the analysis of brain imaging patterns throughout the lifespan. Neuroimage. 2020;208(July 2019).

284. Bethlehem RAI, Seidlitz J, White SR, Vogel JW, Anderson KM, Adamson C, et al. Brain charts for the human lifespan. Nature. 2022;604(7906):525–33.

285. Delvecchio G, Maggioni E, Pigoni A, Crespo-Facorro B, Nenadić I, Benedetti F, et al. Sexual Regional Dimorphism of Post-Adolescent and Middle Age Brain Maturation. A Multi-center 3T MRI Study. Front Aging Neurosci. 2021;13(February):1–11.

286. Grydeland H, Walhovd KB, Tamnes CK, Westlye LT, Fjell AM. Intracortical myelin links with performance variability across the human lifespan: Results from T1- and T2- weighted MRI myelin mapping and diffusion tensor imaging. J Neurosci. 2013;33(47):18618–30.

287. Yeatman JD, Wandell BA, Mezer AA. Lifespan maturation and degeneration of human brain white matter. Nat Commun. 2014;5.

288. Romero JE, Coupe P, Lanuza E, Catheline G, Manjón J V. Toward a unified analysis of cerebellum maturation and aging across the entire lifespan: A MRI analysis. Hum Brain Mapp. 2021;42(5):1287–303.

289. Chang YS, Owen JP, Pojman NJ, Thieu T, Bukshpun P, Wakahiro MLJ, et al. White matter changes of neurite density and fiber orientation dispersion during human brain maturation. PLoS One. 2015;10(6).

290. Kiely M, Triebswetter C, Cortina LE, Gong Z, Alsameen MH, Spencer RG, et al. Insights into human cerebral white matter maturation and degeneration across the adult lifespan. Neuroimage. 2022;247(October 2021):118727.

291. Westlye LT, Walhovd KB, Dale AM, Bjørnerud A, Due-Tønnessen P, Engvig A, et al. Life-span changes of the human brain white matter: Diffusion tensor imaging (DTI) and volumetry. Cereb Cortex. 2010;20(9):2055–68.

292. Lätt J, Nilsson M, Wirestam R, Ståhlberg F, Karlsson N, Cand M, et al. Regional values of diffusional kurtosis estimates in the healthy brain. J Magn Reson Imaging. 2013;37(3):610–8.

293. Das SK, Wang JL, Bing L, Bhetuwal A, Yang HF. Regional Values of Diffusional Kurtosis Estimates in the Healthy Brain during Normal Aging. Clin Neuroradiol. 2015;27(3):283–98.

294. Cheung MM, Hui ES, Chan KC, Helpern JA, Qi L, Wu EX. Does diffusion kurtosis imaging lead to better neural tissue characterization? A rodent brain maturation study. Neuroimage. 2009;45(2):386–92.

295. Rahman N, Xu K, Budde M, Brown A, Baron C. A longitudinal microstructural MRI dataset in healthy C57Bl/6 mice at 9.4 Tesla. Sci Data. 2023;10(94):1–16.

296. Hamilton J, Xu K, Brown A, Baron CA. Robust frequency-dependent diffusion kurtosis computation using an efficient direction scheme, axisymmetric modelling, and spatial regularization Authors. arXiv. 2023;

297. Borsos KB, Tse DHY, Dubovan PI, Baron CA. Frequency tuned bipolar oscillating gradients for mapping frequency dispersion of diffusion kurtosis in the human brain. 2023;89:756–66.

298. Barriere DA. Turone Mouse Brain Template and Atlas [Internet]. NeuroImaging Tools and Research Collaboratory. 2019. Available from: https://www.nitrc.org/projects/tmbta_2019/

299. Lebel C, Deoni S. The development of brain white matter microstructure. Neuroimage. 2018;182(June 2017):207–18.

300. Song SK, Sun SW, Ramsbottom MJ, Chang C, Russell J, Cross AH. Dysmyelination revealed through MRI as increased radial (but unchanged axial) diffusion of water. Neuroimage. 2002;17(3):1429–36.

301. Morterá P, Herculano-Houzel S. Age-related neuronal loss in the rat brain starts at the end of adolescence. Front Neuroanat. 2012;6(OCTOBER 2012):1–9.

302. Anderson AW, Xie J, Pizzonia J, Bronen RA, Spencer DD, Gore JC. Effects of cell volume fraction changes on apparent diffusion in human cells. Magn Reson Imaging. 2000;18(6):689–95.

303. Xu J, Does MD, Gore JC. Sensitivity of MR diffusion measurements to variations in intracellular structure: Effects of nuclear size. Magn Reson Med. 2009;61(4):828–33.

304. Aggarwal M, Burnsed J, Martin LJ, Northington FJ, Zhang J. Imaging neurodegeneration in the mouse hippocampus after neonatal hypoxia-ischemia using oscillating gradient diffusion MRI. Magn Reson Med. 2014;72(3):829–40.

305. Paolicelli RC, Bolasco G, Pagani F, Maggi L, Scianni M, Panzanelli P, et al. Synaptic pruning by microglia is necessary for normal brain development. Science (80-). 2011;333(6048):1456–8.

306. Szczepankiewicz F, van Westen D, Englund E, Westin CF, Ståhlberg F, Lätt J, et al. The link between diffusion MRI and tumor heterogeneity: Mapping cell eccentricity and density by diffusional variance decomposition (DIVIDE). Neuroimage. 2016;142:522–32.

307. Nishiyama A, Shimizu T, Sherafat A, Richardson WD. Life-long oligodendrocyte development and plasticity. Semin Cell Dev Biol. 2021;116(December 2020):25–37.

308. Yazdi A, Baharvand H, Javan M. Enhanced remyelination following lysolecithin-induced demyelination in mice under treatment with fingolimod (FTY720). Neuroscience. 2015;311:34–44.

309. Safaiyan S, Kannaiyan N, Snaidero N, Brioschi S, Biber K, Yona S, et al. Age-related myelin degradation burdens the clearance function of microglia during aging. Nat Neurosci. 2016;19(8):995–8.

310. Sloane JA, Hollander W, Rosene DL, Moss MB, Kemper T, Abraham CR. Astrocytic hypertrophy and altered GFAP degradation with age in subcortical white matter of the rhesus monkey. Brain Res. 2000;862(1–2):1–10.

311. Sabbatini M, Barili P, Bronzetti E, Zaccheo D, Amenta F. Age-related changes of glial fibrillary acidic protein immunoreactive astrocytes in the rat cerebellar cortex. Mech Ageing Dev. 1999;108(2):165–72.

312. Wang S, Lai X, Deng Y, Song Y. Correlation between mouse age and human age in anti-tumor research: Significance and method establishment. Life Sci. 2020;242(December 2019).

313. Arshad M, Stanley J, Raz N. Adult Age Differences in Subcortical Myelin Content Are Consistent with Protracted Myelination and Unrelated to Diffusion Tensor

Imaging Indices. Neuroimage. 2016;143:26–39.

314. Bouhrara M, Cortina L, Rejimon A, Khattar N, Bergeron C, Bergeron J, et al. Quantitative age-dependent differences in human brainstem myelination assessed using high-resolution magnetic resonance mapping. Neuroimage. 2020;206(1):116–307.

315. Dvorak A V., Swift-LaPointe T, Vavasour IM, Lee LE, Abel S, Russell-Schulz B, et al. An atlas for human brain myelin content throughout the adult life span. Sci Rep. 2021;11(1):1–13.

316. Kaczkurkin AN, Raznahan A, Satterthwaite TD. Sex differences in the developing brain: insights from multimodal neuroimaging. Neuropsychopharmacology. 2019;44(1):71–85.

317. Mouton PR, Long JM, Lei DL, Howard V, Jucker M, Calhoun ME, et al. Age and gender effects on microglia and astrocyte numbers in brains of mice. Brain Res. 2002;956(1):30–5.

318. Nelson LH, Saulsbery AI, Lenz KM. Small cells with big implications: Microglia and sex differences in brain development, plasticity and behavioral health. Prog Neurobiol. 2019;176(September 2018):103–19.

319. Falangola MF, Jensen JH, Babb JS, Hu C, Castellanos FX, Di Martino A, et al. Age-related non-Gaussian diffusion patterns in the prefrontal brain. J Magn Reson Imaging. 2008;28(6):1345–50.

320. Helpern JA, Adisetiyo V, Falangola MF, Hu C, Di Martino A, Williams K, et al. Preliminary evidence of altered gray and white matter microstructural development in the frontal lobe of adolescents with attention-deficit hyperactivity disorder: A diffusional kurtosis imaging study. J Magn Reson Imaging. 2011;33(1):17–23.

321. Lu H, Jensen JH, Ramani A, Helpern JA. Three-dimensional characterization of non-gaussian water diffusion in humans using diffusion kurtosis imaging. NMR Biomed. 2006;19(2):236–47.

322. Alves R, Henriques RN, Kerkelä L, Chavarrías C, Jespersen SN, Shemesh N. Correlation Tensor MRI deciphers underlying kurtosis sources in stroke. Neuroimage. 2022;247(December 2021):118833.

323. Novello L, Henriques RN, Ianuş A, Feiweier T, Shemesh N, Jovicich J. In vivo Correlation Tensor MRI reveals microscopic kurtosis in the human brain on a clinical 3T scanner. Neuroimage. 2022;254(November 2021).

324. Varma G, Duhamel G, De Bazelaire C, Alsop DC. Magnetization transfer from inhomogeneously broadened lines: A potential marker for myelin. Magn Reson Med. 2015;73(2):614–22.

325. Duhamel G, Prevost VH, Cayre M, Hertanu A, Mchinda S, Carvalho VN, et al. Validating the sensitivity of inhomogeneous magnetization transfer (ihMT) MRI to myelin with fluorescence microscopy. Neuroimage. 2019;199(January):289–303.

326. Maas AIR, Menon DK, David Adelson PD, Andelic N, Bell MJ, Belli A, et al.

Traumatic brain injury: Integrated approaches to improve prevention, clinical care, and research. Lancet Neurol. 2017;16(12):987–1048.

327. Report to Congress on mild traumatic brain injury in the United States : steps to prevent a serious public health problem. National Center for Injury Prevention and Control (U.S.). 2003.

328. Inglese M, Makani S, Johnson G, Cohen BA, Silver JA, Gonen O, et al. Diffuse axonal injury in mild traumatic brain injury: A diffusion tensor imaging study. J Neurosurg. 2005;103(2):298–303.

329. Mayer AR, Ling J, Mannell M V., Gasparovic C, Phillips JP, Doezema D, et al. A prospective diffusion tensor imaging study in mild traumatic brain injury. Neurology. 2010;74(8):643–50.

330. Bruce ED, Konda S, Dean DD, Wang EW, Huang JH, Little DM. Neuroimaging and traumatic brain injury: State of the field and voids in translational knowledge. Mol Cell Neurosci. 2015;66(PB):103–13.

331. Nakayama N, Okumura A, Shinoda J, Yasokawa YT, Miwa K, Yoshimura SI, et al. Evidence for white matter disruption in traumatic brain injury without macroscopic lesions. J Neurol Neurosurg Psychiatry. 2006;77(7):850–5.

332. Xu J, Rasmussen IA, Lagopoulos J, Haberg A. Diffuse axonal injury in severe traumatic brain injury visualized using high-resolution diffusion tensor imaging. J Neurotrauma. 2007;24(5):753–65.

333. Sinson G, Bagley LJ, Cecil KM, Torchia M, McGowan JC, Lenkinski RE, et al. Magnetization transfer imaging and proton MR spectroscopy in the evaluation of axonal injury: Correlation with clinical outcome after traumatic brain injury. Am J Neuroradiol. 2001;22(1):143–51.

334. Narayana PA, Yu X, Hasan KM, Wilde EA, Levin HS, Hunter J V., et al. Multi-modal MRI of mild traumatic brain injury. NeuroImage Clin. 2015;7:87–97.

335. Lehto LJ, Sierra A, Gröhn O. Magnetization transfer SWIFT MRI consistently detects histologically verified myelin loss in the thalamocortical pathway after a traumatic brain injury in rat. NMR Biomed. 2017;30(2):1–13.

336. Macruz FB de C, Feltrin FS, Zaninotto A, Guirado VM de P, Otaduy MCG, Tsunemi MH, et al. Longitudinal assessment of magnetization transfer ratio, brain volume, and cognitive functions in diffuse axonal injury. Brain Behav. 2022;12(3):1–13.

337. Vutskits L, Xie Z. Lasting impact of general anaesthesia on the brain: Mechanisms and relevance. Nat Rev Neurosci. 2016;17(11):705–17.

338. Jevtovic-Todorovic V, Olney JW. PRO: Anesthesia-induced developmental neuroapoptosis: Status of the evidence. Anesth Analg. 2008;106(6):1659–63.

339. Hoogenboom WS, Rubin TG, Ye K, Cui MH, Branch KC, Liu J, et al. Diffusion Tensor Imaging of the Evolving Response to Mild Traumatic Brain Injury in Rats. J Exp Neurosci. 2019;13(Md).

340. Bajwa NM, Lee JB, Halavi S, Hartman RE, Obenaus A. Repeated isoflurane in adult male mice leads to acute and persistent motor decrements with long-term modifications in corpus callosum microstructural integrity. J Neurosci Res. 2019;97(3):332–45.

341. Bodnar CN, Roberts KN, Higgins EK, Bachstetter AD. A Systematic Review of Closed Head Injury Models of Mild Traumatic Brain Injury in Mice and Rats. J Neurotrauma. 2019;36(11):1683–706.

342. Rowson S, Duma SM. Brain injury prediction: Assessing the combined probability of concussion using linear and rotational head acceleration. Ann Biomed Eng. 2013;41(5):873–82.

343. Cecyn MN, Abrahao KP. Where do you measure the Bregma for rodent stereotaxic surgery? IBRO Neurosci Reports. 2023;15(July):143–8.

344. Gold EM, Vasilevko V, Hasselmann J, Tiefenthaler C, Hoa D, Ranawaka K, et al. Repeated Mild Closed Head Injuries Induce Long-Term White Matter Pathology and Neuronal Loss That Are Correlated With Behavioral Deficits. ASN Neuro. 2018;10.

345. Mouzon B, Bachmeier C, Ojo J, Acker C, Ferguson S, Crynen G, et al. Chronic White Matter Degeneration, but No Tau Pathology at One-Year Post-Repetitive Mild Traumatic Brain Injury in a Tau Transgenic Model. J Neurotrauma. 2019;36(4):576–88.

346. Soni N, Mohamed AZ, Kurniawan ND, Borges K, Nasrallah F. Diffusion Magnetic Resonance Imaging Unveils the Spatiotemporal Microstructural Gray Matter Changes following Injury in the Rodent Brain. J Neurotrauma. 2019;36(8):1306–17.

347. To XV, Benetatos J, Soni N, Liu D, Mehari Abraha H, Yan W, et al. Ultra-High-Field Diffusion Tensor Imaging Identifies Discrete Patterns of Concussive Injury in the Rodent Brain. J Neurotrauma. 2021;38(8):967–82.

348. Hamilton J, Xu K, Geremia N, Prado VF, Prado MAM, Brown A, et al. Robust frequency-dependent diffusional kurtosis computation using an efficient direction scheme, axisymmetric modelling, and spatial regularization. Imaging Neurosci. 2024;2(December 2023):1–22.

349. Carlén M. What constitutes the prefrontal cortex? Science (80-). 2017;358(6362):478–82.

350. White ER, Pinar C, Bostrom CA, Meconi A, Christie BR. Mild Traumatic Brain Injury Produces Long-Lasting Deficits in Synaptic Plasticity in the Female Juvenile Hippocampus. J Neurotrauma. 2017;34(5):1111–23.

351. Namjoshi DR, Good C, Cheng WH, Panenka W, Richards D, Cripton PA, et al. Towards clinical management of traumatic brain injury: A review of models and mechanisms from a biomechanical perspective. DMM Dis Model Mech. 2013;6(6):1325–38.

352. Molina ISM, Salo RA, Abdollahzadeh A, Tohka J, Gröhn O, Sierra A. In vivo

diffusion tensor imaging in acute and subacute phases of mild traumatic brain injury in rats. eNeuro. 2020;7(3):1–18.

353. Hulkower MB, Poliak DB, Rosenbaum SB, Zimmerman ME, Lipton ML. A Decade of DTI in Traumatic Brain Injury : 10 Years and 100 Articles Later. AJNR. 2013;34(11):2064–74.

354. Lampinen B, Zampeli A, Björkman-Burtscher IM, Szczepankiewicz F, Källén K, Compagno Strandberg M, et al. Tensor-valued diffusion MRI differentiates cortex and white matter in malformations of cortical development associated with epilepsy. Epilepsia. 2020;61(8):1701–13.

355. Skinner NP, Kurpad SN, Schmit BD, Budde MD. Detection of acute nervous system injury with advanced diffusion-weighted MRI: A simulation and sensitivity analysis. NMR Biomed. 2015;28(11):1489–506.

356. Zhou M, Stobbe R, Szczepankiewicz F, Budde M, Buck B, Kate M, et al. Tensor-valued diffusion MRI of human acute stroke. Magn Reson Med. 2023;(August):1–16.

357. Madathil SK, Wilfred BS, Urankar SE, Yang W, Leung LY, Gilsdorf JS, et al. Early Microglial Activation Following Closed-Head Concussive Injury Is Dominated by Pro-Inflammatory M-1 Type. Front Neurol. 2018;9(NOV):1–14.

358. Ojo JO, Bachmeier C, Mouzon BC, Tzekov R, Mullan M, Davies H, et al. Ultrastructural changes in the white and gray matter of mice at Chronic time points after repeated concussive head injury. J Neuropathol Exp Neurol. 2015;74(10):1012–35.

359. Mannix R, Berglass J, Berkner J, Moleus PE, Qiu J, Ews NA, et al. Chronic gliosis and behavioral deficits in mice following repetitive mild traumatic brain injury. J Neurosurg. 2014;121(6):1342–50.

360. de Faria O, Pivonkova H, Varga B, Timmler S, Evans KA, Káradóttir RT. Periods of synchronized myelin changes shape brain function and plasticity. Nat Neurosci. 2021;24(11):1508–21.

361. Armstrong RC, Mierzwa AJ, Sullivan GM, Sanchez MA. Myelin and oligodendrocyte lineage cells in white matter pathology and plasticity after traumatic brain injury. Neuropharmacology. 2016;110:654–9.

362. Taib T, Leconte C, Van Steenwinckel J, Cho AH, Palmier B, Torsello E, et al. Neuroinflammation, myelin and behavior: Temporal patterns following mild traumatic brain injury in mice. PLoS One. 2017;12(9).

363. Spader HS, Dean DC, Curt LaFrance W, Raukar NP, Rees Cosgrove G, Eyerly-Webb SA, et al. Prospective study of myelin water fraction changes after mild traumatic brain injury in collegiate contact sports. J Neurosurg. 2019;130(4):1321–9.

364. Thal SC, Neuhaus W. The Blood-Brain Barrier as a Target in Traumatic Brain Injury Treatment. Arch Med Res. 2014;45(8):698–710.

365. Campbell JN, Low B, Kurz JE, Patel SS, Young MT, Churn SB. Mechanisms of

dendritic spine remodeling in a rat model of traumatic brain injury. J Neurotrauma. 2012;29(2):218–34.

366. Steuer E, Schaefer ML, Belluscio L. Using the olfactory system as an in vivo model to study traumatic brain injury and repair. J Neurotrauma. 2014;31(14):1277–91.

367. Petraglia AL, Plog BA, Dayawansa S, Chen M, Dashnaw ML, Czerniecka K, et al. The spectrum of neurobehavioral sequelae after repetitive mild traumatic brain injury: A novel mouse model of chronic traumatic encephalopathy. J Neurotrauma. 2014;31(13):1211–24.

368. Callahan CD, Hinkebein JH. Assessment of anosmia after traumatic brain injury: Performance characteristics of the University of Pennsylvania smell identification test. J Head Trauma Rehabil. 2002;17(3):251–6.

369. Yoon Y, Kim S, Seol Y, Im H, Park U, Han HB, et al. Increases of Phosphorylated Tau (Ser202/Thr205) in the Olfactory Regions Are Associated with Impaired EEG and Olfactory Behavior in Traumatic Brain Injury Mice. Biomedicines. 2022;10(4).

370. To XV, Vegh V, Owusu-Amoah N, Cumming P, Nasrallah FA. Hippocampal demyelination is associated with increased magnetic susceptibility in a mouse model of concussion. Exp Neurol. 2023;365(December 2022):114406.

371. Frankowski JC, Kim YJ, Hunt RF. Selective vulnerability of hippocampal interneurons to graded traumatic brain injury. Neurobiol Dis. 2019;129(July 2018):208–16.

372. Nonaka M, Taylor WW, Bukalo O, Tucker LB, Fu AH, Kim Y, et al. Behavioral and Myelin-Related Abnormalities after Blast-Induced Mild Traumatic Brain Injury in Mice. J Neurotrauma. 2021;38(11):1551–71.

373. Gupte R, Brooks W, Vukas R, Pierce J, Harris J. Sex Differences in Traumatic Brain Injury: What We Know and What We Should Know. J Neurotrauma. 2019;36(22):3063–91.

374. Späni CB, Braun DJ, Van Eldik LJ. Sex-related responses after traumatic brain injury: Considerations for preclinical modeling. Front Neuroendocrinol. 2018;50(January):52–66.

375. Duncan KA. Estrogen Formation and Inactivation Following TBI: What we Know and Where we Could go. Front Endocrinol (Lausanne). 2020;11(May):1–9.

376. Raghava N, Das BC, Ray SK. Neuroprotective effects of estrogen in CNS injuries: insights from animal models. Neurosci Neuroeconomics. 2017;Volume 6:15–29.

377. Dollé JP, Jaye A, Anderson SA, Ahmadzadeh H, Shenoy VB, Smith DH. Newfound sex differences in axonal structure underlie differential outcomes from in vitro traumatic axonal injury. Exp Neurol. 2018;300(October 2017):121–34.

378. Mack CM, Boehm GW, Berrebi AS, Denenberg VH. Sex differences in the distribution of axon types within the genu of the rat corpus callosum. Brain Res. 1995;697(1–2):152–6.

379. Pesaresi M, Soon-Shiong R, French L, D.R. Kaplan, Miller FD, Paus T. Axon diameter and axonal transport: In vivo and in vitro effects of androgens. Neuroimage. 2015;115:191–201.

380. Alexander DC, Hubbard PL, Hall MG, Moore EA, Ptito M, Parker GJM, et al. Orientationally invariant indices of axon diameter and density from diffusion MRI. Neuroimage. 2010;52(4):1374–89.

381. Perrin JS, Hervé PY, Leonard G, Perron M, Pike GB, Pitiot A, et al. Growth of white matter in the adolescent brain: Role of testosterone and androgen receptor. J Neurosci. 2008;28(38):9519–24.

382. Reeves TM, Phillips LL, Povlishock JT. Myelinated and unmyelinated axons of the corpus callosum differ in vulnerability and functional recovery following traumatic brain injury. Exp Neurol. 2005;196(1):126–37.

383. Streifer M, Brown AM, Porfido T, Anderson EZ, Buckman JF, Esopenko C. The potential role of the cervical spine in sports-related concussion: Clinical perspectives and considerations for risk reduction. J Orthop Sports Phys Ther. 2019;49(3):202–8.

384. Nutt S, McKay MJ, Gillies L, Peek K. Neck strength and concussion prevalence in football and rugby athletes. J Sci Med Sport. 2022;25(8):632–8.

385. Caccese JB, Buckley TA, Tierney RT, Arbogast KB, Rose WC, Glutting JJ, et al. Head and neck size and neck strength predict linear and rotational acceleration during purposeful soccer heading. Sport Biomech. 2018;17(4):462–76.

386. Lindhardt TB, Gutiérrez-Jiménez E, Liang Z, Hansen B. Male and Female C57BL/6 Mice Respond Differently to Awake Magnetic Resonance Imaging Habituation. Front Neurosci. 2022;16(June):1–14.

387. Saito T, Mihira N, Matsuba Y, Sasaguri H, Hashimoto S, Narasimhan S, et al. Humanization of the entire murine Mapt gene provides a murine model of pathological human tau propagation. J Biol Chem. 2019;294(34):12754–65.

388. Baglietto-Vargas D, Forner S, Cai L, Martini AC, Trujillo-Estrada L, Swarup V, et al. Generation of a humanized Aβ expressing mouse demonstrating aspects of Alzheimer's disease-like pathology. Nat Commun. 2021;12(1):1–16.

389. Obenaus A, Rodriguez-Grande B, Lee J Bin, Dubois CJ, Fournier ML, Cador M, et al. A single mild juvenile TBI in male mice leads to regional brain tissue abnormalities at 12 months of age that correlate with cognitive impairment at the middle age. Acta Neuropathol Commun. 2023;11(1):1–20.

390. Cao Y, Ni C, Li Z, Li L, Liu Y, Wang C, et al. Isoflurane anesthesia results in reversible ultrastructure and occludin tight junction protein expression changes in hippocampal blood-brain barrier in aged rats. Neurosci Lett. 2015;587:51–6.

391. Wang HL, Ma RH, Fang H, Xue ZG, Liao QW. Impaired spatial learning memory after isoflurane anesthesia or appendectomy in aged mice is associated with microglia activation. J Cell Death. 2015;8:9–19.

392. Hohlbaum K, Bert B, Dietze S, Palme R, Fink H, Thöne-Reineke C. Severity

classification of repeated isoflurane anesthesia in C57BL/6JRj mice - Assessing the degree of distress. PLoS One. 2017;12(6):1–21.

393. Lindhardt TB, Skoven CS, Bordoni L, Østergaard L, Liang Z, Hansen B. Anesthesia-related brain microstructure modulations detected by diffusion magnetic resonance imaging. NMR Biomed. 2023;(July):1–18.

394. Johnson GA, Tian Y, Ashbrook DG, Cofer GP, Cook JJ, Gee JC, et al. Merged magnetic resonance and light sheet microscopy of the whole mouse brain. Proc Natl Acad Sci. 2023;120(17).

395. Jelescu IO, Palombo M, Bagnato F, Schilling KG. Challenges for biophysical modeling of microstructure. J Neurosci Methods. 2020;344(July):108861.

396. Lampinen B, Szczepankiewicz F, Mårtensson J, van Westen D, Sundgren PC, Nilsson M. Neurite density imaging versus imaging of microscopic anisotropy in diffusion MRI: A model comparison using spherical tensor encoding. Neuroimage. 2017;147(July 2016):517–31.

397. Laricchiuta D, Papi M, Decandia D, Panuccio A, Cutuli D, Peciccia M, et al. The role of glial cells in mental illness: a systematic review on astroglia and microglia as potential players in schizophrenia and its cognitive and emotional aspects. Front Cell Neurosci. 2024;18(February):1–26.

398. Uddin MS, Lim LW. Glial cells in Alzheimer's disease: From neuropathological changes to therapeutic implications. Ageing Res Rev. 2022;78(October 2021):101622.

399. He Y, Aznar S, Siebner HR, Dyrby TB. In vivo tensor-valued diffusion MRI of focal demyelination in white and deep grey matter of rodents. NeuroImage Clin. 2021;30.

400. Lu L, Mao H. Quantifying the Effect of Repeated Impacts and Lateral Tip Movements on Brain Responses during Controlled Cortical Impact. J Neurotrauma. 2019;36(11):1828–35.

401. Cole TJ. The development of growth references and growth charts. Ann Hum Biol. 2012;39(5):382–94.

402. Reynolds JE, Long X, Paniukov D, Bagshawe M, Lebel C. Calgary Preschool magnetic resonance imaging (MRI) dataset. Data Br. 2020;29:105224.

403. Wang J, Lytle MN, Weiss Y, Yamasaki BL, Booth JR. A longitudinal neuroimaging dataset on language processing in children ages 5, 7, and 9 years old. Sci Data. 2022;9(1):1–13.

404. HCP Lifespan Studies [Internet]. Connectome Coordination Facility. 2024. Available from: https://www.humanconnectome.org/lifespan-studies

405. Barlow KM, Marcil LD, Dewey D, Carlson HL, Macmaster FP, Brooks BL, et al. Cerebral Perfusion Changes in Post-Concussion Syndrome: A Prospective Controlled Cohort Study. J Neurotrauma. 2017;34(5):996–1004.

406. Drieu A, Lanquetin A, Prunotto P, Gulhan Z, Pédron S, Vegliante G, et al.

Persistent neuroinflammation and behavioural deficits after single mild traumatic brain injury. J Cereb Blood Flow Metab. 2022;42(12):2216–29.

407. Healey K, Fang Z, Smith A, Zemek R, Ledoux AA. Adolescents with a concussion have altered brain network functional connectivity one month following injury when compared to adolescents with orthopedic injuries. NeuroImage Clin. 2022;36(March).

408. Veeramuthu V, Seow P, Narayanan V, Wong JHD, Tan LK, Hernowo AT, et al. Neurometabolites Alteration in the Acute Phase of Mild Traumatic Brain Injury (mTBI): An in Vivo Proton Magnetic Resonance Spectroscopy (1H-MRS) Study. Acad Radiol. 2018;25(9):1167–77.

409. Arezza NJJ, Abbas H, Chadwick C, Johnsrude IS, Burneo J, Khan AR, et al. Microscopic fractional anisotropy asymmetry in unilateral temporal lobe epilepsy. medRxiv. 2023;

410. Cloney MB, Smith ZA, Weber KA, Parrish TB. Quantitative Magnetization Transfer MRI Measurements of the Anterior Spinal Cord Region are Associated with Clinical Outcomes in Cervical Spondylotic Myelopathy. Spine (Phila Pa 1976). 2018;43(10):675–80.

411. Yarnykh VL. Actual flip-angle imaging in the pulsed steady state: A method for rapid three-dimensional mapping of the transmitted radiofrequency field. Magn Reson Med. 2007;57(1):192–200.

412. Köster J, Mölder F, Jablonski KP, Letcher B, Hall MB, Tomkins-Tinch CH, et al. Sustainable data analysis with Snakemake. F1000Research. 2021;10.

413. Hagiwara A, Hori M, Kamagata K, Warntjes M, Matsuyoshi D, Nakazawa M, et al. Myelin Measurement: Comparison between Simultaneous Tissue Relaxometry, Magnetization Transfer Saturation Index, and T1w/T2w Ratio Methods. Sci Rep. 2018;8(1):1–12.

414. Rahman N, Xu K, Budde M, Brown A, Baron C. A longitudinal microstructural MRI dataset in healthy C57Bl/6 mice at 9.4 Tesla. Federated Research Data Repository. 2022.

415. Klein A, Andersson J, Ardekani BA, Ashburner J, Avants B, Chiang MC, et al. Evaluation of 14 nonlinear deformation algorithms applied to human brain MRI registration. Neuroimage. 2009;46(3):786–802.

416. Baron C. Baron Lab Pulse Sequences. 2021.

Curriculum Vitae

Name: Naila Rahman

Post-secondary Education and Degrees:

University of Windsor
Windsor, Ontario, Canada
2019 B.Sc.

Western University
London, Ontario, Canada
2024 Ph.D.

Honours and Awards:

Graduate:

NSERC Canada Graduate Scholarship - Doctoral
2022 – 2024

Best Oral Presentation Award (Imaging Network of Ontario)
2022, 2024

ISMRM Diffusion Workshop Trainee Stipend
2022

ISMRM Educational Stipend
2020, 2021, 2022

Ontario Graduate Scholarship
2020, 2021

NSERC Canada Graduate Scholarship – Master's
2019

Western Graduate Research Scholarship
2019, 2020, 2021, 2022, 2023, 2024

Undergraduate:

Bronze LEAD Medallion Scholar
2019

Joan and Cliff Hatch Scholarship
2016, 2017

Dean's Honour Roll

2016, 2017, 2018, 2019

Ontario Horatio Alger Scholarship
2015 - 2019

Related Work Experience   Teaching Assistant (Physics II), Department of Physics
University of Windsor
2019

Publications:

Peer-reviewed Journal Articles

Rahman N, Xu K, Budde MD, Brown A, Baron CA.
A longitudinal microstructural MRI dataset in healthy C57Bl/6 mice at 9.4 Tesla. 2023. *Scientific Data* 10(94): 1-16.

Rahman N,* Ramnarine J,* Xu K, Brown A, Baron CA.
Test-retest reproducibility of in vivo magnetization transfer ratio and saturation index in mice at 9.4 Tesla. 2022. *J Magn Reson Imaging* 1–11.

Rahman N, Xu K, Omer M, Budde MD, Brown A, Baron CA.
Test-retest reproducibility of in vivo oscillating gradient and microscopic anisotropy diffusion MRI in mice at 9.4 Tesla. 2021. *PLOS ONE* 16(11): e0255711.

Youssef S, Seviaryna I, Shum D, Maeva E, Malyarenko E, **Rahman N**, Maev RG.
High-resolution quantitative acoustic microscopy of cutaneous carcinoma and melanoma: Comparison with histology. 2019. *Skin Res Technol* 25: 662- 671.

Manuscripts in Progress

Rahman N,* Hamilton J,* Xu K, Brown A, Baron CA.
Tensor-valued and frequency-dependent diffusion MRI and magnetization transfer saturation MRI evolution during adult mouse brain maturation. 2023. *arXiv*: 2309.15202 [physics.med-ph].

Presentations

> i.   *Podiums*

Rahman N, Xu K, Budde MD, Brown A, Baron CA.
2023. Probing Microstructural Changes in a Mouse Model of Mild Traumatic Brain Injury Using Diffusion MRI Techniques. *CARO-COMP (Canadian Association of Radiation Oncology – Canadian Organization of Medical Physicists) Joint Scientific Meeting 2023.* Montreal, QC, Canada.

Rahman N.

2023. Advanced Diffusion MRI Techniques Probe Concussion *In Vivo*. *CARO-COMP Joint Scientific Meeting 2023*. Science Spoken Succinctly (S3) Competition. Montreal, QC, Canada.

Santini T, **Rahman N**, Shim A, Inoue W, Everling S, Baron CA.
2022. Oscillating Gradient (OGSE) and Microscopic Anisotropy Diffusion in the in vivo and ex vivo Marmoset Brain. Proceedings of the 30th Annual Meeting of the International Society of Magnetic Resonance in Medicine. London, England, UK.

Rahman N, Xu K, Brown A, Baron CA.
2022. Advanced diffusion MRI metrics reveal acute sensitivity to mild traumatic brain injury in a mouse model. Imaging Network of Ontario 2022. Virtual Meeting. *Best Oral Presentation Award.*

Rahman N, Xu K, Brown A, Baron CA.
2022. Advanced diffusion MRI metrics reveal acute sensitivity to mild traumatic brain injury in a mouse model. Robarts Research Retreat. London, ON, Canada.

Rahman N, Xu K, Arezza N, Borsos K, Brown A, Baron CA.
2021. Microstructural Diffusion MRI in Mouse Models of Severe and Repetitive Mild Traumatic Brain Injury. Imaging Network Ontario 2021. Virtual Meeting.

Omer M, **Rahman N**, Arezza N, Baron CA.
2021. Reliability assessment of cerebrospinal fluid suppressed microscopic fractional anisotropy. Imaging Network Ontario 2021. Virtual Meeting.

Rahman N, Xu K, Brown A, Baron CA.
2021. Frequency Dependent Diffusivity in Mouse Models of Severe and Repetitive Mild Traumatic Brain Injury. Robarts Research Retreat. Virtual Meeting.

Rahman N, Xu K, Brown A, Baron CA.
2020. Validation of Advanced Approaches for Microstructural Diffusion MRI. Robarts Research Retreat. London, ON, Canada.

Rahman N, Mushtaha FN, Kuehn TK, Arezza NJJ, Khan AR, Brown A, Baron CA.
2020. Beyond the Diffusion Tensor: Validation of Advanced Approaches for Microstructural Diffusion MRI. Imaging Network Ontario 2020. Toronto, ON, Canada.

Rahman N, Nazer R, Seviaryna I, Shum D, Malyarenko E, Maev RG.
2018. Ultra-High Resolution Acoustic Microscopy for Cancer Studies. Windsor Cancer Research Group 2018. Windsor, ON, Canada.

Rehse SJ, Paulick A, Piazza A, Heath C, Malenfant DJ, **Rahman N**, Dubovan P, Valente R, Riberdy V.

2018. Biomedical and Biological Applications of Laser-Induced Breakdown Spectroscopy. Pittsburg Conference on Analytical Chemistry and Applied Spectroscopy 2018. Pittsburg, Pennsylvania, USA.

ii.   *Posters*

Park CK, **Rahman N**, Jeon P, Knier N, Kamar F, Tan J, Evans M, Ward A, Surry K, Karnas S.
2023. Enhancing Professional Development for Medical Physicists Through Fostering a Student-Centered Learning Environment: Team-Based Learning & Pedagogical Curriculum Development. Proceedings of the 65th Annual Meeting of the American Association of Physicists in Medicine (AAPM). Houston, TX, United States.

Rahman N, Xu K, Budde MD, Brown A, Baron CA.
2023. Evolution of Microstructural Changes in a Mouse Model of Mild Traumatic Brain Injury. Proceedings of the 31st Annual Meeting of the International Society of Magnetic Resonance in Medicine (ISMRM). Toronto, ON, Canada.

Santini T, **Rahman N**, Shim A, Budde MD, Everling S, Baron CA.
2023. Evidence of axon beading and loss of extracellular fluid following perfusion and fixation of the marmoset brain. Proceedings of the 31st Annual Meeting of the International Society of Magnetic Resonance in Medicine (ISMRM). Toronto, ON, Canada.

Hamilton J, **Rahman N**, Xu K, Brown A, Baron CA.
2023. Investigating Frequency Dependent Kurtosis Evolution in Repeated Mild Traumatic Brain Injury in Mice. Proceedings of the 31st Annual Meeting of the International Society of Magnetic Resonance in Medicine (ISMRM). Toronto, ON, Canada.

Rahman N, Xu K, Budde MD, Brown A, Baron CA.
2022. An open-source *in vivo* rodent microstructural MRI dataset and analysis pipeline. ISMRM Workshop on Diffusion MRI: From Research to Clinic. Amsterdam, The Netherlands.

Santini T, **Rahman N**, Shim A, Inoue W, Everling S, Baron CA.
2022. Investigating microstructure changes between in-vivo and ex-vivo marmoset brains using advanced diffusion MRI at 9.4T and Monte Carlo simulations. ISMRM Workshop on Diffusion MRI: From Research to Clinic. Amsterdam, The Netherlands.

Rahman N, Xu K, Brown A, Baron CA.
2022. Diffusion dispersion and microscopic fractional anisotropy reveal acute sensitivity to mild traumatic brain injury in a mouse model. Proceedings of the 30th Annual Meeting of the International Society of Magnetic Resonance in Medicine. London, England, UK.

Santini T, **Rahman N**, Shim A, Inoue W, Everling S, Baron CA.

2022. Investigating microstructure changes between in vivo and ex vivo marmoset brains using advanced diffusion MRI at 9.4T. Robarts Research Retreat. London, ON, Canada.

Rahman N, Xu K, Arezza N, Borsos K, Budde MD, Brown A, Baron CA.
2021. Microstructural Diffusion MRI in Mouse Models of Severe and Repetitive Mild Traumatic Brain Injury. Proceedings of the 29th Annual Meeting of the International Society of Magnetic Resonance in Medicine. Virtual Meeting.

Rahman N, Nazer R, Seviaryna I, Shum D, Malyarenko E, Maev RG.
2018. Digital Ultrasonic Histology for Skin Cancer Diagnosis. Windsor Cancer Research Group 2018. Windsor, ON, Canada.

Nazer R, **Rahman N**, Seviaryna I, Shum D, Malyarenko E, Maev RG.
2018. Characterizing Cutaneous Skin Carcinomas with High-Resolution Acoustic Microscopy. Windsor Cancer Research Group 2018. Windsor, ON, Canada.